Study of transfer reactions induced by a 16C beam

Xesus Pereira Lopez

Normandie Université

Pour obtenir le diplôme de doctorat

Constituants Élémentaires et Physique Théorique

Préparée au sein de l'Université de Caen-Basse Normandie

En partenariat international avec l'Universidade de Santiago de Compostela, Espagne

Study of transfer reactions induced by a ^{16}C beam

Présentée et soutenue par
Xesús Pereira López

Thèse soutenue publiquement le 20/12/2016 devant le jury composé de		
M. Antonio Matías MORO MUÑOZ	Profesor Titular / Universidad de Sevilla	Examinateur
M. Karsten RIISAGER	Lektor, Dr. Scient / Aarhus Universitet	Examinateur
M. Didier BEAUMEL	Directeur de Recherches / INPO Orsay	Examinateur
M. Nigel ORR	Directeur de Recherches / LPC Caen	Directeur de thèse
Mme Beatriz FERNÁNDEZ DOMÍNGUEZ	Prof. Axudante Doutora / Universidade de Santiago de Compostela	Directrice de thèse

Thèse dirigée par
Nigel ORR, LPCCaen, et Beatriz FERNÁNDEZ-DOMÍNGUEZ, Universidade de Santiago de Compostela

UNICAEN université de Caen Basse-Normandie

ED 181 SIMEM

lpc caen laboratoire de physique corpusculaire

Abstract

It has been demonstrated that the traditional magic numbers evolve when nuclei far from stability are explored. Recent experiments have provided evidence to support the existence of new shell gaps at N=14 and N=16 in neutron-rich oxygen isotopes associated with the vanishing of the N=20 shell gap. However, in the neutron-rich carbon isotopes, the extent to which these gaps persist is unclear. In an effort to answer this question we have attempted to probe the low-lying level structure of ^{17}C using the (d,p) transfer reaction to locate the single-particle orbitals involved in the formation of the N=14 and N=16 shell gaps.

The experiment was carried out at the GANIL facility. A pure secondary beam of ^{16}C at 17.2 AMeV produced by fragmentation in the LISE3 spectrometer was used to bombard a CD_2 target. The light ejectiles were detected using the TIARA and MUST2 silicon (Si) strip arrays while a Si-Si-CsI telescope was placed at zero degrees to identify beam-like residues. In addition, four HPGe-EXOGAM clover detectors were used to measure the gamma-rays arising from ^{17}C bound excited states.

The measured angular distributions of ^{17}C confirm the spin and parity assignments of $3/2^+$, $1/2^+$ and $5/2^+$ for the ground and the first and second excited states located at 217 keV and 335 keV respectively. The spectroscopic factors deduced for these excited states indicate a large single-particle strength (70%), in agreement with shell model calculations. This results seem to indicate the non existence of the N=14 gap. With a strong $\ell = 0$ valence neutron component and a low separation energy, the first excited state of ^{17}C appears as a good one-neutron halo candidate.

Acknowledgments

First of all, my deepest gratitude must go to Dr Beatriz Fernández-Domínguez, who initiated me into the fascinating field of nuclear physics and gave me the opportunity to carry out this work. Thanks you for the constant support and the fruitful discussions we had throughout the last few years. I am also extremely grateful to Dr Franck Delaunay for his excellent guidance, his enduring patience to answer all my questions and his tireless efforts reviewing this manuscript. A massive thanks is due to Dr Nigel Orr for providing me advice using his vast knowledge and experience in numerous analysis meetings. I am very fortunate to have them as my supervisors. I have learnt and enjoyed a lot working with them.

I would like to express my gratitude to those who contributed to get the experiment up and running. The help of the collaborators from the LPC Caen, University of Santiago de Compostela, University of Surrey, IPN Orsay, University of Birmingham, GANIL, CEA Saclay, LNS Catania and iFIN-HH is much appreciated.

Last but not least, I wish to thank my colleagues of the LPC Caen, specially the *Exotiques group*, for the warm welcome and the friendly atmosphere that made me feel at home right away. Special mention to Dr Sylvain Leblond for showing me the ropes during my days in Caen and for his invaluable assistance with the paperwork. And thanks to my fellows of the GENP group, it has been a pleasure to work with them all.

Contents

List of Figures

List of Tables

Introduction

The study of the nuclear structure was first investigated through reactions with stable and near-stable nuclei. These studies brought experimental information supporting the idea of shell structure in nuclei and, as a consequence, led to the single-particle model that successfully explains the magic numbers as shell closures. The single-particle model describes the nucleus as a system of non-interacting nucleons populating energy levels generated by a mean field due to the whole nucleus.

However, there are only 270 stable isotopes and 50 naturally occurring radioactive isotopes, while some models predict up to seven thousand radionuclei, the study of which would challenge the description of the nuclear structure through the single-particle model, derived from stable and near-stable nuclei.

With the development of the beam production techniques, many radioactive ion beam facilities have been built as the will to explore these so-called *exotic nuclei* arose, and the persistence of these magic numbers for nuclei far from stability was investigated for the first time. Experimental evidence gathered during the last three decades pointed out that the magic numbers evolve as one moves from the valley of stability towards the drip lines.

The evolution of the N=20 shell gap in the vicinities of the neutron drip line has been addressed by several studies, both theoretically and experimentally, in recent years. Thanks to these works, the vanishing of the N=20 shell closure and the emergence of a new magic number at N=16 in its place is now widely accepted and much better understood. In particular, the melting of the N=20 shell gap and the emergence of new magic numbers at N=16 and N=14 has been observed in neutron rich oxygen isotopes [27].

The main goal of this work is studying if these new magic numbers are present in neutron rich carbon isotopes by locating the single-particle energies for the $d_{5/2}$, $s_{1/2}$ and $d_{3/2}$ orbitals in ^{17}C via the ^{16}C(d,p)^{17}C one-neutron transfer reaction.

The spectroscopy of ^{17}C has been investigated before. The ground state has a $3/2^+$ configuration and it has two low-lying excited states, very close to the n-separation

threshold at 0.73 MeV, measured at 210 keV and 330 keV, assigned to $1/2^+$ and $5/2^+$ respectively [29]. However, there is no information on the single particle nature of these excited states. Several unbound states have been observed, although the states carrying the $d_{3/2}$ strength have not been located yet since no direct measure of spin and parity has been made so far.

Angular distributions of ^{16}C(d,p) to the three bound states in ^{17}C will be measured and will allow us to deduce the spin and parity assignments that will be compared to previous measurements and to measure their spectroscopic factors for first time. In particular, the spectroscopic factor of the $\ell = 0$ configuration in the $1/2^+$ first excited state of ^{17}C will give further information on the possible development of a neutron halo for this state.

This thesis is organized as follows: Chapter 2 provides a detailed overview of the relevant theory for this work, including the shell modell, magic numbers evolution, direct reactions, and the theoretical models used to describe one-neutron transfer reactions. Current knowledge of the states in ^{17}C is also presented in this chapter. The details of the experimental setup are presented in Chapter 3, together with the description of the detection systems involved, the radioactive beam production and the target thickness measurements. This chapter includes as well information concerning the electronics and the data acquisition system. Chapter 4 explains the data analysis performed and the results are then presented and discussed in Chapter 5, including reaction cross sections and spectroscopic factors of the bound states in ^{17}C.

Chapter 2

Theory

The earliest nuclear model is the *liquid drop model*, according to which the nucleus behaves like a drop of an hypothetical incompressible fluid made of protons and neutrons. It was first proposed by George Gamow [1] in 1930, formulated in 1935 by Carl Friedrich von Weizsäcker [2] and later developed by Niels Bohr and John Archibald Wheeler in 1939 to explain the nuclear fission phenomenon [3]. Although it fails to explain all the nuclear features, it explains the spherical shape of most nuclei and gives an useful prediction of the nuclear binding energy.

The mathematical analysis of this theory produces an equation known as *Bethe-Weizsäcker formula* or, most commonly, *semi-empirical mass formula*, that provides an excellent estimation of the nuclear binding energy, B, in terms of the atomic number, Z, and the mass number, A:

$$B = a_V A - a_s A^{2/3} - a_C \frac{Z(Z-1)}{A^{1/3}} - a_A \frac{(A-2Z)^2}{A} \pm \delta(A,Z) \tag{2.1}$$

The five terms in previous equation are due to volume, surface, Coulomb, symmetry and pairing effects respectively[1], the first three are derived directly from the liquid drop model, while the latter two terms were included to account for the non collective properties of the nuclei.

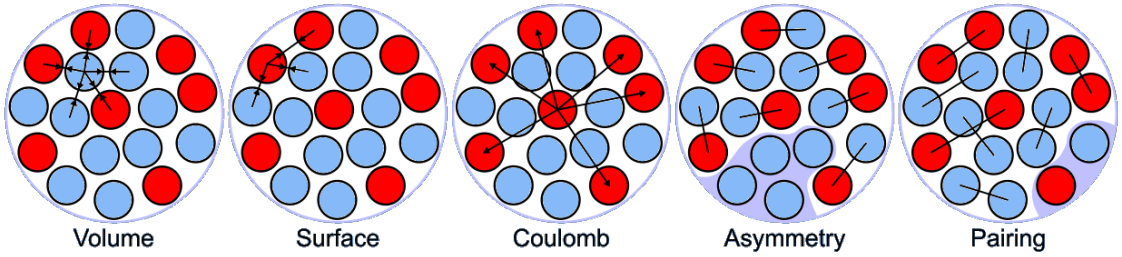

Figure 2.1: Schematics of the 5 terms involved in the semi-empirical mass formula.

[1] A detailed derivation of each term can be found in references [4–6]

Although the coefficients a_V, a_S, a_C, a_A and a_P are adjusted to obtain the best agreement with the experimental binding energy measurements, the semi-empirical mass formula fails to reproduce the local peaks in the B/A experimental points indicated in figure 2.2. This means that nuclei are more tightly bound than expected by the liquid drop model in the vicinity of certain values of the number of protons and neutrons known as *magic numbers*. This evidence hints at existence of internal structure within the nucleus, leading to the nuclear shell model.

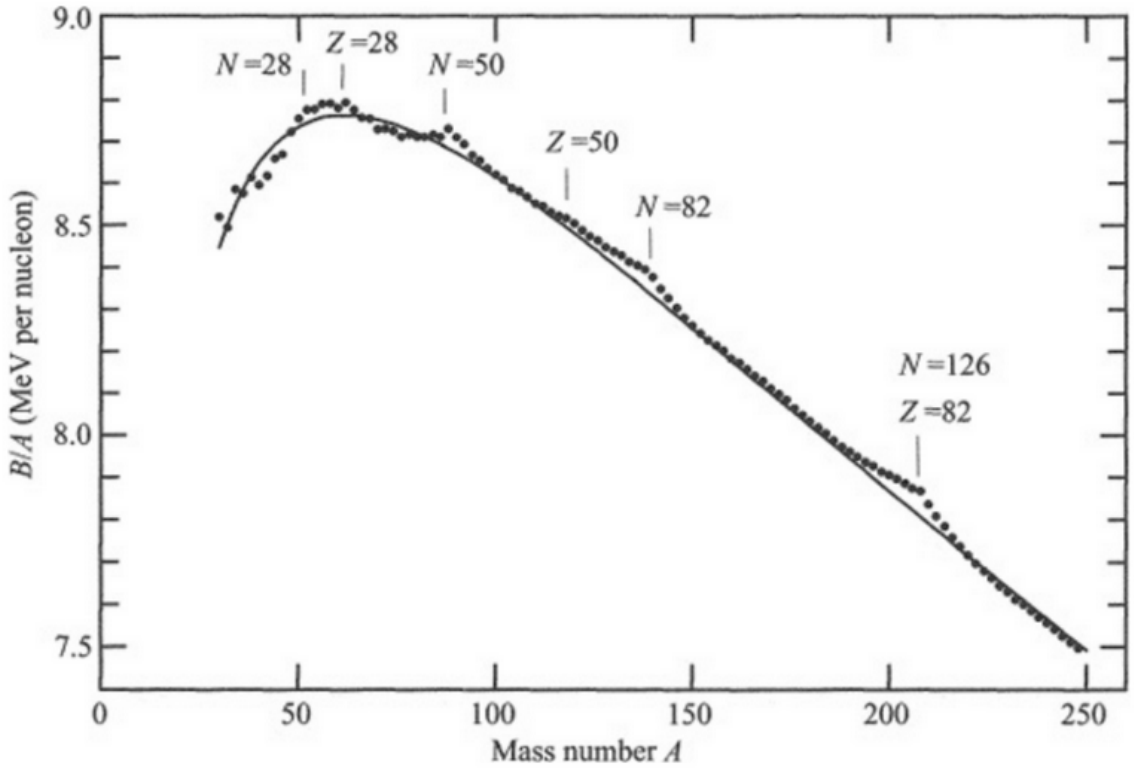

Figure 2.2: Semi-empirical mass formula predictions for the binding energy per nucleon, B/A, as a function of mass number, A, with $a_V = 15.56MeV$, $a_S = 17.23MeV$, $a_C = 0.7MeV$ and $a_A = 23.28MeV$, for odd-even nuclei so that there is no pairing effect. Experimental values are represented by points [5].

2.1 Nuclear Shell Model

The first hypothesis of the existence of shell structure within the nuclei was suggested by James H. Bartlett in 1932 [7], who argued that the stability of ^{4}He and ^{16}O, and hence the *magic numbers* 2 and 8, could be explained with closed shells in a model analogous to the Bohr model of the atom. This idea was further developed by W. Elsasser in 1933 [8], who proposed a model where the nucleons fill energy levels generated by some sort of effective potential well created by all the other nucleons. However, the theory was refused at that time due to the lack of experimental evidence to support it.

One and a half decade later, in 1948, Maria Goeppert-Mayer presented experimental data indicating a particular stability of shells of 50 and 82 protons and 50, 82 or 126 neutrons [9], but the fact that the model was not capable of reproducing the higher shell closures using simple potential wells was still not so convincing.

Much work was done to reproduce the observed shell structure until success was finally achieved one year later in 1949, when Mayer [10] and Haxel, Jensen and Suess [11] found simultaneously that the shell closures could be replicated by adding to the potential well a strong spin-orbit interaction which splits the energy levels in terms of the orientation of the intrinsic spin of the nucleon relative to its orbital angular momentum.

The accomplishment of 1949 opened a new gate to progress in our understanding of nuclear structure. Since then, many theoretical and experimental efforts have been made with the aim of explaining through the shell model nuclear features such as binding energies, spins and parities, excitation energies, decay widths, among others; and the magic numbers became a fundamental observable in nuclear physics.

2.1.1 Mean field model

As the nuclei are subjected to the rules of quantum mechanics, the energy levels that a single nucleon can occupy inside the nucleus can be calculated by solving the Schrödinger equation for a nucleon moving in a potential well due to the nuclear core:

$$\left[-\frac{\hbar^2}{2m}\nabla^2 + V(\vec{r})\right]\psi(\vec{r}) = E\psi(\vec{r}) \tag{2.2}$$

where m is the mass of the nucleon, E is the energy eigenvalue, $\psi(\vec{r})$ is the nucleon wave function, and $V(\vec{r})$ is the potential felt by the nucleon. This equation will have solutions only for certain values of energy E corresponding to the predicted single-particle states, which are strongly dependent on the choice of the potential $V(r)$.

Historically, one of the most fruitful approaches is to assume that the nucleons are moving in an effective potential $V_{eff}(r)$ generated by all the other nucleons within the nucleus. This effective potential includes the central nuclear potential V_N and the spin-orbit coupling term V_{so}, the Coulomb potential V_C and the centrifugal effect due to the relative angular momentum between the nucleon and the nucleus itself.

$$V_{eff}(r) = V_N(r) + V_{so}(r) + V_C(r) + \frac{l(l+1)\hbar^2}{2\mu r^2} \tag{2.3}$$

The Coulomb part of the potential is taken to be that arising from a uniform charge distribution over a sphere of radius R, while the spin-orbit term is written as $V_{so}(r)\vec{l}\cdot\vec{s}$.

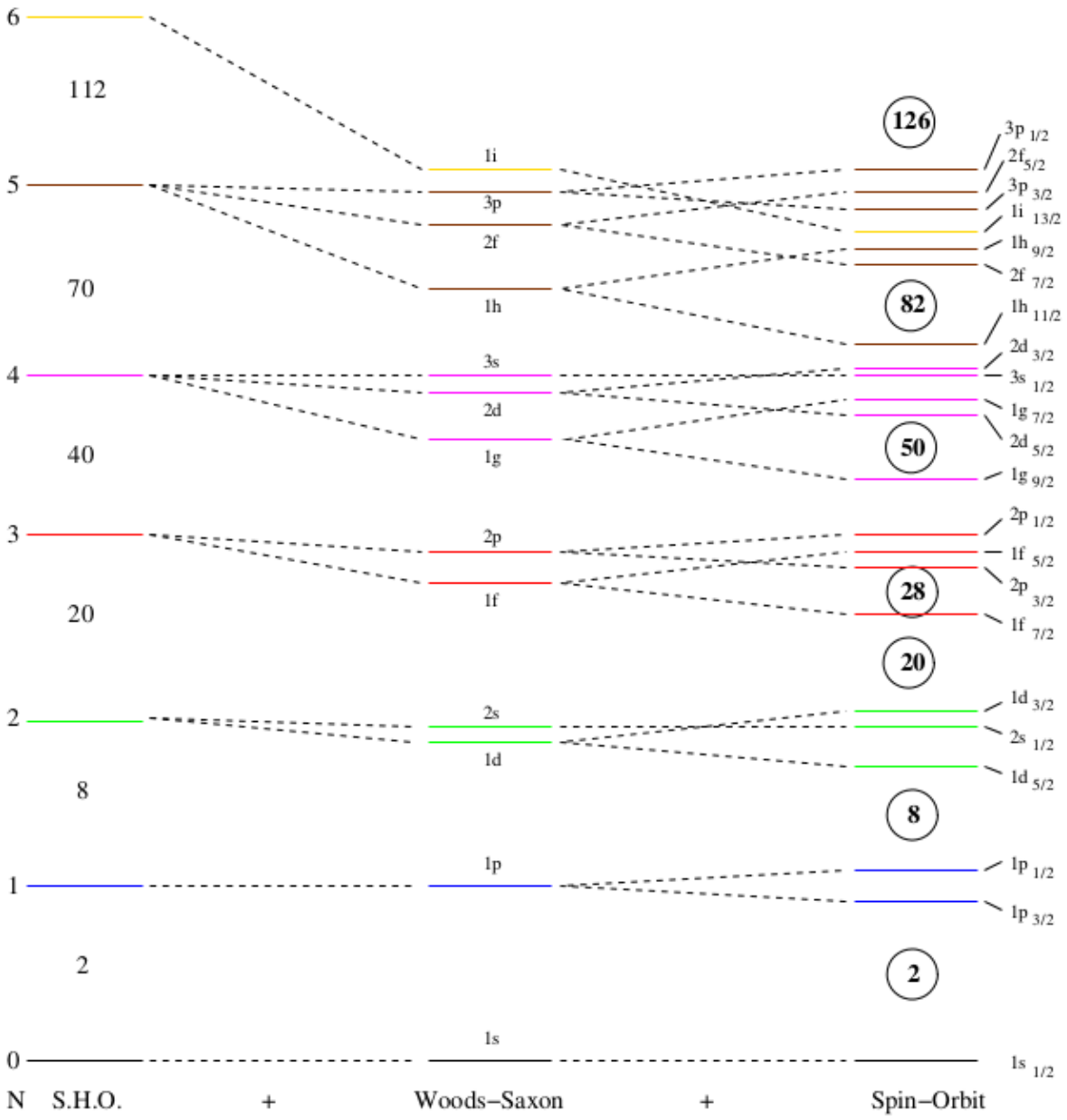

Figure 2.3: Energy level sequence calculated for several potentials. From left to right the spherical harmonic oscillator and the Woods-Saxon potential without and with the spin-orbit term. The levels are tagged with the corresponding quantum numbers nlj*, and their degeneracy is given by* 2j+1*. When several energy levels lie close together they form a nuclear shell, the gaps between these shells are labelled with the corresponding magic numbers.*

The problem here is that quantum chromodynamics (QCD), the theory describing the strong interaction responsible for the nuclear force, does not provide any analytic description of the nuclear potential $V_N(r)$ and the spin-orbit term V_{so}. The most usual parametrization is the *Woods-Saxon potential* [12], a spherically symmetric potential which decreases smoothly to zero for increasing r (figure 2.4), in accordance with the nuclear matter distribution.

$$V_N^{WS}(r) = -\frac{V_0}{1 + exp[(r - R)/a]} \tag{2.4}$$

where R is a measure of the nuclear radius[2], a is the diffuseness of the nuclear surface and V_0 is the well depth, which is adjusted to reproduce the expected separation energies but uses to be around 50 MeV.

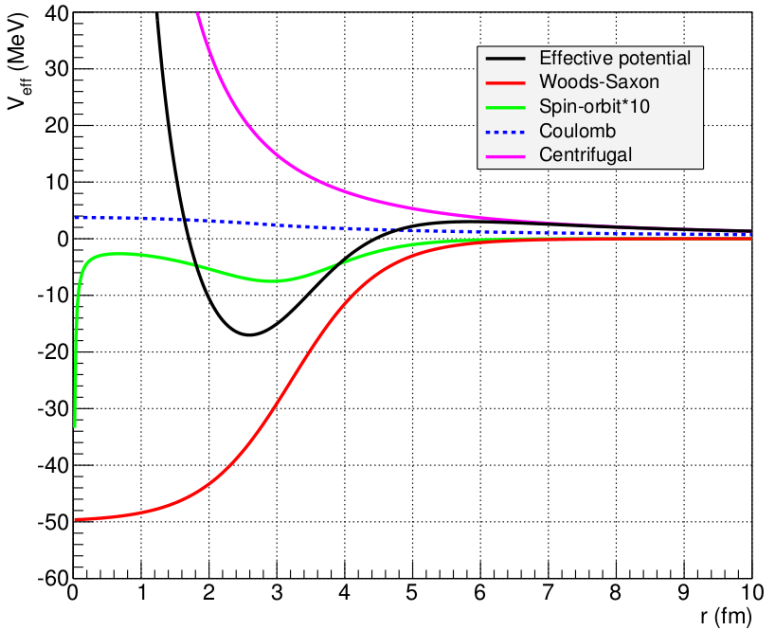

Figure 2.4: Effective potential for the last neutron in ^{17}C, assumed to be in the $d_{5/2}$ orbital (black line). The red line shows the nuclear mean-field, *depicted with a Woods-Saxon of $V_0 = 50\,MeV$, $r_0 = 1.25\,fm$, $a = 0.65\,fm$. The green line shows the spin-orbit term with $V_{so} = 6\,MeV$, multiplied by 10 to enhance data clarity. The pink line reproduces the centrifugal contribution. The blue dashed line indicates the Coulomb effect expected if the particle was a proton instead of a neutron.*

2.1.2 Residual interactions

Despite its simplicity, the single-particle shell model described here is really successful in predicting spins and parities for odd nuclei. However, it relies on the hypothesis that all nucleons except one are paired, and hence the nuclear properties arise from

[2] $R = r_0 A^{1/3}$

the only unpaired nucleon, which is a crude approximation, particularly when nuclei with several valence nucleons outside the last double-magic core are considered [4].

In such nuclei with more than one valence nucleon, the single-particle shell model is not applicable as it is, but we can go one step further and treat all the nucleons in the unfilled shell instead of just the last one. In order to do so, adding a residual interaction to the single-particle hamiltonian is required to take into account the effects not included in the effective potential, such as pairing effects between valence nucleons and p-n interactions.

$$H = H_{SPM} + H_{res} \tag{2.5}$$

This residual interaction acts as a perturbation on the effective potential and allows the single-particle states to mix, leading to a phenomenon called *configuration mixing*.

2.1.2.1 Spectroscopic factors

Within this panorama, arises the need to estimate what single-particle strength a real state in the nucleus carries. In order to fulfill this need, the spectroscopic factors (SF) are introduced as the overlap integral between the wave function in the entrance channel and in the exit channel. For instance, the spectroscopic factor of the ground state of ^{17}C, which has a spin of $3/2^+$, is defined as:

$$C^2S = \left| \left\langle {}^{17}C_{gs} | {}^{16}C_{0^+} \otimes \nu_{d_{3/2}} \right\rangle \right|^2 \tag{2.6}$$

In simple terms, the spectroscopic factor provides a measure of the likeness between a state in ^{17}C with ^{16}C coupled to a neutron in the corresponding orbital. The spectroscopic factor would be 1 in the ideal case of a pure single particle[3] orbital occupied by a single nucleon.

2.2 Shell evolution

The traditional magic numbers 2, 8, 20, 28, 50, 82 and 126 realised by Maria Goeppert-Mayer [9] were assumed to be a fixed constant of Nature for decades. However, the recent development of the radioactive ion beam facilities allowed the nuclei located close to the drip lines to be studied, probing more deeply the effect of the N-Z asymmetry on the nuclear structure. Experimental results brought evidence showing that the classical magic numbers evolve as one moves from the valley of stability to the drip lines, indicating that they are not the constant benchmark they were once thought to

[3]For future reference, the expression *single particle state* refers to those states with a reasonably large C^2S^{exp}, typically 50% or more of the total strength.

be. This discovery attracted much attention to the structure of exotic nuclei, and since then many theoretical [14–17] and experimental [18–25; 27] efforts have been made to study the evolution of the magic numbers in exotic nuclei.

The nucleon-nucleon (NN) interaction is responsible for this shell evolution: the nuclear mean field depends on the angular momentum and spin orientation of the nucleons involved, therefore different orbit populations lead to changes in their single-particle energies. Furthermore, features of the nuclear interaction barely influential binding together stable nuclei such as pairing or coupling between bound states, resonances, scattering states and decay channels effects can play a major role binding together weakly bound nuclei.

2.2.1 New magic number N=16

One hint of the magic number N=16 lies in the nuclide chart: the sharp extension of the neutron drip line at Z=9. The last bound isotope of carbon, nitrogen and oxygen is found at N=16, while one would have expected the supposed double magic nuclei ^{28}O to be bound. However, adding only one proton suddenly shifts the drip line up to N=22 for fluorine isotopes.

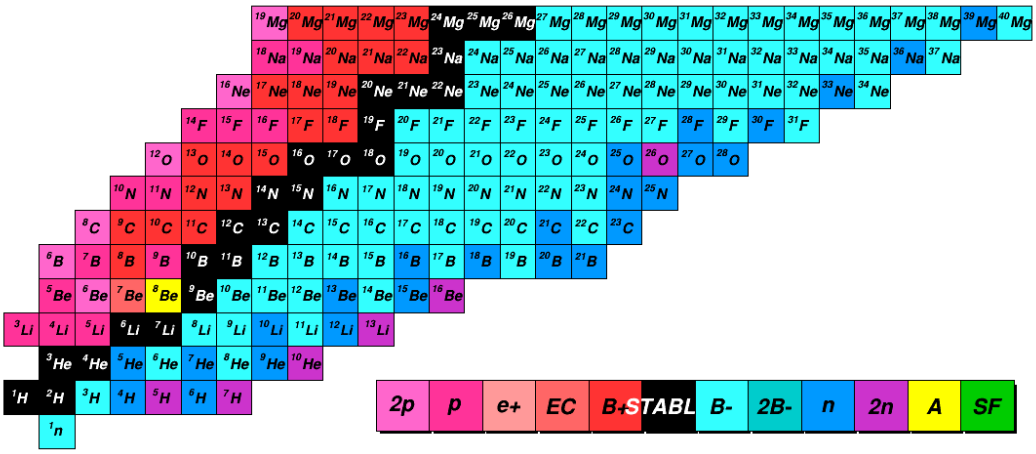

Figure 2.5: Nuclide chart for light elements.

The first experimental evidence of the rising of the N=16 shell closure has been provided by Ozawa *et al.* [18] by studying the neutron number dependence of the interaction cross-sections and neutron separation energies (Figure 2.6) for light neutron rich nuclei. A magic number would appear as a drop in the neutron separation energy trend, due to a neutron after the gap being relatively loosely bound. The observation of a break at N=16 for Z=8 indicates the emergence of a new magic number.

Magic nuclei are particularly stable due to the difficulty of exciting a closed shell structure. This means that the level scheme of magic nuclei has a noticeable lack of low-lying excited states. Thus, another experimental proof of shell evolution is given by

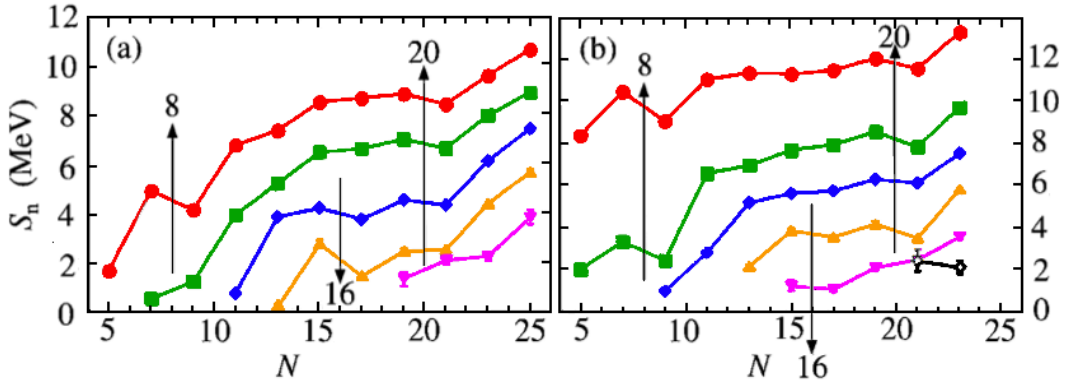

Figure 2.6: Neutron separation energies, S_n, as a function of the neutron number, for odd N even Z nuclei (a) and odd-odd nuclei (b). Each line represents different isospin numbers: from 1/2 to 9/2 (a) and from 0 to 5 (b).

the behaviour of the energy of the first excited state with the neutron number, which is expected to show a local maximum for magic nuclei. Figure 2.7 presents the first 2^+ state dependence on the neutron number for even-even isotopes between carbon (Z=6) and sulphur (Z=16). The maximum found in coincidence with the classical magic number N=20, in silicon and sulphur isotopes, vanishes for magnesium and neon while a new peak appears at N=16 in oxygen [19–22] and neon isotopes [23–25].

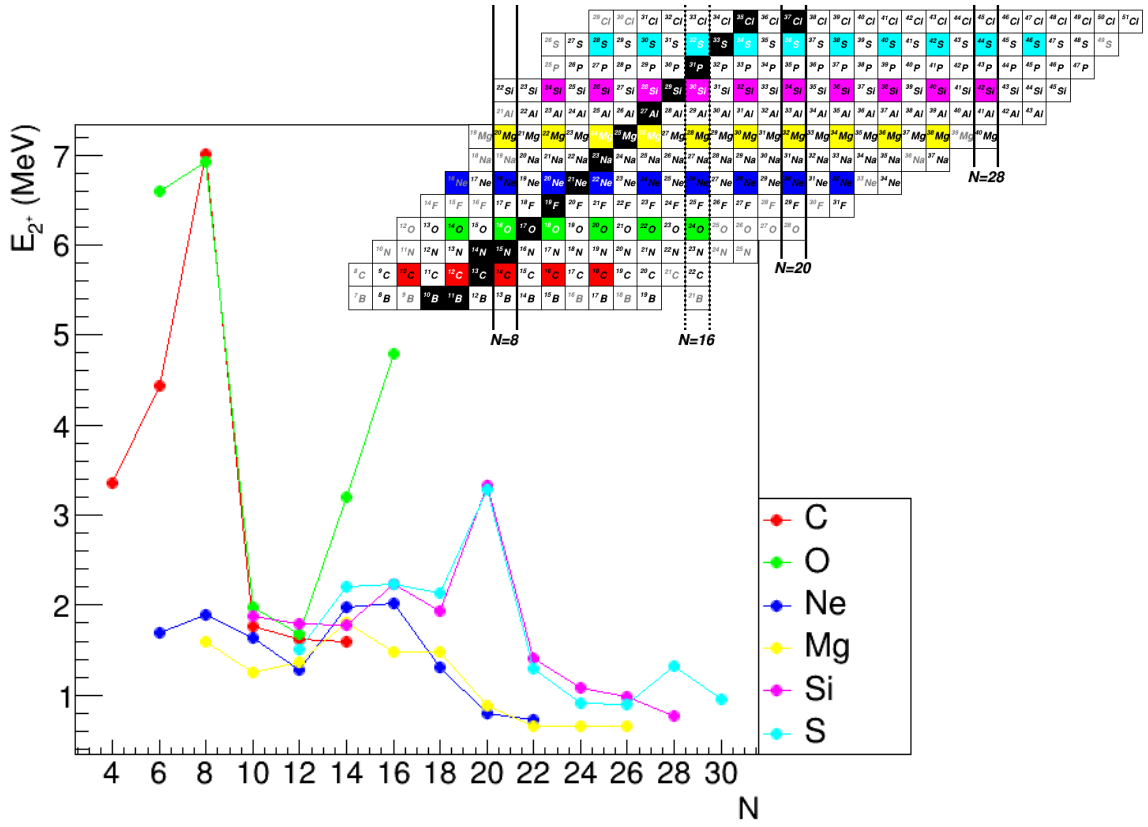

Figure 2.7: Neutron number dependence of the energy of the first 2^+ state of even-even nuclei between Z=6 and Z=16. The inset displays a nuclide chart as guidance to the reader. The magic number N=20 disappears for nuclei with a larger N/Z ratio while a new one emerges at N=16. Similar conclusions can be drawn for magic numbers N=8 and N=28.

As mentioned above, this changing shell structure can be successfully explained through the existence of an NN tensor force acting between protons and neutrons in orbitals with same angular momentum, which has an spin-isospin dependence coupling much more strongly orbitals with opposite spin [15]. Therefore, if the $\pi d_{5/2}$ orbital is empty (Z<9), this interaction vanishes and the $\nu d_{3/2}$ orbital rises towards the fp-shell, closing the N=20 shell gap while enlarging the N=16 one. However, the $\nu d_{3/2}$ orbital is lowered once a proton is put into the $\pi d_{5/2}$ one, and as more protons populate the $\pi d_{5/2}$, the $\nu d_{3/2}$ becomes more bound, leading to the N=20 shell gap (Figure 2.8).

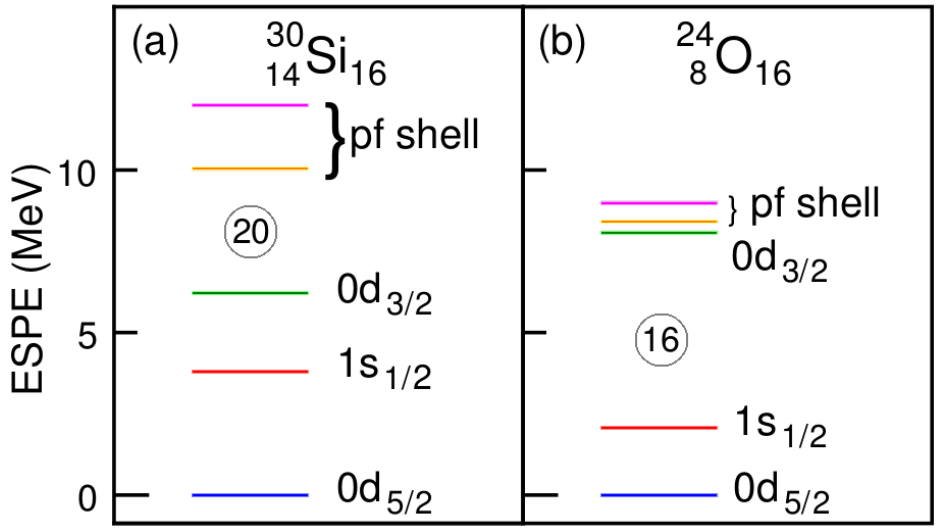

Figure 2.8: Effective single-particle energies for ^{30}Si (a) and ^{24}O (b) relative to $d_{5/2}$, showing shell gaps at N=20 and N=16 respectively [15]. The origin of this change is the raising of the $\nu d_{3/2}$ orbital due its interaction with the $\pi d_{5/2}$ orbital, which is at its strongest in ^{30}Si since the $\pi d_{5/2}$ orbital is full and completely disappears when it is empty in ^{24}O.

2.2.2 Subshell closure N=14

The large neutron subshell gap at N=14 between $\nu d_{5/2}$ and $\nu s_{1/2}$ orbitals recently observed in ^{22}O [26] has its origin in the NN interaction between like nucleons. Although weaker than the neutron-proton interaction, it might lead to changes in the shell gaps as in this particular case or the N=28 subshell gap.

The effect of this interaction is clearly manifested in oxygen isotopic chain: while the neutron $d_{5/2}$ and $s_{1/2}$ orbitals lie very close in energy when $\nu d_{5/2}$ orbital is empty at N = 8, but the gap increases as the $\nu d_{5/2}$ is filled reaching its maximum size of 4 MeV when it is fully occupied at N = 14. The bottom left part of figure 2.9 shows this trend.

2.2.2.1 From O to C isotopic chains

A comparison between carbon and oxygen isotopic chains could provide useful information on the effect of the NN interactions and allows a preliminary discussion on the expected shell closures in carbon isotopes.

Analysing the systematics of the 2^+ energies in carbon and oxygen isotopic chains (see figure 2.7), we observe a similar behaviour up to N = 14, where the 2^+ energy rises for ^{22}O while remains constant for ^{20}C. This indicates that the subshell closure observed at N = 14 observed in ^{22}O is no longer present in ^{20}C.

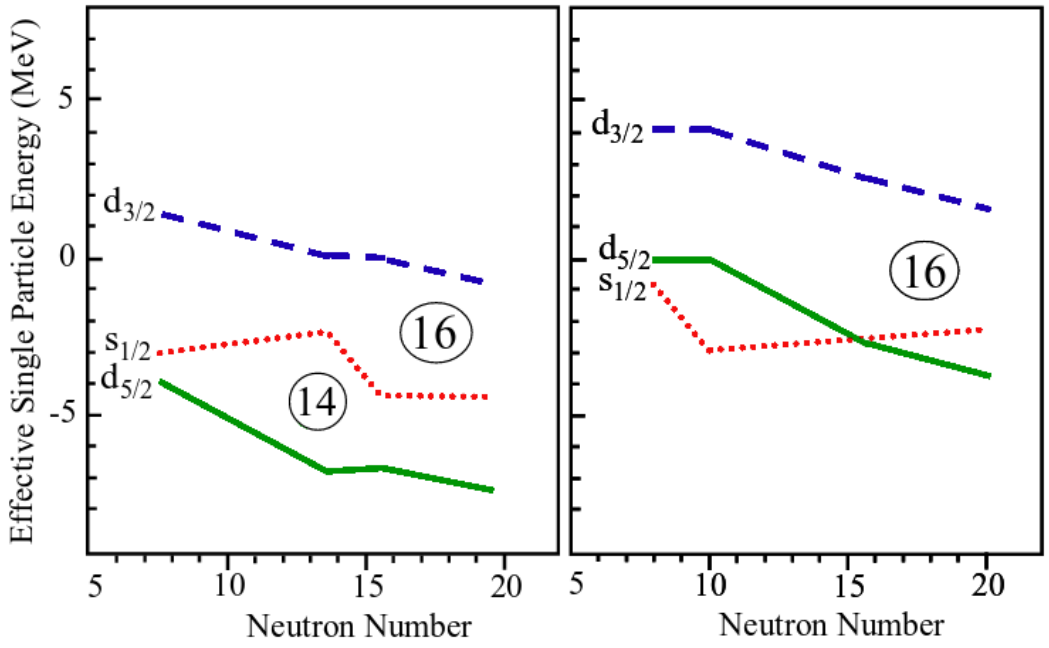

Figure 2.9: Evolution of the single-particle energies of the $d_{5/2}$, $s_{1/2}$ and $d_{3/2}$ orbitals in oxygen (left) and carbon (right) isotopes as a function of neutron number, where the new magic numbers N=14 and N=16 are shown. The ESPE are derived from theoretical calculations using USD and WBT interactions (Adapted from [13]).

The reason for this difference lies in the inversion of the $d_{5/2}$ and $s_{1/2}$ orbitals. This means that, after filling the p-shell, the $s_{1/2}$ orbital is populated first in carbon isotopes, as indicated in figure 2.9.

2.3 Current knowledge on ^{17}C

The neutron rich carbon isotope ^{17}C has six protons and eleven neutrons, with the last 3 neutrons populating the $d_{5/2}$ orbital and the last 4 protons filling the $p_{3/2}$ orbital according to the single-particle shell model (Figure 2.10).

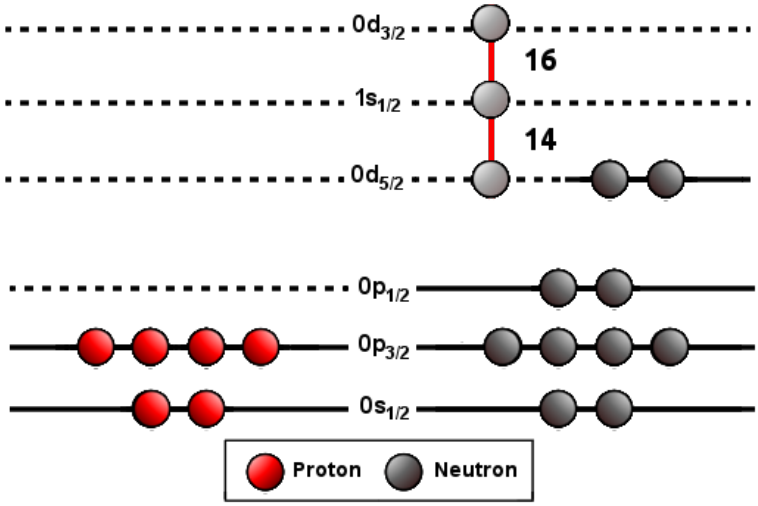

Figure 2.10: Shell structure of ^{17}C showing the orbitals populated by the transferred nucleon.

Since the proton $p_{1/2}$ orbital is empty, a stronger nucleon tensor force is expected when going from oxygen to carbon isotopes. The ^{17}C is, therefore, a suitable candidate to study the implications the NN tensor force might have in the nuclear structure of neutron rich carbon isotopes and determine whether the new magic numbers N=14 and N=16 are present by locating the neutron $d_{5/2}$, $s_{1/2}$ and $d_{3/2}$ orbitals involved in the N=14 and N=16 shell closures.

The low-lying structure of ^{17}C has been studied in recent experiments [27; 28; 30–36]. The ground state has a neutron separation energy of 0.734 ± 0.021 MeV [37], and has an unambiguous assignment of spin and parity of $3/2^+$. Its wave function was measured by Maddalena et al[28] to have three components: the dominant $\ell = 2$ $0d_{5/2}\otimes$ ^{16}C(2^+), a smaller $\ell = 0$ $1s_{1/2}\otimes$ ^{16}C(2^+), and another $\ell = 2$ coupled to the ground state of ^{16}C $0d_{3/2}\otimes$ ^{16}C(0^+):

$$|^{17}C_{gs}\rangle = ^{16}\mathrm{C}(2^+)\otimes 0d_{5/2} + ^{16}\mathrm{C}(2^+)\otimes 1s_{1/2} + ^{16}\mathrm{C}(0^+)\otimes 0d_{3/2} \tag{2.7}$$

It has been shown that the measured cross section is an order of magnitude higher than expected by theoretical shell model calculations, indicating an underestimation of the $0d_{3/2}\otimes$ ^{16}C(0^+) component in the ground state of ^{17}C.

Two low-lying excited states have been studied previously via one-neutron removal [29], γ-ray spectroscopy [27], proton inelastic scattering (p,pγ) [30], multinucleon transfer reaction [31], lifetime measurements [32; 33] and β-delayed neutron measurements [34]. The excitation energies provided by these references show an excellent agreement locating the first and second excited states in ^{17}C at 0.210 and 0.330 MeV. Transverse-momentum distributions measured by Kondo et al [29] confirmed $1/2^+$ and deduced $5/2^+$ assignments, respectively.

Theoretical calculations performed with shell-model using effective interactions WBP and WBT predict three bound states with spins and parities $1/2^+$, $3/2^+$ and $5/2^+$. Although all the interactions reproduce well the ground state they disagree on the ordering of the excited states (Figure 2.11).

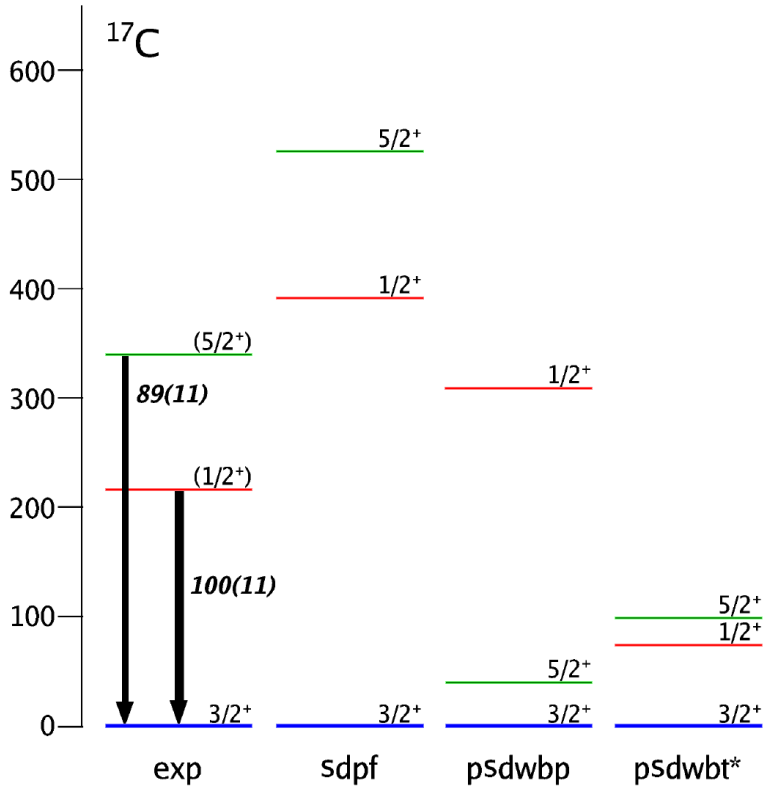

Figure 2.11: Low lying level scheme pf ^{17}C [30]. Different theoretical calculations for WBP and modified WBT interactions are shown.

Unbound states in ^{17}C have also been measured using invariant mass spectroscopy [31; 34–36] and β-decay experiments [34]. Three unbound states were found by one neutron knockout of ^{18}C [35] at 2.74, 3.03 and 4.03 MeV, but only the first one has been assigned to be $J^\pi = 1/2^-$. β-delayed neutron study [34] reported levels at 2.71, 3.93, 4.05, 4.78 and 5.08 MeV, the first three assigned to $1/2^-$, $3/2^-$ and $(5/2^-)$. A proton inelastic scattering experiment [36] has observed states at 2.20, 3.05 and 6.13 MeV, none assigned to $3/2^+$. A three neutron transfer reaction study [31] located 10 states above the neutron separation energy, with no definitive identification of $3/2^+$ states and only one candidate at 2.06 MeV.

The literature seems to agree in finding resonant states around 3, 4 and 6 MeV, though a remarkable disagreement appears in the spin and parity assignments since no direct measure has been made so far (Figure 2.12).

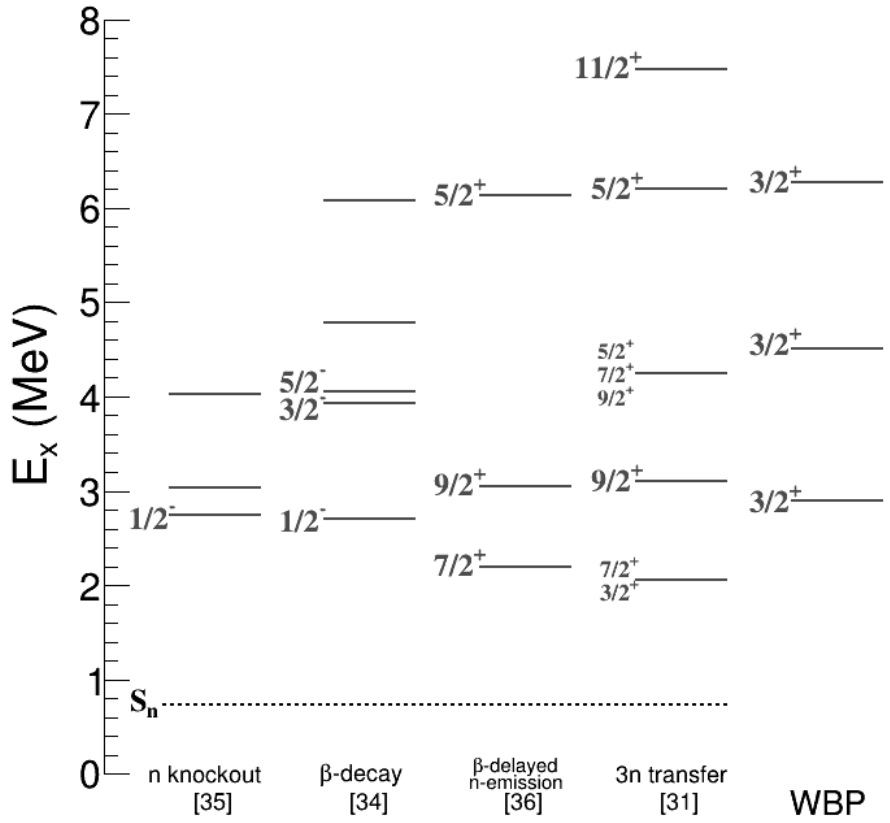

Figure 2.12: ^{17}C unbound states reported in [31; 34–36]. Shell model predictions using WBP are also presented for the $3/2^+$ states.

2.3.1 Halo nuclei

Pairing effects become decisive in binding nuclei as the neutron separation energy decreases when approaching the neutron dripline. There are several examples of unbound nuclei with an odd number of neutrons while the neighbouring isotope with one more neutron is bound. Some of these light bound nuclei, namely ^{6}He, ^{8}He, ^{11}Li, ^{14}Be, ^{17}B, ^{19}B, ^{22}C, have also in common a radius significantly larger than systematics, the so-called *halo*.

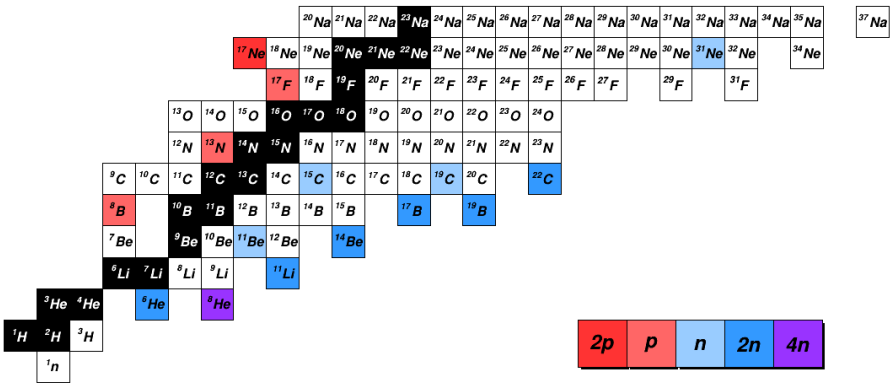

Figure 2.13: Light nuclide chart. Among bound nuclei, proton-halo and neutron-halo nuclei are highlighted in red and blue respectively.

Since the potential depth decreases with the binding energy and the centrifugal barrier increases with the orbital angular momentum ℓ, a larger radius suggests both low binding energy and angular momentum. Consequently, halo configurations appear most likely in loosely bound s and p states [38].

The low binding energies of neutron rich carbon isotopes make them suitable candidates to present halo structure. The study of odd-mass neutron rich carbon isotopes has revealed the appearance of one-neutron halo configurations in the ground states of ^{15}C [39] and ^{19}C [40]. It is interesting to notice that both nuclei have an intruder s state as ground state, while ^{17}C ground state has a dominant d component, and therefore its halo nature is hindered due to the centrifugal barrier. On the contrary, the first excited $1/2^+$ state in ^{17}C, which neutron separation energy is only 0.52 MeV, is a strong candidate to present a halo nature. A hindered B(M1) transition found in the lifetime measurements of the excited states in ^{17}C performed by D.Suzuki et al [32] support this picture.

Although the existence of excited states with halo configuration is expected, very little is known about them due to the lack of means to gather direct evidence. Over the past decades, experimental evidence of halo structure in excited states is found only in two systems: a neutron halo in ^{11}Be (p-wave) [42] and a proton halo in ^{17}F (s-wave) [43; 44].

2.4 Direct reactions

Nuclear reactions are often classified in two main groups according to the time scale of the interaction: the *direct reactions* and the *compound-nucleus reactions*. In the compound nucleus reactions both projectile and target nuclei merge together to form a highly excited *compound nucleus*, that remains bound long enough (10^{-16} s -10^{-18} s) for its nucleons to collide and share the excitation energy. As a consequence, its decay mode does not depend on the process through which it was formed.

Direct reactions, instead, are fast processes (10^{-22} s) that occur in a single step involving only a few nucleons in the nuclear surface while the others remain barely affected. Due to the fast interaction, energy and momentum transfer are relatively small and therefore the states populated are low-lying in energy.

The outcome of a direct reaction depends on what type of reaction occurs. Among the possible scenarios are *elastic scattering*, if both nuclei remain in their ground state, or *inelastic scattering*, if one or both nuclei become excited; *break-up reactions*, where the projectile is fragmented in several lighter nuclei, and *knock-out reactions*, in which one or more nucleons are removed from the projectile. However, the most important

type of direct reactions for this work is *transfer reactions*, where one or several nucleons are transferred from one nucleus to the other.

2.4.1 Angular distributions

The most useful feature of direct reactions is the relationship between the angular momentum transferred in the reaction and the angular distribution of the light particle, that arise directly from the momentum conservation law.

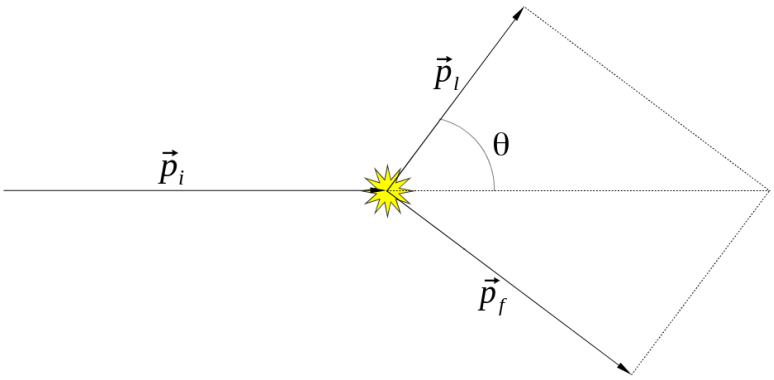

Figure 2.14: Momentum vector diagram. The scattering angle θ and the momenta of the incoming beam particle $\vec{p}_i$, the light ejectile $\vec{p}_l$ and the heavy fragment $\vec{p}_f$ are shown.

Considering the momentum diagram in figure 2.14, it is straightforward to realize that the momentum vectors are related to the scattering angle θ by the cosinus law:

$$p_f^2 = p_l^2 + p_i^2 - 2p_l p_i cos\theta \tag{2.8}$$

If we introduce p and δ defined as $p_i = p$ and $p_l = p - \delta$, the previous equation becomes:

$$p_f^2 = 2p^2(1 - cos\theta)\left(1 - \frac{\delta}{p}\right) = p^2\theta^2\left(1 - \frac{\delta}{p}\right) + \delta^2 \tag{2.9}$$

where the last step includes a first order Taylor expansion for $cos\theta$.

Finally, solving this for θ^2 gives:

$$\theta^2 = \frac{p_f^2 - \delta^2}{p^2\left(1 - \frac{\delta}{p}\right)} \tag{2.10}$$

The orbital angular momentum transferred between beam and target in the reaction is $\hbar\sqrt{\ell(\ell+1)}$, which should not be greater than Rp_f due to conservation of angular momentum, where R stands for the radius at which most of the reactions take place. Applying this on equation 2.10 we get:

$$\theta^2 \geqslant \frac{\left(\frac{\hbar}{R}\right)^2 \ell(\ell+1) - \delta^2}{p^2\left(1 - \frac{\delta}{p}\right)} \tag{2.11}$$

An accurate description of the angular distribution is subject to other factors like the beam energy, target effects and other features of the nuclear potential not taken into account in this crude semi-classical derivation [6]. However, equation 2.11 predicts that the minimum scattering angle increases with the angular momentum transferred ℓ. Since the target-like particle yield will be focused towards the forward direction where the particles are least strongly deflected in the center of mass frame, the intensity would be expected to peak at the minimum angle allowed by the angular momentum conservation. Therefore the first maximum in the angular distribution provides a strong indication of the angular momentum transferred ℓ, as it is shown in figure 2.15 where calculated angular distributions for $\ell = 0, 1, 2$ and 3 are displayed.

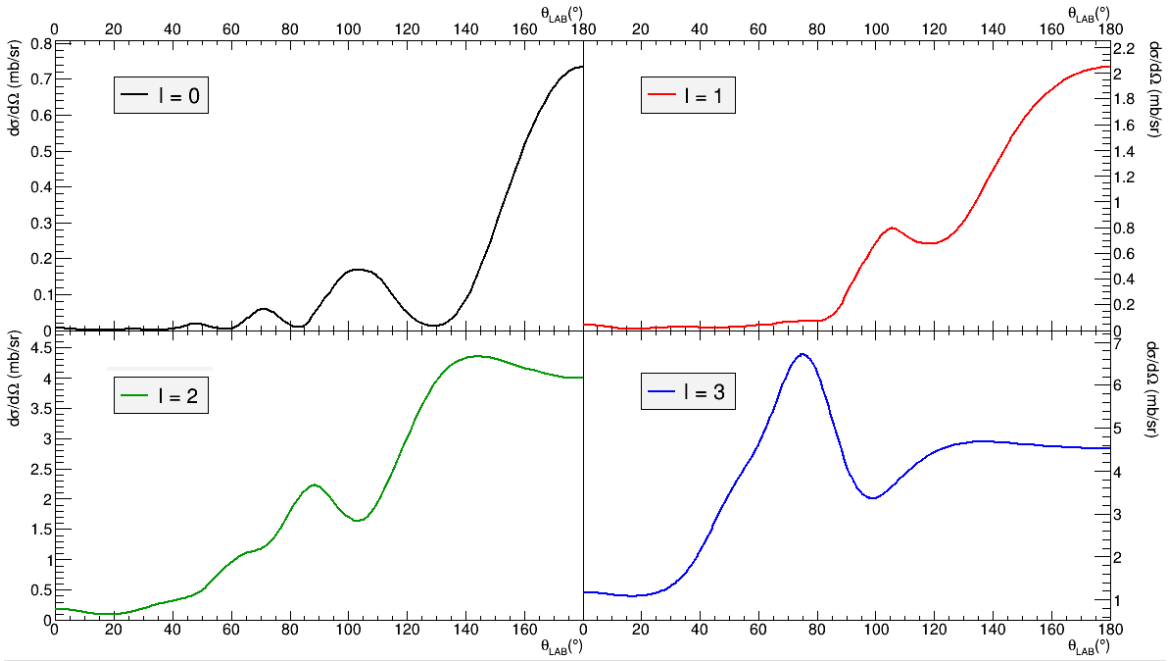

Figure 2.15: Angular distributions for different angular momenta ℓ. Note that the maximum of the angular distribution shifts to larger angles as ℓ increases.

2.4.2 Single-nucleon transfer reactions

Single-nucleon transfer reactions represent one of the best suited tools to probe single-particle states. Due to their peripheral character, the perturbation in the nucleus because of transfer reactions is minimal with the transferred nucleon in an orbit around it, leading to low-lying excited states. In addition, a comparison between the shape of the experimental angular distribution and the theoretical cross section provides a

measurement for the angular momentum transferred ℓ in the reaction. Since spin-orbit effects on angular distributions are weak for reactions with unpolarized nuclei, a experimental value of ℓ will constraint the J^π assignments to spin-orbit partners.

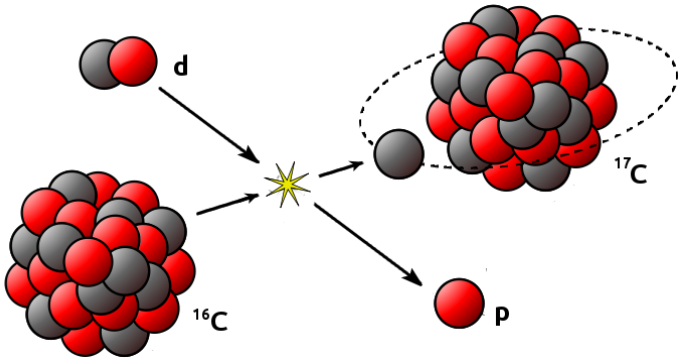

Figure 2.16: Diagram of the single-neutron transfer reaction $^{16}C(d,p)^{17}C$, where the neutron in the deuterium is transferred to the ^{16}C. ^{17}C is depicted as a ^{16}C core plus a neutron populating a single-particle state.

With the advent of radioactive ion beam facilities, beams of exotic nuclei brought the possibility of exploring nuclei at the edge of nuclear existence. Inverse kinematics is required due to the short half lives of nuclei with such a large N/Z ratio, thus an exotic beam is impinged on a light target.

2.4.2.1 Extraction of spectroscopic factors

As mentioned before in section 2.1.2.1, the overlap integral between the wave function of one state in nucleus ^{16}C and another in ^{17}C defines the theoretical spectroscopic factor for transfer between these states. Experimentally, the spectroscopic factor is provided by comparing the measured cross section and theoretical cross-section. Theoretical cross-sections are calculated for pure single-particle states but this is not necessarily the case and the experimental cross-sections will in general be different from theoretical predictions by a certain number [4]. This scaling factor between theoretical and experimental cross-sections is the spectroscopic factor:

$$\left(\frac{d\sigma}{d\Omega}\right)_{exp} = C^2 S \left(\frac{d\sigma}{d\Omega}\right)_{th} \tag{2.12}$$

Thus, scaling the theoretical cross-sections with respect to the experimental ones provides a measurement of the spectroscopic factors.

2.4.3 Theoretical analysis

2.4.3.1 Born approximation

The *Plane Wave Born Approximation* (PWBA) applies the simplest scattering theory to calculate the cross-section of a reaction. The target is treated as a central potential $V(r)$ and the incoming beam particles as plane waves $\psi(z) = Ae^{ikz}$, thus obtaining the angular distributions $I(\theta)$ can be seen as a perturbation problem [6], giving:

$$I(\theta) \propto \left[j_\ell \left(p_f \frac{R}{\hbar} \right) \right]^2 \tag{2.13}$$

where j_ℓ is the spherical Bessel function of order ℓ. Note that p_f has been already proved to be a function of θ in equation 2.10.

Alternatively, the differential cross-section is proportional to the squared transition matrix element $\mathcal{T}_{A(d,p)A+1}$ that describes the transfer reaction $A(d,p)A+1$ [47]. This matrix element can be written as:

$$\mathcal{T}_{A(d,p)A+1} = \langle \phi_{A+1} \phi_p \chi_f | V | \phi_A \phi_d \chi_i \rangle \tag{2.14}$$

where functions χ describe the relative motion of the nuclei, functions ϕ their internal structure and V is the potential governing the transfer.

PWBA calculations can locate the first and eventually the second maximum of the angular distributions, although they fail entirely to predict absolute cross-sections, as the only interaction considered is that leading to the reaction while nuclear and coulomb potentials, which could eventually cause scattering or absorption, are completely ignored.

2.4.3.2 Distorted Wave Born Approximation

The *Distorted Wave Born Approximation* (DWBA) goes one stride further by including an optical potential acting between the two nuclei in the entrance or the exit channel to take into account absorption and elastic scattering.

The optical model[4] reduces the problem to the interaction of beam particles with the potential well due to the target nuclei and treats it with the scattering theory, assuming that the interaction is governed by the distance between the center of both nuclei. However, an interaction with a potential well cannot change the energy of a

[4]The name of *optical model* is due to the analogy to scattering and absorption of light by a medium of complex refractive index.

nucleus or remove a nucleon from it as it eventually happens, it can only be deflected. This behaviour can be assessed by using a complex potential well, in which the imaginary part takes into account all the effects involved in the reaction other than elastic scattering.

$$U = V_C - \frac{(V + iW)}{1 + exp[(r - R)/a]} \tag{2.15}$$

where V and W are the real and imaginary potential depths, R is the radius and a is surface diffuseness parameter. V_C stands for the Coulomb potential, usually described by a homogeneously charged sphere:

$$V_C = \begin{cases} \dfrac{Z_b Z_A e^2}{r} & \text{if } r \leq R \\ \dfrac{Z_b Z_A e^2}{r}\left(3 - \dfrac{r^2}{R^2}\right) & \text{if } r \geq R \end{cases} \tag{2.16}$$

where Z_b and Z_A are the charge of the two nuclei involved in the reaction. Both R and a parameters can have different values for the Coulomb, the real and the imaginary part.

This optical potential is usually phenomenological, with parameters that are adjusted to reproduce elastic scattering experimental data.

Thus, under the DWBA the transition matrix element $\mathcal{T}^{DWBA}_{A(d,p)A+1}$ becomes:

$$\mathcal{T}^{DWBA}_{A(d,p)A+1} = \langle \phi_{A+1}\phi_p\chi_f | V_{pA+1} - U_{pA+1} | \phi_A\phi_d\chi_i \rangle \tag{2.17}$$

where functions $\chi_{i,f}$ are solutions of Schrödinger equation for elastic scattering, governed by optical potentials $U_{i,f}$ describing the elastic scattering, and $V_{i,f}$ is a potential that includes any possible interaction between the two nuclei in the entrance or exit channels. Now if we consider the V_{pA+1} potential as:

$$V_{pA+1} = V_{pA} + V_{pn} \approx U_{pA+1} + V_{pn} \tag{2.18}$$

leading to the usual expression of the DWBA transition matrix element for (d,p) transfer reactions:

$$\mathcal{T}^{DWBA}_{A(d,p)A+1} = \langle \phi_{A+1}\phi_p\chi_f | V_{np} | \phi_A\phi_d\chi_i \rangle \tag{2.19}$$

DWBA is a good approach to describe transfer reactions, but it relies on the assumption that the elastic scattering dominates the relative motion of the two nuclei in the entrance and exit channels, if this does not happen the accuracy of its results will be doubtful, as occurs in the case of weakly bound nuclei, where break-up channels could have a major influence in the dynamics of the reaction.

2.4.3.3 Adiabatic Distorted Wave Approximation

The *Adiabatic Distorted Wave Approximation* (ADWA) was formulated for (d,p) and (d,n) reactions [48], although it can be used to treat transfer reactions involving other loosely bound systems.

ADWA simplifies the (p+n)+A three-body problem into a two-body problem through the *adiabatic approximation*, consisting in assuming that the internal motion in the n-p system, during the reaction, is small compared to the motion of its center of mass. Therefore the interaction governing the reaction is the sum of the interaction of the proton and the neutron with the target, V_{pA} and V_{nA}, at half the energy of the deuteron and folded by deuteron wave-function instead of the interaction responsible for the deuteron elastic scattering. The parametrizations of these adiabatic potentials are taken from optical potentials that describe well the elastic scattering.

Several corrections have been made within the ADWA formalism. For instance, an adiabatic potential with a finite-range correction and a local energy approximation was proposed by Johnson and Tandy [49]:

$$U_{Ad}^{JT} = \frac{\langle \phi_d | V_{np}(U_{Ap} + U_{An}) | \phi_d \rangle}{\langle \phi_d | V_{np} | \phi_d \rangle} \tag{2.20}$$

In this manner, the transition matrix element is given by:

$$\mathcal{T}_{A(d,p)A+1}^{ADWA} = \langle \phi_{A+1} \phi_p \chi_f | V_{np} | \phi_A \phi_d \tilde{\chi}_i \rangle \tag{2.21}$$

where functions $\tilde{\chi}_i$ is solution of a Schrödinger equation governed by adiabatic potentials U_i and $\tilde{\chi}_f$ is a regular distorted wave describing elastic scattering in the exit channel.

The adiabatic distorted wave approximation considers, in addition to elastic scattering, the excitation to break up channels. Therefore, since break up can still be followed by transfer, ADWA calculations are well suited to account for the effect of deuteron break up on transfer cross sections.

Chapter 3

Experimental Details

3.1 Experimental Overview

In this experiment, states in ^{17}C have been populated by the ^{16}C(d,p)^{17}C transfer reaction induced by bombarding a 1.36 mg/cm^2 thick target of deuterated polyethylene (CD_2) with a ^{16}C beam at 17.2 AMeV delivered by the LISE3 spectrometer at GANIL, with a beam intensity of $5{\cdot}10^4$ pps. Before reaching the target, this beam was tracked using two CATS detectors in order to determine the hit position and the angle of incidence of the beam particles on the target.

The highly efficient double-sided silicon strip detector array TIARA was used to detect light particles at central and backward laboratory angles, in the Barrel and the Hyball respectively. Both the energy and the angle were measured as they are required to perform excitation energy and angular distributions calculations. Light particles at forward angles were detected in four MUST2 Si-CsI telescopes. The kinematical lines of the light particles and the angular coverage of the detectors involved are presented in figure 3.1.

Four highly efficient EXOGAM clovers were placed at 90^o surrounding the target, in order to measure the γ-rays emitted by the bound excited states in beam-like fragments. The Si-Si-CsI telescope CHARISSA was placed at zero-degrees to detect beam-like fragments. The energy loss, residual energy, angle and time of flight were measured in order to perform particle identification.

This experimental setup allows to perform triple coincidences on an event-by-event basis by requiring a light particle, a heavy fragment and a γ-ray in coincidence. Figure 3.2 shows the experimental setup described here.

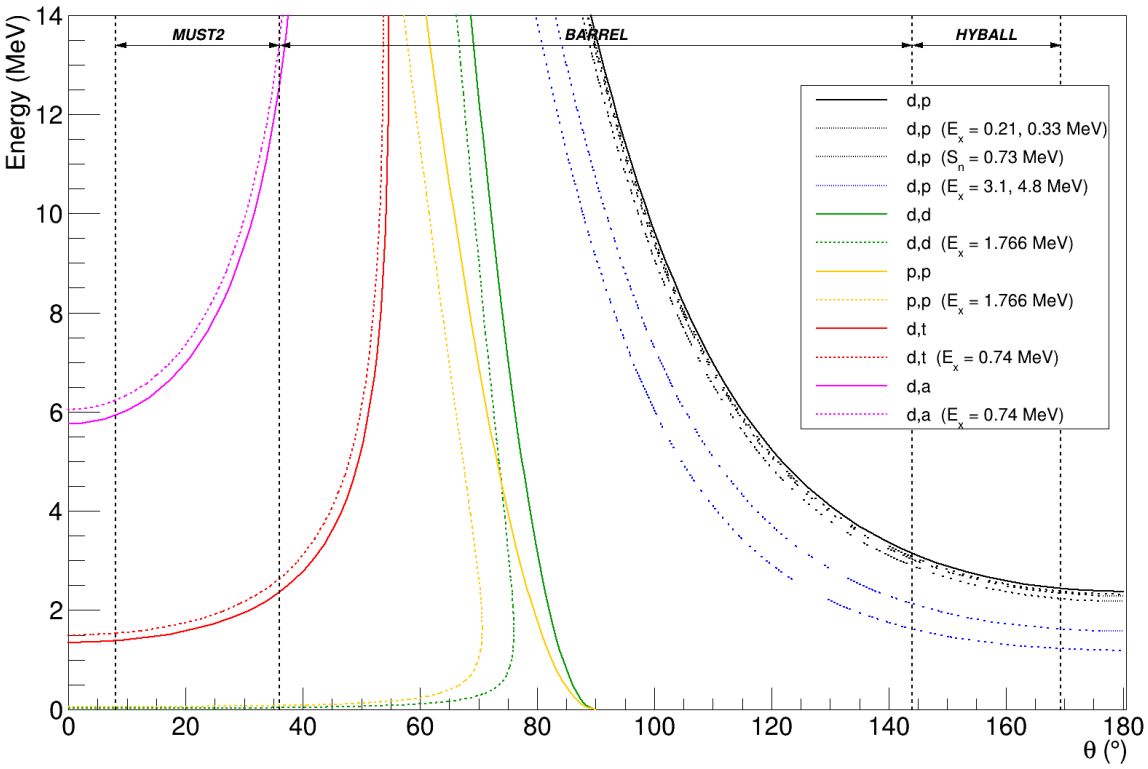

Figure 3.1: Light particle kinematics for the most probable reaction channels. The angular coverage of TIARA spans central and backward laboratory angles, where cross sections of (d,p) reactions are maximal, in order that angular distribution measurements could be made.

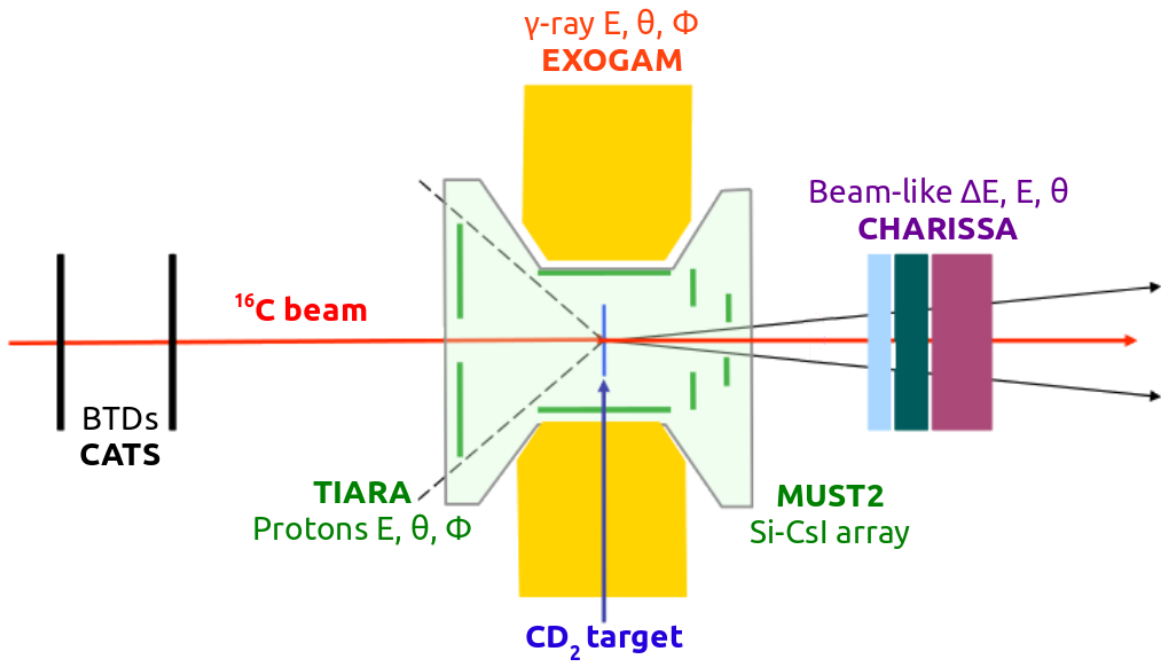

Figure 3.2: Schematic representation of the experimental set up.

3.2 Secondary beam production at GANIL

Many radioactive ion beam facilities have been built as the will to explore more exotic nuclei arose. As a consequence, the radioactive ion beam production techniques have developed a great deal, however, nowadays producing exotic ion beams is still challenging because of their very short half lives and the low cross sections [51].

There are two different methods to overcome these difficulties and produce exotic beams: the *isotope separation on line* (ISOL) technique [52] and the *in-flight separation* technique [53], used in this work.

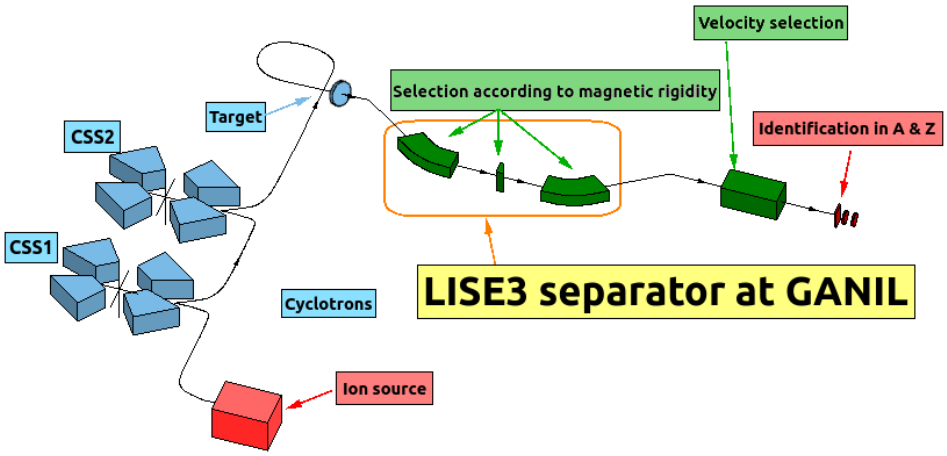

Figure 3.3: Schematic layout of the LISE3 spectrometer. The primary beam is accelarated in CSS1 and CSS2 (blue) cyclotrons. The ^{16}C ions are then selected from the emerging secondary beam in LISE3 separator (green) and delivered to the experimental room.

A primary beam of ^{18}O was produced by ionizing oxygen atoms with an Electron Cyclotron Resonance Ion Source (ECRIS). The ions were thereupon accelerated, first by a K = 25 injector cyclotron and afterwards by CSS1 and CSS2, two K = 400 cyclotrons, up to an energy of 65 AMeV and finally directed towards a 1200 mg/cm^2 thick rotating production target of beryllium, so that the heat was spread over a much larger area than the beam spot.

The ^{16}C ions are then separated from the resulting cocktail beam using the LISE3 spectrometer by a selection according to their magnetic rigidity. An achromatic beryllium degrader of 400 mg/cm^2 was placed at the dispersive plane to combine A/Z separation and energy loss analysis for optimum purity. Finally, the ^{16}C beam was delivered to the experimental room at 17.2 AMeV.

One of the drawbacks of fragmentation beams is that energy and angular spreads of the secondary beams are rather big, owing to multiple Coulomb scattering and energy loss straggling in the production target and in the degrader. However, the beam energy spread is regulated by the slits at the dispersive plane of LISE3 and the uncertainty in the beam emittance is corrected by using the Beam Tracking Detectors.

3.3 Beam Tracking Detectors

3.3.1 CATS

The CATS (Chambres à Trajectoire de Saclay) is a beam detector system designed to track the incident beam particles and provide the hit position on an event-by-event basis. Placing two CATS detectors before the target will allow us to perform a path reconstruction to know the beam interaction point on the target and the incident angle, leading to an accurate determination of the light particle emission angle. They are crucial for this experiment since the secondary beam is produced by fragmentation leading to a beam spot size of the order of mm.

The CATS are multiwire proportional chambers with an active area of 70x70 mm^2. The anode, at center of the detector, is made up of 71 golden tungsten wires of 10 µm of diameter and placed every 1 mm. At a distance of 3.2 mm we find the cathode planes, two Mylar layers of 1.5 µm where 28 gold strips of 2µm were deposited. The cathode pitch is 2.54 mm and the interstrip is 0.2 mm. Finally, closing the gas chamber, which is filled with pure isobutane (C_4H_{10}) at a pressure ranging from 6 to 15 Torr, there are two additional Mylar layers of 1.5 µm [57].

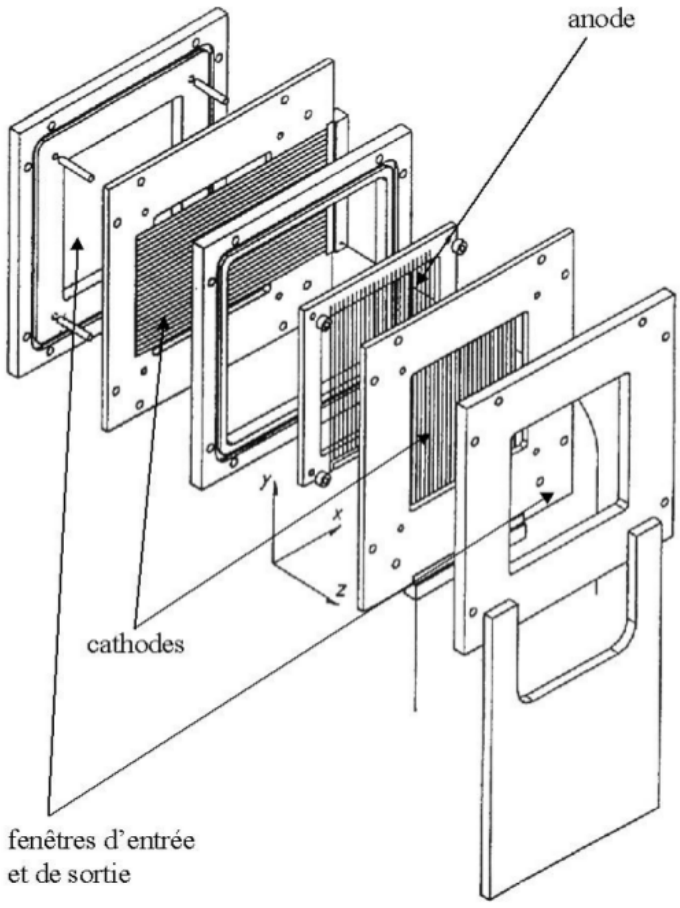

Figure 3.4: CATS scheme, layer by layer

3.3.2 Working principle

The reduced field E/P (electric field divided by the gas pressure) is very high in the detector, leading to two amplification regions. In the first region, the ionized electrons from incident heavy ions immediately cause an electron multiplication along their tracks. In the second region, close to the wires, there is a second charge multiplication comparable to the typical avalanche in usual MWPCs. This phenomenon of double charge amplification makes possible to obtain a significant signal with a small thickness of gas, thereby minimizing the disturbance of incident particles trajectories. The fast component of the signal generated by electron avalanche in the first region grants the detector a good timing resolution. The fast positive ions collection, due to a small anode-cathode gap, gives high counting rate capabilities. Finally, the charge induced on each cathode is obtained by integrating the signal with a QDC.

3.4 Light charged particle detection

3.4.1 Semiconductor Diode Detectors

In a p-n junction, without any external voltage applied, holes drift towards the n-region and the electrons towards the p-region to recombine in the vicinity of the p-n interface. This charge carriers motion creates an electric field across the junction that prevents further diffusion leading to a steady charge distribution (figure 3.5).

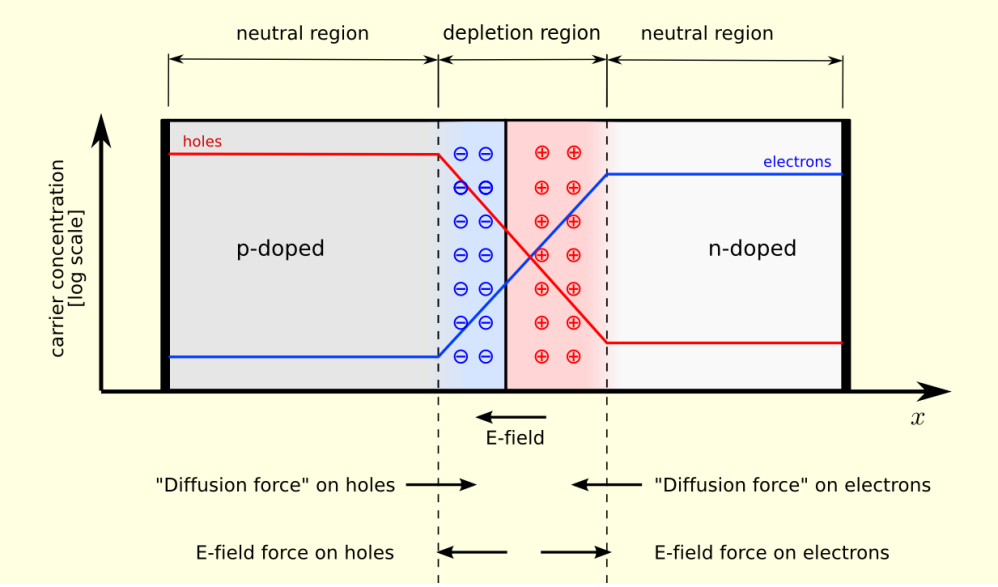

Figure 3.5: When n-type and p-type semiconductors are brought into contact, the region around the interface shows a lack of charge carriers due to the electron-hole recombination and thus is called depletion region.

Semiconductor diode detectors take advantage of the favourable properties that arise in the depletion region of a p-n junction: if radiation enters the depletion region and creates electron-hole pairs, the existing electric field causes electrons flow in one direction, holes in the other, and the charge carriers can be collected into a signal whose amplitude is proportional to the energy loss of the radiation [4; 50].

A large reverse bias is commonly applied to the p-n junction to boost the performance of the p-n junction as radiation detector due to two reasons: it increases the active volume of the detector by further depleting the p-n junction, and it increases the electric field in the depletion region, thus the charge carriers will move faster and hence the charge collection will be more efficient.

3.4.1.1 Dead Layer

When there is a difference in the concentration of impurities, the depletion region extends even further into the high purity side, meaning that the heavily doped layer remains undepleted and therefore outside of the active area of the detector. This insensitive layer of the detector is called *dead layer*, through which the incoming charged particles must pass before entering the active area, hence losing a fraction of its energy before it can be measured.

3.4.2 Silicon Strip Detectors

Nowadays, the silicon strip detectors (SSD) are the most common choice when it comes to detecting charged particles. These detectors can cover a wider solid angle, raising the statistics, due to their large active area, which is, moreover, segmented into several independent detector elements in order to measure the detection position.

Silicon strip detectors can be classified according to the approach used to provide the position of the hit along the strip: double-sided silicon strip detectors (DSSSD) and position sensitive silicon strip detectors (PSSSD).

In the DSSSDs there are strips on the front and the back sides of the detector, in such a way (usually perpendicular to each other) that the hit position is determined by which strip was fired on the front and the back. Instead, in the PSSSDs strips are created in one side and are made of a resistive material, which divides the charge collection into two signals that are taken at both ends of the strip. The collected charge at each end is inversely proportional to the distance from the hit position.

3.4.3 TIARA

The Transfer and Inelastic All-angle Reaction Array (TIARA) is a large solid angle silicon detector array designed for transfer reactions in inverse kinematics. In the configuration for this experiment, the angular coverage of TIARA spans from 36^o to 169.4^o. It allows to identify the reaction channel and to determine the excitation energies by measuring position and deposited energy of the target-like particles.

The TIARA array comprises a set of several stand-alone silicon detectors, including an octagonal barrel made up of eight resistive charge division detectors mounted surrounding the target holder, an annular DSSSD detector called *Hyball* placed upstream of the target and two CD shaped silicon strip detectors [61] (S1 and S2, which have not been used in this experiment. Instead 4 MUST2 telescopes were used downstream).

3.4.3.1 Barrel

The Barrel detector consists of eight resistive charge division detectors forming a octagonal barrel, placed surrounding the target and parallel to the beam direction. Its angular coverage ranges from 36^o to 144^o in the laboratory frame. This barrel arrangement is 96.8 mm long and presents an octagonal cross-section of 27.6 mm side length and 33.3 mm inner radius.

Each detector has a thickness of 400 µm and an active surface 94.6 mm long and 22.5 mm wide, which is segmented in four position-sensitive resistive strips along the beam direction. The strip pitch is 5.65 mm and inter-strip gap is 100 µm.

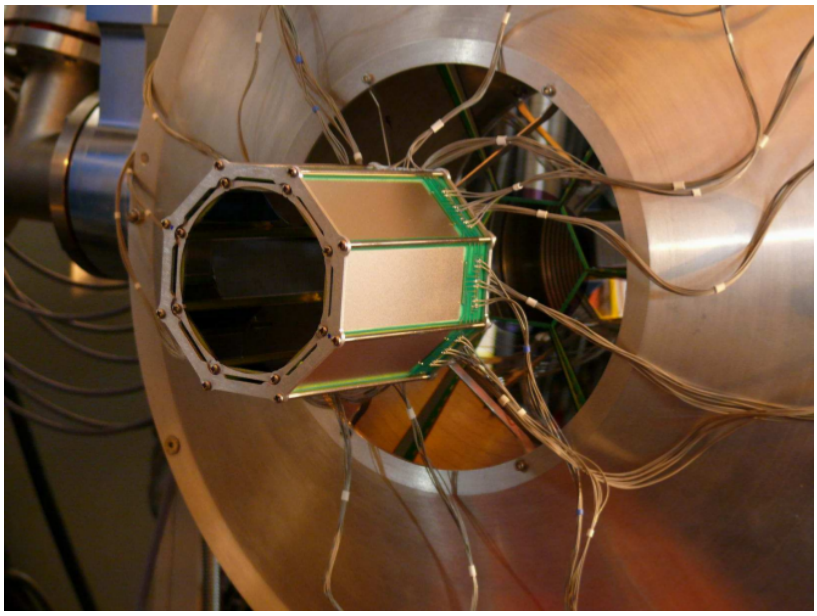

Figure 3.6: The Barrel array mounted in the experimental room.

The Barrel was upgraded to increase its dynamic range by installing a second layer of eight 700 µm thick silicon detectors forming an Outer Barrel, each of them segmented in four strips in the same way that the Inner Barrel is, although they are not position-sensitive since this information is given by the Inner Barrel and would be redundant.

For 5.5 MeV α-particles, the position resolution along the beam axis is determined to be better than 1 mm and the energy resolution provided is 140 keV (FWHM).

3.4.3.2 Hyball

The Hyball detector is an annular array of six individual wedge-shaped Double Sided Silicon Strip Detector (DSSSD), situated 154.3 mm upstream of the target covering the most backward angles from 137^o[1] to 169.4^o [62]. All the six wedges are shaped in such a way that, once assembled together, there is a hole in the center of the Hyball to allow the beam to pass through.

Each wedge has a thickness of 400 µm and an active surface spanning 55^o approximately in the azimuthal angle, delimited by inner and outer radii of 32.6 mm and 135.1 mm respectively. This active surface is segmented in 16 ring-shaped strips of 6.4 mm pitch facing the target and in 8 azimuthal sectors spanning 6.8^o at the other side.

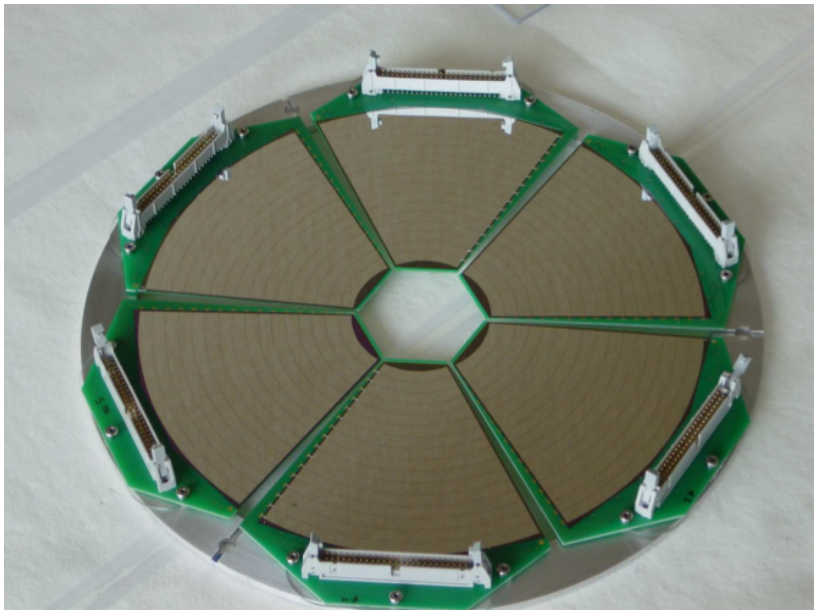

Figure 3.7: The Hyball array, where we can see the segmentation in the front face of the detector (target side).

For 5.5 MeV α-particles, the expected energy resolution is typically 40 keV for rings and 70 keV for sectors (FWHM).

[1] In the present configuration the angular coverage of the Barrel spans from 36^o to 144^o, and the outer rings in the Hyball are shadowed by the Barrel.

3.4.4 MUST2

The MUST2 array is made of several telescopes (up to eight, but only four were mounted for this experiment) designed for the detection of light particles produced by direct reactions with radioactive beams in inverse kinematics. Each telescope presents three detection layers to the incoming particles.

DSSSD A 300 µm thick Double Sided Silicon Strip Detector, with an area of 100x100 mm^2 and 128 strips on each side. The typical strip resolution is around 40 keV in energy and 500 ps in time for 5 MeV α-particles [63].

Si(Li) This layer is made of two 4.5 mm thick Lithium-drifted Silicon detectors, each one segmented in 8 pixels. This layer was not used as the DSSSD provides a energy range good enough with better resolution.

CsI 16 40 mm thick CsI crystal scintillators build up this layer. Protons up to 115 MeV can be stopped in these crystals.

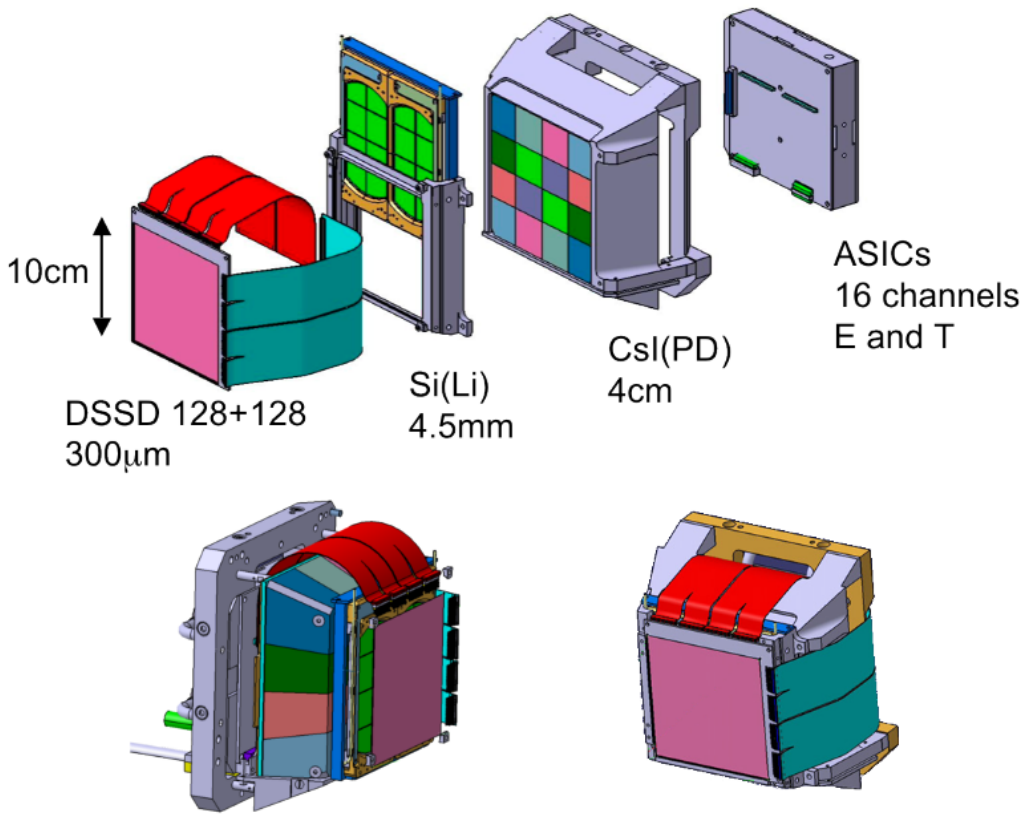

Figure 3.8: MUST2 telescope and a detailed view of the different layers.

MUST2 has not been involved in the analysis since it covered forward angles whereas our particles of interest (protons from ^{16}C(d,p) reaction) are produced mainly at backward angles.

3.5 Recoil detection

3.5.1 CHARISSA telescope

The CHARged particle Instrumentations for Solid State Array (CHARISSA) is a zero-degree telescope used to detect the heavy residues from direct reactions and perform particle identification by energy loss methods. The detector is made of three detection stages:

ΔE A 65 µm thick Double Sided Silicon Strip Detector, with an active area of 50x50 mm^2 and 16 strips on each side [62]. The experimental resolution achieved is around 150 keV (FWHM) in energy for α-particles of 5.5 MeV.

E A 500 µm thick Double Sided Silicon Strip Detector, with the same size and segmented in the same way as the previous one. For α-particles of 5.5 MeV, the measured energy resolution is 110 keV (FWHM).

CsI A 25 mm thick CsI crystal scintillator with and active area of 49x49 mm^2 is used to stop the incoming particles and measure the residual energy. For α-particles of 5.5 MeV, the energy resolution obtained is 230 keV (FWHM).

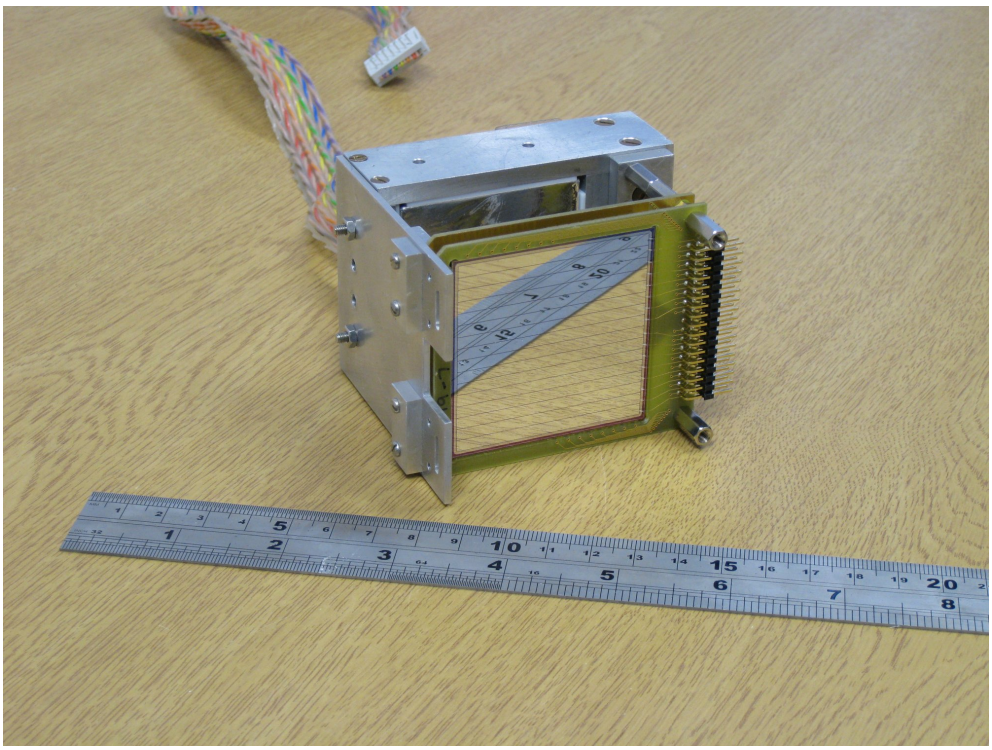

Figure 3.9: Charissa telescope. The segmentation of the front side of the first silicon is noticeable. The CsI behind the silicon layers is also visible.

3.6 γ-ray Detection

As γ-rays pass through a material they only interact in sudden and discrete interactions, instead of the continuous energy loss of charged particles as they are not governed by the Coulomb or the nuclear forces.

There are mainly three processes through which γ-rays can interact with matter: *photoelectric absorption*, *Compton scattering* and *pair production*. The type of interaction is random but their relative probabilities depend on the atomic number of the absorbing material and the photon energy, being the photoelectric absorption the predominant interaction at low energies (up to 200 keV), the pair production the dominant process at high energies (above 5 MeV) and the Compton scattering the most probable effect at intermediate energies.

3.6.1 Germanium Detectors

The biggest issue in semiconductor detectors intended for γ-ray spectroscopy is the efficiency that can be achieved. This happens due to the large mean free path of the γ-rays that requires a big active volume or depletion depth in order to enhance the probability of γ-rays interacting within the detector and hence the detection efficiency.

The thickness of the depletion region, d, in a semiconductor junction is given by the equation:

$$d = \sqrt{\frac{2\epsilon V}{eN}} \tag{3.1}$$

where V is the voltage, N the concentration of impurities in the semiconductor, ϵ is the permittivity and e the electronic charge. As ϵ and e are constants and the breakdown voltage sets an upper limit to V for proper operation, the only way to get greater depletion depths is by reducing the impurities in the semiconductor. For this reason, germanium crystals of high-purity (HPGe) are therefore the most suitable material for high resolution γ-ray detectors [50].

Concerning the detector configuration, the most common approach is the coaxial configuration because it allows to produce much larger active volumes than any other known configuration. In this configuration, the detector is built in a long cylindrical germanium crystal, where a hole is drilled along its axis and a metal contact is made inside the hole. The second electrode is fabricated at the outer surface of the crystal, as illustrated in figure 3.10.

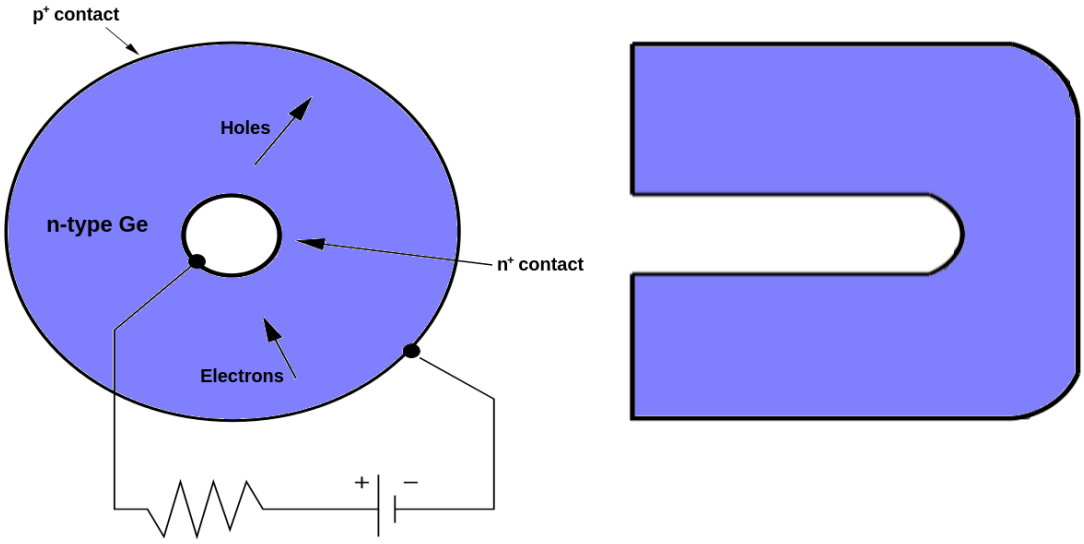

Figure 3.10: At the left a cross section perpendicular to the cylindrical axis of the crystal is shown. At the right a cross section through the axis of the crystal is represented.

3.6.2 EXOGAM

EXOGAM is a highly efficient and segmented germanium detector array, specially designed for γ-ray spectroscopy with exotic beams at the Grand Accélérateur National d'Ions Lourds (GANIL). Each detector consists of four hyper-pure germanium crystals, closely packed together in a four-leaf clover configuration in the same cryostat sharing the same cooling system.

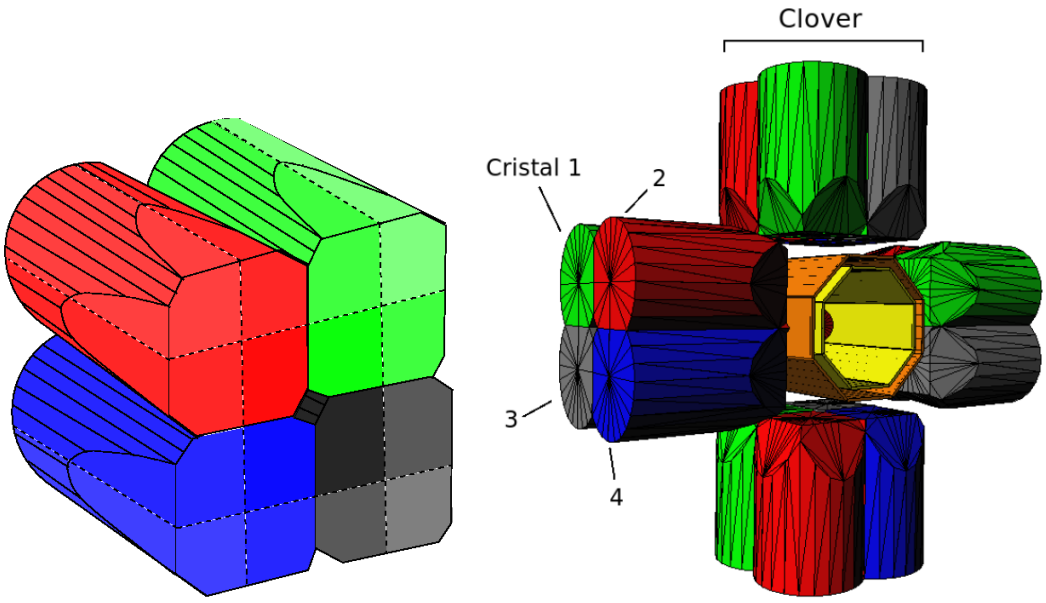

(a) EXOGAM clover *(b) EXOGAM arrangement around TIARA*

Figure 3.11: Schematic diagram of an individual clover of EXOGAM (a) and a representation of the placement of the 4 EXOGAM clovers around the Barrel at 90º (b).

Each germanium crystal is 90 mm thick and has an active surface area of 60x60 mm^2, and is electronically segmented in four sectors (GOCCEs) to enhance the position resolution and reduce the Doppler broadening [64]. The γ-ray energy is measured with the central contact (ECC), where the charge from the whole crystal is collected.

In this experimental set up, four EXOGAM clovers were placed at 90^o surrounding the Barrel in a compact arrangement at around 55 mm from the target, in order to increase the angular coverage and thus the detection efficiency, although it reduces the energy resolution and maximizes the Doppler broadening.

3.7 Time of flight

Magnetic spectrometers bend the trajectories of charged ions according to their magnetic rigidity in order to perform particle identification. However, the dipole magnets cannot distinguish between ions with equal charge-mass ratio. Time of flight measurements provide a tool to separate ions having optically degenerate trajectories within the spectrometer since different nuclei with the same magnetic rigidity are bound to have different velocities and, therefore, different times of flight. Thus, times of flight will be a very useful tool to help clean up the spectra and a key ingredient in our particle identification routine.

3.7.1 TACs

These time of flights measurements have been performed by using several Time-to-Amplitude Converters (TAC), which are electronic modules intended for the measurement of small time intervals between two input signals, a start pulse and a stop pulse, by producing an output signal proportional in amplitude to the time lapse between them both, providing a time resolution of 0.1 ns approximately.

A list of the different times of flights measured during this experiment is presented in table 3.1. It is worth mentioning that the signal of the detector placed more downstream (usually CHARISSA or TIARA) is always chosen as the start signal while the signal from the upstream is artificially delayed in order to guarantee that a stop signal will always follow a start signal, rather than triggering the TAC for every single event in the upstream detector (commonly CATS or EXOGAM), some of which might not have a hit in the downstream detector from which the TAC would have to wait for the stop signal. Therefore, the times of flight obtained are reversed.

[2]At GANIL the beam is pulsed (beam pulses of 2 ns every 100 ns), and hence the high-frequency signal of the cyclotron can be used to measure a time of flight before the reaction target.

Number	Start signal	Stop signal
1	HF^2	CATS 1
2	CATS 2	CATS 1
3	CHARISSA	CATS 1
4	Hyball	CATS 1
5	Barrel	CATS 1
6	CATS 1	EXOGAM
7	CHARISSA	EXOGAM
8	Hyball	EXOGAM
9	Barrel	EXOGAM

Table 3.1: Time of flights measured during the experiment.

3.8 Data Acquisition and Electronics

3.8.1 Data Acquisition

The read out of the signals from all the detection systems involved in the experiment (CATS, TIARA, MUST2, CHARISSA and EXOGAM) were processed by the GANIL Data Acquisition System. In this configuration, each one of these detectors have its own stand alone Data Acquisition (DAQ) system, managed by a local trigger produced by its individual electronics.

These local triggers are sent to the GANIL Master Trigger (GMT) unit, which produces, if the acquisition is not busy with another event, the Fast Analysis Gate (FAG), a logic signal that decides if an event is to be accepted or not, and memorizes the inputs that triggered the FAG.

If the event is accepted, a validation signal is sent to each local DAQ to read out the data. While the acquisition is processing an event, the GMT is vetoed by the OR of the busy signals of the local DAQs. The DAQ dead time is measured by counting the signals from a pulser in coincidence with this veto signal. The ratio between the counting of the pulser alone and the pulser in coincidence with the veto signal will provide an estimation of dead time, which results to be 10.015 $\pm$ 0.003 %.

Number	Trigger
1	MUST2 1
2	MUST2 2
3	MUST2 3
4	MUST2 4
5	CATS1 %
6	CATS2 %
7	TIARA
8	CHARISSA %
9	EXOGAM %
10	TIARA or MUST2
11	Hyball
12	Barrel

Table 3.2: GMT inputs. In our case, any of these inputs except 7 and 10 prompts the FAG and hence validates the event for further processing.

3.8.2 Scalers

A scaler is an electronic unit intended for counting the total number of incoming signals. In particular, we have fed the triggers into the scalers to record how many times each detector is fired. This will be specially useful later in the analysis to provide a measurement of the number of beam particles passing through CATS, needed for the cross-section normalization.

Chapter 4

Data analysis

4.1 Measurement of the target thicknesses

In the present experiment, two different polyethylene targets have been used: a deuterated polyethylene (C_3D_6, from now on referred as CD_2) target, used to run the experiment, and a pure polyethylene (C_3H_6, called CH_2 from here on) target, useful to obtain the (p,p) and (p,p') angular distributions. According to the manufacturer, the quoted thicknesses are 1.2 and 2 mg/cm^2, respectively.

An accurate measurement of the target thickness is needed both for taking into account the energy losses in the target when determining the total energy of the reaction products and for cross-section normalization. Also it is required to estimate the mean beam energy at the interaction point (since it cannot be known, the center of the target will be taken to be the average reaction position), which is a variable that will play a role in the cross-section normalization and the excitation energy reconstruction.

There are several methods to determine the target thickness, but the approach used here relies on the measurement of the energy loss of α particles in the target to deduce the thickness by comparing it to energy-loss calculations.

4.1.1 Setup and calibration

The setup used to measure the target thickness involves an α source and a silicon detector. This detector was calibrated placing a 3-α source in front of it at a distance of 27 cm. This source is a mixture of ^{239}Pu, ^{241}Am and ^{244}Cm, and produces α lines at 5.157 MeV, 5.486 and 5.805 MeV respectively, plus other weaker lines at 5.144 MeV, 5.443 MeV and 5.763 MeV.

The centroid channel numbers were determined from a gaussian fit to each α-line (figure 4.1a). Then a linear fit was done to the theoretical energy versus centroid position plot to determine the calibration parameters, that is, offset and gain (figure 4.1b).

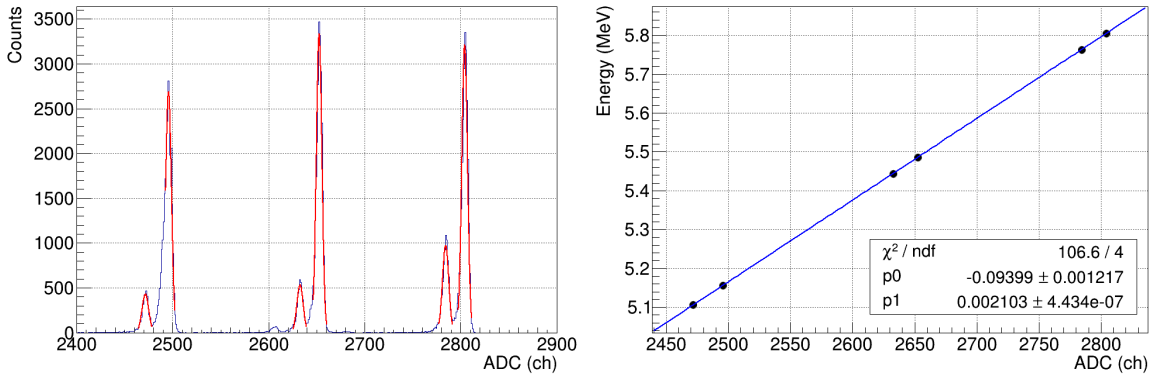

(a) Spectrum *(b) Calibration*

Figure 4.1: Spectrum of the 3-α source (a) and the calibration plot (b). Despite the standard deviation of the fit respect to the expected values is just 0.6 keV, the χ^2 value is high due to the fact that the statistical errors are quite small and cannot account for these differences.

4.1.2 Procedure and results

The target thickness was determined by measuring the energies of the 3-α source spectrum with the target placed between the source and the detector (table 4.1) and calculating, using range and stopping power tables [55; 56], the thickness of the CD_2 and the CH_2 target required to reproduce the energy losses (table 4.2) from the initial energy measured without target.

Target	α_1	α_2	α_3
CD_2	3.860 ± 0.035	4.269 ± 0.031	4.628 ± 0.028
CH_2	2.880 ± 0.058	3.360 ± 0.052	3.801 ± 0.051

Table 4.1: Energy (MeV) measured when a target is placed between source and detector. The uncertainties are statistical.

Now with the target in, the separation deteriorates and the different decays are no longer separated, only the three strongest peaks are visible, the energy value associated to each one to obtain the energy loss is a weighted average of the energies of all the α decays included under each one of them.

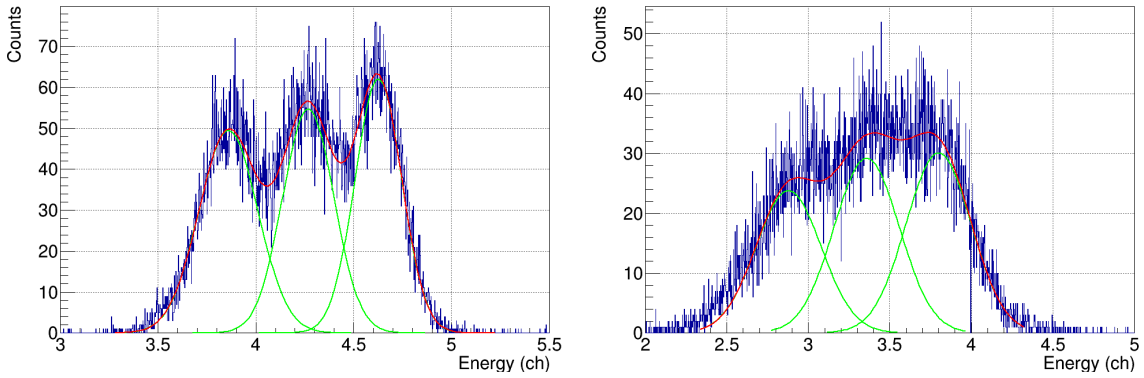

(a) CD_2 target *(b) CH_2 target*

Figure 4.2: α energy spectra after passing through the CD_2 target (a) and the CH_2 target (b).

Target	α_1	α_2	α_3
CD_2	1.288 ± 0.036	1.211 ± 0.032	1.167 ± 0.029
CH_2	2.275 ± 0.059	2.125 ± 0.053	2.002 ± 0.052

Table 4.2: Energy loss (MeV) and statistical uncertainty.

In the next step, we have performed several calculations to determine the target thickness required to reproduce the energy loss of each peak shown in table 4.2. These calculations have been performed following the methods illustrated on figure 4.3 using both range and stopping power tables for α particles passing through polypropilene (C_3H_6) obtained from SRIM [55] and α-star [56] databases, in order to compare the results obtained by different techniques and with different datasets. The following table contains the resulting thicknesses:

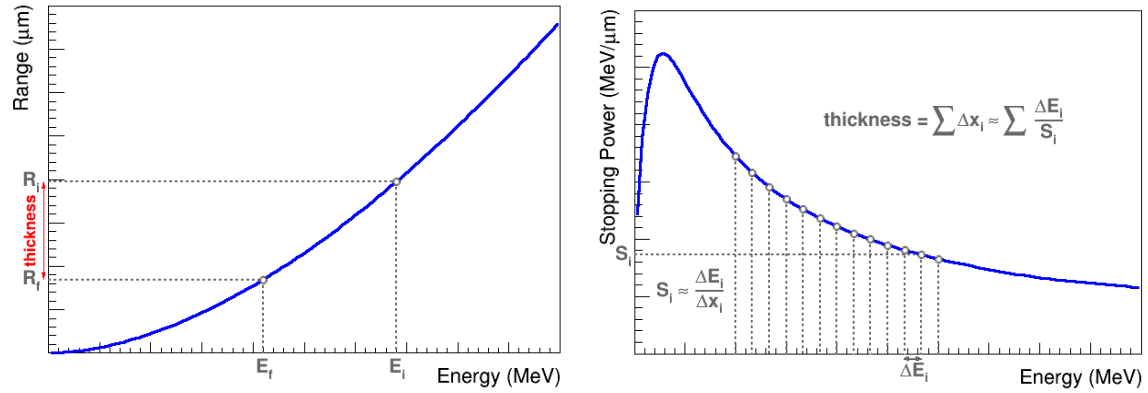

(a) Range method *(b) Stopping power method*

Figure 4.3: Methods of target thickness measurement: the range technique (a) provides the target thickness as the difference between the range at the incident energy and the one corresponding to the residual energy after passing through the target. The stopping power approach (b) consists in dividing the energy loss in small intervals, $\Delta E \approx 1$ keV, over which the stopping power S is assumed to be constant. Therefore, the total target thickness is then obtained by summing all the small thicknesses of the different energy loss intervals.

		α_1		α_2		α_3	
		Range	dE/dx	Range	dE/dx	Range	dE/dx
CD_2	α-star	$13.52^{+0.34}_{-0.34}$	$10.96^{+0.28}_{-0.27}$	$13.44^{+0.32}_{-0.32}$	$10.89^{+0.32}_{-0.32}$	$13.59^{+0.26}_{-0.26}$	$11.02^{+0.25}_{-0.25}$
	SRIM	$13.03^{+0.32}_{-0.33}$	$13.05^{+0.33}_{-0.33}$	$12.97^{+0.31}_{-0.31}$	$12.99^{+0.31}_{-0.31}$	$13.12^{+0.30}_{-0.30}$	$13.14^{+0.30}_{-0.30}$
CH_2	α-star	$21.94^{+0.45}_{-0.46}$	$17.80^{+0.37}_{-0.37}$	$21.96^{+0.45}_{-0.45}$	$17.81^{+0.36}_{-0.37}$	$21.95^{+0.48}_{-0.49}$	$17.80^{+0.39}_{-0.39}$
	SRIM	$21.21^{+0.44}_{-0.44}$	$21.25^{+0.44}_{-0.44}$	$21.20^{+0.44}_{-0.44}$	$21.23^{+0.44}_{-0.44}$	$21.18^{+0.46}_{-0.47}$	$21.22^{+0.47}_{-0.47}$

Table 4.3: Target thickness (μm). The uncertainties are due to statistical errors carried through the calculations.

We observe that the tables from SRIM [55] and α-star [56] databases show a better agreement for the range (1%) than for the stopping power (16%). Therefore, we have only considered the results provided by the range calculation. The final target thickness is 13.29 ± 0.12 µm and 21.56 ± 0.19 µm, for the CD_2 target and the CH_2 one respectively.

Note that at this stage it is not possible to give an accurate measurement of these thicknesses in mass per unit area as the purity of the targets is still not well known, so neither are their densities. Nevertheless, these values are calculated in order to compare the target thickness measurements with those provided by the manufacturer. Hence, assuming that both targets are 100% pure[1], we found 1.367 ± 0.012 mg/cm^2 for the CD_2 target and 1.940 ± 0.017 mg/cm^2 for the target of CH_2.

4.2 CATS calibration

4.2.1 Alignment

The CATS alignment method applied for the analysis will be presented in this section. It is important to notice that an absolute charge measurement is not required for these detectors as the relative gains between strips are the only thing that matters to get the hit position.

Therefore, relative calibration was performed using a pulser signal fed into the anode wires to induce a charge on the cathode strips. This was repeated 6 times using different attenuation settings to cover the widest range possible.

[1]The question on purity concerns mainly the CD_2 target. CH_2 target is most probably 100% pure.

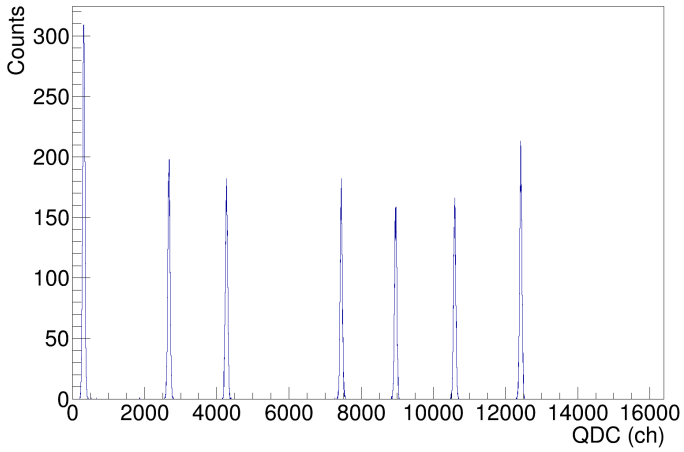

Figure 4.4: Pulser spectrum for one strip in CATS. The first peak is the pedestal while the others represent a different output voltage from the pulser.

4.2.1.1 Pedestal subtraction

When a strip is fired, all others strips are also recorded, even if there is nothing more than noise on most of them. The accumulation of such events will lead to the appearance of a peak around zero, that is called *pedestal*.

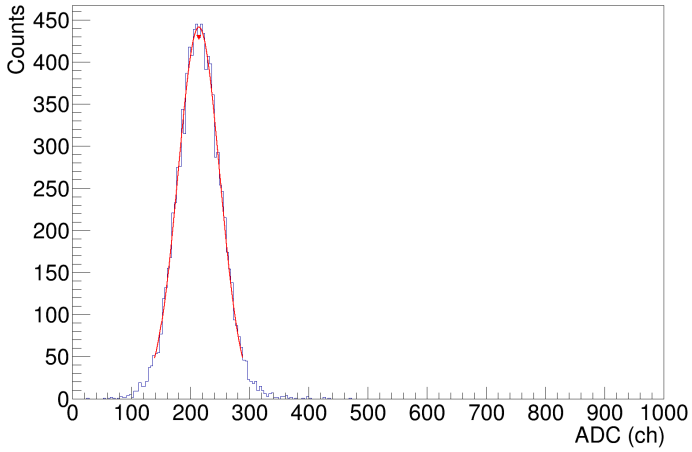

Figure 4.5: The pedestal is fitted with a Gaussian in order to obtain its position, which is important to set an absolute zero.

Knowing that, the pedestal is fitted with a Gaussian in order to get the channel number and subtract it to the data to set the zero:

$$Q_i^{ped} = Q_i^{raw} - ped_i \tag{4.1}$$

where Q_i^{ped} is the value of the charge after the pedestal subtraction for the i^{th} channel, Q_i^{raw} is the raw value of the charge and ped_i is the position of the pedestal, given by the mean of the Gaussian fit.

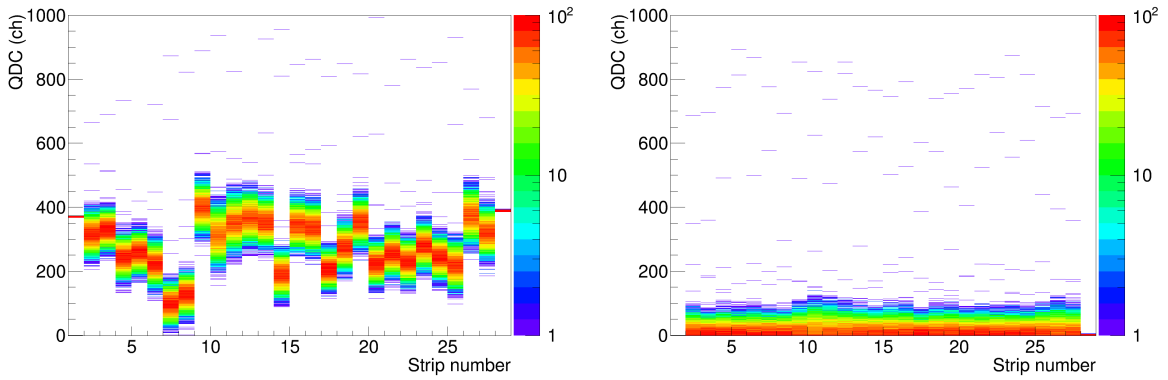

(a) Before, Q_i^{raw} *(b) After, Q_i^{ped}*

Figure 4.6: Comparison of raw charges before (a) and after (b) the pedestal substraction in the near-zero region.

4.2.1.2 Gain matching

Since an absolute calibration is not needed, the gain of all the strips have been matched to the first one.

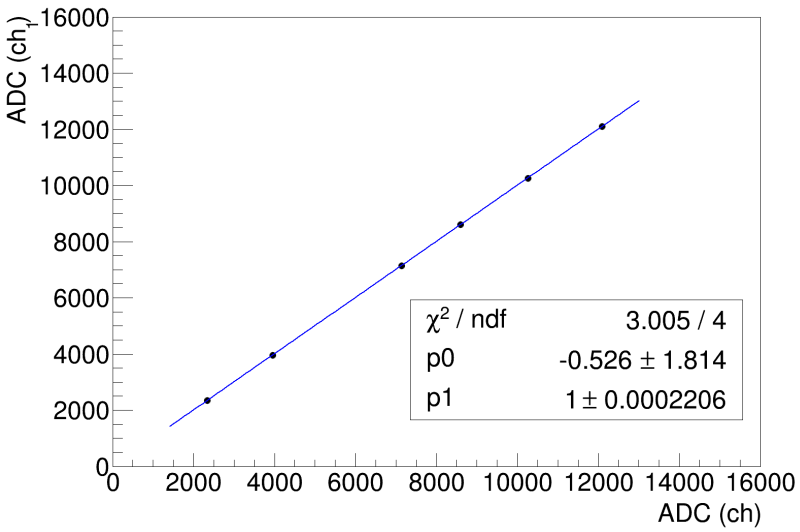

Figure 4.7: Gain matching linear fit.

For a given strip, the pulser peaks are fitted with Gaussians to determine their positions and these positions are plotted against the positions in the strip chosen as reference. Finally, the gain matching parameters are calculated doing a linear fit, and then applied in the following way:

$$Q_i^{gm} = a_i + b_i * Q_i^{ped} \tag{4.2}$$

where Q_i^{gm} is the gain matched charge for the i^{th} channel, a_i and b_i are the offset and the slope of the linear fit, respectively.

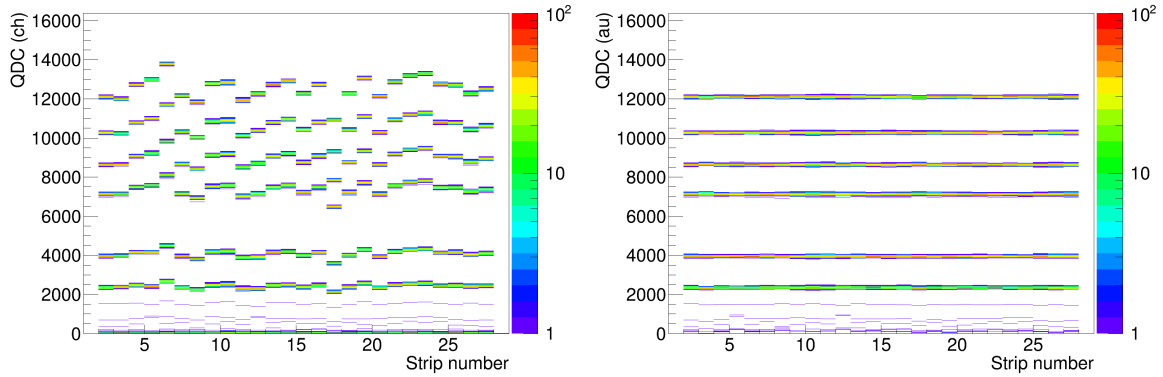

(a) Before, Q_i^{ped} *(b) After, Q_i^{gm}*

Figure 4.8: Comparison of charges on the x-strips of CATS1 before (a) and after (b) the gain matching.

4.2.1.3 Thresholds

Once the strips are gain matched, the pedestal was fitted with a Gaussian in order to set the thresholds for the path reconstruction. Those thresholds were defined according to the equation:

$$threshold_i = \mu_i + 3 * \sigma_i \tag{4.3}$$

where $threshold_i$ is the threshold for the i^{th} channel, μ_i and σ_i are the mean and the sigma values of the Gaussian fit of the pedestal, respectively. After applying these thresholds, we have seen that the multiplicity distributions peak at 4 and 5 for CATS1 and CATS2, respectively. This means that most likely the beam passes through an interstrip in CATS1 and through the middle of a strip in CATS2.

4.3 Beam path reconstruction

4.3.1 Position reconstruction

There are several algorithms to determine the charge centroid and can be classified in two classes: the algorithms performing a calculation of the center of gravity of the charge distribution and those assuming that the charge distribution can be described with an analytical function, frequently Gaussians, Lorentzians or squared hyperbolic secants.

Among the algorithms falling in the later group, the squared hyperbolic secants method is the one used in this work because it is proven to give the best results [58].

The squared hyperbolic secants algorithm [59; 60] relies on the assumption that the charge distribution is well described by the analytic function:

$$Q_x = \frac{p_1}{cosh^2\left(\frac{\pi(x-p_2)}{p_3}\right)} \tag{4.4}$$

where p_1 is the height of the distribution, p_2 is the position of the centroid and p_3 is the width of the distribution.

Under the previous assumption, the parameters p_2 and p_3 are given by:

$$p_2 = \frac{p_3}{\pi} tanh^{-1}\left(\frac{\sqrt{Q_1/Q_3} - \sqrt{Q_1/Q_2}}{2sinh\left(\frac{\pi w}{p_3}\right)}\right) \tag{4.5}$$

$$p_3 = \frac{\pi w}{cosh^{-1}\left(\frac{1}{2}\left(\sqrt{Q_1/Q_3} + \sqrt{Q_1/Q_2}\right)\right)} \tag{4.6}$$

where w is the strip pitch, Q_1 is the highest value of charge, and Q_2 and Q_3 are the charges of the strips at the right and at the left of Q_1, respectively.

4.3.1.1 Absolute position

Note that the position a_2 is measured from the center of the strip where Q_1 was measured, it is not an absolute position. It is necessary then to take into account the position of the strip fired within the detector, the absolute position in the LAB frame is given by:

$$p_2' = p_2 + w * (i - 14.5) \tag{4.7}$$

where p_2' is the absolute position in the lab frame, p_2 is the position previously determined, i is the index (ranging from 1 to 28) of the strip where Q_1 was measured, and w is the strip pitch.

4.3.1.2 Corrections

The previous absolute position was obtained assuming that the CATS detectors were centered on the beam axis. However, a correction has to be included in order to account for any possible misalignment of the detectors. Although a surveyor has measured the detector positions by laser alignment, the corrections have been determined empirically to achieve the most accurate reconstruction of the mask at target position.

CATS1		CATS2	
X[2](mm)	Y (mm)	X (mm)	Y (mm)
+3.43	0.07	0.0	+0.7

Table 4.4: Position corrections.

4.3.2 Path reconstruction

After calculating the hit position on CATS1 and CATS2 and taking into account the position of the CATS detectors with respect to the target (CATS1 at -1193 mm and CATS2 at -684 mm), it is possible to perform a path reconstruction and extrapolate the position on the z=0 plane, where the target is placed, by applying basic algebra:

$$x^{target} = x^{CATS2} - \frac{x^{CATS2} - x^{CATS1}}{z^{CATS2} - z^{CATS1}} * \left(z^{CATS2} - z^{target}\right) \tag{4.8}$$

$$y^{target} = y^{CATS2} - \frac{y^{CATS2} - y^{CATS1}}{z^{CATS2} - z^{CATS1}} * \left(z^{CATS2} - z^{target}\right) \tag{4.9}$$

4.3.3 Reconstruction validation

4.3.3.1 Mask on CATS

In order to ensure a good position reconstruction, a mask made of a metallic drilled plate, whose holes form an asymmetrical pattern, was placed over both detectors (one at a time). Comparing the position reconstruction with the mask itself allow us to verify the position reconstruction and notice any possible inversion of strip.

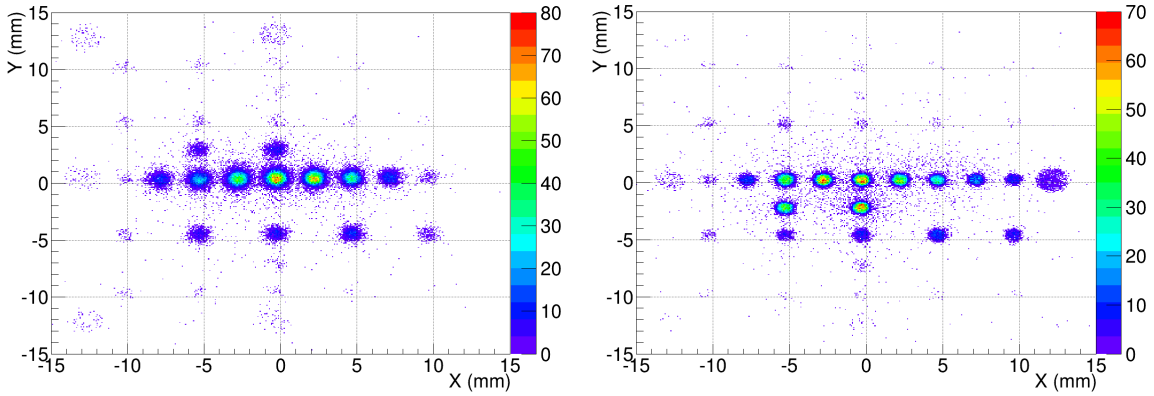

(a) Mask on CATS1, Z=-1356mm

(b) Mask on CATS2, Z=-849mm

Figure 4.9: The reconstruction at CATS position shows a well reproduced mask pattern.

[2]The beam axis is taken to be the Z axis, while the X and Y are the horizontal and vertical axis respectively. The point $(0, 0, 0)$ is assumed to be the center of the target.

4.3.3.2 Mask on target

Once the positions obtained from CATS1 and CATS2 are proved to be trustworthy, we follow the same philosophy to check the path reconstruction and a different mask was placed at target position. A comparison between the reconstruction with the mask pattern will give us an idea of the accuracy of the path reconstruction.

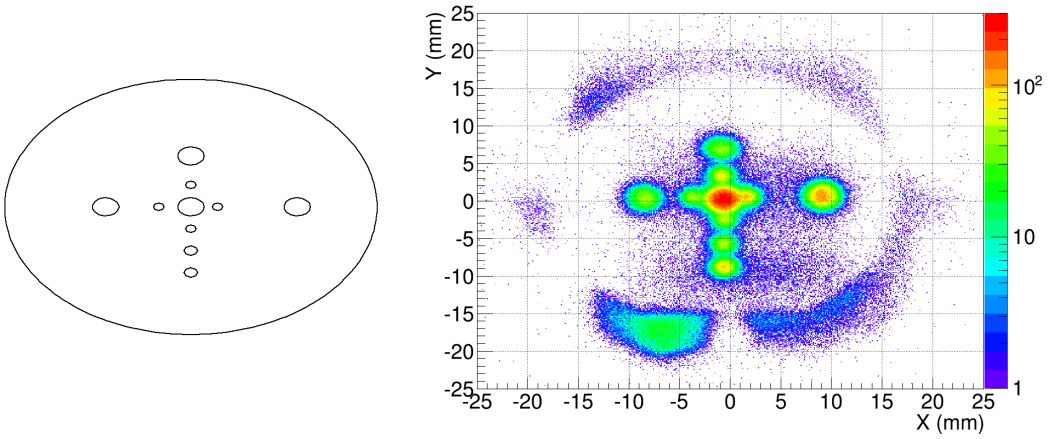

(a) Mask *(b) Mask on target, Z=0mm*

Figure 4.10: Reconstruction at target position (b) with a mask (a) at the target position.

Resolution

The best way to measure the position resolution at target position would be using a beam with a negligible divergence, but this is not possible. Instead, we have used the mask in our advantage, as it behaves like a collimator, reducing the beam divergence. We got the position resolution by measuring the FWHM of the peak corresponding to the central hole of the mask, once the deconvolution of its size has been performed.

The CATS position resolution has been deduced by applying the uncertainty propagation law, assuming it was the same for both detectors.

	X (mm)	Y (mm)
Intrinsic resolution (FWHM)	0.414	0.440
Resolution at target position (FWHM)	1.528	1.621

Table 4.5: CATS position resolution and position resolution at the target plane.

4.3.3.3 Beam reconstruction at target position

The beam reconstruction at target position is shown in figure 4.11. It is worth remarking that the beam is well focused on the target, although it extends over 8.96 mm and 6.27 mm, on X and Y axis respectively, at half maximum.

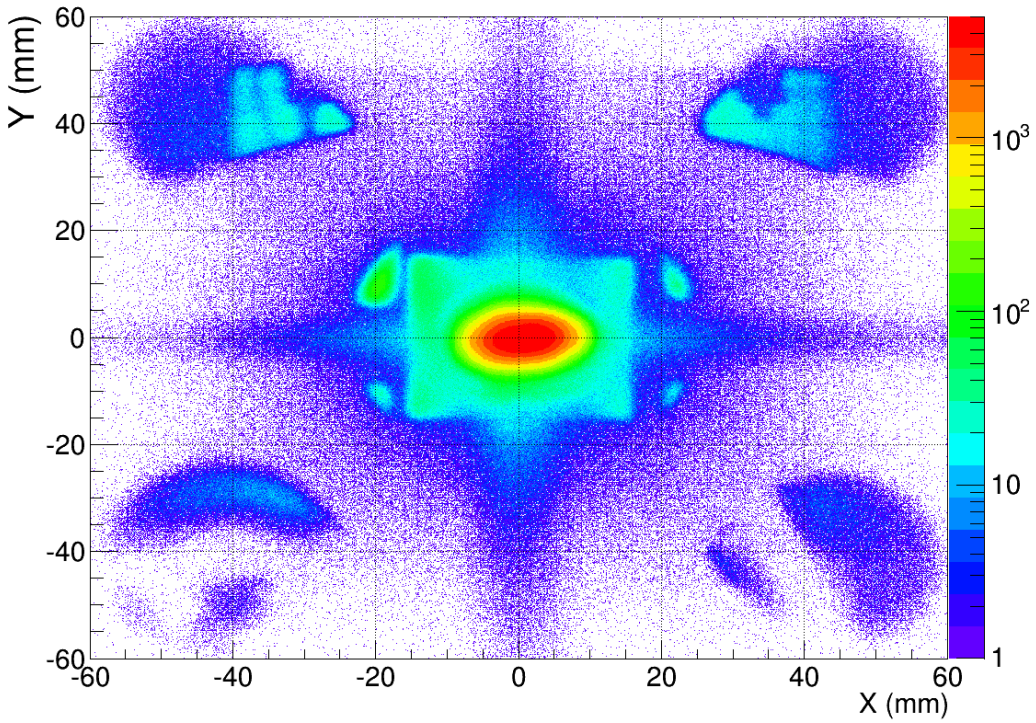

Figure 4.11: Beam reconstruction on target. The square pattern surrounding the beam is the target frame. A hint of MUST2 telescopes appears in the corners.

4.4 Barrel calibration

4.4.1 Offset subtraction

A pulser calibration is performed aiming to correct for any offset or non-linearities, that would have a significant impact on the position measurement.

The offset is obtained by using a pulser, whose signals were fed into the preamplifiers in order to have peaks within the widest range possible the attenuation settings were modified.

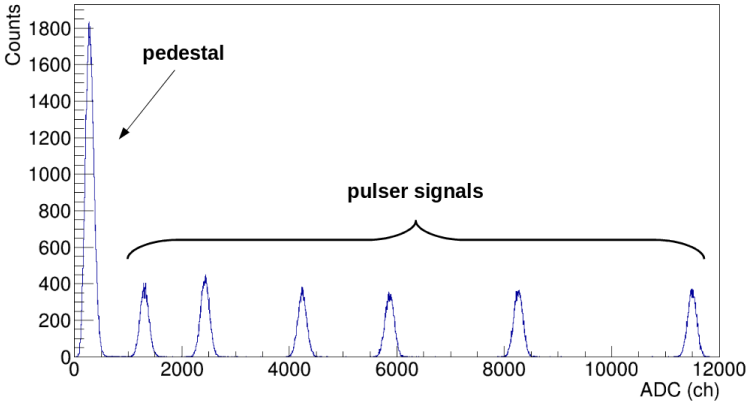

Figure 4.12: Pulser spectrum for a strip-end. The pedestal is followed by six peaks.

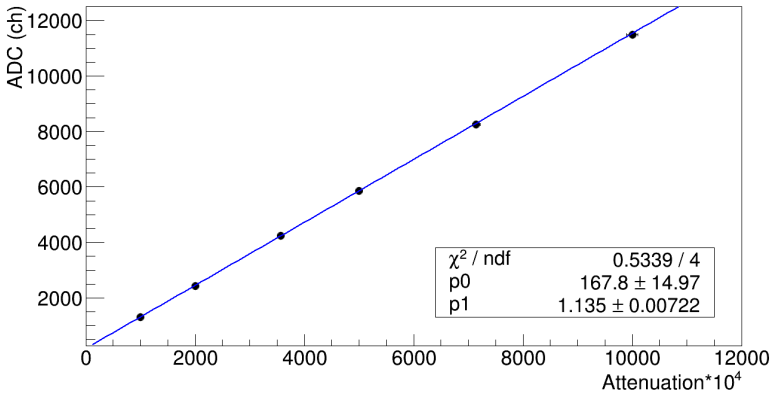

Figure 4.13: Offset determination of inner barrel strips.

For each strip, the position of the peaks is determined by fitting them to a Gaussian function. These positions are plotted against the attenuation settings corresponding to each one and finally, a linear fit provides the offset-subtracted raw energies:

$$x_i = x_i^{raw} - a_i \tag{4.10}$$

where x_i is the offset-subtracted raw energy, x_i^{raw} is raw energy value for the i^{th} channel, and a_i is the offset given by the linear fit.

The offset determination has been applied to strips and back signals in both inner and outer barrels.

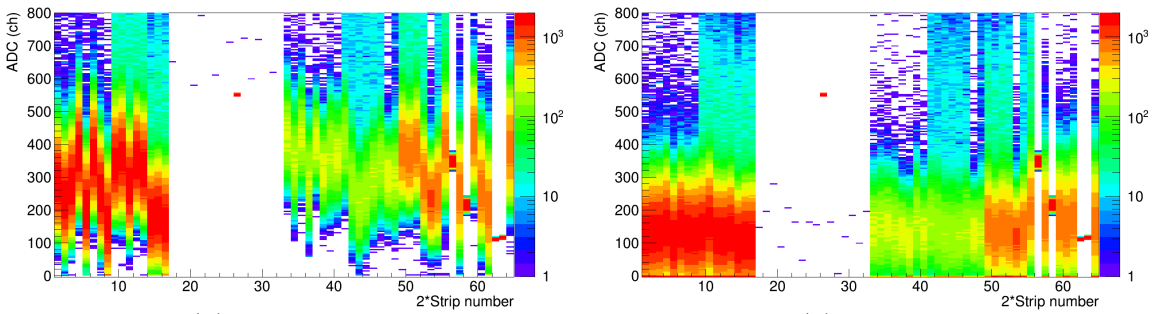

(a) Before, x_i^{raw} *(b) After, x_i*

Figure 4.14: Comparison of low channel spectra of barrel strips before and after the offset subtraction.

4.4.2 Energy and position calibration

The α calibrations have been performed using a double-sided 3α-source placed at the target position. As mentioned before, this source produces three main α lines at 5.157, 5.486 and 5.805 MeV, plus other weaker peaks that are hardly resolvable with TIARA. The energy losses in the dead layer (1 µm) on the front side of the Si detectors were taken into account for each decay at the barrel ends and a weighted average was taken for each radionuclide: 4.896, 5.234 and 5.562 MeV.

Since the strips in the barrel are position sensitive, the total energy of the particle is obtained by adding the signals from the two strip ends, while the position is given by the difference between the signals at the ends of the strip. Figure 4.15 illustrates the correlations between the signal amplitudes from the two ends of a given strip.

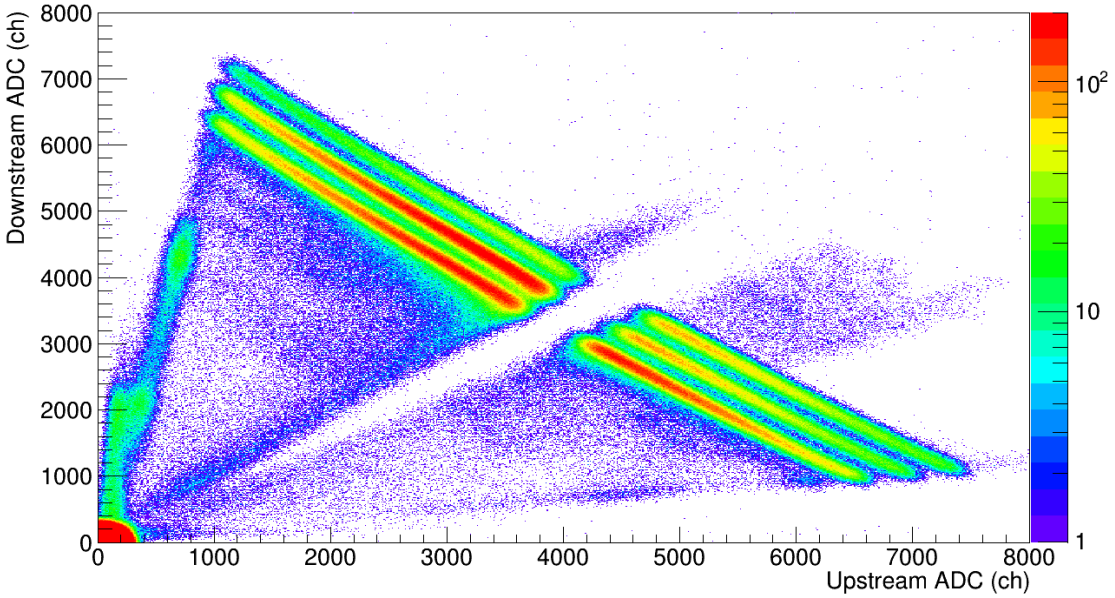

Figure 4.15: Downstrip vs upstream signal amplitudes for a strip in the Inner Barrel, showing the correlation between strip ends.

4.4.2.1 Energy calibration

The energy is given by summing the amplitude of the signal at both strip ends after calibrating the charge.

$$\begin{cases} E^{\alpha} = G_i^{up} x_i^1 + G_i^{down} y_i^1 \\ E^{\alpha} = G_i^{up} x_i^2 + G_i^{down} y_i^2 \end{cases} \tag{4.11}$$

where E^{α} is the energy deposited in the detector, G_i^{up} and G_i^{down} are the gain-matching parameters for the upstream and downstream ends of the i^{th} strip, and (x_i^1, y_i^1) and (x_i^2, y_i^2) are two points[3] extracted from figure 4.15 in order to solve the system (4.11) and get the G_i^{up} and G_i^{down} as follows:

$$G_i^{up} = \frac{E^{\alpha}(y_i^2 - y_i^1)}{x_i^1 y_i^2 - x_i^2 y_i^1} \qquad G_i^{down} = \frac{E^{\alpha}(x_i^1 - x_i^2)}{x_i^1 y_i^2 - x_i^2 y_i^1} \tag{4.12}$$

The gain-matching coefficients G_i^{up} and G_i^{down} have been calculated for the three E^{α} values and a weighted average was taken to perform the calibration.

[3]Note that there are no position requirements the points (x,y) have to meet to perform the energy calibration. Thus, for the sake of simplicity, the same points used for the position calibration have been used for the energy calibration.

4.4.2.2 Position calibration

The position along the theoretical beam axis is determined by the difference between the gain-matched strip end signals, which is divided by the total energy in order to normalize the position between -1 and 1 for the upstream and downstream end, respectively:

$$p_i = \frac{G_i^{down} y_i - G_i^{up} x_i}{G_i^{up} x_i + G_i^{down} y_i} \tag{4.13}$$

where p_i is the position, x_i and y_i are the upstream and downstream signals, respectively, of the i^{th} strip, and G_i^{up} and G_i^{down} are the corresponding gain-matching parameters previously obtained.

This would be true if the signals could reach near zero values, but this is not the case because of the effect of the offset resistors. Thus p_i instead of going from -1 to 1 spans from p_i^{up} to p_i^{down}, but this new limits can be determined by picking two points $(x_i, y_i)^{up}$ and $(x_i, y_i)^{down}$ from figure 4.15, as close as possible to each end of the strip:

$$p_i^{up} = \frac{G_i^{down} y_i^{up} - G_i^{up} x_i^{up}}{G_i^{up} x_i^{up} + G_i^{down} y_i^{up}} \qquad p_i^{down} = \frac{G_i^{down} y_i^{down} - G_i^{up} x_i^{down}}{G_i^{up} x_i^{down} + G_i^{down} y_i^{down}} \tag{4.14}$$

Finally, using p_i^{up} and p_i^{down} it is possible to renormalize p_i and get a new position P_i ranging from 0 at the downstream end to 1 at the upstream end:

$$P_i = \frac{p_i^{down} - p_i}{p_i^{down} - p_i^{up}} \tag{4.15}$$

The position calibration has been performed for all three α-lines and an average was done to the three sets of parameters to obtain the coefficients used.

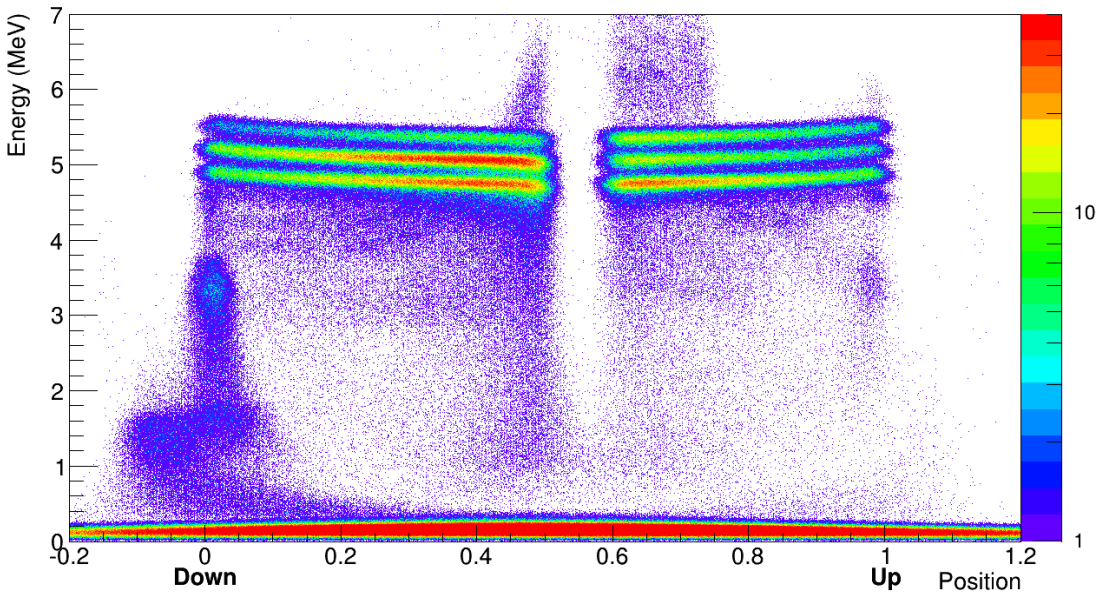

Figure 4.16: Energy vs position for a strip in the Inner Barrel.

4.4.3 Ballistic deficit correction

The amplitude of a signal produced by a semiconductor detector should be proportional to the charge produced by the incoming particle, leading to a dependency of the amplitude on the charge collection time: no charge will be lost if the measurement is done in a very long time compared to charge collection time, but unfortunately the shaping time has to meet some constraints to allow high rate operation and to keep a good signal-to-noise ratio and some charge carriers can be lost, causing ballistic deficit effects.

It would not be a problem if the charge collection time was constant, because it would be corrected through the gain-matching stage, but this is not our case as the charge collection depends on the hit position along the beam axis. If the particle hit is close to a strip end, most of the charge would be collected in the nearest end within the shaping time minimizing the ballistic deficit effect. On the other hand, a hit near the center will produce charge carriers that need to travel across half the length of the strip to produce the strip end signals. Therefore, the longer charge collection time results in a stronger ballistic deficit effect.

With a shaping time of 1 µs, the barrel presents a non-linear dependency of the energy as a function of the position because of the ballistic deficit effect as shown in figures 4.16 and 4.17.

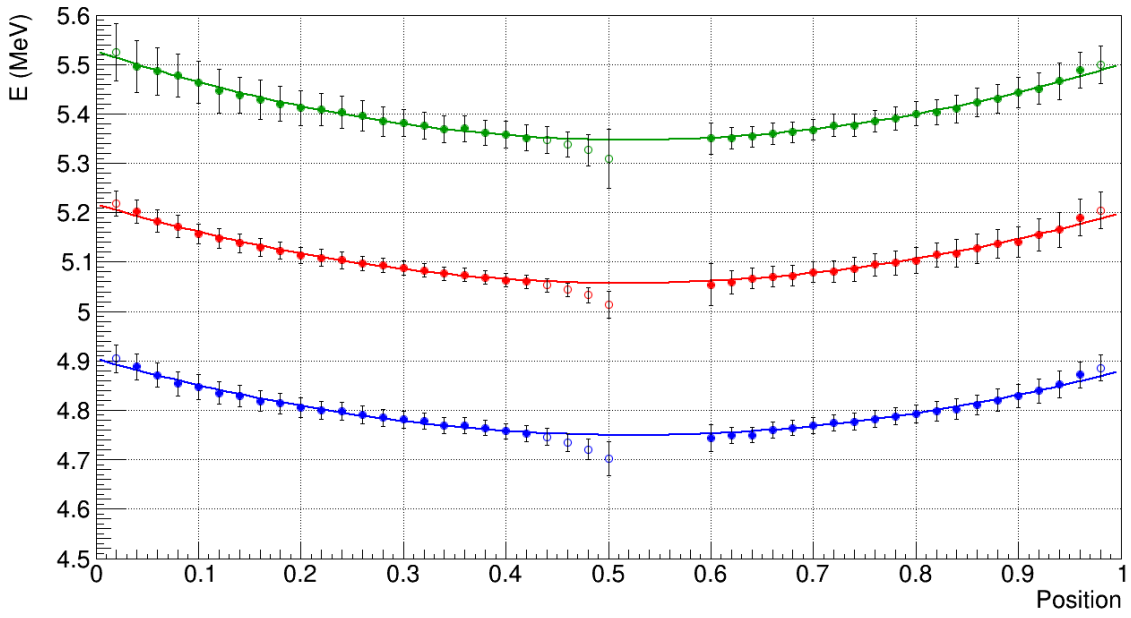

Figure 4.17: The ballistic deficit correction has been performed by taking 50 slices in position on figure 4.16 and fitting them to 3 Gaussians. Their centroids were then plotted versus the position of the slice along the strip. Finally a fit was done to describe the energy-position dependency, only on the points with closed symbols to avoid those affected by energy losses in the source layer, which is thick enough to stop α particles as .

Figure 4.17 shows how this behaviour was corrected by fitting each α-line to a 2^{nd}-order polynomial function. The average coefficients were taken to be applied as follows:

$$E_i^{IB} = \frac{E^{\alpha}}{a + bP_i + cP_i^2} \tag{4.16}$$

where E_i^{IB} is the energy deposited in the i^{th} strip, and a, b and c are the ballistic deficit correction parameters. The result is displayed in figure 4.18:

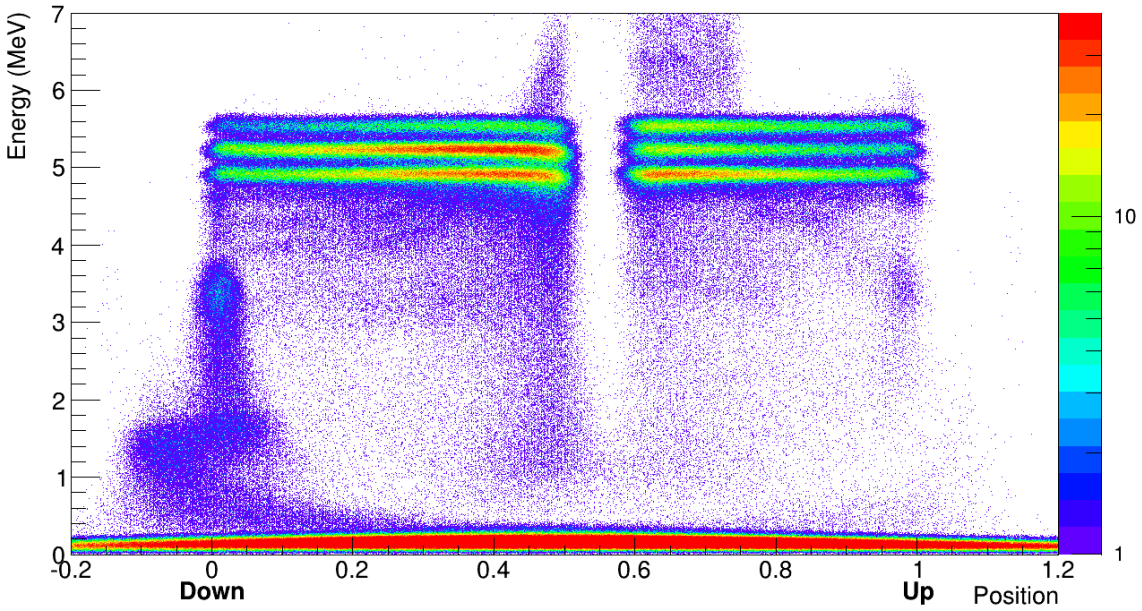

Figure 4.18: Energy vs position, after applying the ballistic deficit correction.

4.4.4 Features of the Energy vs Position spectrum

The energy versus position plots presented in figures 4.16 and 4.18, and even the downstream versus upstream signal plot in 4.15 show some characteristic features other than the main three α-lines. The lack of events in positions between 0.5 and 0.6 is due to the shadow cast by the target holder and the source frame. Energy loss effects are also visible in the boundaries of this gap.

The events at low energies (below 0.5 MeV) are the pedestal events that are clearly seen in the downstream versus upstream signal plot in figure 4.15 around $(0, 0)$. The large statistics accumulated here is due to the data acquisition: the barrel read out is triggered by common gates provided by the OR of the back signals of two detectors, therefore for each strip fired we are reading 7 strips in noise. These events will be rejected in the analysis of ^{16}C(d,p) data by requesting a coincidence between front and back energy values.

The structure at the downstream end below the α-lines is due particles hitting one of the tracks running around the silicon strips to route the signals to the connectors in coincidence with noise in the opposite end. This effect is more pronounced in the downstream end because the wiring of these signals is crossing the PCB board to reach the output connector at the upstream side of the PCB board. It is worth mentioning that the effect of *crosstalk* is even less significant in the analysis of this work since most of the interesting data is at backward angles, which corresponds to the upstream end of the Barrel.

4.5 Hyball energy calibration

The energy calibration has been done with the same 3α-run used for the Barrel. The dead layer on the front side of the Si detectors (0.5 µm of aluminium) was taken into account and the resulting energies were used: 5.071, 5.404 and 5.727 MeV[4].

Since the Hyball resolution is better it allows to distinguish the weaker decays, the energy spectrum of each strip is fitted with a combination of six Gaussian functions to take into account not only the three main α peaks, but also the less intense decays. Once the peak centroids have been determined, we assume a linear relationship between the ADC channel number and the energy deposited:

$$E_i^{HY} = a_i + b_i * E_i^{gm} \tag{4.17}$$

where E_i^{gm} and E_i^{HY} are the gain-matched[5] and the calibrated energies for the i^{th} channel, and a_i and b_i are the calibration parameters.

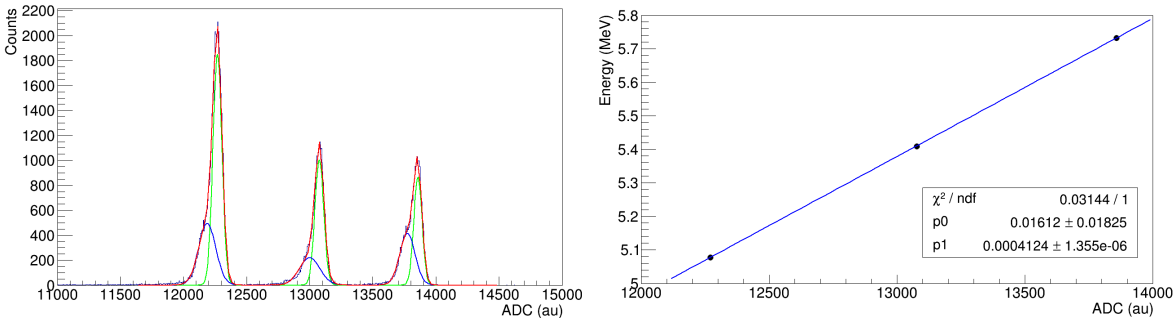

(a) α-peak finding and fit *(b) α calibration*

Figure 4.19: The energy calibration was obtained from a fit to a first order polynomial.

[4]As the effect of the dead layer is different for each ring, a different energy was taken for each one. The quoted energies are weighted averages of all the ring energies, which are also the ones used for sectors.

[5]The gain matching is achieved following a method similar to that described for the Barrel (see section 4.4.1).

4.6 Scattering angle

4.6.1 Barrel

Once the position of the light particle hit along the strip P_i is known, the corresponding z coordinate is given by

$$z = L\left(P_i - \frac{1}{2}\right) \tag{4.18}$$

where L stands for the length of the Barrel strips.

Then, assuming that the reaction takes place at the (0,0,0), the scattering angle θ' of the light particles hitting the Barrel is given by

$$\theta' = acos\left(\frac{z}{\sqrt{x^2+y^2+z^2}}\right) \tag{4.19}$$

where (x,y,z) is the position of the hit in the Barrel, being z is the coordinate along the theoretical beam axis calculated as indicated in equation 4.28, and x and y the coordinates orthogonal to the beam axis, which have been calculated geometrically based on the Barrel strip dimensions and randomized within the strip size.

4.6.2 Hyball

The scattering angle θ' of the particles hitting the Hyball is given by equation 4.19 as well, where z is the position of the Hyball along the theoretical beam axis (-15 cm) and x and y are given by

$$x = rcos\phi \qquad y = rsin\phi \tag{4.20}$$

where r is the distance to the theoretical beam axis and ϕ is the angle between r and X axis. Both r and ϕ are provided by the number of ring and sector hit, respectively.

4.6.3 Beam corrections

However, equation 4.19 relies on the assumption that the reaction always take place at $(0,0,0)$ and the beam arrives parallel to the Z axis and hits the target perpendicularly and we have already seen that this not the case: the beam reconstruction at target position (figure 4.11) shows that the beam spot extends over 9 mm and 6 mm on X and Y axis respectively. And the beam axis can be tilted up to 2^o with respect to the theoretical beam axis.

Therefore, a different approach is needed in order to take into account the direction of the incoming beam particle and its point of interaction on target in the calculation of the scattering angle θ:

$$\theta = acos\left(\frac{x_{beam}(x - x^{target}) + y_{beam}(y - y^{target}) + z_{beam}(z - z^{target})}{\sqrt{(x-x^{target})^2+(y-y^{target})^2+(z-z^{target})^2}\sqrt{x_{beam}^2+y_{beam}^2+z_{beam}^2}}\right) \quad (4.21)$$

where (x_{beam},y_{beam},z_{beam}) is a direction vector of the beam path and (x^{target},y^{target},z^{target}) is the position of the point of interaction on target. The beam direction vector and x^{target} and y^{target} coordinates are provided in an event-by-event basis by the CATS reconstruction, however z^{target} cannot be measured or extracted since there is no way to know where the reaction took place inside the target, and hence z^{target} is assumed to be zero since the center of the target supposed to be the average reaction position. The position of the hit in the Barrel (x,y,z) remains the same as in equation 4.19.

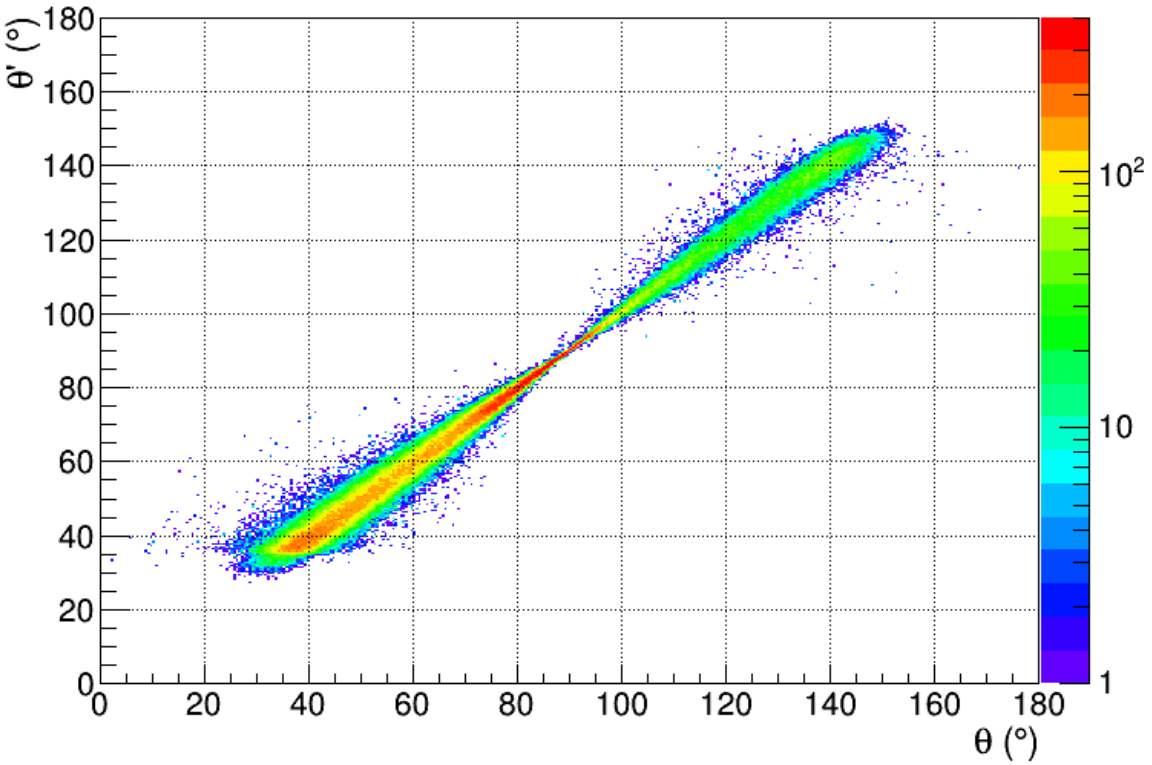

Figure 4.20: Representation of the scattering angle θ' (equation 4.29) versus the corrected scattering angle θ (equation 4.30) for particles detected in the Barrel. The shape of the pattern, wider at the strip ends of the Barrel and narrower at 90º, is a clear indication that the main contribution to the correction is due to the effect of the beam interaction point being off-center, since its effect is maximal at the edges of the Barrel and cancels at 90º. The inclination of the beam direction is barely influential as the beam path is not more tilted than 2º with respect to the theoretical beam axis.

4.7 Energy loss corrections

The initial energy of the target-like ejectile is required for the reconstruction of the excitation energy of the states populated in the beam-like fragment. However, in semiconductor detectors there is an insensitive layer called *dead layer*, through which the incoming particles must pass before entering the active area, and hence losing a fraction of its kinetic energy before it can be measured. Furthermore, since the reaction takes place within the target, another fraction of its kinetic energy is loss leaving the target.

The nominal dead layer thickness was 1 µm of silicon and 0.5 µm of aluminium, respectively, for the Barrel and the Hyball. Concerning the target, only half the measured thickness was taken for the energy loss correction for consistency with the assumption made in equation 4.19 of the reaction taking place at the center of the target.

The effective thickness of the target and the detector dead layer is calculated on an event by event basis depending on the beam interaction point and the scattering angle. Then, the energy losses in the detector dead layer and the target are estimated using range tables in order to recover the initial energy of the ejectile.

The measured energy is first corrected for losses in the dead layer using the SRIM tables for silicon to obtain the energy of the particle after leaving the target. Then, the resulting dead-layer-corrected energy is corrected for losses in the target using the CD_2 SRIM tables to get the initial energy of the particle. The procedure is described in figure 4.21.

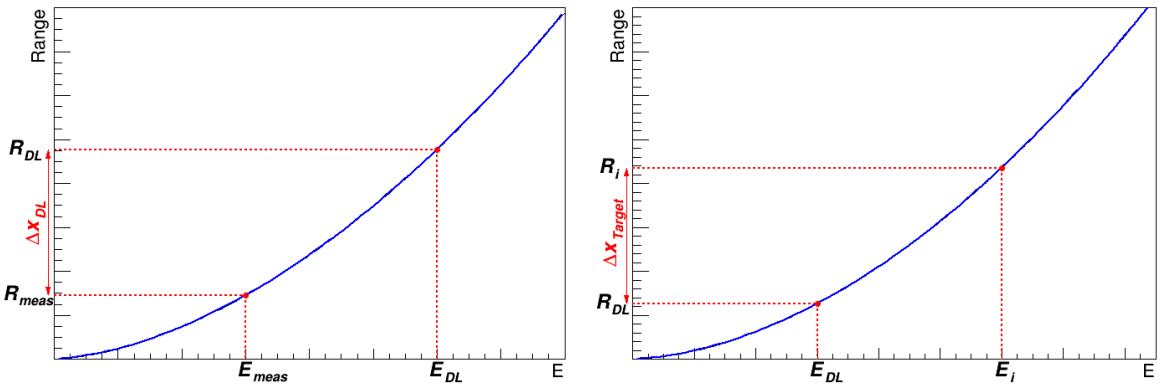

(a) Dead Layer *(b) Target*

Figure 4.21: The correction for energy losses in the target the dead layer makes use of range versus energy graphs for both dead layer and target materials: silicon (a) and CD_2 (b). E_{meas} is the measured energy and Δx_{DL} the effective dead layer thickness, from which the energy of the particle at the entrance of the detector E_{DL} is extracted as indicated (a). Same philosophy is followed in (b) to obtain the initial energy E_i from energy of the particle at the exit of the target E_{DL} and the effective target thickness Δx_{Target}.

4.7.1 Particles stopped in TIARA

The initial kinetic energy of the particles stopped in TIARA is given by the measured energy plus the energy lost in the detector dead layer and the target.

4.7.2 Punchthrough events

For punchthrough events, the initial kinetic energy of particle is the energy measured in the inner barrel plus the energy lost in the detector dead layer and the target plus the remaining energy after leaving the Inner Barrel.

A relationship between the energy at the entrance of the active volume of the silicon detector, E_{ent}, and the energy deposited in the Inner Barrel, E_{dep}, for a given angle of incidence is determined by mapping the energy versus range curve taking 50 points (E_{ent},E_{dep}) corresponding to the effective thickness of silicon given by the measured scattering angle, as indicated in figure 4.22a. Once this relationship is known, a simple interpolation of E_{ent} at the energy measured in the Inner Barrel, E_{meas}, provides the kinetic energy of the particle at the entrance of the active detector volume, E_{Si} (figure 4.22b).

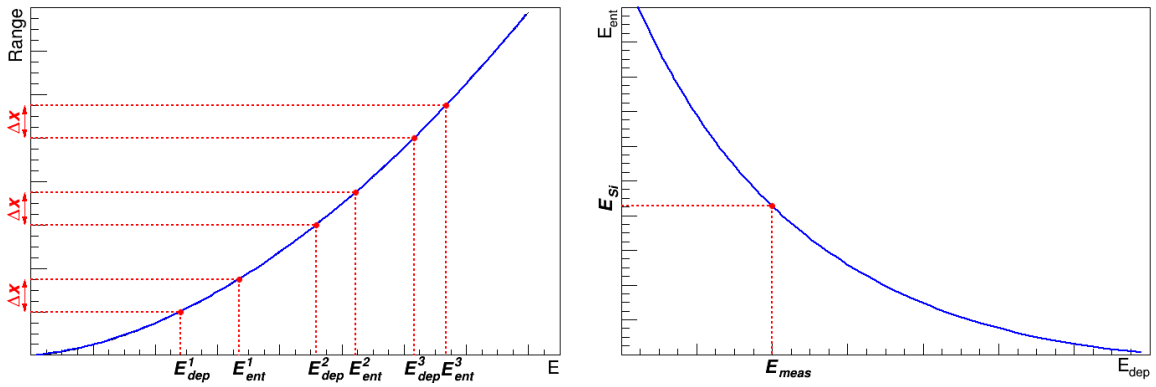

(a) Range versus energy in silicon *(b) E_{ent} versus E_{dep}*

Figure 4.22: The reconstruction of the energy at the entrance of the active detector volume, E_{Si}, is based on the range versus energy curve, in which bins of fixed length in range have been projected in energy to obtain a set of points (E_{ent},E_{dep}) (a). These points provide the relationship that allows to extract E_{Si} by extrapolating E_{ent} at the energy measured in the Barrel.

Once the energy at the entrance of the active volume of the silicon detector is obtained, the correction described in figure 4.21 is applied in order to correct the energy losses in the dead layer and the target.

4.8 CHARISSA calibration

The energy calibration method applied for the DSSSD will be presented in this section. Note that exactly the same method was used for all the strips, no matter in what layer or on what side they are, that is why all the following plots correspond to the front of the first silicon.

4.8.1 Gain matching

As for the previous detectors, the gain matching relies on a pulser run. This time, 6 different pulser signals were sent into the preamplifiers, one by one, to fire each strip of the detectors covering the widest range possible.

For a given strip, the pulser peaks are fitted with Gaussians to determine their centroid and these centroids are plotted against the centroids corresponding to the strip chosen as reference[6].

Subsequently, a linear fit provides the gain matching parameters, that are finally applied according the equation below:

$$E_i^{gm} = a_i + b_i * E_i^{raw} \tag{4.22}$$

where E_i^{gm} is the gain matched energy and E_i^{raw} is the raw energy value for the i^{th} channel, while a_i and b_i are the offset and the slope of the linear fit, respectively.

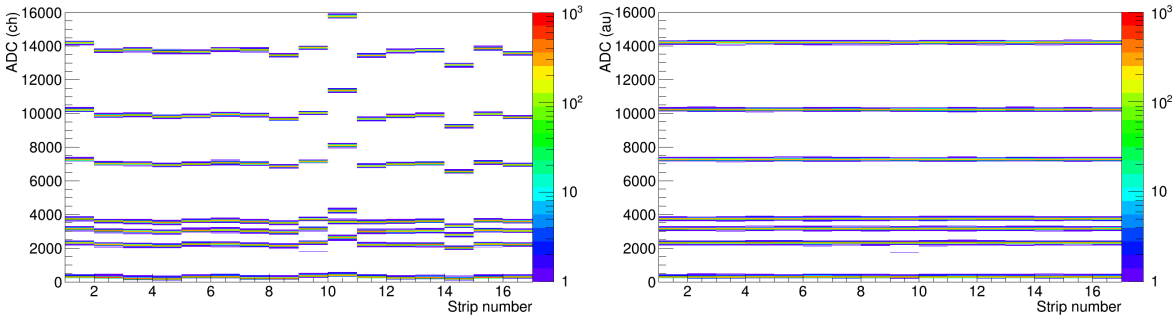

(a) Before, E_i^{raw} *(b) After, E_i^{gm}*

Figure 4.23: Comparison of pulser data for the front side of the first silicon detector before and after the gain matching.

[6]The first working strip on each side of each silicon was taken as reference and the slope and the offset of every other strip in the same side have been extracted to match this one.

4.8.2 Energy calibration

4.8.2.1 α calibration

The α calibrations have been done using a 3α-source placed at target position. As we did for TIARA, the dead layer on the entrance side of the detector (0.3 µm) was taken into account and the weighted average energy was used for each nuclide of the source: 5.1133, 5.4442 and 5.7653 MeV.

The energy spectrum of each strip is fitted with a combination of three gaussian functions to take into account the three main α peaks and determine their centroids. Once the peak locations has been determined, we assume a linear relationship between the ADC channel number and the energy deposited in the silicon detector:

$$E_i^{\alpha-cal} = \tilde{a}_i + \tilde{b}_i * E_i^{gm} \tag{4.23}$$

where $E_i^{\alpha-cal}$ is the α-calibrated energy, E_i^{gm} the gain matched energy for the i^{th} channel, and $\tilde{a}_i$ and $\tilde{b}_i$ are the offset and the slope, respectively, of the linear fit between the gain matched centroid energies of the peaks and their corresponding deposited energies.

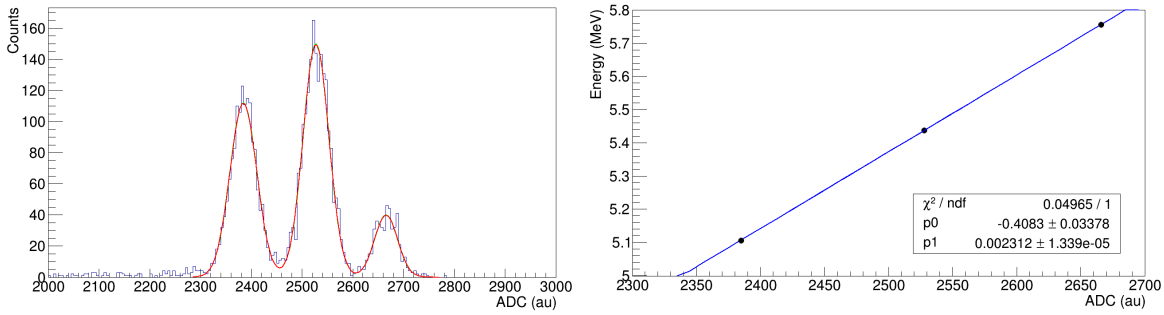

(a) Centroid search *(b) α calibration*

Figure 4.24: Calibration fits.

4.8.2.2 Beam calibration

Unfortunately, the energy deposited by the α particles is far from the energy region where we expect to measure our beam-like products, so a second calibration was done using the data taken during the beam time to extend the calibration range towards this region. For that purpose, we picked up several points in two different ways: using the punch through energies and taking advantage of the kinematics of reactions such as ^{16}C(d,p)^{17}C* and ^{16}C(d,d)^{16}C.

It is important to mention that this beam calibration is applied after the previously discussed α-calibration.

4.8.2.2.1 Punch through

When a charged particle passes through a given material, it loses energy continuously along its path until either it is stopped or escapes the material. The energy at which it is no longer stopped is known as *punch through*.

Figure 4.25 shows several energy loss patterns, that can be easily distinguished to use as reference in the calibration. These are the punch-throughs of the ^{4}He, ^{7}Li and ^{16}C ions. Their corresponding energies are shown in table 4.6.

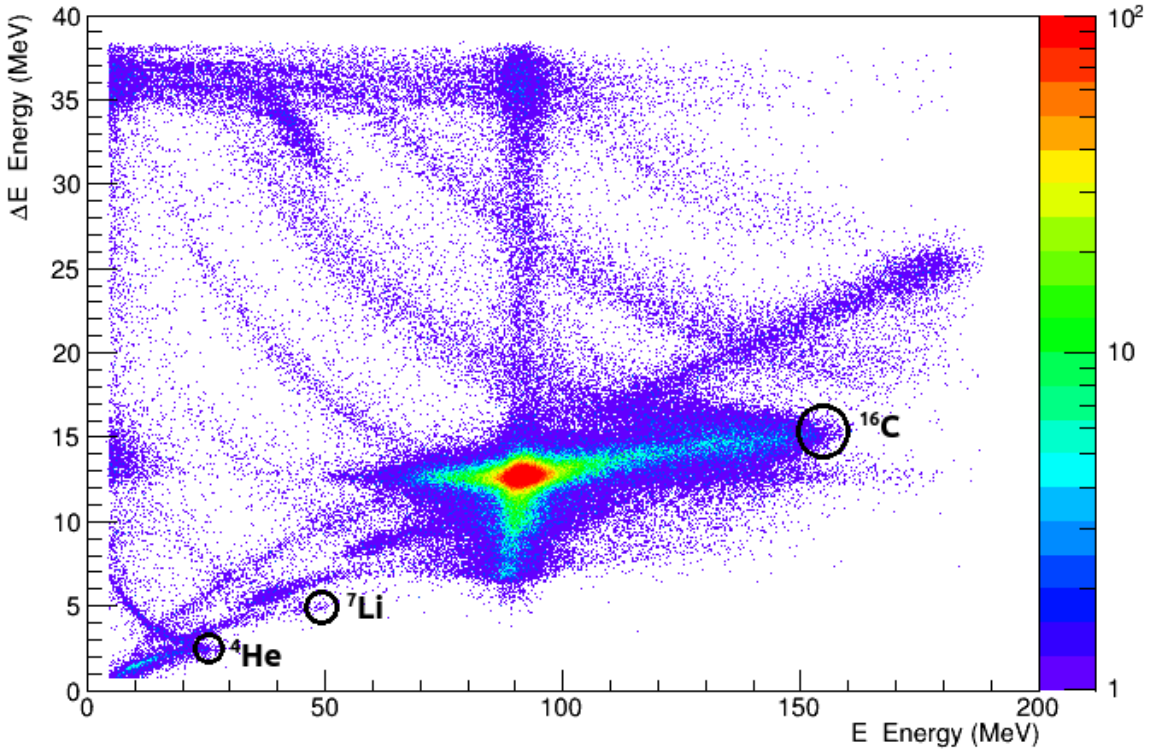

Figure 4.25: The ΔE Vs E plot shows several energy loss patterns for isotopes between Z=2 and Z=7, but only the punch-throughs of ^{4}He, ^{7}Li and ^{16}C can be identified.

Isotope	Theoretical values		Experimental values	
	ΔE (MeV)	E (MeV)	ΔE (MeV)	E (MeV)
^{4}He	2.43	33.02	2.40	26.39
^{7}Li	4.92	66.62	4.84	51.14
^{16}C	15.45	204.71	15.26	156.39

Table 4.6: Calibration points taken from the punch throughs.

4.8.2.2.2 Kinematics

The method consists in selecting data from a single reaction by gating on the associated kinematical pattern in the E vs angle plot in Tiara. In this way we obtain the experimental values for beam-like and target-like particle energies. Then, using just the equations from the kinematics we deduce a theoretical value for the beam-like particle energy from the experimental target-like particle energy.

The calibration technique is identical for both silicon detectors. However, for the sake of simplicity, the following description is focused on the first silicon detector.

^{16}C(d,p)^{17}C*

Our first choice was gatting on the (d,p) channel and, therefore, on the γ-rays around 330 keV in order to select the events populating the second excited state of ^{17}C.

A correlation between the fragment energy loss measurement provided by CHARISSA and the energy deposited by the light ejectile in TIARA is shown in figure 4.26, from where a point ($\Delta E^{exp}_{^{17}C}$,E^{exp}_{p}) is taken:

E^{exp}_{p} (MeV)	$\Delta E^{exp}_{^{17}C}$ (MeV)
2.4991	13.7236

Table 4.7: Proton energy in TIARA and corresponding ^{17}C energy loss in CHARISSA.

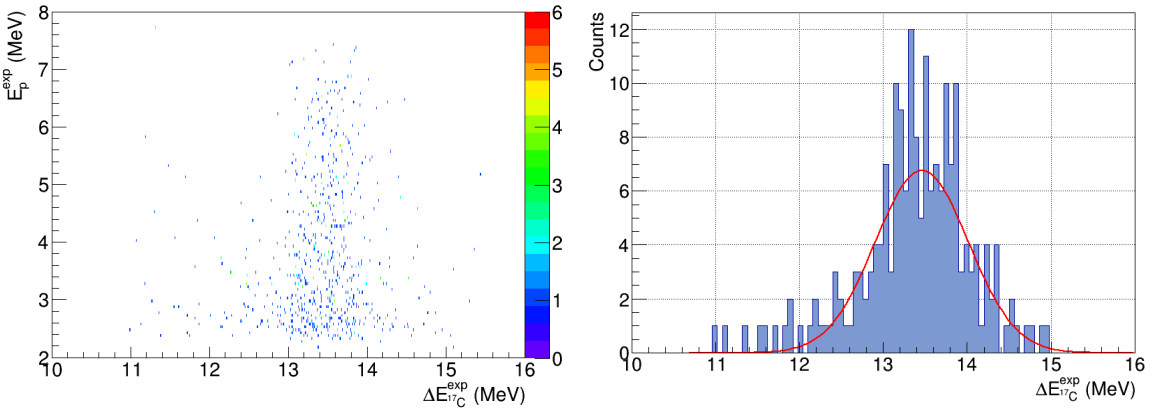

(a) E^{exp}_{p} versus $\Delta E^{exp}_{^{17}C}$ *(b) Slice in E^{exp}_{p}*

Figure 4.26: Proton energy measured in TIARA, E^{exp}_{p}, versus $^{17}C*$ energy loss in the first layer of CHARISSA, $\Delta E^{exp}_{^{17}C}$ (a). In order to obtain a pair of ($\Delta E^{exp}_{^{17}C}$,E^{exp}_{p}) correlated values, a thin slice around E^{exp}_{p} is projected in the X-axis and fitted with a Gaussian to determine the corresponding $\Delta E^{exp}_{^{17}C}$ value (b). Due to the lack of statistics, only one point at low energy was taken.

This correlation is used to obtain a theoretical energy loss, $\Delta E^{th}_{^{17}C}$, derived from the proton energy by considering the kinematics of the reaction (figure 4.27).

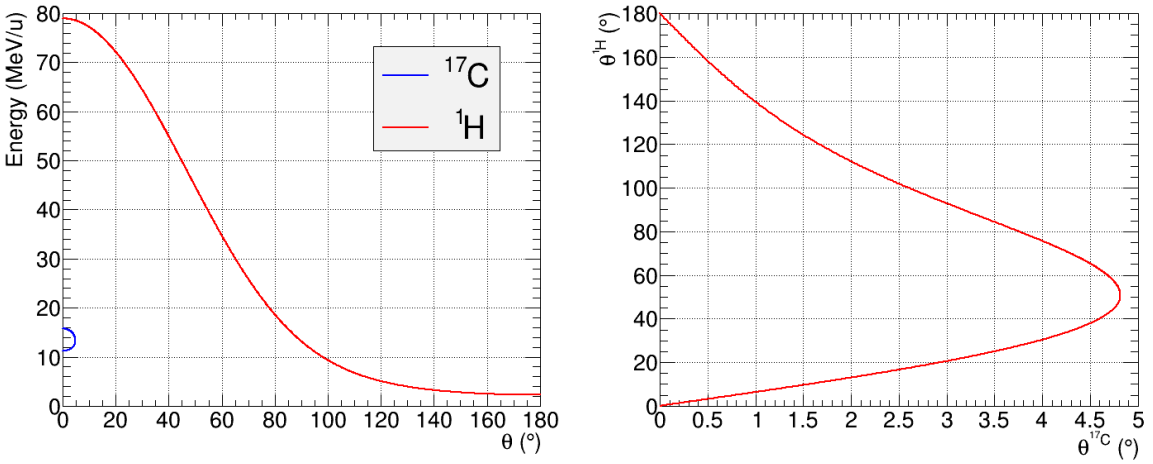

(a) Energy versus angle *(b) $\theta_{^{17}C}$ versus θ_p*

Figure 4.27: $^{16}C(d,p)^{17}C^*$ kinematics. Energy versus angle for both fragment and ejectile (a) and fragment angle versus ejectile angle (b).

Finally, we have a point ($\Delta E^{th}_{^{17}C}$,$\Delta E^{exp}_{^{17}C}$) to add to the calibration.

Target-like particle		Beam-like particle		CHARISSA
E_p (MeV)	θ_p (°)	$\theta_{^{17}C}$ (°)	$E_{^{17}C}$ (MeV/u)	$\Delta E^{th}_{^{17}C}$ (MeV)
2.4991	160.48	0.4461	15.8254	13.739

Table 4.8: Kinematics of the $^{16}C(d,p)^{17}C^*$ reaction

^{16}C(d,d)^{16}C

The next reaction chosen to gate on is the elastic scattering. Since the cross-section is higher and therefore also the statistics, two points are taken from this reaction channel.

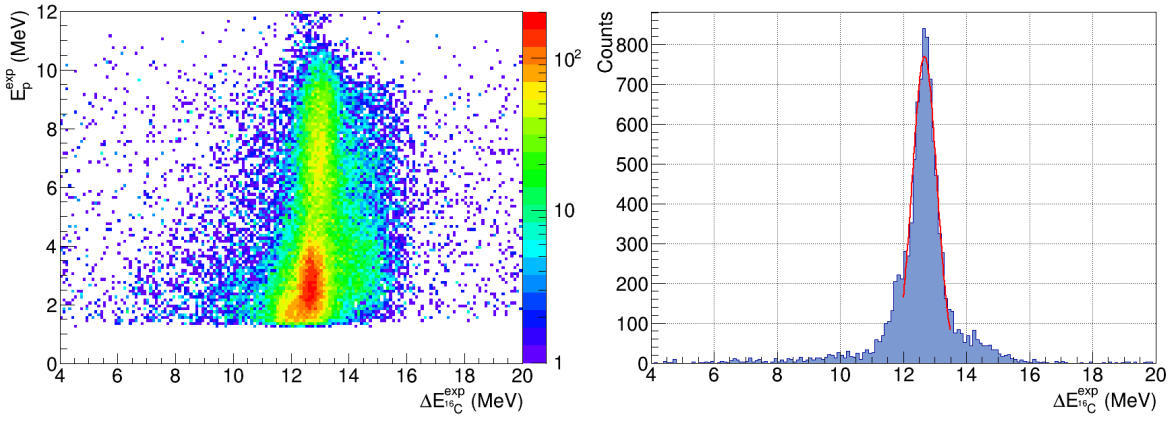

(a) E_d^{exp} versus $\Delta E^{exp}_{^{16}C}$ *(b) Slice in E_d^{exp}*

Figure 4.28: Correlation between the deuterium energy, E_d^{exp}, and ^{16}C energy loss, $\Delta E^{exp}_{^{16}C}$ (a). Slice in E_p^{exp} and fitted with a Gaussian to obtain the associated $\Delta E^{exp}_{^{16}C}$ (b).

E_d^{exp} (MeV)	$\Delta E^{exp}_{^{16}C}$ (MeV)
1.43129	12.9567
6.55737	13.2197

Table 4.9: Deuterium energy in TIARA and corresponding ^{16}C energy loss in CHARISSA.

The reaction is different, but the aim remains the same: to find the expected ^{16}C energy loss, $\Delta E^{th}_{^{16}C}$. In order to do so, we use the reaction kinematics (figure 4.29).

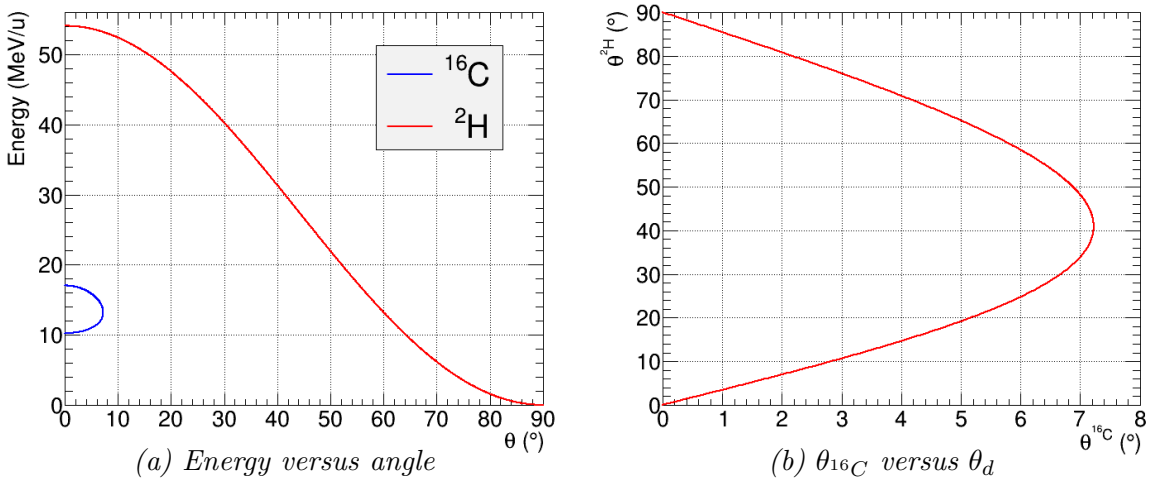

(a) Energy versus angle *(b) $\theta_{^{16}C}$ versus θ_d*

Figure 4.29: $^{16}C(d,d)^{16}C$ kinematics. Energy versus angle for both fragment and ejectile (a) and fragment angle versus ejectile angle (b).

Target-like particle		Beam-like particle		CHARISSA
E_d^{exp} (MeV)	θ_d (°)	$\theta_{^{16}C}$ (°)	$E_{^{16}C}$ (MeV/u)	$\Delta E^{th}_{^{16}C}$ (MeV)
1.43129	83.342	1.4538	17.0233	12.938
6.55737	75.647	3.0630	16.7056	13.164

Table 4.10: Kinematics of the $^{16}C(d,d)^{16}C$ reaction

As a result, we obtain two points ($\Delta E^{th}_{^{16}C}$,$\Delta E^{exp}_{^{16}C}$) to include in the calibration.

4.8.2.2.3 Calibration

Finally, a linear fit was done to the theoretical energy vs experimental energy plot to determine the calibration parameters.

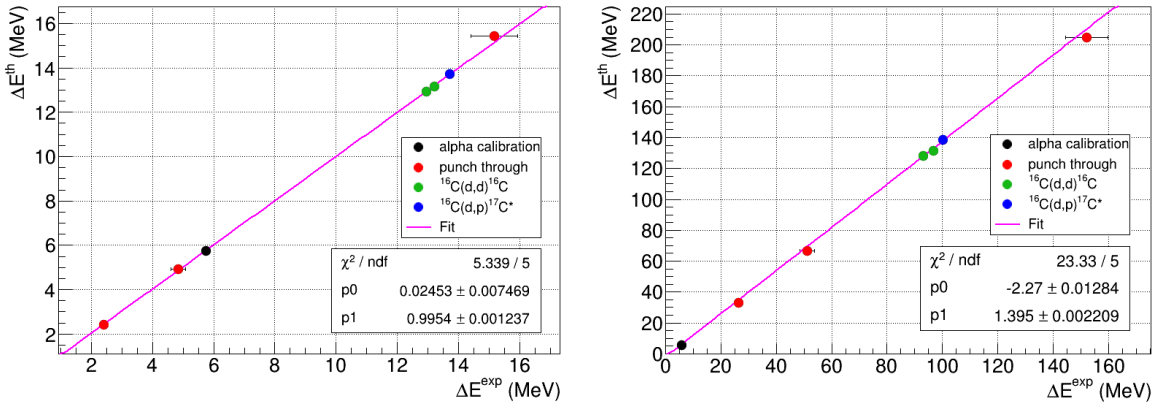

(a) ΔE beam calibration *(b) E beam calibration*

Figure 4.30: The calibration reveals that the first silicon remains barely unchanged. The second silicon needed an important correction to provide accurate measurements at high energies.

4.9 EXOGAM energy calibration

The EXOGAM calibration has been done using ^{60}Co, ^{133}Ba and ^{152}Eu sources, which have been selected in order to cover the widest energy range possible. In particular, the ^{133}Ba was chosen in order to have some additional peaks at low energies and hence enhance the reliability of the energy calibration in the region where we are expecting to measure our γ-rays.

The centroid position of each known peak was determined from a Gaussian fit plus a linear background. These positions were plotted against the quoted energy for each γ-ray line (table 4.11) and, finally, the calibration parameters were then obtained by a second-order polynomial fit (fig4.31).

E_γ (MeV)	Intensity (%)
1.1732	99.85
1.3325	99.98

(a) ^{60}Co.

E_γ (MeV)	Intensity (%)
0.0806	32.98
0.2764	7.16
0.3029	18.34
0.3560	62.05
0.3838	8.95

(b) ^{133}Ba.

E_γ (MeV)	Intensity (%)
0.1218	28.67
0.2447	8.37
0.3443	27.65
0.4111	2.29
0.4440	3.15
0.7789	12.99
0.8674	4.26
0.9641	14.54
1.0858	10.15
1.1120	13.44
1.4080	20.86

(c) ^{152}Eu.

Table 4.11: Energies and intensities of the γ-ray lines used in the EXOGAM calibrations. (a) ^{60}Co [65], (b) ^{133}Ba [66], (c) ^{152}Eu [67].

The energy spectra corresponding to each source are shown in figure 4.31. The calibration was rather stable and did not change through the duration of the experiment.

4.9.1 Addback

Ideally, a γ-ray interacts with only one crystal depositing its full energy, thus the resulting charge collected will be proportional to its energy. However, a γ-ray may scatter from one crystal to a neighbouring one, resulting in the total energy being shared by several crystals. In order to take into account cases such as this, a process

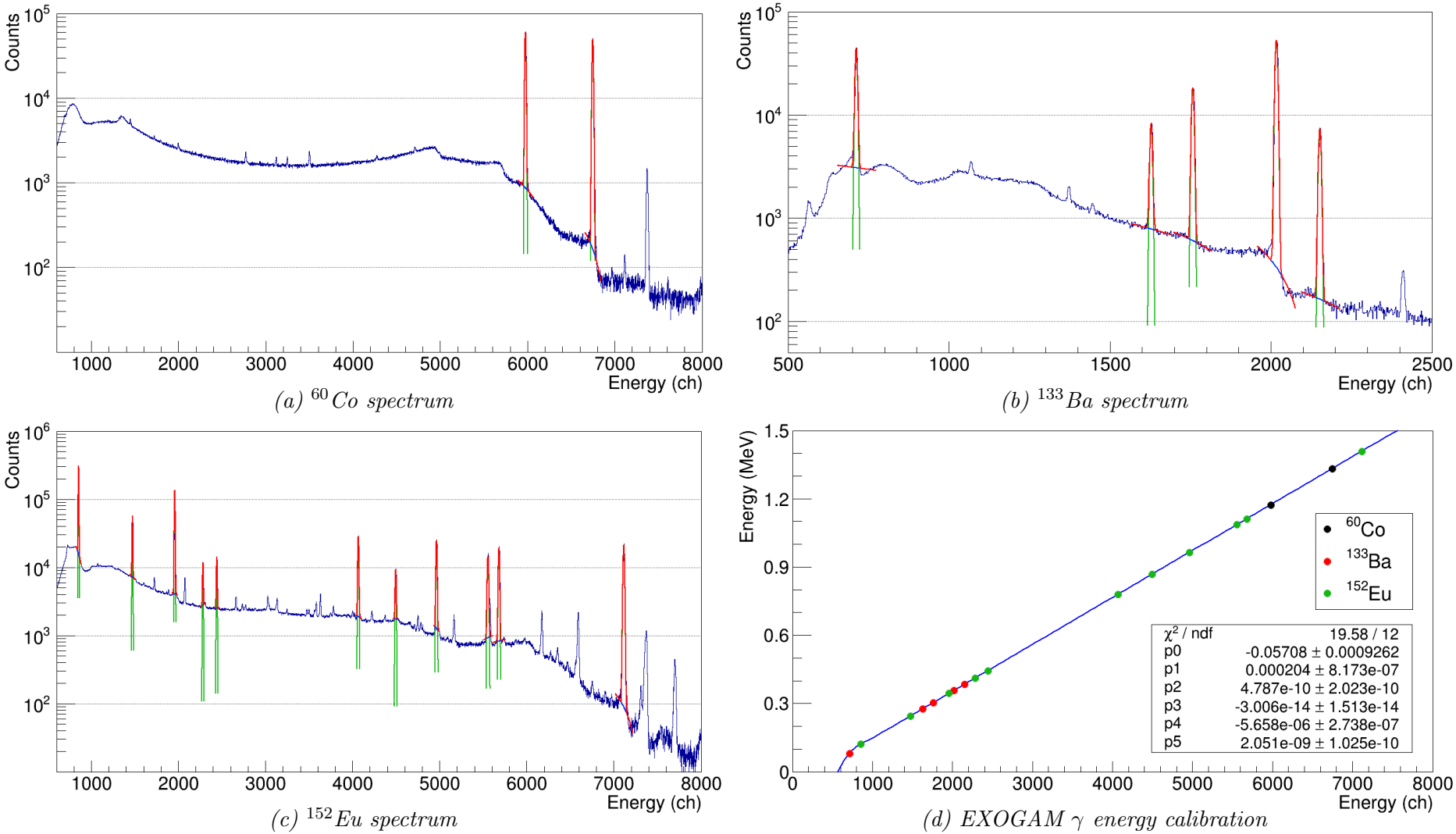

(a) ^{60}Co spectrum

(b) ^{133}Ba spectrum

(c) ^{152}Eu spectrum

(d) EXOGAM γ energy calibration

Figure 4.31: ^{60}Co, ^{133}Ba and ^{152}Eu spectra and gamma calibration.

known as *addback* is applied to determine the energy of the incident γ-ray by adding the charge collected in each fired crystal within a clover detector. This way, the peak efficiency is enhanced and a better peak-to-background ratio is obtained.

4.10 Doppler correction for EXOGAM

The energy deposited by a γ-ray in the germanium crystals must be corrected, as it is affected by the Doppler shift due to the speed of the emitting nucleus with respect to the detector. For a nucleus travelling at a velocity β and emitting a γ-ray of energy E_0, the energy observed in the detector would be:

$$E_{obs} = \frac{E_0}{\gamma(1 - \beta cos\theta)} \tag{4.24}$$

From this equation, we can see that the observed energy depends on the angle θ of γ-ray emission with respect to the path of the emitting nucleus. A lower energy will be measured for a γ-ray hitting the detector at backward angles while the γ-rays forward emitted will deposit a higher energy. This phenomenon is known as Doppler shift.

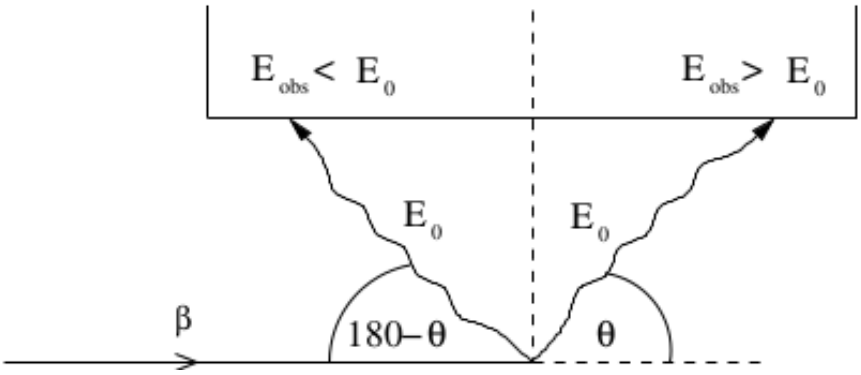

Figure 4.32: Doppler shift phenomenon.

If the angle of emission θ and the speed β were exactly known, the Doppler shift could be corrected perfectly. However, the uncertainty in their determination will affect the Doppler correction and, in consequence, worsen the energy resolution due to the Doppler broadening effect. The Doppler broadening has been estimated by taking into account the contribution of each uncertainty affecting θ (γ-ray hit, fragment hit and reaction point) or β (beam energy spread).

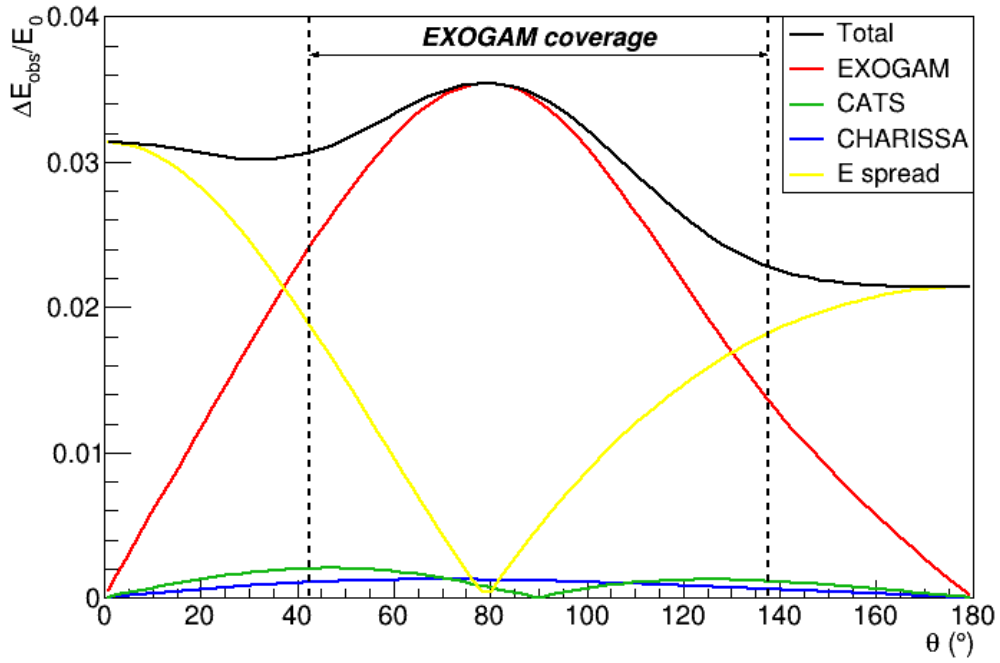

Figure 4.33: Estimation of the Doppler broadening effect. The dominant contribution within the γ-ray detection angular coverage is due to the EXOGAM position resolution.

4.11 EXOGAM Efficiency

Given the nature of the γ-ray interaction with matter, a γ-ray has a high possibility of passing through the detector without leaving any trace at all. This means that the detector will be unable to detect all the incoming γ-rays. Therefore, a crude geometrical calculation cannot account for the intrinsic detection efficiency and hence the total detection efficiency is defined as the ratio of the number of γ-rays actually detected in the full-energy peak and the total number of γ-rays emitted:

$$\epsilon = \frac{N}{A\, BR\, t(1 - DT)} \tag{4.25}$$

where N is the integral of the full-energy peak, A the source activity, BR the intensity of the γ-ray line, t the exposure time and DT the DAQ dead time fraction.

The total detection efficiency of EXOGAM has been measured placing ^{60}Co, ^{133}Ba and ^{152}Eu sources at target position. The photopeaks selected for this purpose were the same as those used for the energy calibration, their energies and intensities can be found in table 4.11.

The activity of each source was provided with an accuracy of $\pm 1\%$ for a given date, so they have been extrapolated to the date when the measurements were done according to the universal law of radioactive decay (table 4.12).

Source	Initial Activity	Date	Calculated Activity	Date
^{60}Co	5638 Bq	23/09/2013	5313 Bq	12/03/2014
^{133}Ba	9789 Bq	17/07/2013	9374 Bq	13/03/2014
^{152}Eu	17798 Bq	03/06/2011	15846 Bq	14/03/2014

Table 4.12: Activities

In order to extract the numbers of counts under the photopeak, the background has to be removed. Therefore, a background run was removed from the spectrum.

Next step is fitting each photopeak to extract the integral, but unfortunately all the fitting procedures employed here were unsuccessful as the shape of the photopeaks are not well described by any function tried (Gaussian, asymmetric-Gaussian, Lorentzian, Landau, etc. with linear or parabolic backgrounds).

Another approach was needed and an algorithm[7] was utilized to subtract the background [68], then the number of counts under the photopeak can be obtained as the difference between the integral of the source spectrum and the same integral in the background spectrum.

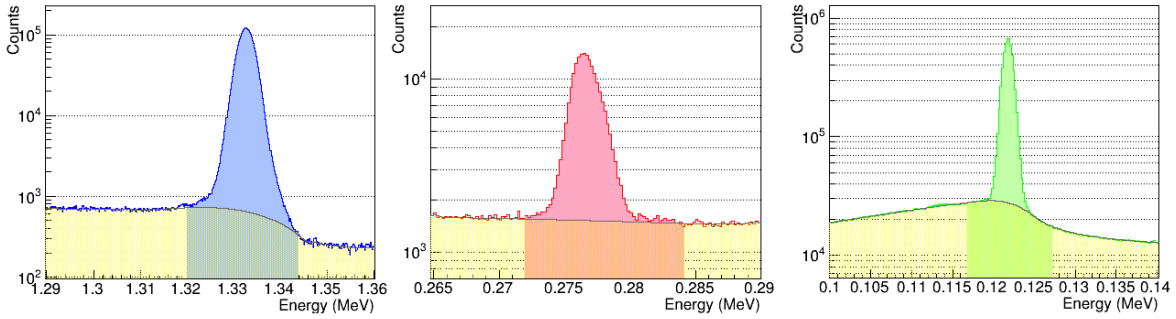

(a) ^{60}Co peak at 1.332 MeV (b) ^{133}Ba peak at 0.276 MeV (c) ^{152}Eu peak at 0.122 MeV

Figure 4.34: Photopeak integration. Source spectra in blue/red/green and background in yellow, the coloured area represents the range of intregration.

The number of counts N under each peak is now known and the efficiency can be obtained by applying equation 4.25. Figure 4.35 shows the results, where the efficiency curve is fitted with the following function [50]:

$$\epsilon_i = e^{a+b\ln\frac{E}{E_0}+c\left(\ln\frac{E}{E_0}\right)^2} \tag{4.26}$$

The photopeak efficiency points corresponding to the ^{152}Eu γ-ray lines are well described by the efficiency curve. According to this curve, the expected efficiency at

[7]This algorithm estimates the background spectrum, which was verified to reproduce the underlying component of the histogram.

217 keV and 335 keV is 16.47 (25) % and 13.65 (20) %, respectively. The uncertainty is dominated by the source activity.

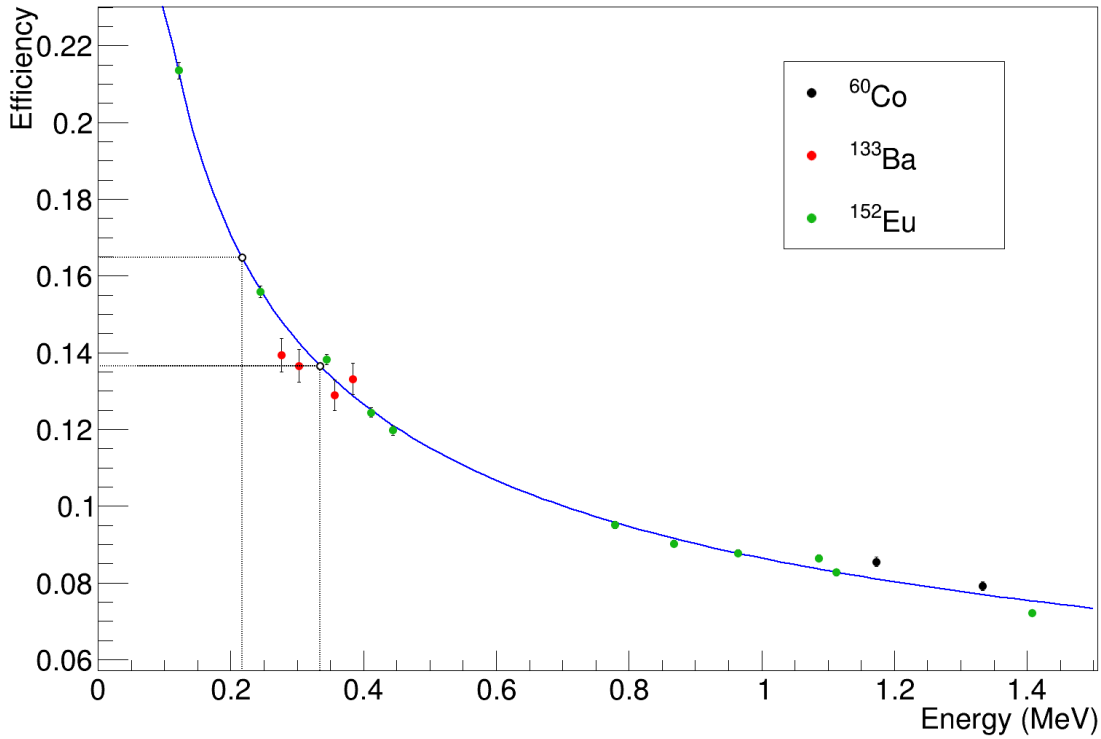

Figure 4.35: Photopeak detection efficiency (dots with statistical error bars) and EXOGAM efficiency curve.

4.12 Time of flight calibration

Each TAC module was calibrated over a range 640 ns or 1.28 µs wide depending on the TAC dynamic range, by using a time pulser in order to send periodically a stop signal every 40 or 80 ns, respectively (figure 4.36a).

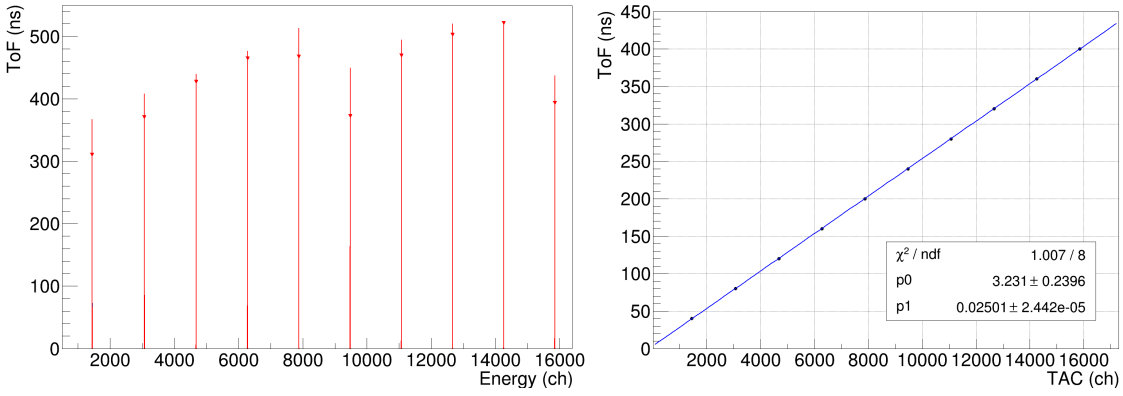

(a) Time-pulser run *(b) Time of flight calibration*

Figure 4.36: Time of flight calibration.

The peaks are fitted with Gaussians to determine their positions and these positions are plotted against the time past since the start signal was sent. Finally, the calibration parameters are calculated by doing a linear fit (figure 4.36b), and then applied in the following way:

$$ToF = a + b * ToF^{raw} \tag{4.27}$$

where ToF is the calibrated time of flight, ToF^{raw} is the raw time of flight value, a and b are the offset and the slope of the linear fit, respectively.

Note that after this calibration, the times of flight are expressed in nanoseconds but the measurements are not absolute since they are affected by a delay due to the cabling and the electronic processing.

4.13 Event selection

The very first condition applied in the data analysis consists in requiring a coincidence between front and back signals of the same silicon detector, with energy values compatible with each other.

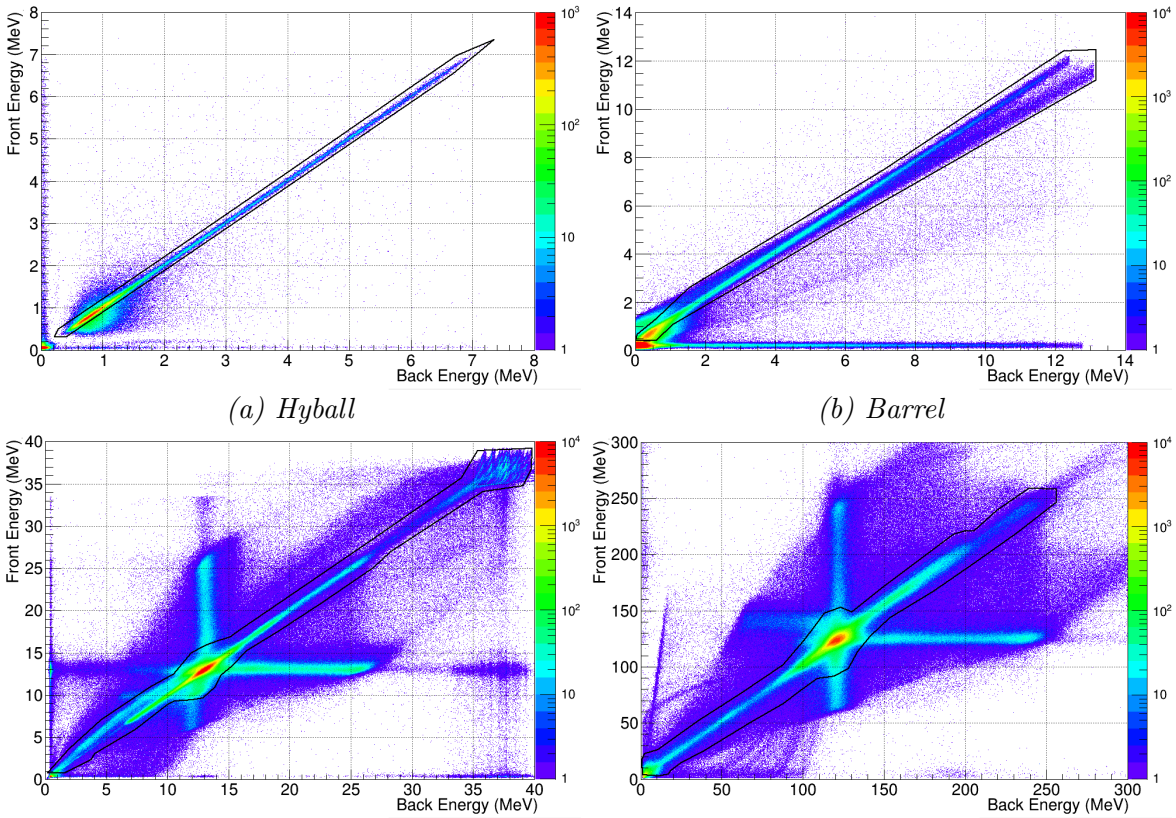

(a) Hyball *(b) Barrel*

(c) CHARISSA ΔE *(d) CHARISSA E*

Figure 4.37: Front versus back energies in the silicon detectors with the gates used to select events.

Figure 4.37 shows the front versus back plots with the gates around the pattern of the events having a similar energy in both sides. These gates are used to select the events that are accepted for further analysis.

This condition is intended to clean up the data by removing any possible noisy signal triggering a silicon detector.

4.14 Particle identification

This section outlines the different selection criteria that were applied to identify the beam particle, the beam-like and the target-like particles are presented. These conditions are intended to clean up the spectra and gate on a specific reaction channel.

4.14.1 Beam particle identification

The HF-CATS time of flight, measured between the cyclotron radiofrequency and the first CATS detector, is a very useful parameter since it is the only measurement governed by the flight path before the reaction target, and therefore provides an excellent tool to select the beam particles and to remove any possible beam contamination from the analysis.

Figure 4.38 shows that most of the events have the same time of flight, indicating that the purity of the ^{16}C beam is close to 100%.

4.14.2 Hit on target condition

In addition to allowing for measurements of the position and incident angle of incoming ions, the beam position reconstruction on the target plane discussed in section 4.3.3.3 serves the purpose of developing a condition for selecting the events that reached the target.

Knowing that the radius of the target is 1 cm, this condition is applied by defining a circle of radius of 0.9 cm around the position of the center of the target measured by the surveyor, as shown in figure 4.39. The events falling outside this circumference are rejected while the events within it are accepted.

A radius 1 mm smaller than the actual target radius was chosen taking into account the resolution of the position reconstruction on target so as to reject reactions of the beam particles with the target frame or the target holder.

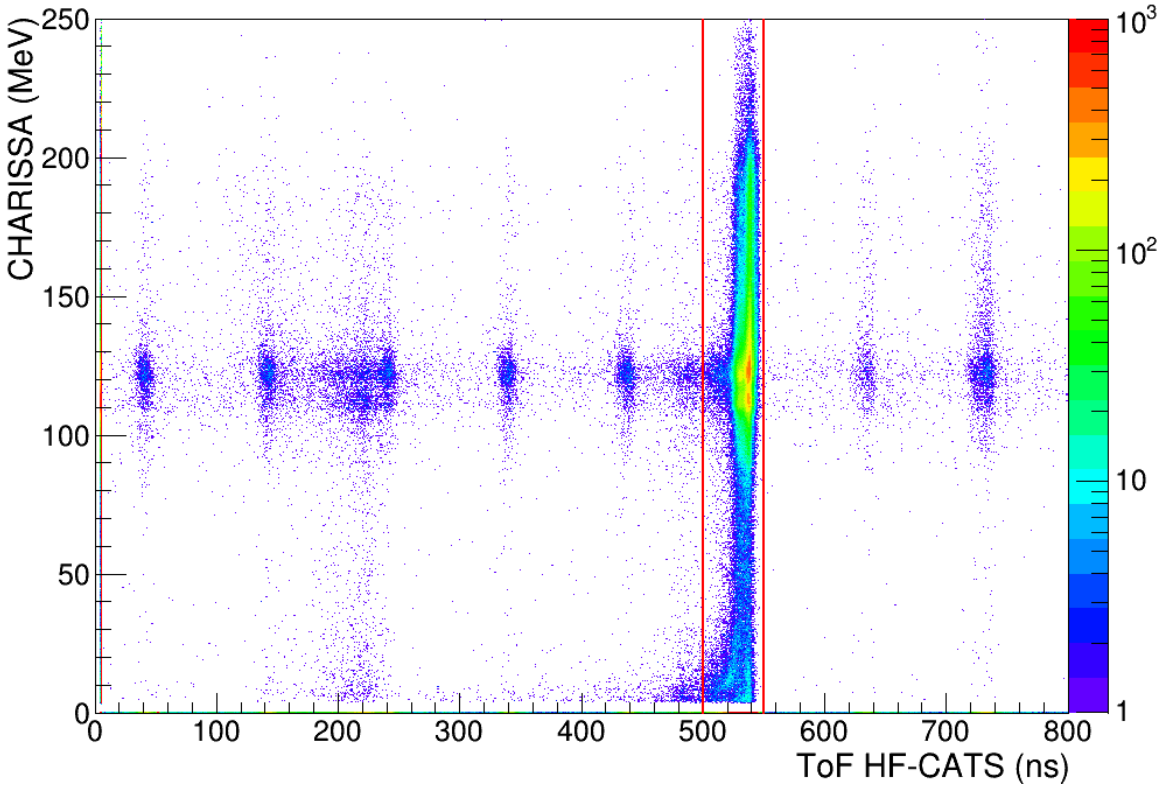

Figure 4.38: Energy loss in the second silicon of CHARISSA versus the ToF HF-CATS1. Two red lines limit the time of flight interval of accepted events for further analysis.

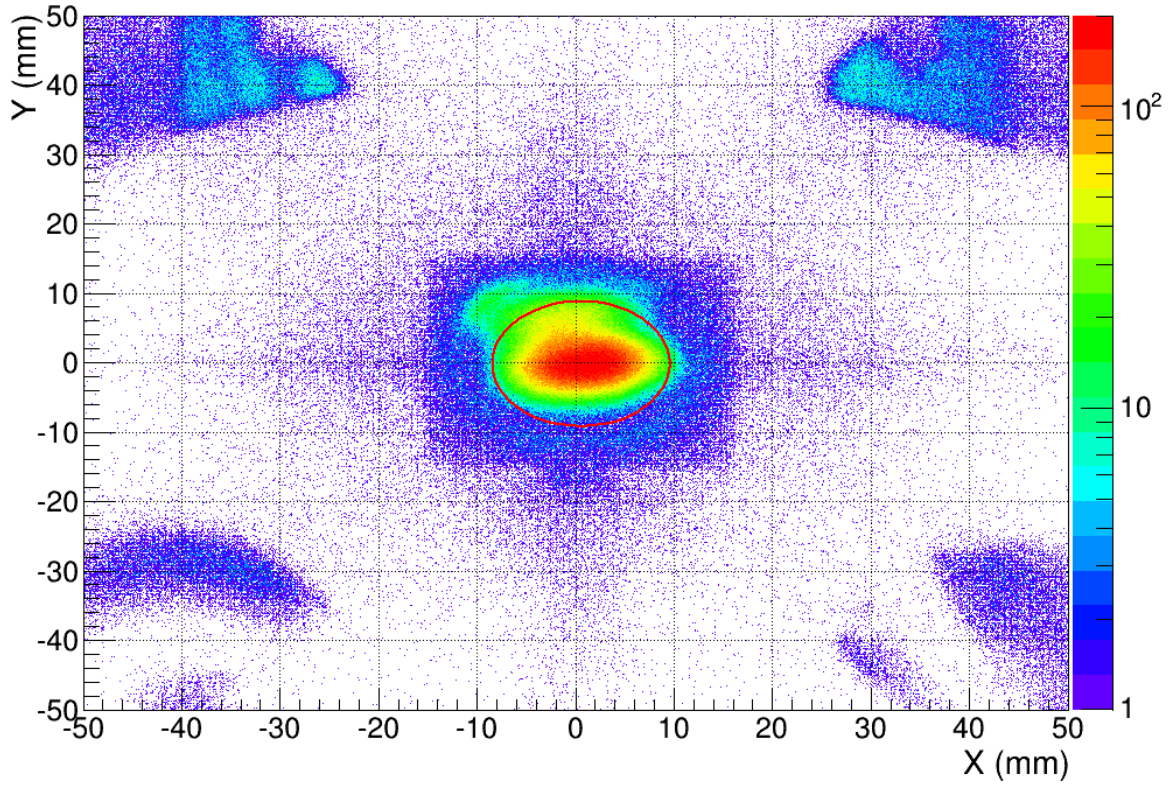

Figure 4.39: Beam reconstruction on the target plane with the contour on the target superimposed. We can see that the beam focusing was excellent and the majority of the events meet this condition.

4.14.3 Fragment identification

4.14.3.1 Z=6 fragments selection

The identification of the ^{17}C and the ^{16}C isotopes among the beam-like particles detected in CHARISSA is delicate, especially due to the lack of a useful energy signal from the CsI crystal that prevents us from achieving isotopic separation. Besides, 35 % of the recorded events in the CsI are affected by pile-up.

Unfortunately, the ΔE-E scatter plot presented in figure 4.40 provides just charge identification. Therefore, only a selection of Z=6 fragments was possible from the ΔE-E plot.

4.14.3.2 CHARISSA-CATS1 time of flight

The time of flight between the CATS1 and CHARISSA could be used to improve the fragment identification, as we know that a difference in the mass of the fragment is associated with a variation in the time of flight for particles with the same kinetic energy.

The time of flight considered here is measured over a flight path that has a first part before and a second part after the reaction target. Since the beam-particles are always ^{16}C isotopes and the beam path has a maximum deviation of only 2^o with respect to the theoretical beam axis, the time of flight selectivity is due to the differences in the mass of the reaction products and their flight path from the target to CHARISSA. However, figure 4.41 shows that the flight path after the reaction target is too small for these differences in the time of flight to be larger than the time resolution achieved with our experimental setup.

4.14.4 Light ejectile identification

4.14.4.1 Time of flight selection

The time of flight measured between CATS and the silicon detectors of TIARA gave us valuable information on the flight path of the target-like particles. These times of flight are measured over a flight path from a point before to a point after the reaction target and, similarly to what happens with the times of flight between CATS and CHARISSA, the differences arise from the times of flight measured from the reaction target and the silicon detector.

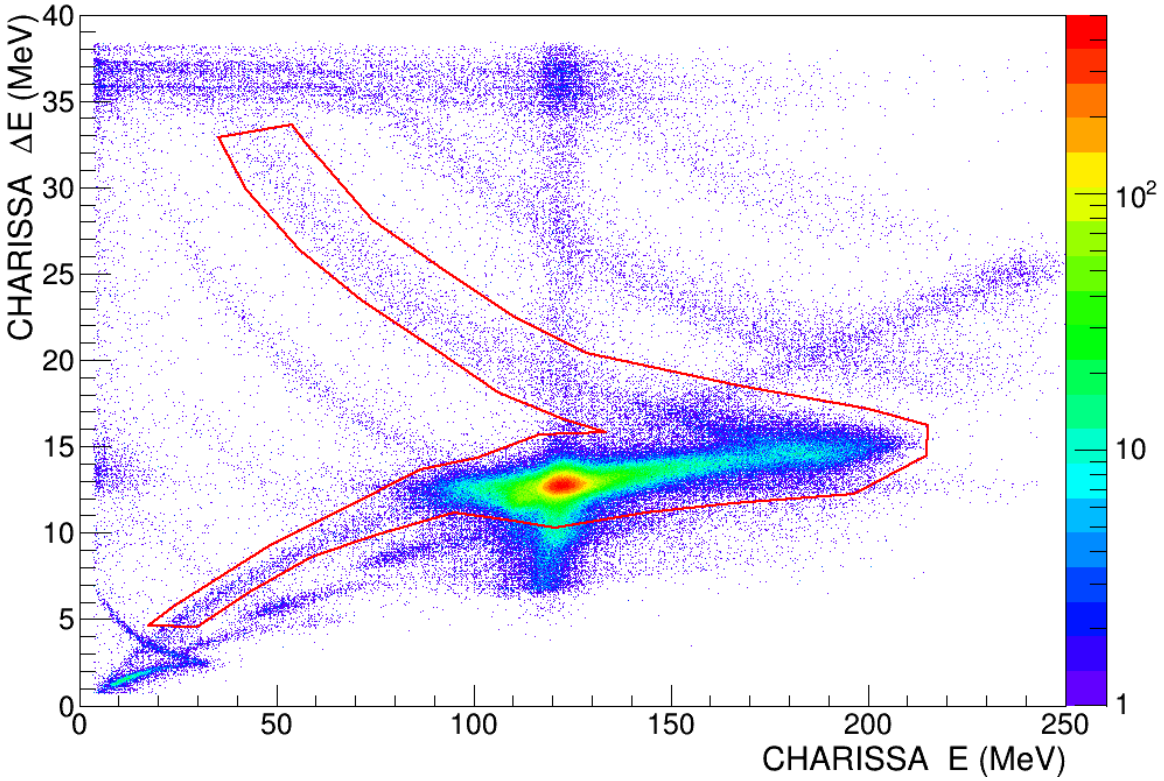

Figure 4.40: ΔE-E scatter plot, where it is clear that the resolution does not allow isotopic identification. The Z=6 graphical cut used is presented in red.

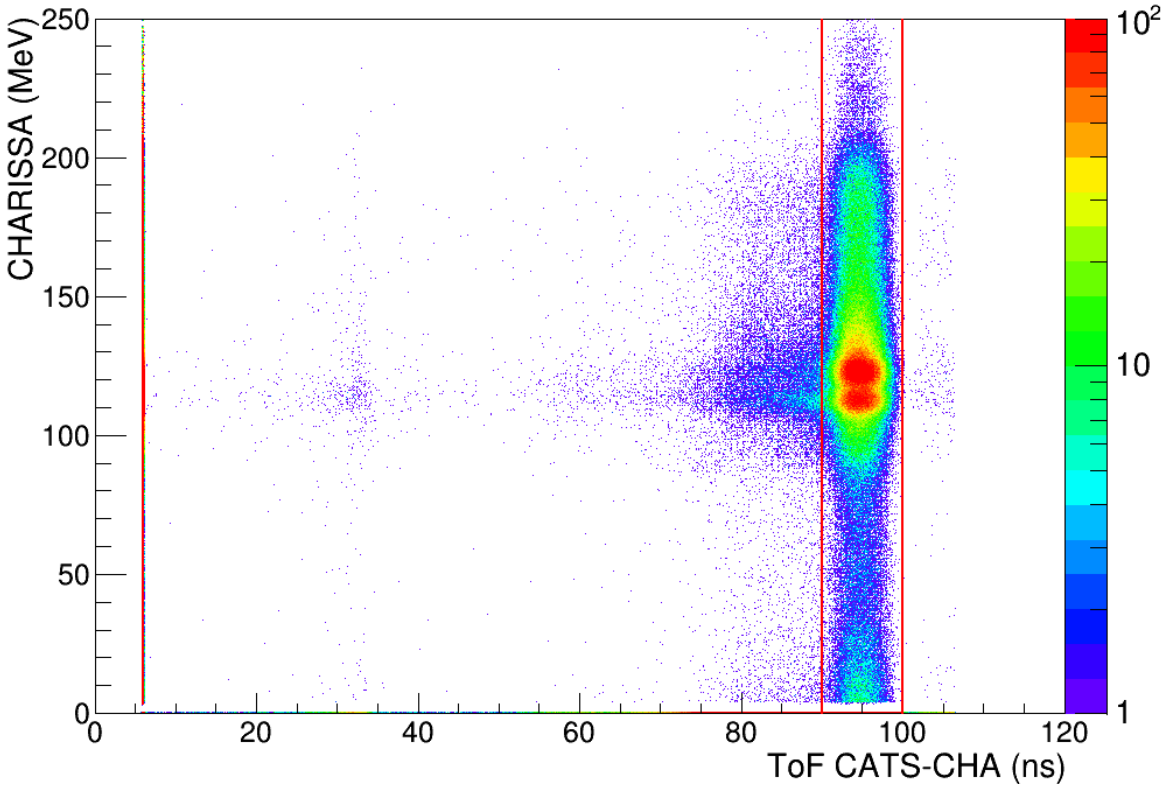

Figure 4.41: Energy loss in the second silicon of CHARISSA versus ToF CHA-CATS1.

The relationship between the time of flight Δt, the energy E and the flight path distance L of particle of mass m is given by:

$$E = \frac{1}{2}mv^2 = \frac{1}{2}m\left(\frac{L}{\Delta t}\right)^2 \quad \Longrightarrow \quad \Delta t = \sqrt{\frac{mL^2}{2E}} \tag{4.28}$$

Although the times of flight between CATS1 and TIARA silicon detectors do not provide information on the mass difference, the correlation between the time of flight Δt and the energy E and the flight path distance L is used in our advantage.

4.14.4.1.1 Hyball-CATS1 time of flight

The time of flight Δt dependence on the flight path distance L indicated by equation 4.28 is lost due to the alignment of times of flight corresponding to different rings in the Hyball.

The time of flight Δt dependence on the energy E remains and is used to select the (d,p) events in the energy versus time of flight plot with a graphical cut on the correlated events in the energy range of interest (up to 3.3 MeV) as shown in figure 4.42.

4.14.4.1.2 Barrel-CATS1 time of flight

The time of flight between CATS1 and the inner barrel, however, still presents the correlations with the energy E and the scattering angle θ[8] expressed by equation 4.28, and both are used to clean up the kinematical spectrum.

Figure 4.43 shows the time of flight Δt between CATS1 and the inner barrel plotted against the scattering angle θ[9] and the correlated events are selected with a graphical cut. Events falling within this gate are then plotted in a time of flight Δt versus energy E plot, where the uncorrelated events at low energies are rejected with another graphical cut (figure 4.44).

[8]There is a direct relationship between the flight path distance L and the scattering angle θ. Assuming that the reaction takes place at the (0,0,0) point, this relationship can be assessed as:

$$L = hcos\theta \tag{4.29}$$

where h stands for the radius of the Barrel. However, we took into account the beam interaction point on target and therefore previous expression is no longer accurate.

[9]The background in the time of flight Δt versus the scattering angle θ spectrum is due to the nature of the read out of the Barrel signals: each pair of detectors shares a common ADC gate and therefore 16 signals are read when one is fired.

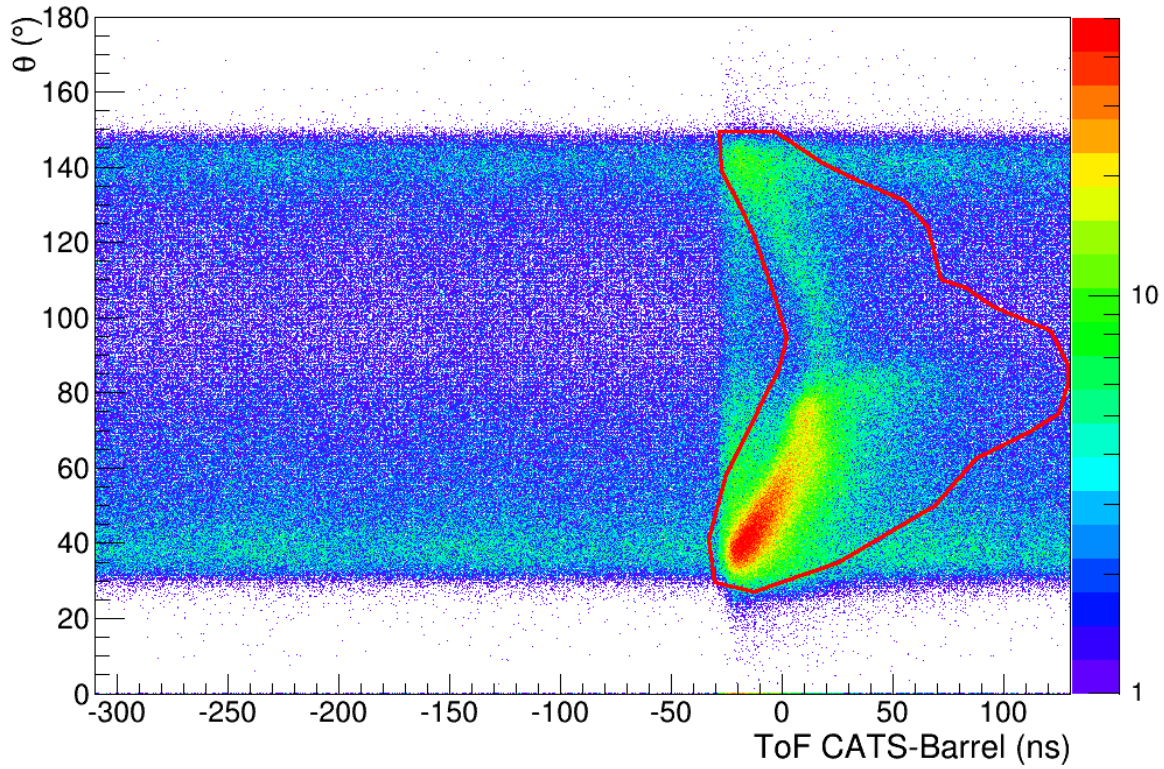

Figure 4.43: Scattering angle θ versus the ToF IB-CATS1. The background all over the spectrum is due to the common ADC gates utilized in the Barrel. A graphical cut is employed to select the events showing a correlation between the time of flight and the scattering angle.

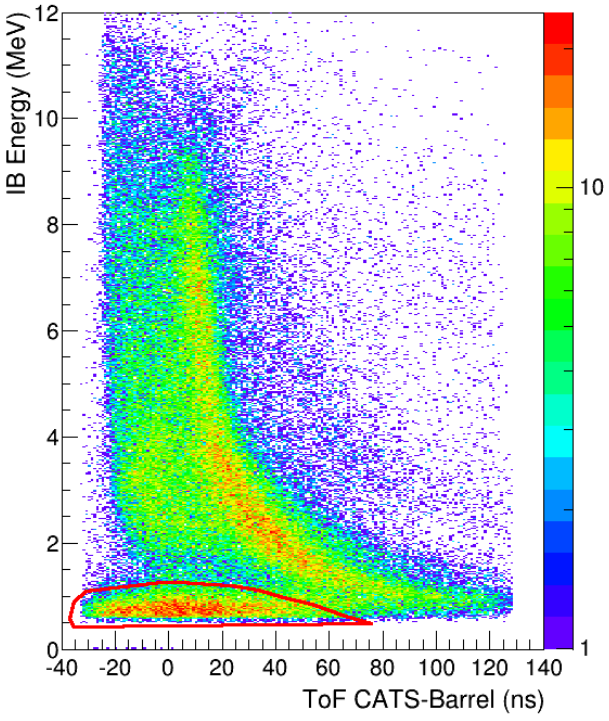

Figure 4.44: IB energy versus ToF IB-CATS1. A graphical cut is used to reject the non correlated events at low energies.

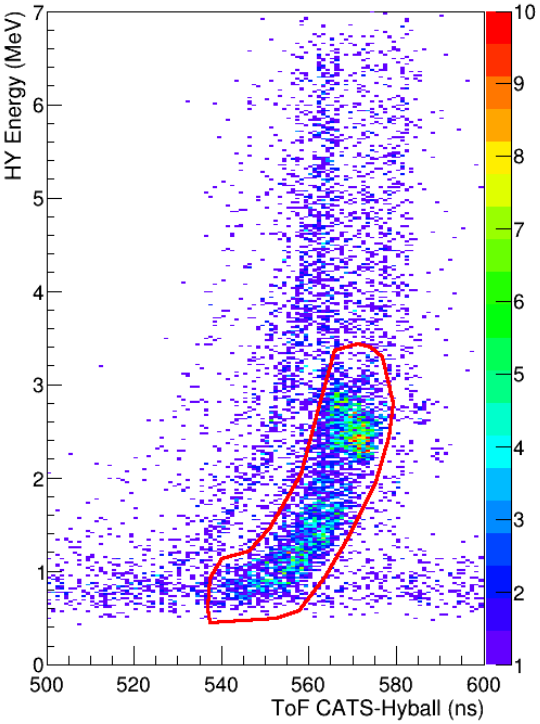

Figure 4.42: Hyball energy versus ToF HY-CATS1. The events within the graphical cut are accepted for further analysis.

4.14.4.2 Energy loss identification

Inner and Outer Barrel signals are used to produce a Barrel ΔE versus E spectrum where several regions of physical interest are defined, as indicated in figure 4.45. One of these regions corresponds to the particles stopped in the Inner Barrel, which are those events that meet the condition of absence of hit in the Outer Barrel that is going to be useful to extract the angular distributions (see sections 5.2 and 5.3).

In addition to this, the Barrel ΔE versus E spectrum presents the characteristic energy-loss pattern that allows to perform a particle identification in order to identify the punchthrough events as protons or deuterons.

Protons and deuterons that punched through the Inner Barrel are easily resolvable if they lose more than 4 MeV in the Inner Barrel and therefore they are stopped in the Outer Barrel. However, if they passed through both Inner and Outer Barrel, and hence the energy deposited in the Inner Barrel is lower than 4 MeV, proton and deuteron energy-loss patterns merge together and, therefore, it is not possible to distinguish between them.

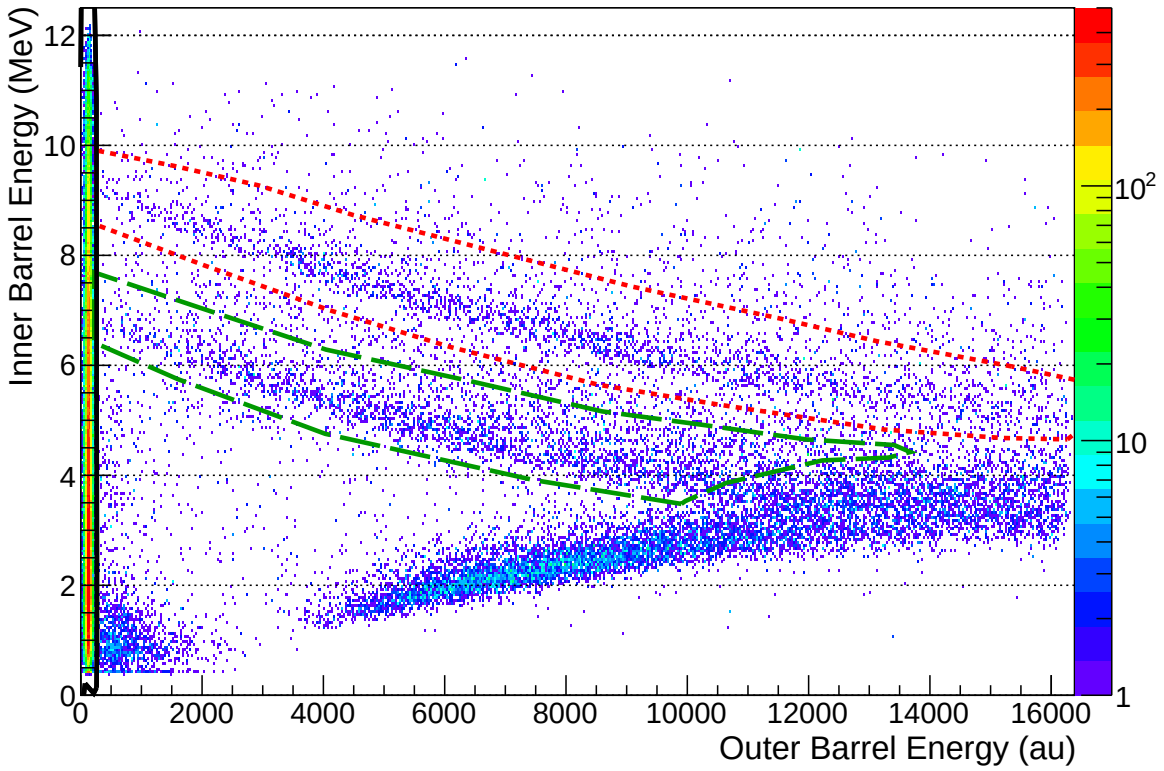

Figure 4.45: Barrel ΔE versus E spectrum, where several regions of interest are highlighted: patterns of protons and deuterons punching through the Inner Barrel and stopping in the Outer Barrel are shown within a dashed green and a dotted red line respectively. The events falling outside these two gates cannot be identified as protons or deuterons with this method, including those events stopped in the Inner Barrel (black).

Figure 4.45 displays several gates that were useful in this analysis. The black cut contains the particles stopped in the Inner Barrel and hence, those events that meet the condition of no hit in the Outer Barrel. The dashed green and the dotted red gates take the protons and deuterons, respectively, that punched through the Inner Barrel and were stopped in the Outer Barrel. These two gates were used for the energy corrections mentioned in section 4.7.

4.14.5 Event selection summary

Finally, figure 4.46 presents the energy versus the laboratory scattering angle measured in TIARA, after applying the previous gates. The kinematical patterns associated to the elastic scattering and ^{16}C(d,p)^{17}C transfer reactions are clearly visible.

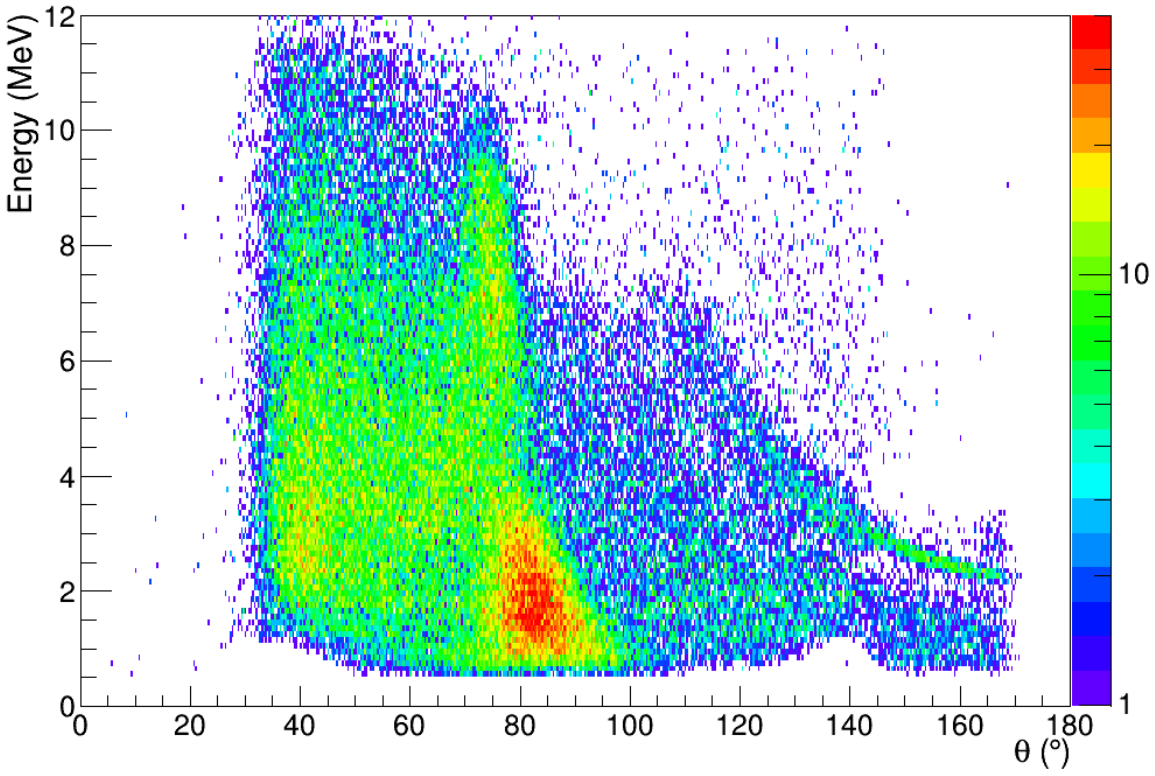

Figure 4.46: Energy versus laboratory scattering angle measured in TIARA.

In particular, the effect of each one of the event selection criteria previously discussed is displayed in figure 4.47, where these conditions were applied one after the other in order to show the evolution of the energy versus scattering angle plot.

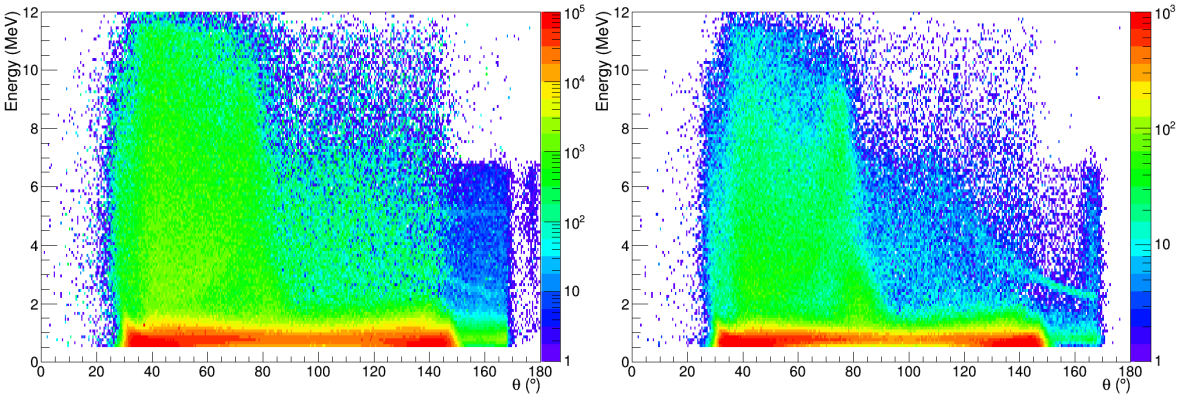

(a) No condition

(b) ToF HF-CATS1

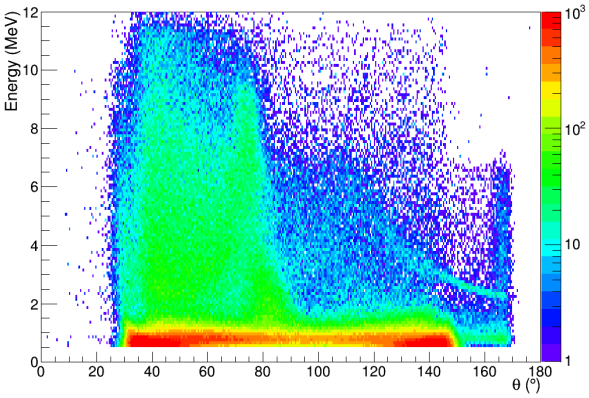

(c) Hit on target

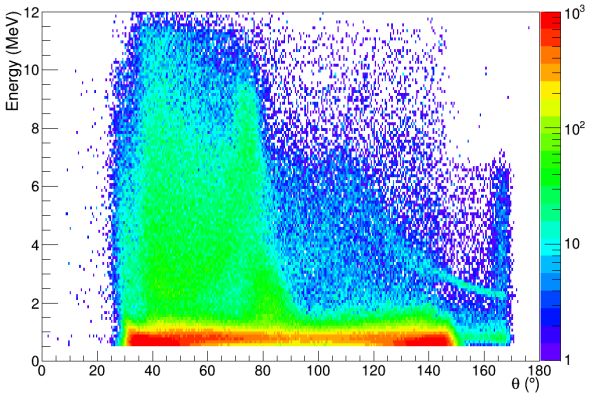

(d) ToF CATS1-CHA

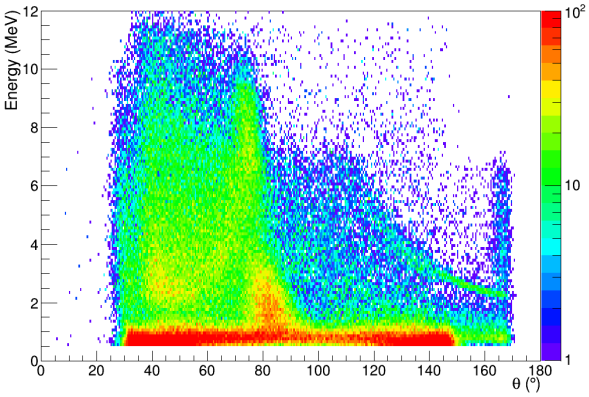

(e) Z = 6

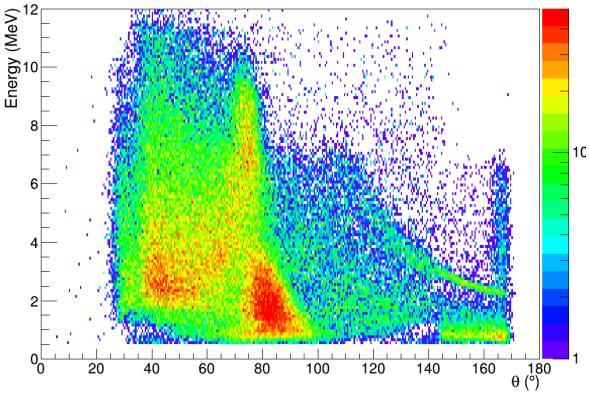

(f) ToF CATS1-IB

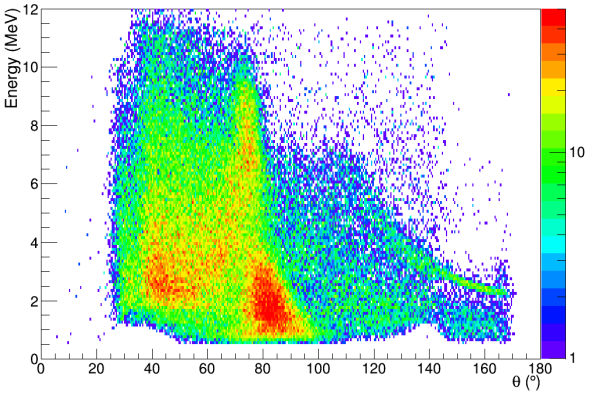

(g) ToF CATS1-HY

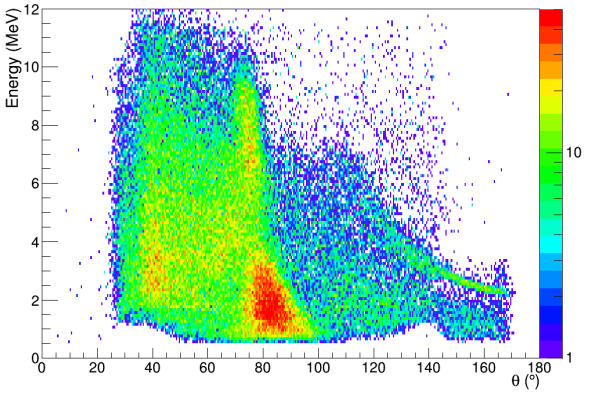

(h) No hit in the OB

Figure 4.47: Energy versus scattering angle plots with the previously discussed conditions applied successively.

4.15 Momentum conservation condition

Figure 4.47 shows the measured kinematics in TIARA, where we can distinguish clearly the typical pattern of the elastic scattering between 70º and 90º and the kinematical line of (d,p) events populating bound states in ^{17}C at backward angles. In addition to this, other reaction channels are expected such as deuteron breakup and ^{16}C(d,p) transfer reactions to resonant states in ^{17}C, which promptly decay into ^{16}C plus a neutron.

The main difference between the latter two reaction channels with respect to the former two is their three-body character. This feature can be exploited to separate the three body yield from the two-body reaction events by analysing the momentum of particles detected in TIARA and CHARISSA:

$$\Delta\vec{p} = \vec{p}_{^{16}C} - \vec{p}_{TIARA} - \vec{p}_{CHA} \tag{4.30}$$

where $\vec{p}_{^{16}C}$ is the momentum of the beam particle, $\vec{p}_{TIARA}$ is the momentum of the light particle detected in TIARA and $\vec{p}_{CHA}$ is the momentum of the heavy fragment detected in CHARISSA.

Then, considering the longitudinal momenta, previous equation becomes:

$$\Delta p = \sqrt{2m_{^{16}C}T_{^{16}C}} - p_{TIARA}cos\theta_{TIARA} - p_{CHA}cos\theta_{CHA} \tag{4.31}$$

where $T_{^{16}C}$ is the beam energy, θ_{TIARA} is the scattering angle of the light particle and θ_{CHA} is the scattering angle of the heavy fragment.

In two-body reactions, the momentum of the particles detected in TIARA and CHARISSA will meet the momentum conservation condition and therefore, such events are expected to appear around zero in the Δp spectrum. Instead, the most probable three-body channels, deuteron breakup and transfer to ^{17}C unbound states, have in common the emission of a neutron in addition to the proton. This neutron can not be detected by our setup and will carry away a significant amount of momentum that will be missing in the Δp spectrum.

Figure 4.48a shows four regions of interest that are defined for the following interpretation of the Δp spectrum shown in figure 4.48b: the first one is highlighted in blue and corresponds to the transfer leading to ^{17}C bound states. The second one limited by a red graphical cut, spans over the region where one-neutron transfer reactions populating bound and unbound states in ^{17}C are expected to appear according to the reaction kinematics. The region limited by a green line contains the elastic scattering events and finally the pink line defines the region where the breakup is expected.

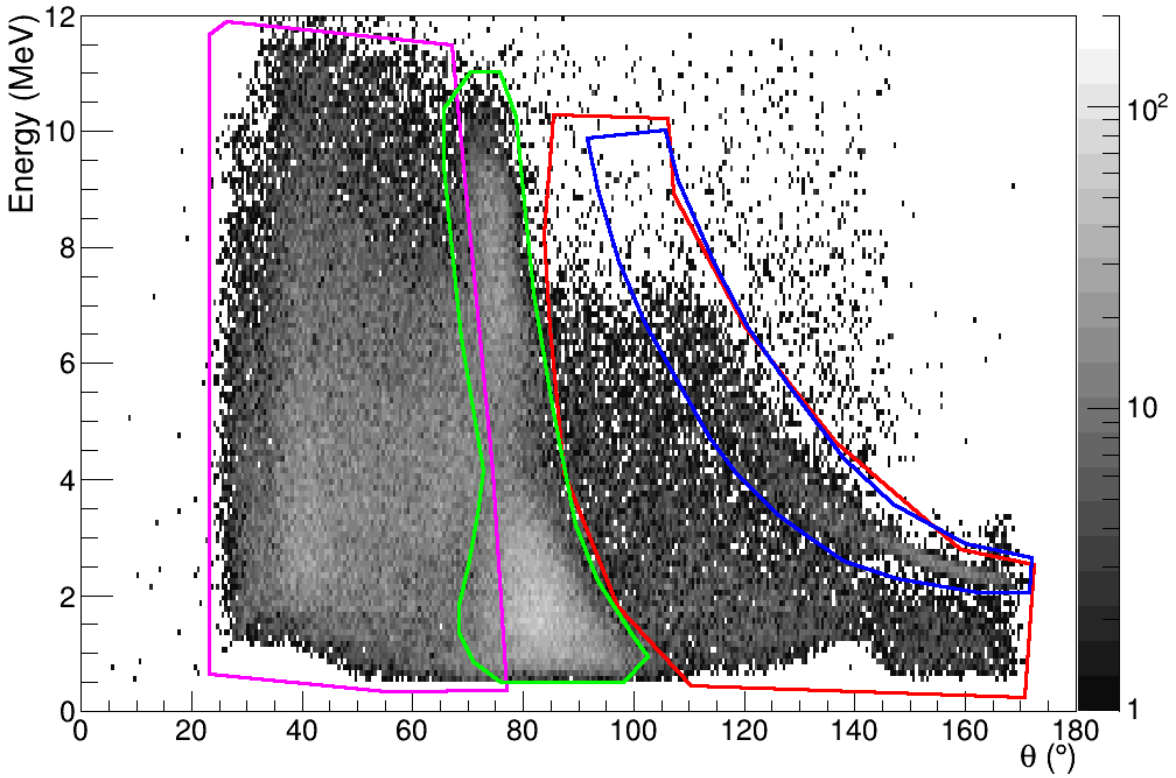

(a) Energy versus laboratory scattering angle measured in TIARA

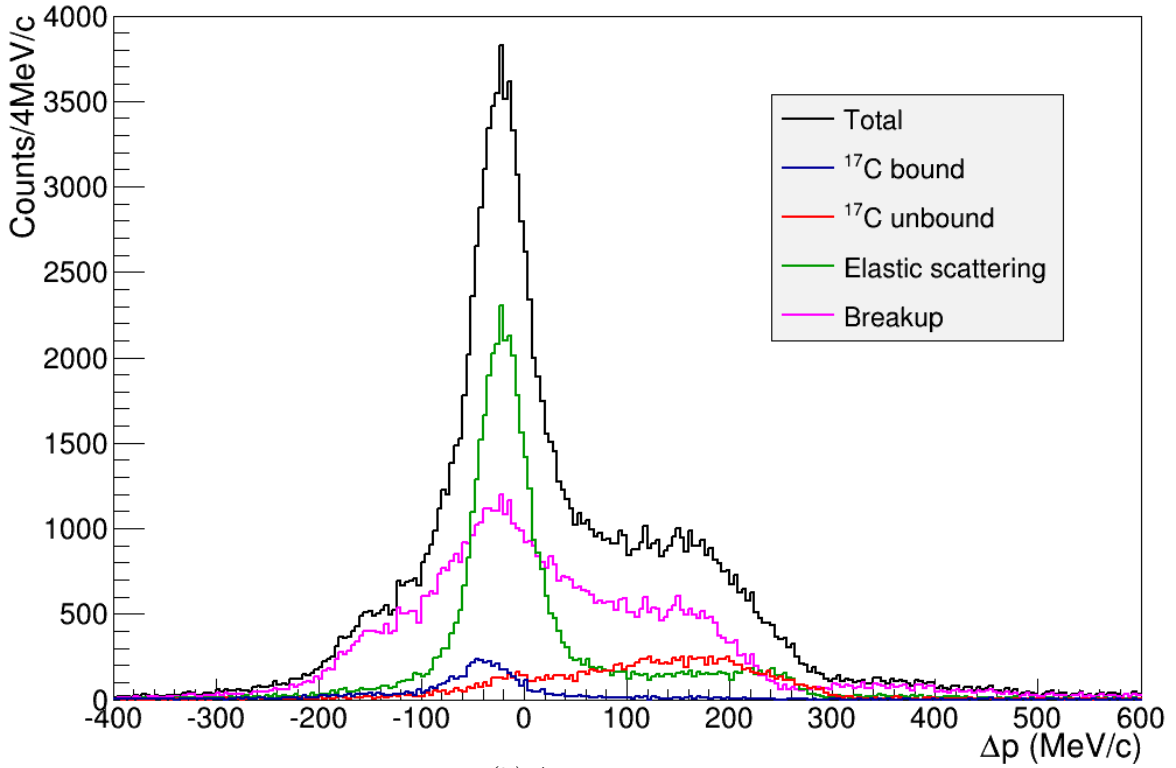

(b) Δp spectrum

Figure 4.48: Four regions are highlighted in red, blue, green and pink in the energy versus laboratory scattering angle plot (a) corresponding to ^{17}C bound and unbound states, elastic scattering and breakup events respectively. These reaction channels were identified in the Δp spectrum (b) gating on these regions.

These graphical cuts allow us to gate on the ^{17}C bound states, ^{17}C unbound states[10], elastic and breakup[10] regions in order to identify where these events appear in the Δp spectrum and support the interpretation.

The gated Δp spectra shown in figure 4.48b indicate that the larger peak close to zero is due to the elastic scattering and ^{16}C(d,p) transfer reactions to bound states in ^{17}C also appear within this region. As expected, the two-body reaction events accumulate in the vicinity of zero in the Δp spectrum, while transfer to resonant states in ^{17}C and breakup events show a broader distribution typical from their three-body character.

Therefore, it is possible to reject a significant amount of the three body yield by gating on the two-body reaction range in the Δp spectrum, as is shown in figure 4.49 for a selection of events in the Δp range $[-100, 50]$ MeV/c.

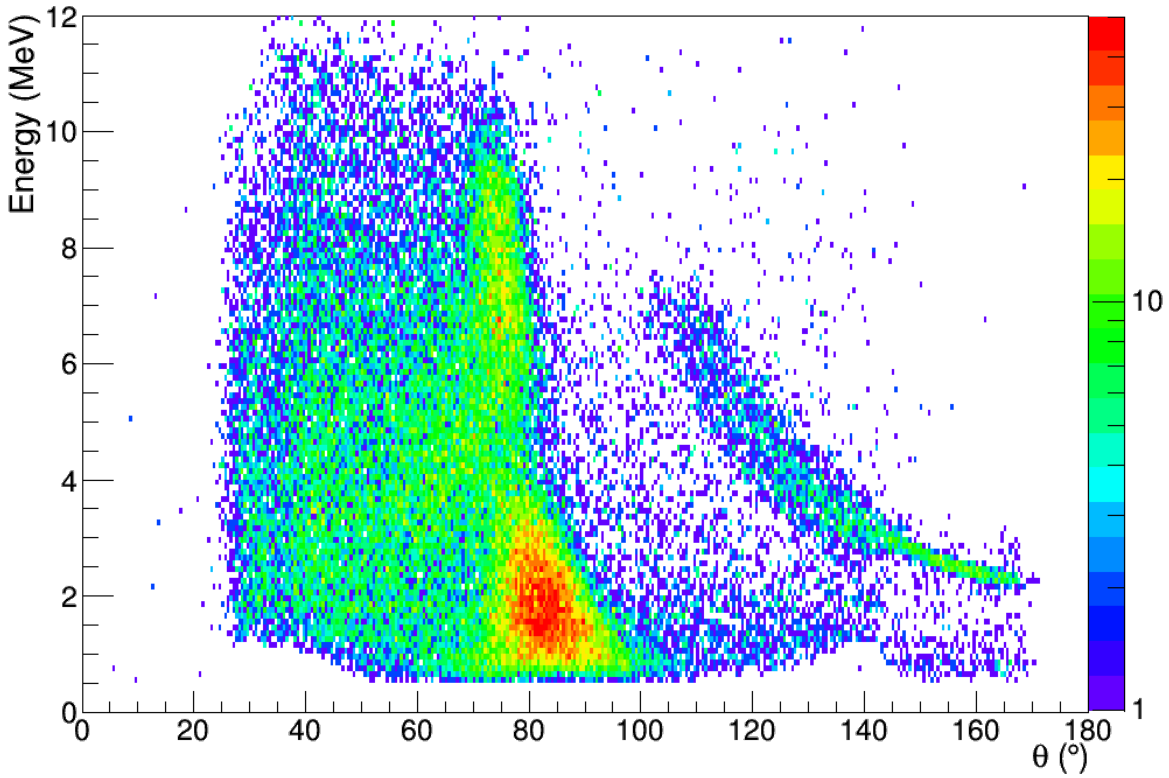

Figure 4.49: Energy versus scattering angle plots with the selection criteria discussed in section 4.14 plus a gate on the $[-100, 50]$ *MeV/c region of the* Δp *spectrum.*

It is worth mentioning that the Δp spectrum is systematically shifted to negative values due to the fact that energy losses in the target and the dead layer were not taken into account for this calculation, and neither was any possible γ-ray emitted in coincidence.

[10]Note that vetoes where used to cope with the gates overlap: ^{17}C bound and elastic events were vetoed when gating on ^{17}C unbound states and breakup events, respectively.

Chapter 5

Results

In this chapter, the experimental cross sections for the ^{16}C(d,p) one-neutron transfer reaction and the ^{16}C elastic scattering on two different targets are presented. The chapter begins with a description of the ^{16}C(p,p)^{16}C and ^{16}C(d,d)^{16}C cross section measurements and then a detailed analysis for each of the bound states populated in ^{17}C by (d,p) is discussed individually.

5.1 Cross sections

The differential cross section for N_{beam} incoming beam particles hitting a target with N_{target} particles per cm^{-2} is given by

$$\frac{d\sigma}{d\Omega} = \frac{N}{\Delta\Omega\, N_{beam}\, N_{target}\varepsilon_\gamma} \tag{5.1}$$

where N is the measured yield in each angular bin, $\Delta\Omega$ is the solid angle subtended by each angular bin and ε_γ is the photopeak efficiency, that will be considered only when dealing with γ-gated events.

For this experiment, the number of particles in the target N_{target} was derived from the target thickness measurements (section 4.1) while the beam tracker detectors provide the number of beam particles, N_{beam}. The solid angle $\Delta\Omega$ at a given angle is provided by the Geant4 simulation detailed in appendix B.2, in which the efficiency of TIARA was taken into account.

Assuming an isotropic γ-ray distribution, the photopeak efficiency of EXOGAM, ε_γ, is 16.71 % and 14.11 % for 217 keV and 335 keV γ-rays respectively, according to the efficiency curve in figure 4.35.

Finally, it is worth noting that the effect of the acquisition dead time cancels out because it affects both N and N_{beam}.

5.2 Analysis of the $^{16}C(p,p)^{16}C$ elastic scattering

The elastic scattering of ^{16}C on the CH_2 target was analysed and the corresponding proton angular distribution was measured by taking slices in energy in figure 5.1, measuring their integral N and projecting the slice onto the scattering angle axis to obtain the associated angular bin. The solid angle $\Delta\Omega$ subtended by each one of these angular bins was calculated using a Geant4 simulation (section B.2), in which the efficiency ϵ of the detectors involved has been taken into account. The scattering angle corresponding to the mean energy value was given by the kinematical line corrected for energy losses in the target and dead layer.

The data were sampled from 1 MeV to 8 MeV (punchthrough of protons in the Inner Barrel) and the energy slices were 400 keV wide, broad enough to accumulate sufficient statistics to reduce fluctuations while sampling the angular distribution with as many points as possible.

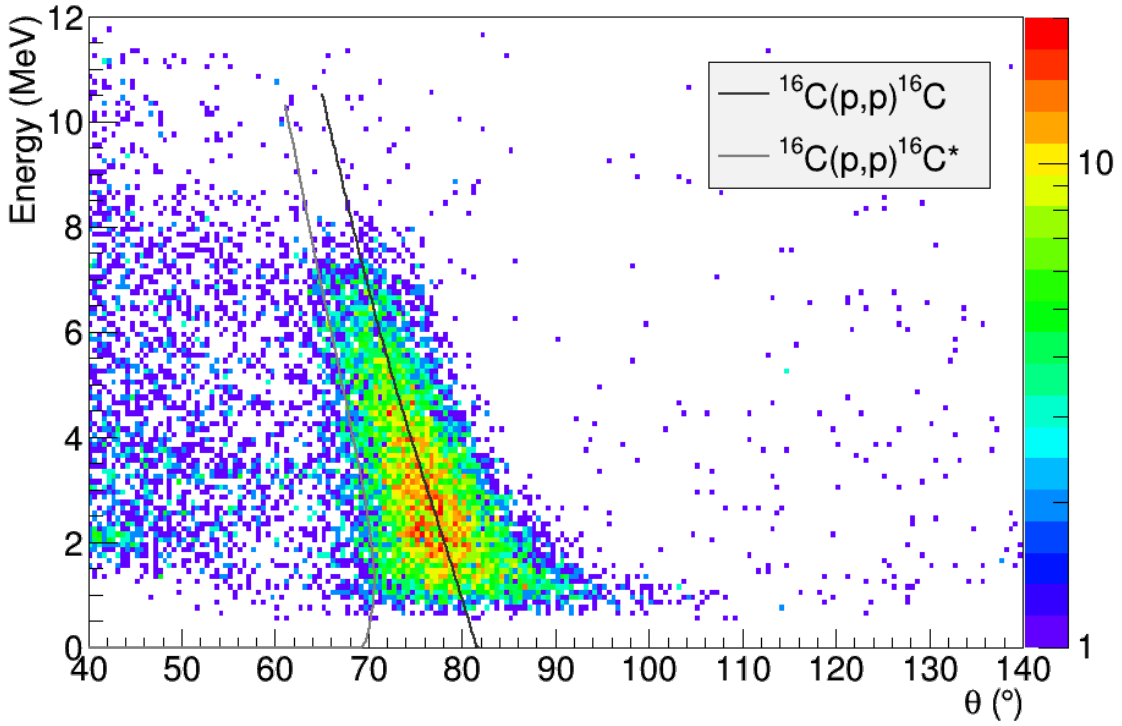

Figure 5.1: Energy versus laboratory scattering angle for non-punchthrough events measured in TIARA with the CH_2 target. The black line represents the calculated kinematics corrected for energy losses for the $^{16}C(p,p)^{16}C$ elastic scattering, while the gray line depicts the $^{16}C(p,p)^{16}C^*$ inelastic scattering calculation.

In order to guarantee that punchthrough events do not affect the shape of the angular distribution, we used a condition of no hit in the Outer Barrel (see section 4.14.4.2). Despite the punchthrough removal efficiency not being 100% due to geometrical reasons (particle hitting an active area of the Inner Barrel but an interstrip in the Outer Barrel), the influence of the remaining punchthrough events on the angular

distributions is negligible. As for the inelastic scattering, the low statistics measured in coincidence with 1.766 MeV γ-rays indicates that its impact will not be significant either.

5.2.1 Optical model calculations

The angular distributions for the (p,p) channel were compared to theoretical calculations obtained using the reaction code FRESCO [69]. The Chapel Hill [70], Koning-Delaroche [71] and Watson [72] parameter sets were used to define the optical potential. These optical models are different global parameterizations for the nucleon-nucleus optical potential obtained from analysis of elastic scattering experimental data, including data involving nuclei from the ^{16}C mass-region or the same energy range.

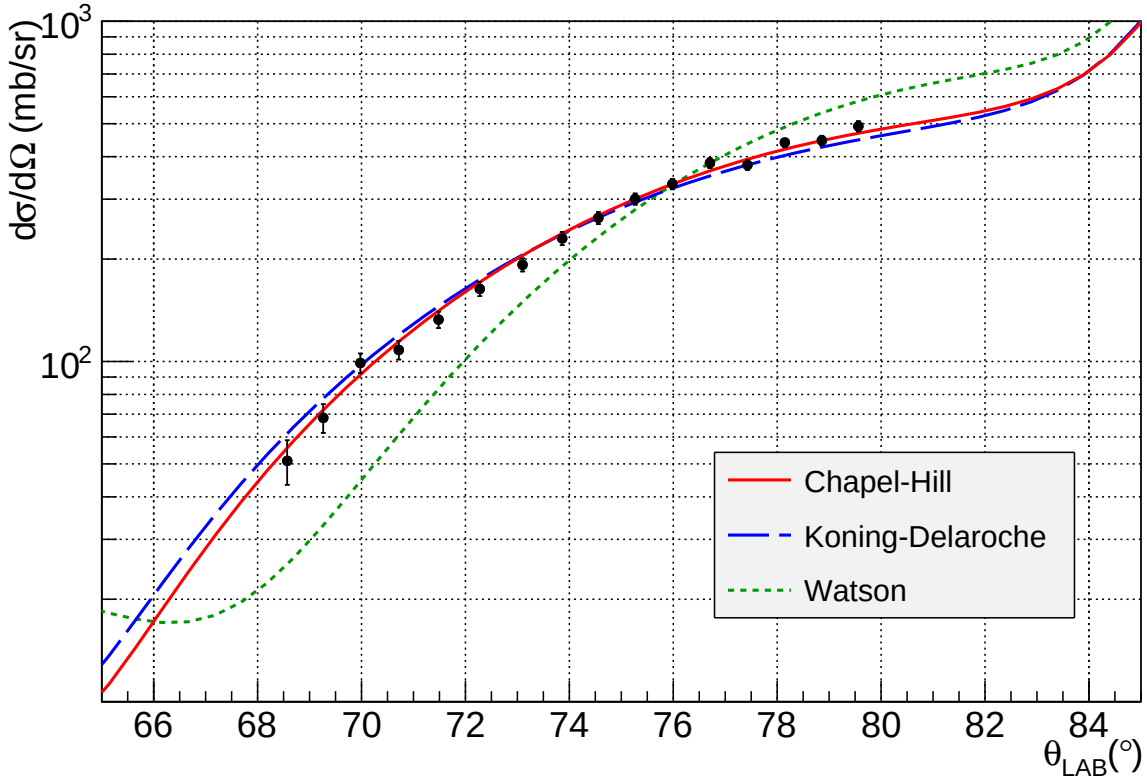

Figure 5.2: $^{16}C(p,p)^{16}C$ cross section in the lab frame. Statistical error bars are included for all the data points, but they are sometimes smaller than the markers. Chapel Hill [70], Koning-Delaroche [71] and Watson [72] optical model calculations are also presented in red full line, blue dashed line and green dotted line respectively.

The experimental angular distribution of the proton elastic scattering of ^{16}C is presented in figure 5.2, with the three optical model calculations superimposed. It is shown in this figure that the Chapel Hill optical potential provides the best description of the experimental angular distribution ($\chi^2 = 0.76$), although the Koning-Delaroche optical potential successfully reproduces the whole angular distribution too ($\chi^2 = 1.19$). Watson optical potential, however, fails to reproduce the shape of the angular distribution

and the absolute cross section is underestimated at scattering angles smaller than 76°. This comparison gives confidence on Chapel-Hill and Koning-Delaroche parameterizations of the ^{16}C plus nucleon optical potential that are going to be used to build the ^{16}C plus deuteron adiabatic potentials for the calculations of ^{16}C(d,p) cross-sections.

5.3 Analysis of the ^{16}C(d,d)^{16}C elastic scattering

The angular distribution of the elastic scattering of ^{16}C on deuteron has been extracted from the experimental data using equation 5.1 following a technique similar to that described for the proton elastic scattering in section 5.2.

The experimental data were evaluated between 1 MeV and 10 MeV (punchthrough of deuterons in the Inner Barrel), while the energy bin width was chosen between 400 and 600 keV in order to reduce the statistical fluctuations while keeping a sufficient number of points to sample the angular distribution. The solid angle $\Delta\Omega$ is also provided by the Geant4 simulation described in section B.2.

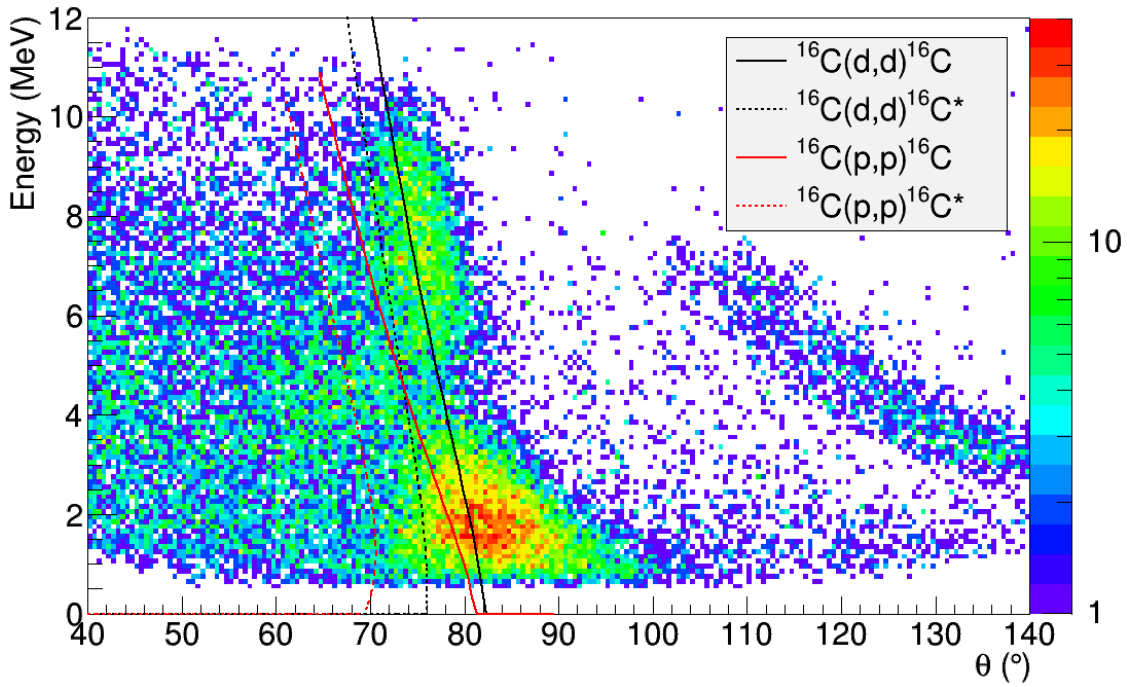

Figure 5.3: Energy versus laboratory scattering angle for non-punchthrough events measured in TIARA with the CD_2 target. The black line represents the calculated kinematics for the $^{16}C(d,d)^{16}C$ scattering, while the red line shows the $^{16}C(p,p)^{16}C$ kinematics. The black and red dashed lines stand for the $^{16}C(d,d')^{16}C$ and $^{16}C(p,p')^{16}C$ inelastic scattering calculations corrected with energy losses respectively.

A condition of no hit in the Outer Barrel (see section 4.14.4.2) was required to minimize the effect of punchthrough events on the shape of the experimental elastic cross section. This condition was reinforced by requiring that the momentum conservation,

assuming a two body reaction, is fulfilled within a margin of ±75 MeV/c (see figure 4.48). The punchthrough removal efficiency is found to be roughly 100%, as proved by figure 5.3 where no punchthrough line is visible in the (d,p) pattern. However, this momentum conservation condition can not completely suppress the deuteron break up background at lower scattering angles.

In order to remove any inelastic contribution, the events in coincidence with a γ-ray of 1.76 MeV were normalised with the corresponding γ-detection efficiency (6.82 %) and subtracted from the measured yield.

5.3.1 Optical model calculations

The experimental angular distribution obtained from the (d,d) data is compared in figure 5.4 to theoretical calculations performed using the FRESCO [66] reaction code. The optical potentials employed for that purpose were defined according to Daehnick et al. [73], Haixia et al. [74], Bojowald et al. [75] and Newman et al. [76] global parameterizations. Besides, Newman et al. best-fit potentials at 17.2 MeV for ^{12}C and ^{16}O, both with and without the spin orbit coupling, were also utilized.

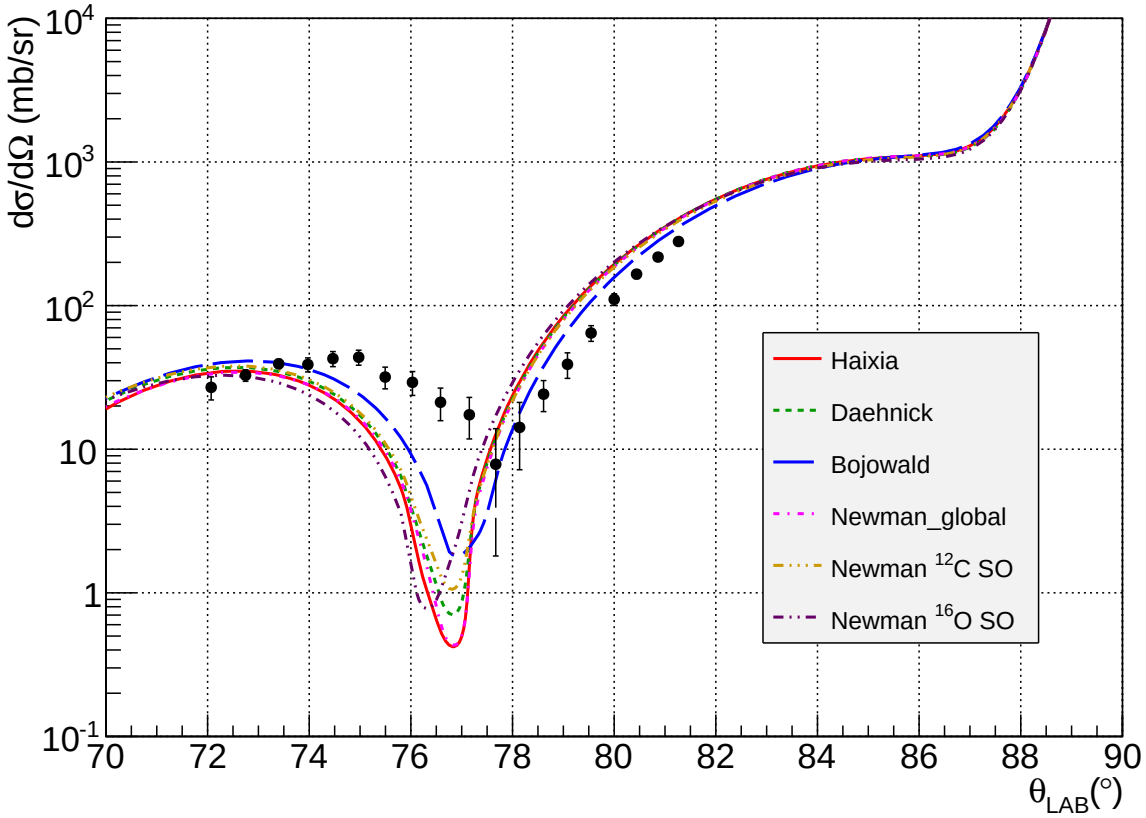

Figure 5.4: $^{16}C(d,d)^{16}C$ experimental cross section (dots with statistical error bars) in the lab frame compared to theoretical calculations performed with FRESCO with different global parameterizations and best-fit potentials for ^{12}C and ^{16}O at 17.2 MeV. Statistical error bars are included for all the experimental data points.

Although these optical models are intended to provide a global parameter prescription for an optical potential describing the deuteron-nucleus elastic scattering, they all fail at describing the ^{16}C(d,d)^{16}C experimental cross section.

This could be explained by the fact that Daehnick et al. [73] and Bojowald et al. [75] are based on data sets that do not include experimental data with targets lighter than ^{27}Al and hence, one may expect ^{16}C to fall beyond the range of applicability of these models. Haixia et al. [74] and Newman et al. [76] include deuteron elastic scattering data on light nuclei: ^{12}C and ^{16}O for the former and ^{12}C, ^{14}N and ^{16}O for the latter, which are all stable nuclei. This, combined with the fact that ^{12}C and ^{16}O Newman best-fit parametrizations are unable to describe ^{16}C(d,d)^{16}C experimental cross section, indicates that the description of deuteron elastic scattering on ^{16}C might require a much more exotic parameterization.

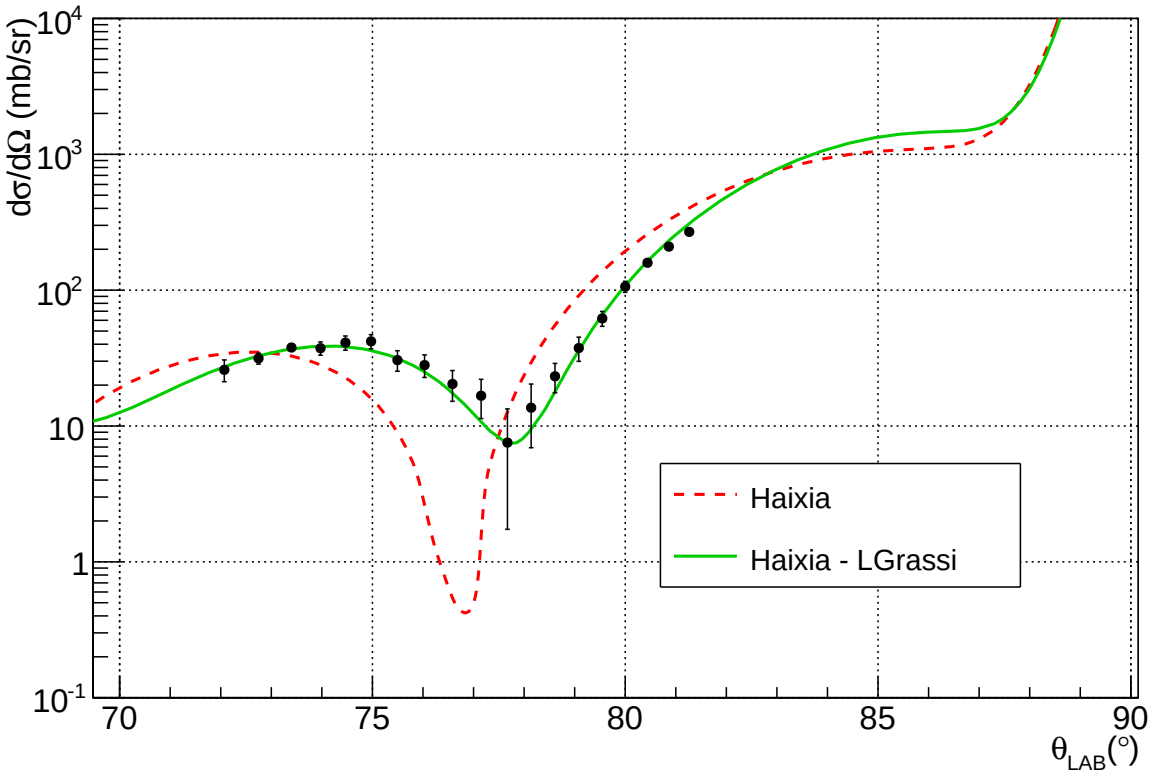

Figure 5.5: ^{16}C(d,d)^{16}C experimental cross section (dots with statistical error bars) compared to the theoretical calculation depicted in a green full line performed with the potential depths given by Haixia et al. and the radii and diffusenesses values used by L.Grassi et al. [77] in their work. The unmodified Haixia et al. [74] optical potential is also displayed in a red dashed line to show the effect of the new radii and diffusenesses on the angular distribution.

In reference [77], L.Grassi et al presented a best-fit potential for their experimental deuteron elastic scattering angular distribution of ^{16}C measured at 50 MeV/A, however their work shows that an exceptionally large diffuseness in the imaginary potential is needed to reproduce the experimental data.

A theoretical calculation was performed replacing the values of radius and diffuseness in the Haixia et al. [74] optical potential parametrization by those presented in L.Grassi et al's work [77], while keeping the potential depths in order to respect the energy dependence of the optical potential model. Figure 5.5 presents this theoretical calculation together with the experimental ^{16}C(d,d)^{16}C cross section, where the success of this calculation reproducing the experimental cross section is clear.

As indicated previously, an exceptionally large diffuseness in the imaginary potential is needed to reproduce the experimental cross section (see appendix C). A possible interpretation of this exotic behaviour could be the effect of a stronger coupling to the continuum states in deuteron break up channels, as suggested by L.Grassi et al [77] and supported by some literature [78–80].

A stronger coupling of break up channels of ^{16}C to the elastic channel brings another reason that could explain why the global parametrizations previously used failed to reproduce the experimental ^{16}C-deuteron elastic scattering cross section, as they are based on deuteron elastic scattering data on stable nuclei barely affected by this feature and can therefore reproduce well the data without taking into account this effect.

5.3.2 Estimation of proton contamination in the CD_2 target

Previous experiments have shown that CD_2 targets might have some proton contamination. In order to estimate a possible proton contamination in the target, the experimental elastic scattering cross section has been fitted with a linear combination of the theoretical calculations describing well the elastic scattering data as indicates the following equation:

$$\left(\frac{d\sigma}{d\Omega}\right)^{exp} = (1-x)\left(\frac{d\sigma}{d\Omega}\right)^{th}_{(d,d)} + x\left(\frac{d\sigma}{d\Omega}\right)^{th}_{(p,p)} \tag{5.2}$$

where x represents the fraction of proton impurities in the CD_2 target and has been left free to vary.

Figure 5.6 presents the result of this fit, that led to an estimate of 1.1 % of proton contamination in the CD_2 target. It can be concluded from this data, therefore, that there is no significant proton contamination and, considering the other sources of uncertainties, its effect will have a negligible influence on the (d,p) cross sections.

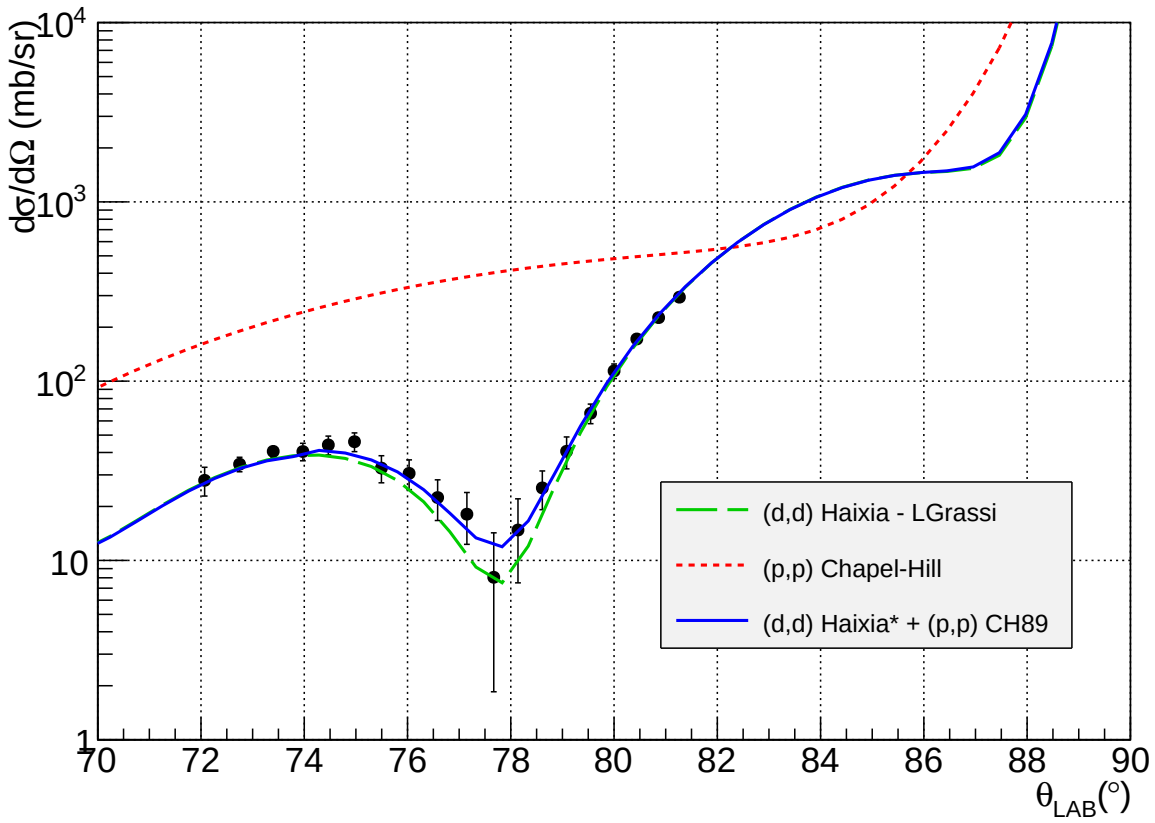

Figure 5.6: Experimental cross section of ^{16}C elastic scattering on the CD_2 target (dots with statistical error bars) fitted with a linear combination (blue) of the theoretical calculations describing (p,p) (red) and (d,d) (green) elastic scattering, shown in figures 5.2 and 5.5 respectively. The relative contribution of (p,p) and (d,d) to the fit function was left free to vary in order to estimate the proton contamination present in the CD_2 target, obtaining 1.1 % of proton impurities.

5.4 Analysis of the ^{16}C(d,p)^{17}C reaction

5.4.1 γ-coincidence yield

The angular distributions of the protons leading to the first and second excited states in ^{17}C were measured for the events falling within the ^{17}C bound states kinematical pattern (see section 4.14.5) in coincidence with the excellent corresponding γ-rays peaks of 217 and 335 keV. This procedure exploits the finer energy resolution of the γ-ray detectors compared to the resolution in excitation energy provided by TIARA.

The laboratory differential cross section for each angular bin is given by equation 5.1, where the measured proton yield N in coincidence with each γ-line is obtained using the γ simulations presented in section B.3 normalized to the data.

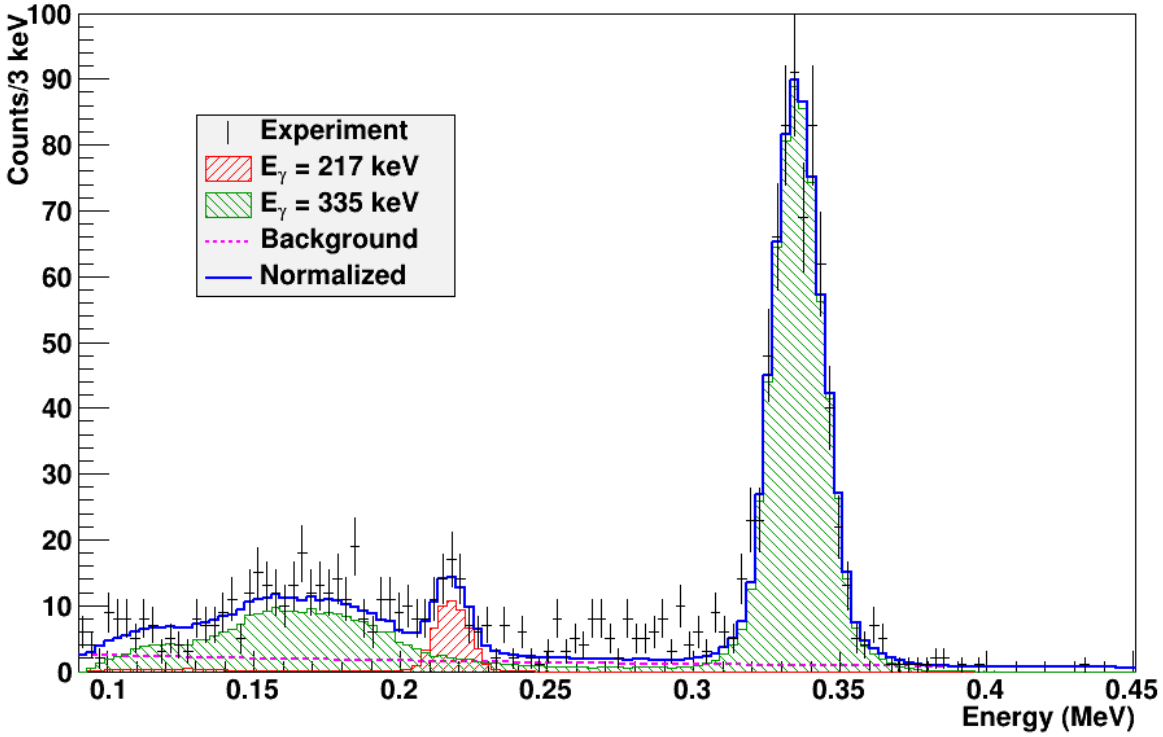

Figure 5.7: γ-spectrum gated on ^{17}C bound states. The best fit is added in blue on top of it. The contribution of the normalized γ-ray simulations is depicted in red and green, respectively, for the γ-rays of 217 keV and 335 keV. The exponential background is shown in pink.

For each angular bin, the γ-spectrum is fitted with the simulated response functions, for which the normalization factor is left free to vary, plus an exponential background (figure 5.7). The measured proton yield N is therefore provided by the integral under the photopeaks of the normalized simulations.

5.4.2 ADWA calculations

The theoretical cross sections were calculated using the TWOFNR reaction code [81] under the Adiabatic Distorted Wave Approximation (ADWA). The Chapel-Hill [70] and Koning-Delaroche [71] parametrizations for the nucleon-nucleus optical potential were used to describe the p+^{17}C potential in the exit channel, while in the entrance channel we used an adiabatic d+^{16}C potential. This adiabatic potential was built using the Johnson-Tandy prescription [82] (see equation 2.19) using p+^{16}C and n+^{16}C potentials at 17 AMeV from Chapel-Hill and Koning-Delaroche parameterizations and a deuteron wave function obtained with the Reid soft-core np interaction. All calculations are performed within the zero-range approximation with the standard finite-range correction parameter of 0.746 fm. Non-locality corrections with a range parameter of 0.85 fm for the p+^{17}C channel were also included.

The geometry of the neutron binding potential has a Woods-Saxon shape with radius and diffuseness of 1.25 fm and 0.65 fm, respectively. The depth is adjusted to reproduce the neutron separation energy. A spin-orbit term is included with the same geometry as the central potential and a potential well depth of 6 MeV.

5.4.3 Spectroscopic factors

As explained in section 2.4, a comparison between the experimental angular distributions and the theoretical cross sections provides an estimation of the transferred angular momentum, ℓ, in the reaction and a measurement of the spectroscopic factors.

Thus the theoretical calculations have been scaled to the experimental cross sections by minimizing the χ^2 function. The scaling factor provides a measurement of the spectroscopic factors while the calculation that fits better the angular distribution indicates the transferred angular momentum ℓ. Finally, if possible, a spin assignment will be inferred with the help of the shell model predictions.

It is worth mentioning that there is an intrinsic uncertainty in the potentials and the geometry of the binding potential well chosen to perform the theoretical calculations that will affect the spectroscopic factors. It is widely admitted that the determination of the spectroscopic factor using a direct reaction has an intrinsic uncertainty around 20 % [83], estimated by comparing experimental angular distributions for (d,p) and (p,d) reactions with predicted cross-sections over a wide range of nuclei.

5.4.4 Second excited state

Figure 5.8a presents the angular distribution of the protons leading to the second excited state in ^{17}C measured at 335 keV, together with theoretical cross sections performed using Koning-Delaroche optical potential for a transferred angular momentum of $\ell = 0$, $\ell = 1$ and $\ell = 2$. A simple comparison indicates that the experimental cross section is best described by the $\ell = 2$ calculation, in agreement with the spectroscopic study of ^{17}C via one neutron removal reactions by Y.Kondo et al. [29]. This result indicates that the spin and parity assignment should to be either $3/2^+$ or $5/2^+$. Remembering the shell model prediction of two excited states $1/2^+$ and $5/2^+$, the only possible assignment would be $5/2^+$.

Figure 5.8b shows a comparison between the experimental angular distribution with the theoretical calculations with $\ell = 2$ performed using Chapel-Hill and Koning-Delaroche optical potentials. The spectroscopic factor of 0.63 was extracted for both potentials assuming transfer to the $0d_{5/2}$ orbital in agreement with the preferred spin-

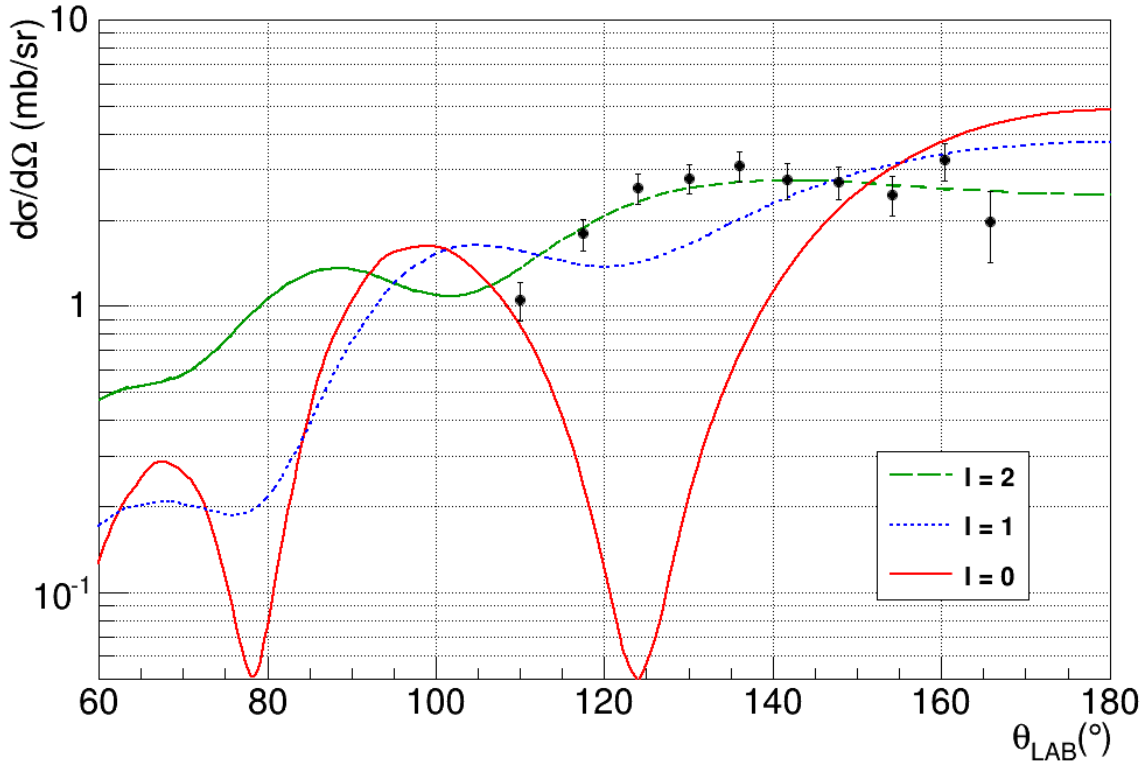

(a) Second excited state in ^{17}C at 335 keV

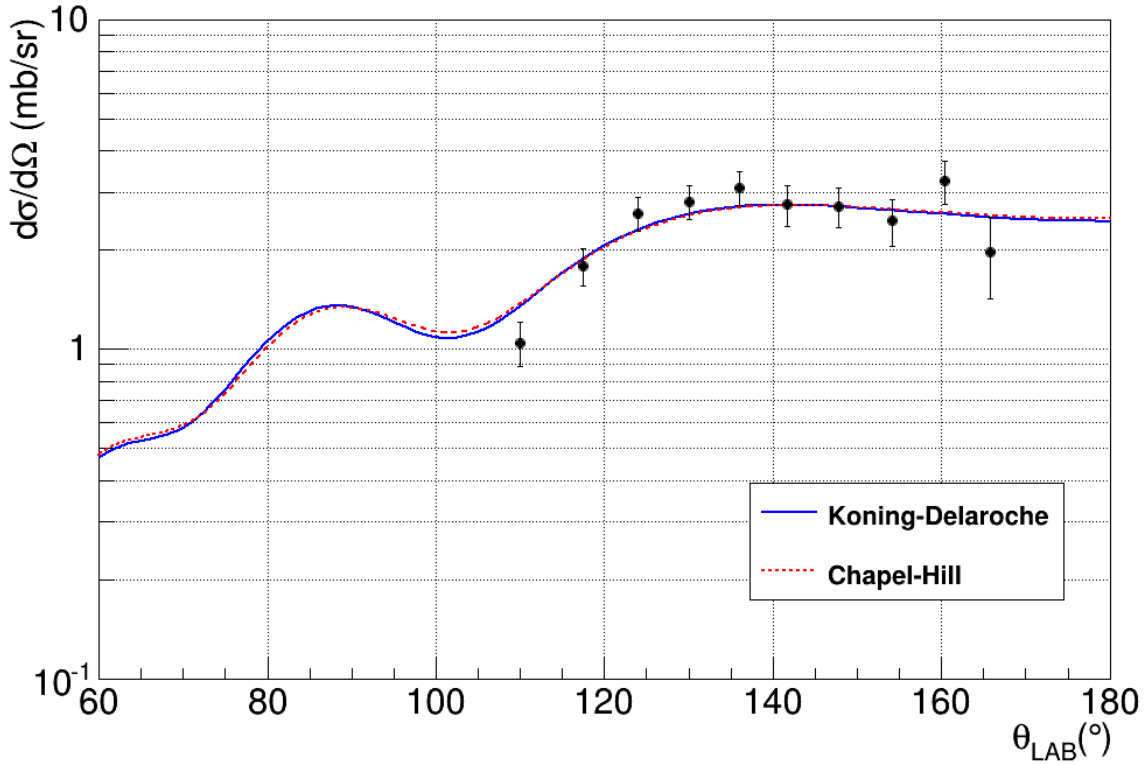

(b) Calculation for $\ell = 2$ with Chapel-Hill and Koning-Delaroche optical potentials

Figure 5.8: (a) Experimental angular distribution of the second excited state (dots with statistical error bars) in ^{17}C, located at 335 keV, compared with theoretical calculations for $\ell = 0$ (full red), $\ell = 1$ (dotted blue) and $\ell = 2$ (dashed green). (b) Theoretical calculations for $\ell = 2$ using Chapel-Hill (dotted red) and Koning-Delaroche (full blue) optical models are compared to the experimental data.

parity assignment. This result seems to indicate that the influence of the choice of optical potential on the spectroscopic factor is not very important. In addition, It is worth noticing that such a large spectroscopic factor will almost exhaust the $0d_{5/2}$ strength in the simplest picture of ^{16}C ground state, where there are two neutrons populating the neutron $0d_{5/2}$ orbital.

The experimental angular distribution presented in figure 5.8 relies on the assumption of an isotropic γ-ray distribution and this hypothesis may not be strictly correct. Since EXOGAM clovers are placed at 90^o covering a limited angular range, a deviation from the isotropic distribution could eventually affect the γ-ray geometrical detection efficiency and, therefore, the experimental angular distribution and the spectroscopic factors. However, the influence of a non-isotropic γ-ray distribution in the spectroscopic factors was investigated using the same EXOGAM configuration in S. Brown's Ph. D. thesis [84], where this effect was measured smaller than 4 %. Therefore, the uncertainty due to the assumption of isotropy in the spectroscopic factors will be negligible in comparison with the uncertainty due to the choice of optical potential.

5.4.5 First excited state

The angular distribution of the first excited state in ^{17}C is shown in figure 5.9a with theoretical calculations for $\ell = 0$, $\ell = 1$ and $\ell = 2$ using the Koning-Delaroche optical potential. It can be observed that the theoretical cross section corresponding to $\ell = 0$ reproduces better the data. This result provides solid evidence of $1/2^+$ spin and parity assignment for this state, in agreement with the one neutron removal from ^{18}C by Y.Kondo et al. [29].

Figure 5.9b presents a comparison between the experimental angular distribution and theoretical calculations for $\ell = 0$ using two different optical potentials: Chapel-Hill and Koning-Delaroche, from which spectroscopic factors of 0.88 and 0.67 were derived respectively. Both optical potentials reproduce equally well the experimental angular distribution, although there is a significant difference between the spectroscopic factors, it lies within the 20 % uncertainty typical of any spectroscopic factor measurement.

5.4.6 Ground state

The angular distribution of ^{16}C(d,p) events populating bound states in ^{17}C is extracted by removing any condition on the γ-rays and considering all the particles detected within the kinematical pattern corresponding to ^{17}C bound states (see section 4.14.5). The result is displayed in figure 5.10.

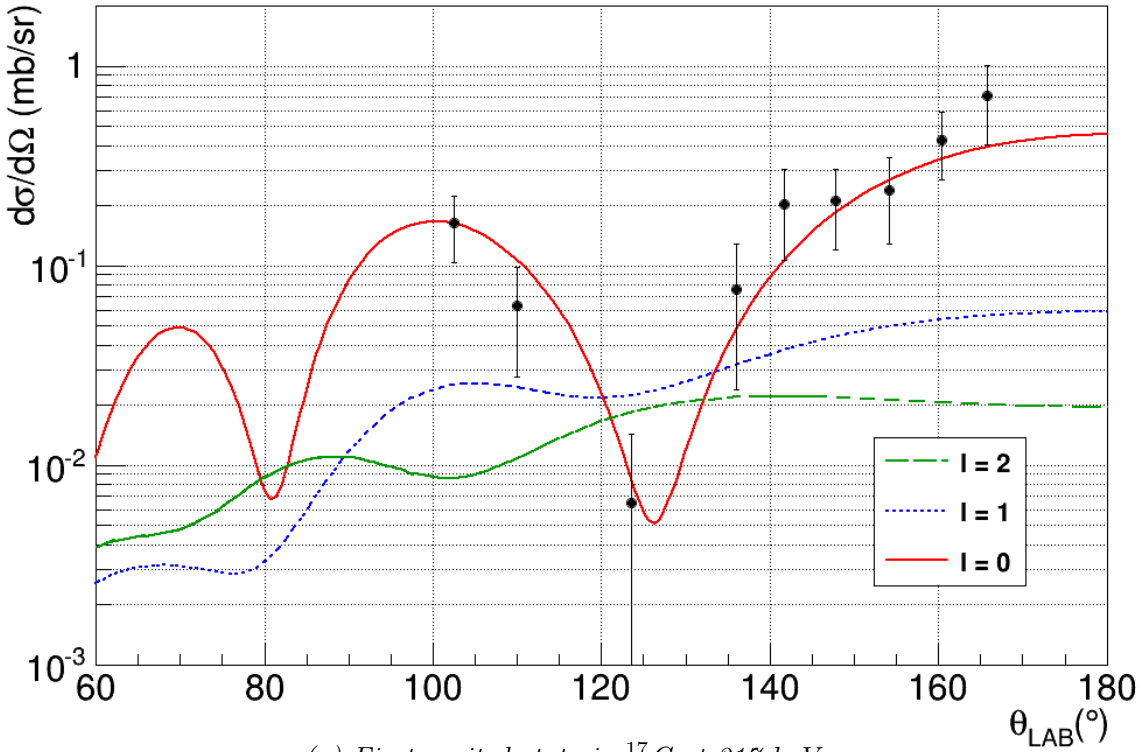

(a) First excited state in ^{17}C at 217 keV

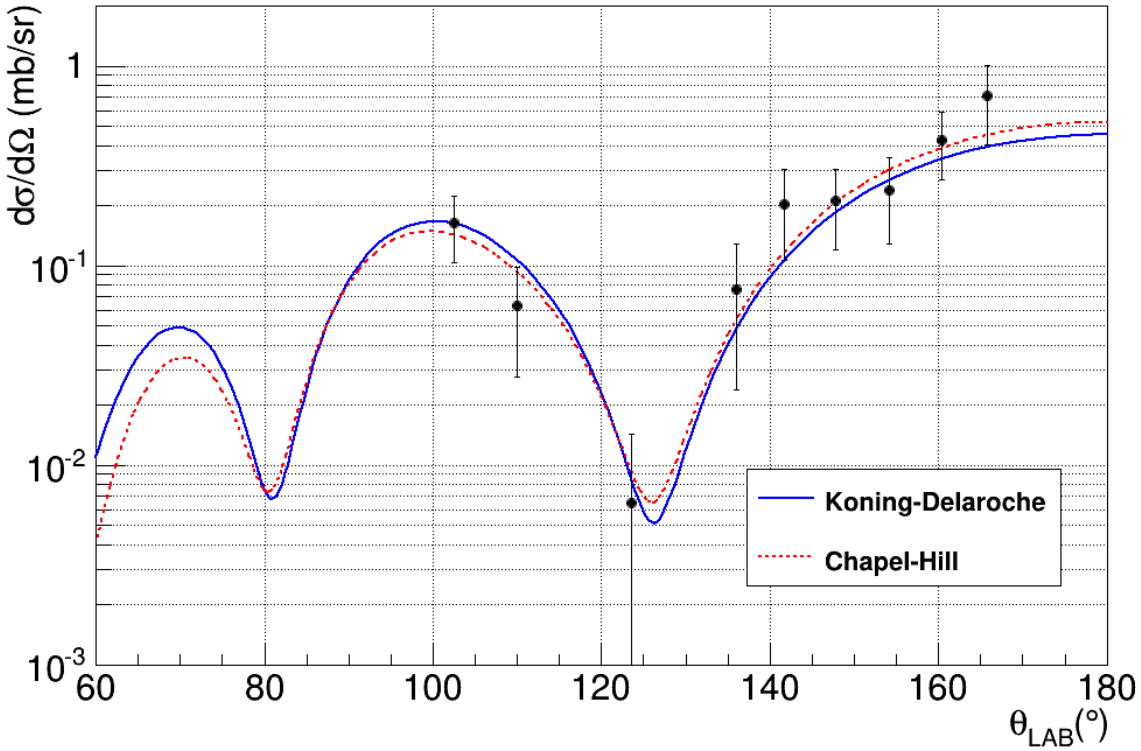

(b) Calculation for $\ell = 0$ with Chapel-Hill and Koning-Delaroche optical potentials

Figure 5.9: Experimental angular distributions $^{16}C(d,p)$ for the first excited state (dots with statistical error bars) in ^{17}C, located at 217 keV, compared with theoretical calculations for $\ell = 0$ (full red), $\ell = 1$ (dotted blue) and $\ell = 2$ (dashed green). (b) Theoretical calculations for $\ell = 0$ using Chapel-Hill (dotted red) and Koning-Delaroche (full blue) optical models are compared to the experimental data.

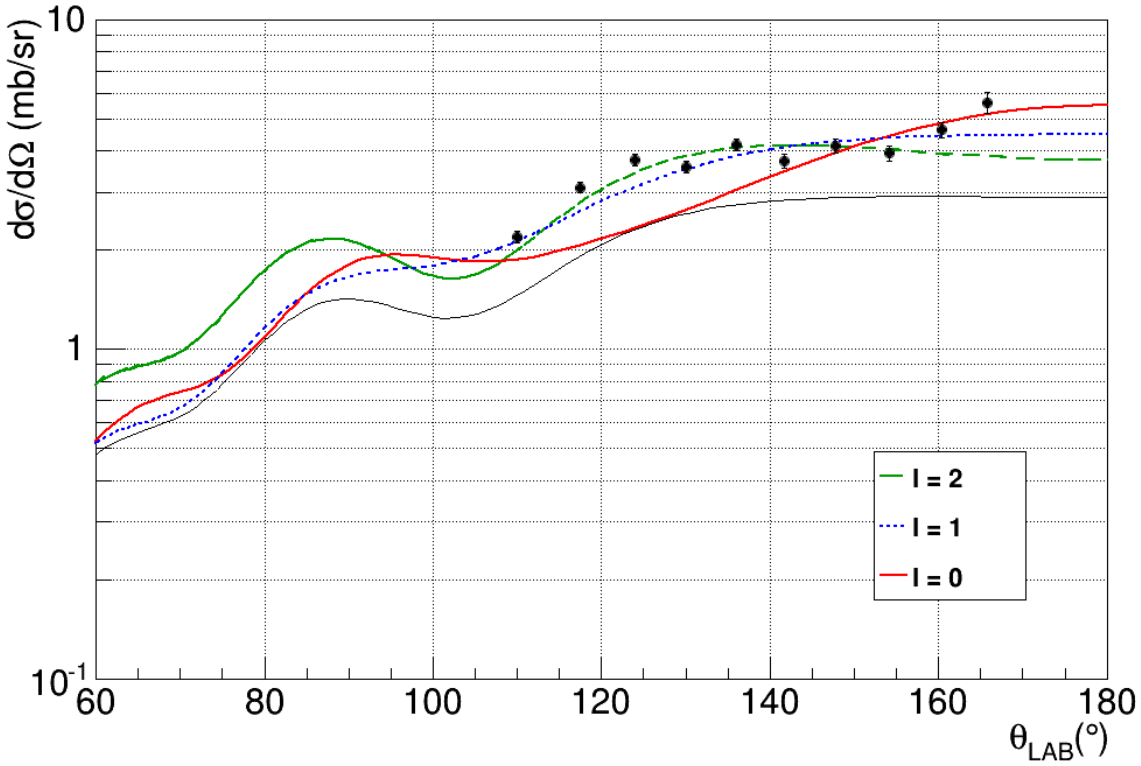

(a) Angular distribution of the protons leading to bound states in ^{17}C

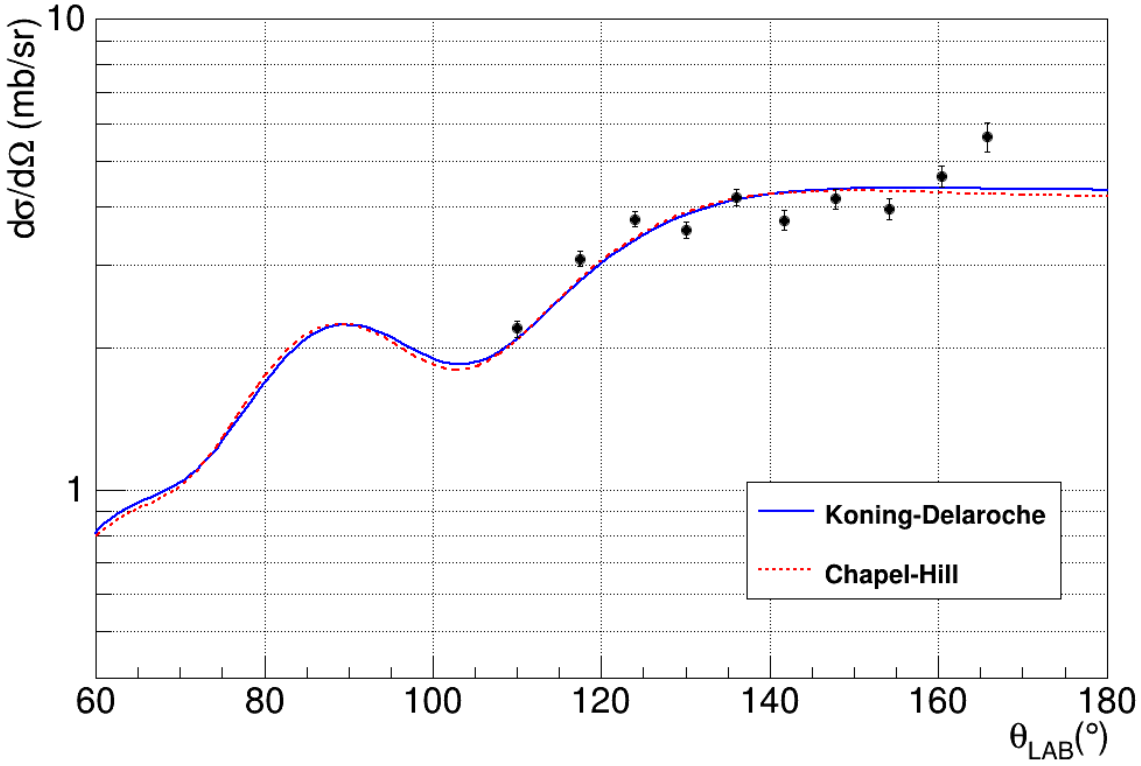

(b) Calculation for $\ell = 2$ with Chapel-Hill and Koning-Delaroche optical potentials

Figure 5.10: (a) Experimental angular distributions of ^{16}C(d,p) events to all the bound states in ^{17}C. The thin black line represents the contribution of the measured excited states, on top of which theoretical calculations for the ground state were summed, assuming $\ell = 0$ (red full line), $\ell = 1$ (blue dotted line) and $\ell = 2$ (green dashed line). (b) Theoretical calculations for $\ell = 2$ using Chapel-Hill (dotted red) and Koning-Delaroche (full blue) optical models are shown.

As shown in the measured γ-spectrum (figure 5.7), the structure below the neutron separation threshold in ^{17}C contains only two excited states and the ground state. Therefore, the ground state angular distribution could be then extracted from the total angular distribution to all the bound states in ^{17}C by subtracting away the angular distribution of the first and second excited states. However, the induced uncertainties are rather large, preventing any detailed study. We have used an alternative method that relies on the sum of the best fits to the measured first and second excited states (see sections sections 5.4.5 and 5.4.4) and the theoretical calculations for the ground state assuming $\ell = 0$, $\ell = 1$ and $\ell = 2$.

As it can be seen in figure 5.10a The bound states angular distribution is best reproduced when assuming a $\ell = 2$ state for the ground state, in agreement with the existing $3/2^+$ spin and parity assignment.

Figure 5.10b presents the experimental angular distribution compared to the theoretical calculations for a transferred angular momentum $\ell = 2$ performed using Koning-Delaroche and Chapel-Hill optical potentials, from which spectroscopic factors of 0.53 and 0.52 were obtained respectively, assuming transfer to the $0d_{3/2}$ orbit in agreement with the spin-parity of $3/2^+$. Once again, the choice of optical potential does not seem to have a significant influence on the spectroscopic factor, contrarily to what was observed for the $1/2^+$ state.

Note that the method used to deduce the spectroscopic factor of the ground state relies on the spectroscopic factors of the two bound excited states previously discussed and therefore, will be affected by their uncertainty. The uncertainty of the spectroscopic factor of the ground state is estimated of 40 %.

5.4.7 Shell model calculations

In order to obtain theoretical predictions for the ^{17}C level scheme and the spectroscopic factors for the one-neutron transfer reaction ^{16}C(d,p), shell model calculations were performed using OXBASH shell model code [85]. In this work, the WBP, WBT interactions [86] and a modified version of the WBT hamiltonian with a reduction of the 25 % in the two body matrix elements (TBME), as suggested in reference [26], were used to describe the structure of ^{17}C and ^{16}C. The calculations were performed in the full spsdpf-model space truncated to limit to two the number of excitations across a major shell gap ($2\hbar\omega$) and restricted to positive parity states.

Other hamiltonians are also available in the literature and will be used here for comparison. The ^{17}C level scheme calculated using the sdpf interaction was obtained from Z.Elekes et al. work [30] while the results from the SFO-tls hamiltonian, developed recently for this mass-region, were provided to us by T.Suzuki and T.Otsuka [87].

J^π	E^{ex}_{exp}	C^2S^{exp}		WBP		WBT		WBT*		SFO-tls		sdpf
		CH89	KD02	E^{ex}	C^2S	E^{ex}	C^2S	E^{ex}	C^2S	E^{ex}	C^2S	E^{ex}
$3/2^+$	0 keV	0.53(23)	0.52(23)	0 keV	0.03	77 keV	0.03	77 keV	0.02	0 keV	0.05	0 keV
$1/2^+$	217(1) keV	0.88(18)	0.67(13)	295 keV	0.64	267 keV	0.56	91 keV	0.50	72 keV	0.72	395 keV
$5/2^+$	335(1) MeV	0.63(13)	0.63(13)	32 keV	0.70	0 keV	0.75	0 keV	0.77	140 keV	0.65	525 keV

Table 5.1: Excitation energies and spectroscopic factors deduced for the states in ^{17}C observed in this work compared to theoretical predictions. The corresponding 20 % uncertainty applies to the experimental spectroscopic factors C^2S^{exp}.

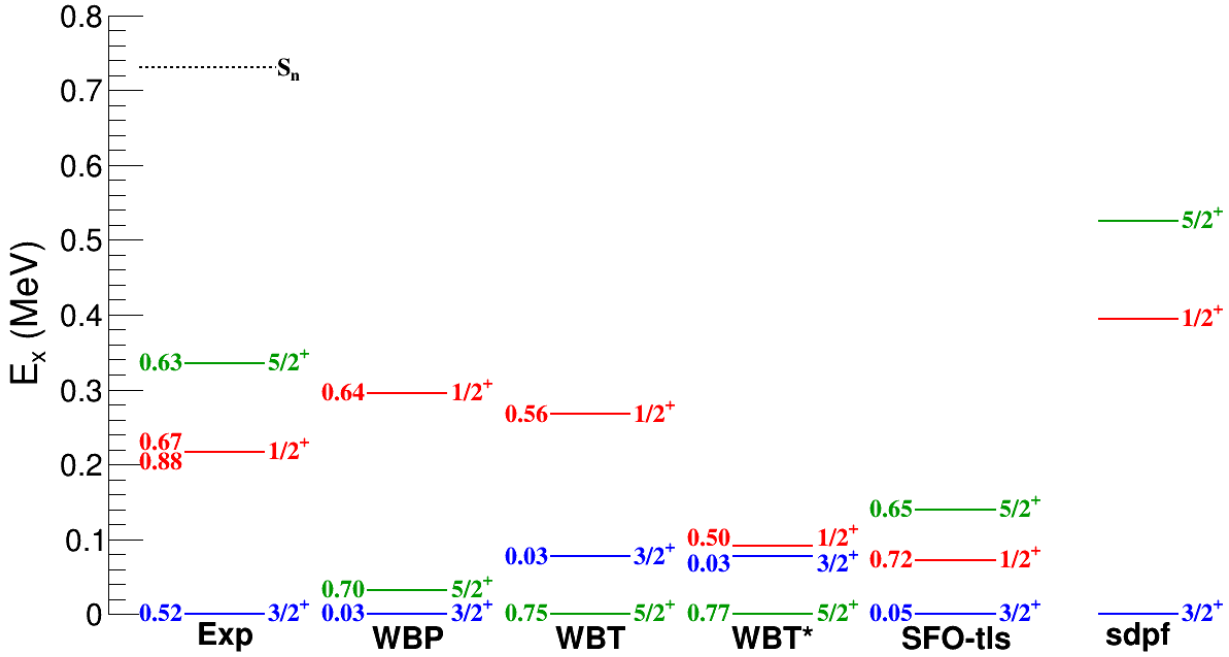

Figure 5.11: Experimental level scheme of ^{17}C, together with WBP, WBT, WBT, SFO-tls and sdpf theoretical predictions. The corresponding spectroscopic factors are also presented.*

The excitation energies measured, the spin and parity assignments and the spectroscopic factors deduced from the angular distributions for the ground state and both excited states in ^{17}C are listed in table 5.1 and plotted in figure 5.11, together with WBP, WBT, WBT*, sdpf and SFO-tls theoretical predictions.

Calculations performed with the WBP and WBT interaction show some limitations when trying to reproduce the right ordering of the states in ^{17}C. The WBP gets the spin and parity of the ground state right, but inverts the spin and parity assignment of the excited states. However, given the accuracy of the shell model calculations in this region to be of the order of 300 keV, the agreement with the experimental data is within the uncertainty. Besides, the effect of reducing the TBME a 25 %, owing to the loosely bound nature of ^{17}C as suggested by [26], makes the spectra compressed in energy, almost degenerated. The sdpf interaction gives a better agreement in terms of J^{π} of the states, although it predicts the excited states higher up in energy. Finally, the best agreement is found with the SFO-tls hamiltonian. This interaction includes tensor and spin-orbit terms arising from meson-exchange forces in the p-sd crossing terms and a revised T = 1 monopole term in order to reproduce the experimental ordering of the low-lying levels in ^{17}C [87].

The WBP and WBT hamiltonians are derived from a fit to all the available data from the mass region $10 \leq A \leq 20$, therefore it could have been possible to get a better agreement in terms of excitation energy by tuning the TBME. However, this would not lead to a significant changes in the spectroscopic factors observed in table 5.1 showing the reliability of these calculations.

Concerning the spectroscopic factors, shell model calculations with different interactions predict a spectroscopic strength between 0.50-0.64 and 0.70-0.77 for the first and second excited states in ^{17}C respectively. These results agree really well with the spectroscopic factors deduced in this work within the uncertainties and confirm the single particle nature of the $1/2^+$ and $5/2^+$ states in ^{17}C.

On the contrary, the spectroscopic factor obtained for the ground state is in stark disagreement with the prediction from the shell model. In fact, the spectroscopic factor deduced in this work is one order of magnitude higher than the value expected by shell model calculations with WBP, WBT, WBT* and SFO-tls for the $3/2^+$ state. This result indicates the presence of a stronger $0d_{3/2} \otimes$ ^{16}C(0^+) component in the ground state of ^{17}C underestimated in the shell model predictions.

Previous experimental information gathered via knockout from ^{17}C by Maddalena et al. work [28] support this finding. In this experiment, the ground state cross section from ^{17}C to the ground state of ^{16}C was also measured an order of magnitude higher than what was expected by theoretical calculations using the WBP interaction. In summary, the $0d_{3/2}$ strength in the ground state of ^{17}C appears to be underestimated

in the WBP and WBT interactions.

5.4.8 N = 11 isotonic chain

The analysis of the single-particle states in the N = 11 isotonic chain is well suited to discuss the shell evolution of the $0d_{3/2}$, $1s_{1/2}$ and $0d_{5/2}$ orbitals when approaching the neutron drip line. However, pure single-particle states do not exist and therefore it is required to combine the measurements of the excitation energies with the corresponding single-particle strength measured experimentally [88–90].

Figure 5.12 presents the systematics of the $1/2^+$, $3/2^+$ and $5/2^+$ states in the isotopic chain N = 11 from the drip line (^{15}Be is unbound) to the valley of stability (^{21}Ne is stable). The gap between the $1/2^+$ and $5/2^+$ states is decreasing when moving towards the drip line, from 2.4 MeV in ^{21}Ne until the apparent inversion of the ordering in ^{17}C. Since a large single-particle strength was measured for the $1/2^+$ and $5/2^+$ states along the N=11 isotonic chain, we can see the reduction of this gap as a first indication of the non existence of the N=14 gap in ^{17}C[1].

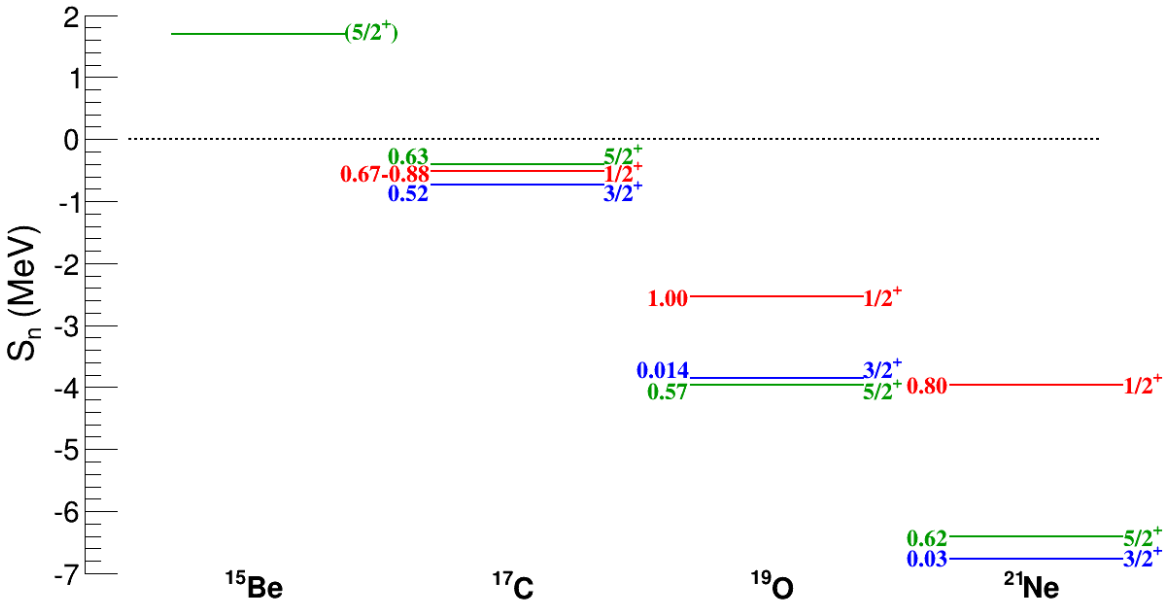

Figure 5.12: Systematics of the positive parity states in the N = 11 isotonic chain and the corresponding experimental spectroscopic factors (^{15}Be: [88], ^{17}C: this work, ^{19}O: [89], ^{21}Ne: [90]).

It is important to note that a good agreement is found between the spectroscopic factors measured for the $1/2^+$ and $5/2^+$ states in ^{17}C, ^{19}O and ^{21}Ne. However, the spectroscopic factors measured for ^{19}O and ^{21}Ne ground states are one order of magnitude smaller than the value found in this work for ^{17}C ground state.

[1]The melting of N = 14 sub-shell gap in ^{17}C does not meant that it was present in ^{19}O or ^{21}Ne.

5.4.9 Halo configurations in ^{17}C bound states

The appearance of one-neutron halo structures have been measured in odd-mass neutron rich carbon isotopes ^{15}C [39] and ^{19}C [40]. The first excited state of ^{17}C has been suggested as a halo candidate due to its neutron separation energy of 0.51 MeV and a $1/2^+$ spin and parity assignment, indicative of a $\ell = 0$ valence neutron configuration. Our transfer analysis clearly shows that this state has a dominant neutron s-wave component, which reinforces the suspicion that it could have a well developed halo.

In order to investigate that possibility, we can apply the scaling law derived by K. Riisager for the nuclei exhibiting halo features [91]. This scaling method for two body systems relates a dimensionless measure of the radius with a dimensionless measure for the binding energy of the system, assessed as:

$$\begin{cases} \dfrac{\langle r^2 \rangle}{R^2} & \text{where} \quad R^2 = \dfrac{5}{3}\left(\langle r^2 \rangle_{\text{core}} + 3.3 \text{ fm}^2\right) \\ \dfrac{\mu B R^2}{\hbar^2} \end{cases} \tag{5.3}$$

where B is the separation energy, μ stands for the reduced mass of the system, for which the masses were taken from the 2012 Atomic Mass Evaluation [37]. R represents the distance at which the binding energy is compensated by the potential energy and $\langle r^2 \rangle$ stands for the root mean square radius. As the bound states in ^{17}C have a rather strong single-particle nature, we can estimate the root mean square radius of the valence neutron from that of the dominant component. This rms radius can then be calculated in a potential model.

Table 5.2 shows the two quantities involved in Rissager's scaling law, computed for the three bound states of ^{17}C. Each rms radius is the one of a single particle state in a Woods-Saxon potential with $r_0 = 1.25$ fm and $a = 0.65$ fm, whose depth is adjusted to reproduce the experimental separation energy.

J^π	ℓ	E^{ex} (MeV)	S_n (MeV)	$\sqrt{\langle r^2 \rangle}$ (fm)	$\frac{\langle r^2 \rangle}{R^2}$	$\frac{\mu S R^2}{\hbar^2}$
$3/2^+$	2	0.000	0.734	4.02	0.916	0.294
$1/2^+$	0	0.217	0.517	7.17	2.913	0.207
$5/2^+$	2	0.335	0.399	4.46	1.127	0.160

Table 5.2: Excitation and separation energies, spin and parity assignment, transferred angular momenta and root mean square radii corresponding and both dimensionless quantities required for the discussion of each bound state in ^{17}C.

A widely accepted criterion to consider a nuclei as a well developed halo system is a probability of having a halo particle outside the potential range higher than 50 %. This criterion translated to figure 5.13 means that a value higher than 2 for the dimensionless measure of the radius is required to identify good halo systems.

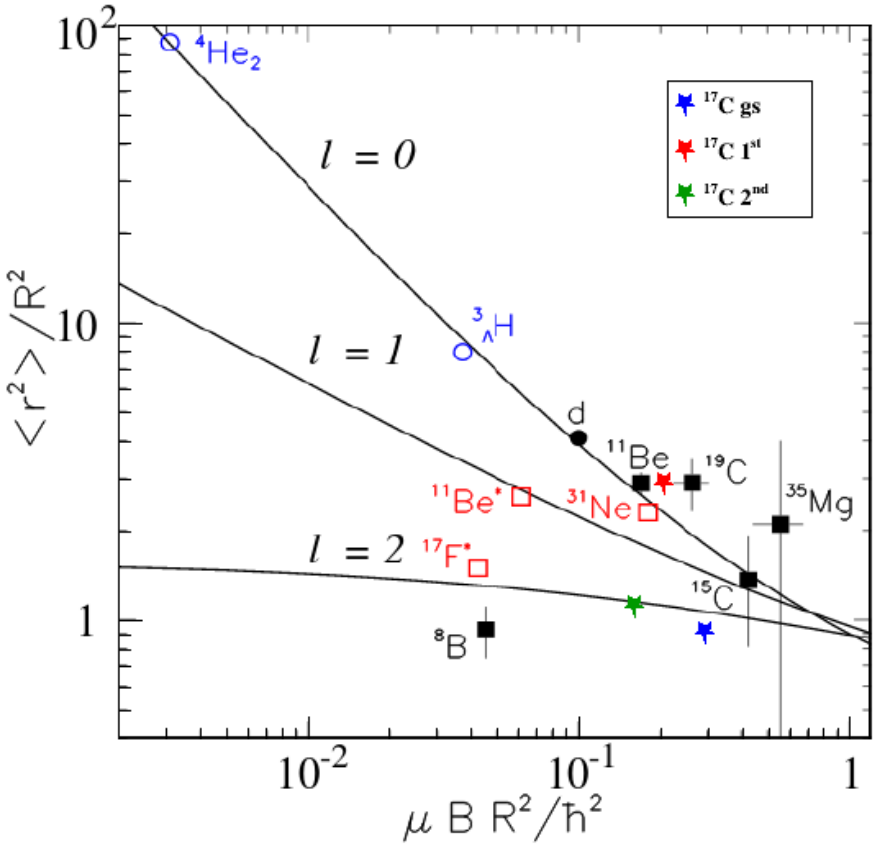

Figure 5.13: Dimensionless radius of the system versus dimensionless binding energy, defined according Riisager's scaling law for two-body halo systems. Black circle represents the deuteron, open blue circles and red squares stand for model estimates and theoretical calculations respectively, while black squares are deduced from experimental data. Blue, red and green stars represent the ground, the first and second excited states in ^{17}C (Adapted from [91])

At light of the results presented in table 5.2 and figure 5.13, it seems that the first excited state of ^{17}C located at 217 keV evidence a well-developed halo. According to the scaling law, its halo nature would be comparable to that of the ^{11}Be, probably the most studied one-neutron halo, with a similar neutron separation energy (0.5 MeV) and a ground state wave function dominated by a $\ell = 0$ component. This conclusion follows the trend observed in odd-mass neutron rich carbon isotopes, all of them presenting a one-neutron halo configuration in the $1s_{1/2}$ orbital [39; 40].

On the contrary, the ground and the second excited states of ^{17}C do not present halo configuration, in spite of a similar separation energy. However, having the valence neutron populating an orbital with a relatively high angular momentum ($\ell = 2$) gives

rise to the centrifugal barrier that confines much more their matter distribution and hampers the formation of a halo.

Chapter 6

Conclusions and outlook

The shell structure of stable and near-stable nuclei and the associated magic numbers are key elements in nuclear structure. It has been demonstrated, however, that the traditional magic numbers evolve when nuclei far from stability are explored. Since then, many theoretical and experimental efforts have been devoted to the study of the shell evolution. Recent experiments have indicated the existence of new shell closures at N=14 and N=16 in exotic nuclei and the disappearance of the magic number N=20. Within this context, this work is intended to extend these measurements to the carbon isotopic chain to gather new information about the disappearance of the N=20 shell closure and the emergence of the N=14 and N=16 shell gaps observed in neutron rich oxygen isotopes. To that end, the low-lying level structure of ^{17}C has been investigated using one-neutron transfer reactions in order to locate the neutron $0d_{5/2}$, $1s_{1/2}$ and $0d_{3/2}$ single-particle orbitals involved in the formation of the N=14 and N=16 shell gaps.

An experiment was performed at the GANIL facility using a secondary beam of ^{16}C produced by fragmentation of a primary beam of ^{18}O at 60 AMeV on a production target of beryllium. The ^{16}C was then selected from the resulting cocktail beam using the LISE3 spectrometer, slowed down to 17.2 AMeV, and delivered to the experimental room with a intensity of $5{\cdot}10^4$ pps and a purity of 99 %. The experimental setup was designed to the study of direct reactions in inverse kinematics. The double-sided silicon strip detector array TIARA was used to detect light particles at central and backward angles, in the Barrel and the Hyball respectively, measuring both the energy and the scattering angle. The Si-Si-CsI telescope CHARISSA was placed at zero-degrees to detect and identify the beam-like fragments. Four EXOGAM clovers were placed the target in order to measure the γ-rays emitted in coincidence.

The study of the one-neutron transfer reaction ^{16}C(d,p) has allowed us to improve our knowledge on the low lying structure of ^{17}C providing important information on the halo character of the $1/2^+$ state in ^{17}C. Two excited states have been populated

in ^{17}C at 217 keV and 335 keV and the corresponding angular distributions have been extracted, providing a clean and clear $1/2^+$ spin and parity assignment for the first excited state and a direct measurement of the transferred angular momenta of $\ell = 2$ for the second excited state, in agreement with previous measurements. The measured angular distribution for the ground state has provided a $\ell = 2$ angular momentum, in concordance with the rather well established spin and parity assignment of $3/2^+$. The experimental ordering of the bound states in ^{17}C is better reproduced by the SFO-tls interaction, whereas the WBP and WBT interactions agree with the experimental spectrum within the rms deviations of the shell model.

We have measured for the first time the spectroscopic factors for the bound states in ^{17}C. Large spectroscopic factors of 0.67 and 0.63 were measured for the first and second excited states using Koning-Delaroche optical potential (small variations were observed for the first excited state when using Chapel-Hill optical potential), indicating their single particle nature. A very good agreement between the theoretical calculations and the experimental spectroscopic factors in found for both states. However, the preliminary spectroscopic factor for the ground state (0.52) is one order of magnitude higher than expected by shell model calculations (0.03). This feature indicates the existence of a strong $0d_{3/2}\otimes^{16}\mathrm{C}(0^+)$ contribution in the ground state of ^{17}C that appears to be underestimated by the shell model calculations. A complete analysis including CCBA will allow us to draw a final conclusion.

The study of single-particle states in the N=11 isotones shows that the gap between $1/2^+$ and $5/2^+$ states drops dramatically when going from ^{21}Ne (stable) to ^{17}C (see figure 5.12). This reduction, together with the large single-particle strength measured in this work, seems to indicate the non existence of the N=14 gap in ^{17}C.

Proton and deuteron elastic scattering angular distributions have also been obtained and compared with theoretical predictions. The global potentials Chapel-Hill and Koning-Delaroche reproduced really well the proton elastic scattering data. For the deuteron elastic scattering, the global parametrizations were unable to describe the deuteron elastic scattering and an adapted potential with a large diffuseness in the imaginary part (1.90 fm) was required. Further analysis of the deuteron inelastic scattering will be undertaken.

In addition to this, the possible halo configuration of the bound states in ^{17}C has been investigated using a dimensionless scaling law that allows to compare different systems. The results seem to reveal that the first excited state in ^{17}C has a well developed halo configuration.

During this campaign unbound states in ^{17}C were also measured, however the analysis is still ongoing. As predicted by shell model calculations, a significant part of the neutron $0d_{3/2}$ strength is expected to be located above the neutron separation energy in

^{17}C: according to shell model calculations the remaining neutron $0d_{3/2}$ strength is fragmented in three $3/2^+$ expected at 2.90, 4.52 and 6.27 MeV (see figure 2.12). Therefore information regarding the persistence of N = 16 shell closure in the carbon isotopic chain will be obtained in the future from the excitation energy spectrum above the threshold.

Appendices

Appendix A

Electronic diagrams

In this appendix the electronic diagrams describing the electronic employed for each detector involved in the analysis are presented. In the following list, the different labels and abbreviations used in the electronic diagrams that are detailed.

ADC (Amplitude to Digital Converter) this module converts an analog signal to a digital signal.

Dual Gate Generator module introducing a delay and generates a gate.

ECC energy signal provided by EXOGAM clovers.

FAG (Fast Analysis Gate) logic signal that opens a gate when an input is fired and the GMT is ready. It is used to decide if an event is to be accepted by the DAQ.

FIFO (Fan In Fan Out) this module replicates the input in several output signals.

GMT (GANIL Master Trigger) this module memorizes the inputs fired while the FAG is open.

GOCCE energy signal provided by EXOGAM segments.

NIM to ECL converter from NIM to ECL signal format.

QDC (Charge to Digital Converter) this module integrates the current and produces a proportional digital signal.

Quad Coincidence module providing the logical AND of its input signals.

TAC (Time to Amplitude Converter) this produces an output signal proportional in amplitude to the time between a start and a stop signal.

TDC (Time to Digital Converter) module converting a time between a start and a stop signal into a digital signal.

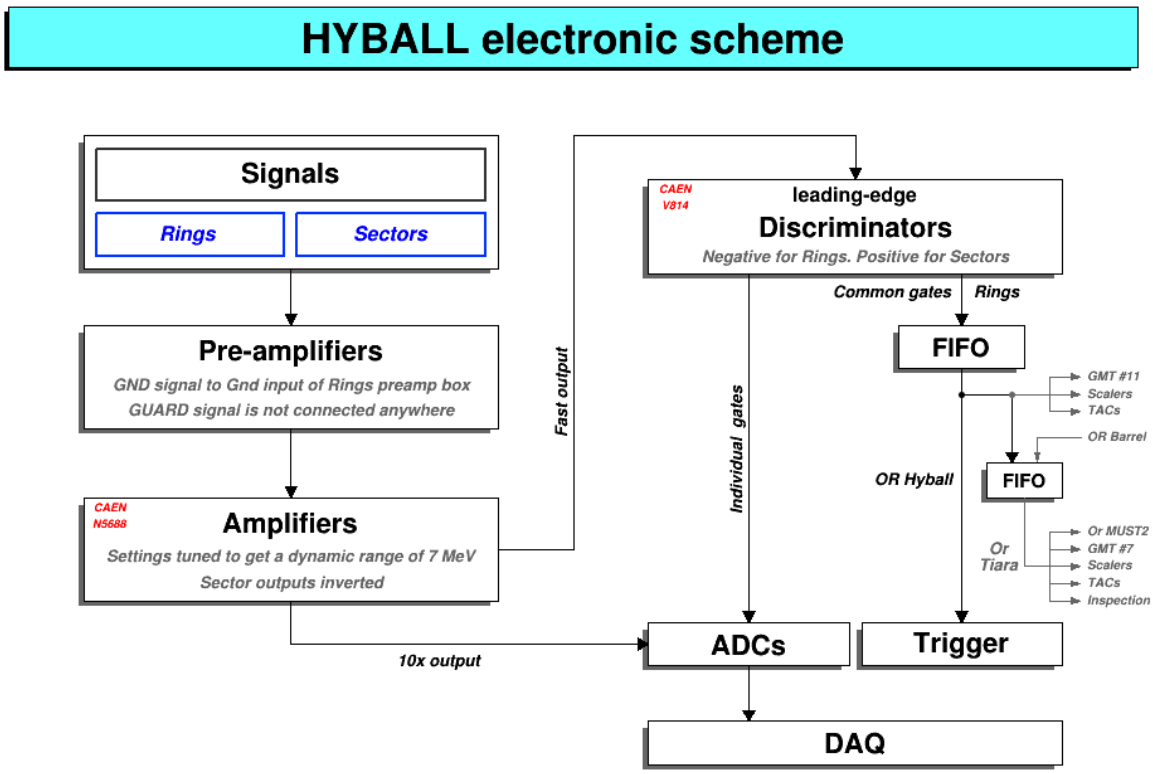

(a) HYBALL electronic scheme

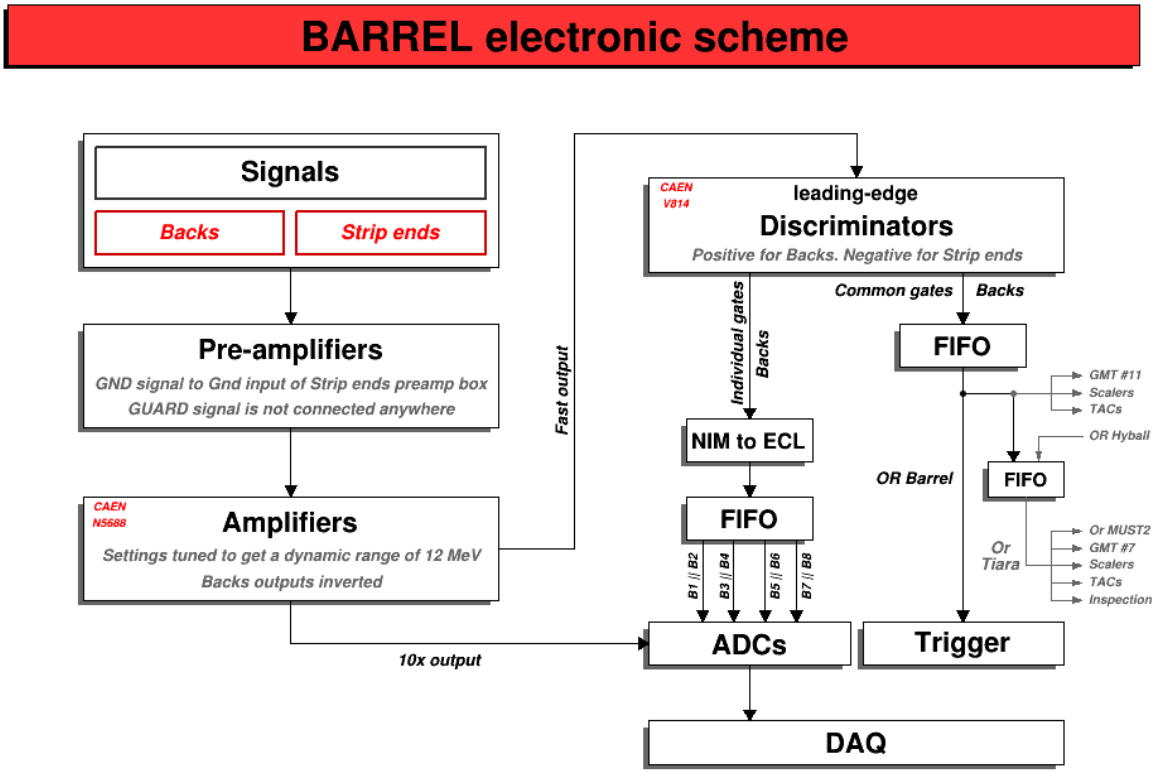

(b) BARREL electronic scheme

Figure A.1: HYBALL and BARREL electronic schemes.

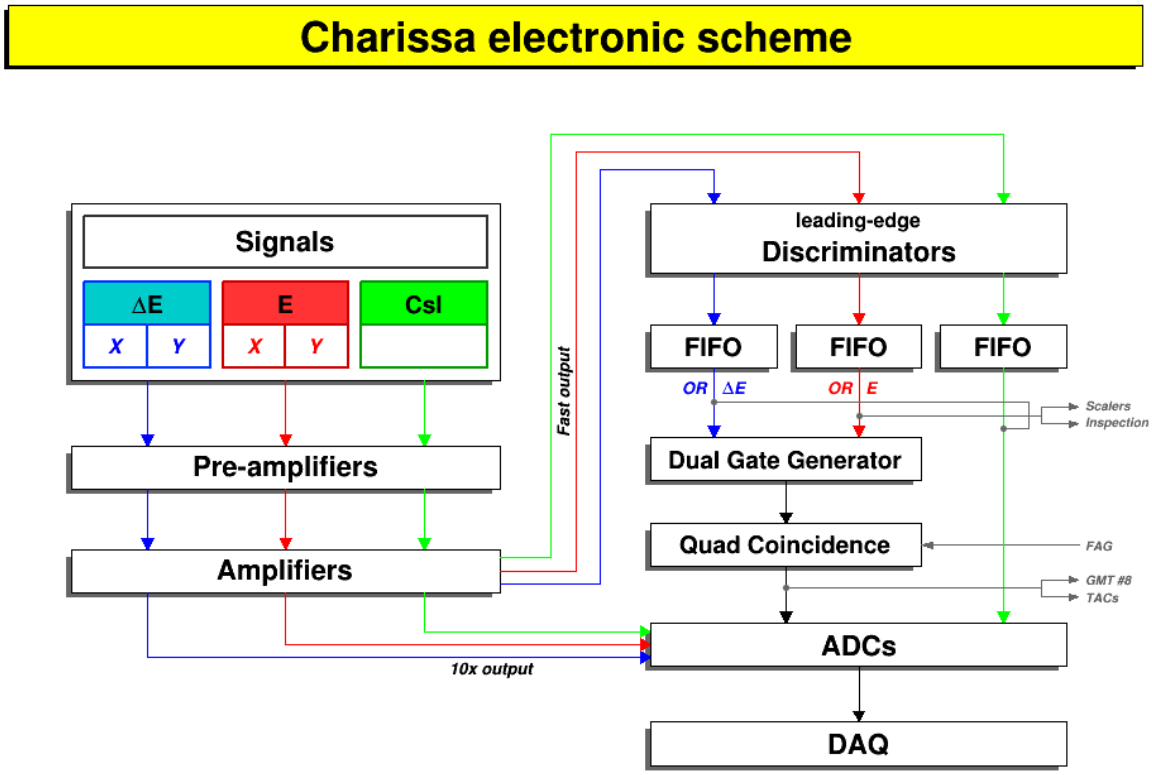

(a) CHARISSA electronic scheme

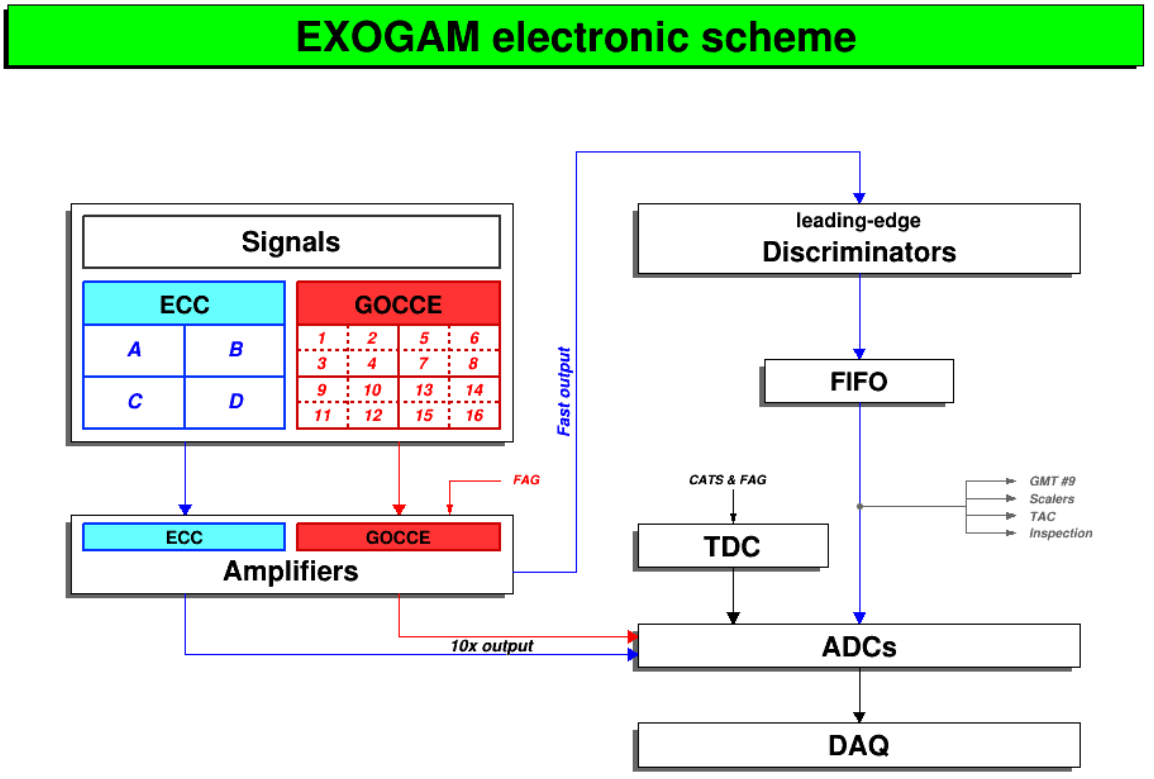

(b) EXOGAM electronic scheme

Figure A.2: CHARISSA and EXOGAM electronic schemes.

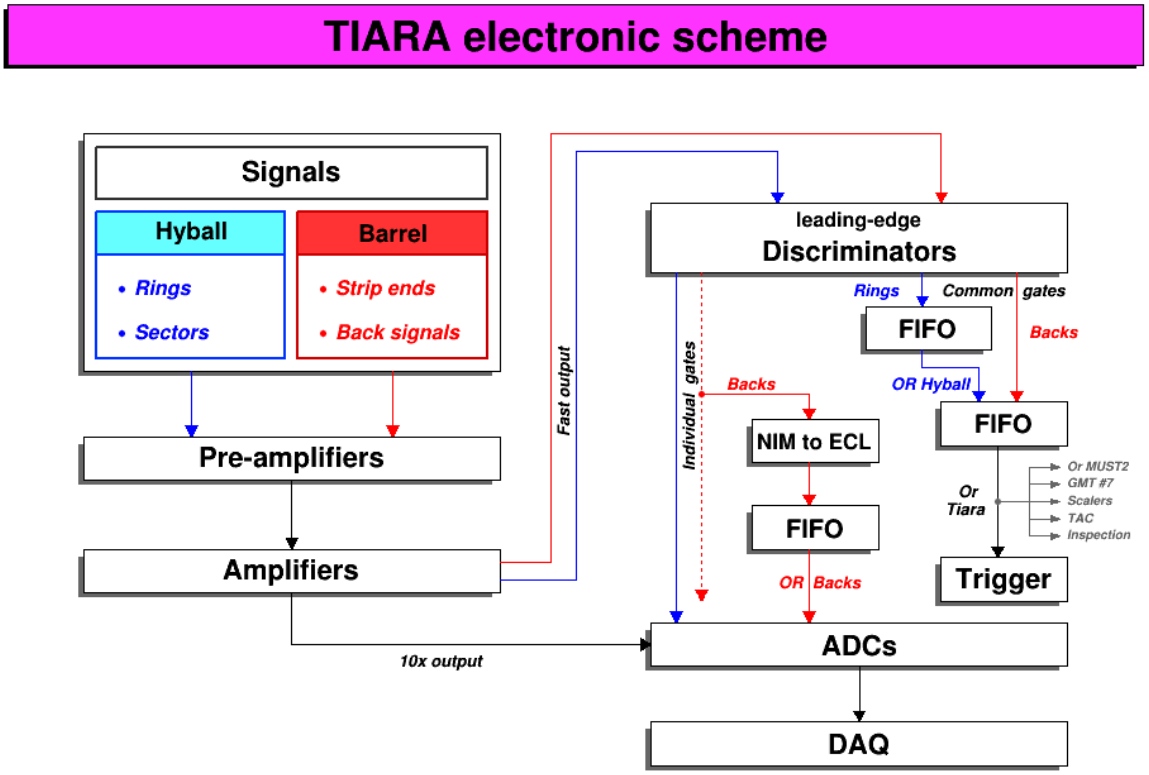

Figure A.3: TIARA electronic scheme.

Appendix B

Simulation

In this section the simulation used to estimate the position resolution and the geometrical efficiency of TIARA (see section 3.4.3) is presented.

GEANT4 [92] is a software toolkit for modelling the passage of particles through matter, based on Monte Carlo simulations. The geometry of the detectors together with the non-active volumes involved in the experimental setup were implemented in order to simulate the response of our experimental setup to the the incoming particles.

In our case, an existing simulation of EXOGAM and TIARA (both Hyball and Barrel) was used for several purposes, including estimations of achievable position resolution and efficiency calculations.

The code does not simulate the beam itself, instead, the events begin at the point of interaction at the target position. In order to take into account the large emittance of the secondary beam, the point of interaction was randomized according the beam distribution obtained with CATS (figure 4.11). Only one reaction channel was simulated at a time.

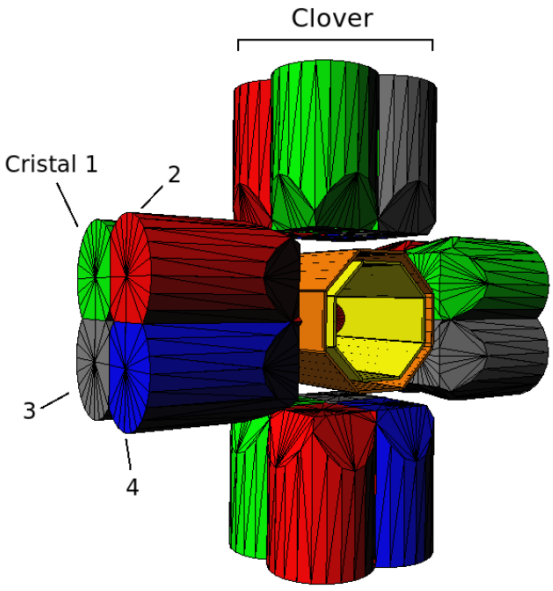

Figure B.1: Visualization of the simulation of four EXOGAM clovers surrounding the Barrel.

B.1 Barrel position resolution

The dependence in energy of the scattering angle resolution provided by the Inner Barrel strips was investigated by comparing the experimental ^{16}C(p,p)^{16}C data with a series of simulations assuming a constant position resolution for the Barrel ranging from 1.5 mm to 5 mm (figure B.2). The elastic scattering of ^{16}C on the CH_2 target (figure 5.1) has been chosen for this purpose instead of the elastic scattering on the CD_2 target (figure 5.3) since it allows a cleaner measurement of the experimental scattering angle resolution due to the absence of deuteron break up.

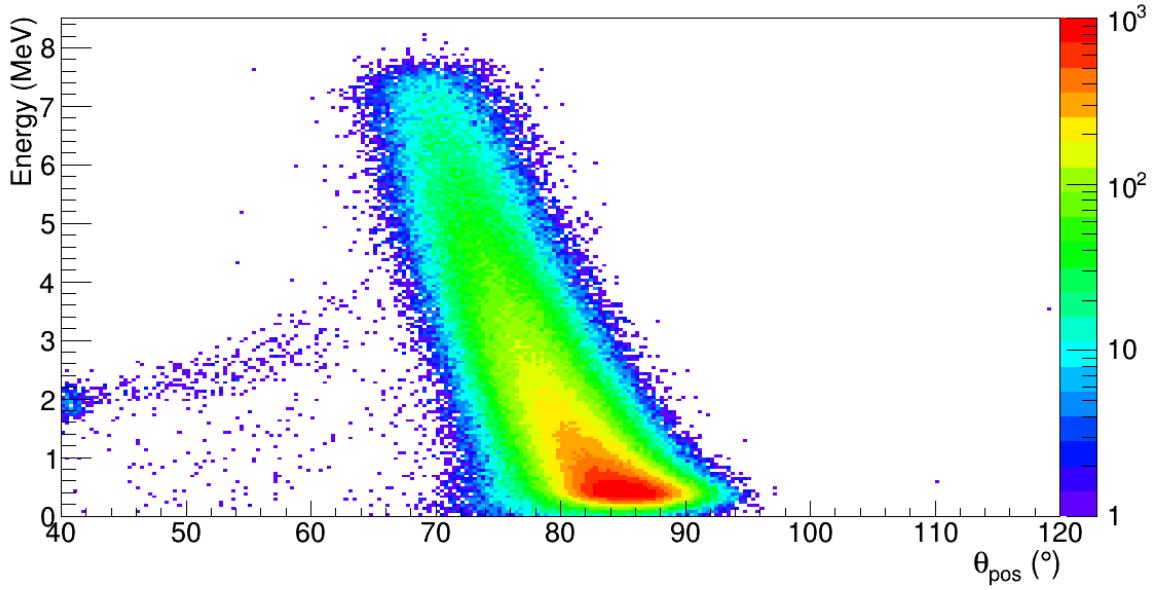

Figure B.2: $^{16}C(p,p)^{16}C$ simulation, assuming a constant position resolution in the Barrel of 1.5 mm.

Slices in energy between 1 and 7 MeV were used to determine the dependence in energy of the Barrel position resolution. For each simulation the scattering angle resolution has been measured at the same energies as for the experimental spectrum in order to find the position resolution required to reproduce the experimental scattering angle resolution.

As shown in figure B.4a, The position resolution at a given energy is the one corresponding to the simulation matching the experimental scattering angle resolution at this energy. The values matching the experiment were fitted to equation B.1 in order to parameterize the scattering angle resolution dependence with the energy (figure B.4b).

$$\sigma_{pos}(E) = \begin{cases} a + \frac{b}{E} & \text{if } E \leq E_0 \\ \\ a + \frac{b}{E_0} & \text{if } E \geq E_0 \end{cases} \tag{B.1}$$

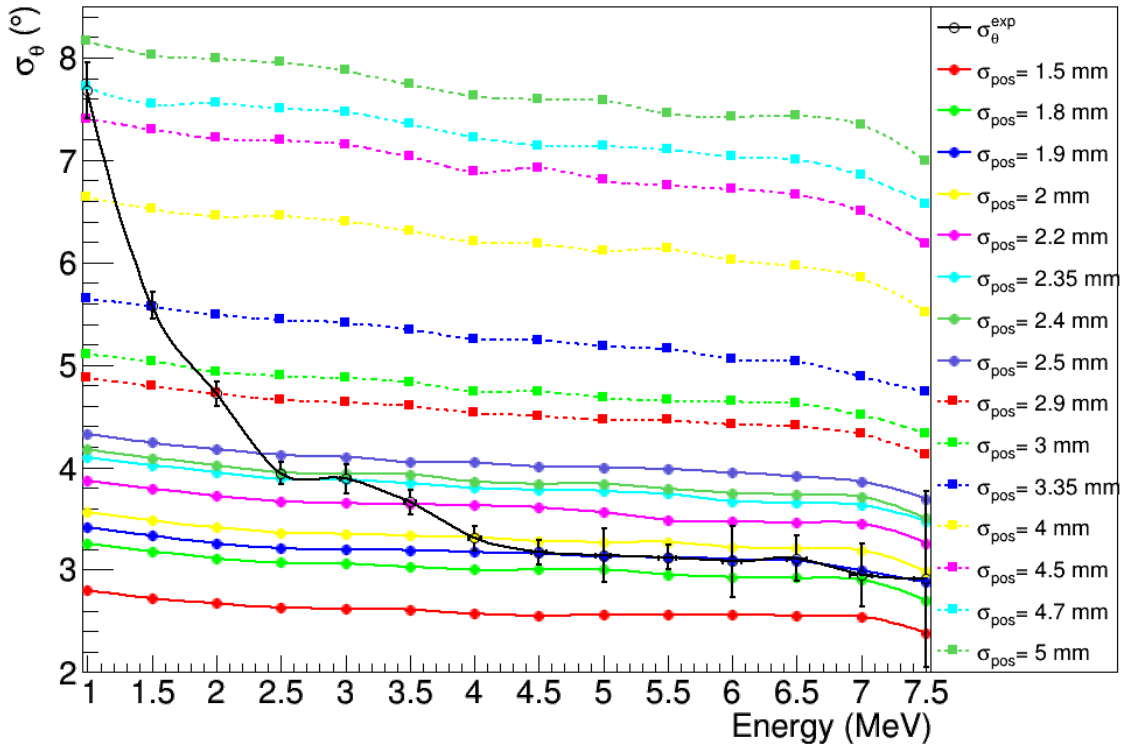

(a) Scattering angle resolution

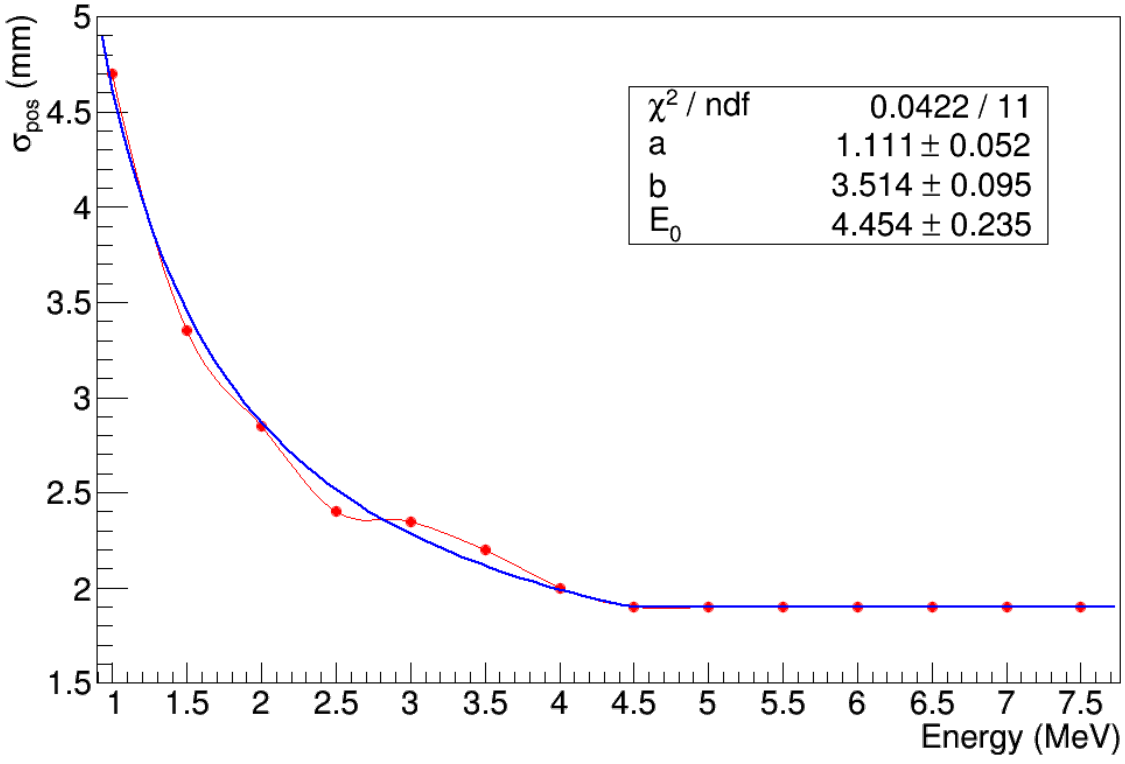

(b) Position resolution

Figure B.3: Energy dependence of the scattering angle resolution provided by the Barrel(a), estimated using the standard deviation for experimental (black) and simulated (colored) data. Position resolution as a function of the energy (b), extracted from (a) and fitted with equation B.1.

B.2 TIARA efficiency

The energy loss by a charged particle in its way through a given material is due to Coulomb scattering. Because the Coulomb interaction has infinite range, the charged particles interact with many electrons at the same time and thus lose energy continuously along their path through the medium in which they are travelling, until they are stopped or have crossed the material. Therefore, the intrinsic efficiency for charged particle detection is close to 100 % and hence, TIARA efficiency calculation is merely reduced to a geometric calculation of the detector angular coverage.

In order to perform a numerical integration of the solid angle covered by TIARA, charged particles were launched isotropically using the optimized simulation described previously. The beam interaction point on target was taken into account by randomizing its position following its experimental distribution obtained with CATS (figure 4.11). The effect of the incident angle of the incoming ions measured with CATS has also been included.

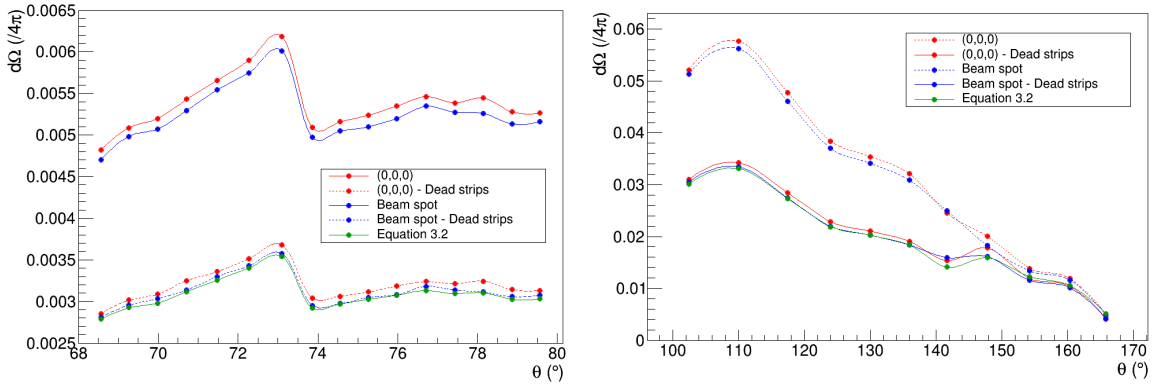

(a) Elastic angular bins *(b) (d,p) angular bins*

Figure B.4: Solid angle calculation for the angular bins that are used for the elastic (a) and the (d,p) angular distributions (b). The calculations presented in red are done assuming the beam interaction point on target is always at (0,0,0), in blue however the beam interaction point on target follows the distribution provided by CATS (figure 4.11). Results obtained with equation B.2 are shown in green. The dashed lines show the calculation for the whole Barrel/Hyball, while the continuous line represent the same results taking into account the missing channels.

The same procedure of numerical integration has been performed for the different angular bins that will be used later to extract the angular distributions, and the resulting solid angle for each angular bin is compared to the corresponding solid angle calculated with the equation:

$$\Delta\Omega = 2\pi(cos\theta_l - cos\theta_u)\epsilon \tag{B.2}$$

where θ_u and θ_l are the the upper and lower limits of each angular bin, and ϵ is the detection efficiency.

B.3 Exogam simulations

These simulations will be used later to obtain the yield corresponding to each γ-line needed to extract the angular distributions of the protons leading to the bound excited states in ^{17}C. For that purpose, the response function of EXOGAM γ-ray for γ-rays of 217 keV and 335 keV corresponding to the bound states in ^{17}C was simulated, including addback and Doppler corrections.

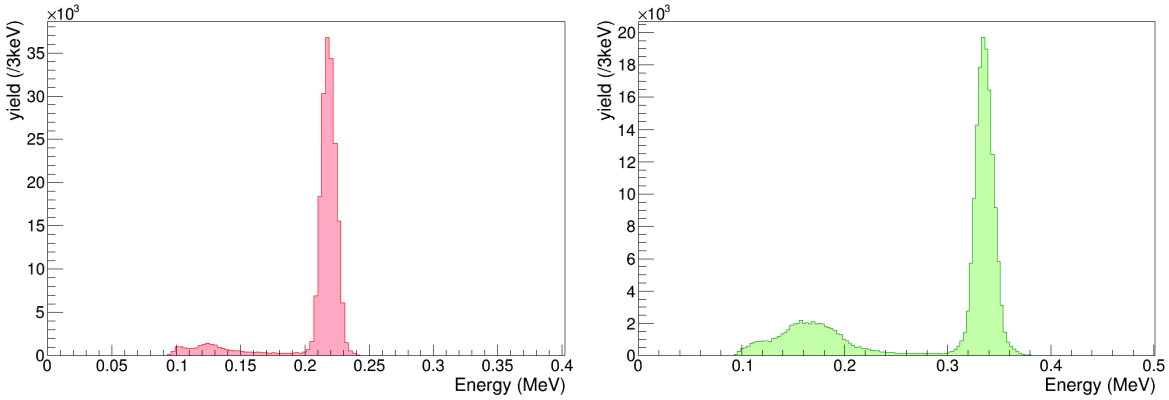

(a) $E_\gamma = 217\ keV$ *(b)* $E_\gamma = 335\ keV$

Figure B.5: Simulated EXOGAM response function for γ-rays of (a) 217 keV and (b) 335 keV rising from the ^{17}C bound states. The energy of the γ-ray is provided by the mean value of a Gaussian fit on the corresponding γ-line in the experimental γ-spectrum. EXOGAM resolution is set to 1.1 and 1.3 keV respectively also from experimental data.

Appendix C

Optical Models

The phenomenological optical model potential for nucleus-nucleon scattering is described as:

$$U = -V_V - iW_V - iW_S + V_{so} + iW_{so} + V_C \tag{C.1}$$

where the subindexes V, S, so and C refer to the volume, surface, spin-orbit and coulomb components of the potential respectively. This components are complex numbers, being V the real part and W the imaginary part. All the components have a potential well energy dependent while the geometry of the potential depends on the nucleus considered and is usually assessed with a Woods-Saxon function.

C.1 Global parametrizations

The optical model parameters have been phenomenologically investigated many times using different experimental data sets that led to different global parameterizations. Therefore, the applicability of these global optical models depends on the mass region and the energy range covered by the data of the on which they are based.

The purpose of this section is to provide basic information on the data sets considered for the construction of the phenomenological optical model potentials employed in this work.

Chapel-Hill [70] parametrization of the nucleon-nucleus optical potential for proton and neutrons suitable for nuclei in the mass region $40 \leq A \leq 209$, proton energies between 16 and 65 MeV and neutron energies from 10 to 26 MeV.

Koning-Delaroche [71] global parameterization of the optical model potential for protons and neutrons based on experimental data of spherical and near-spherical nuclei with $24 \leq A \leq 209$ and incident energies from 1 keV to 200 MeV.

Daehnick [73] global optical model potential for deuteron-nucleus scattering obtained from experimental data from targets between ^{27}Al and ^{238}Th at energies ranging from 11.8 to 90 MeV.

Haixia [74] global optical model potential intended to describe deuteron scattering obtained from a data set including targets ranging in mass from ^{12}C to ^{238}U at incident energies below 183 MeV.

Bojowald [75] phenomenological optical model potential based on experimental data of deuteron elastic scattering on ^{27}Al, ^{89}Y, ^{120}Sn and ^{208}Pb at 58.7 and 85 MeV.

C.2 Optical potential parameters

	parameter		^{16}C + p		^{16}C + n		^{16}C + d			
			CH89	KD02	CH89	KD02	Bojowald	Daehnick	Haixia	Haixia*
Volume	V	(MeV)	52.0306	54.4690	44.524	43.685	76.536	81.6514	85.0180	85.0180
	r_0	(fm)	1.1607	1.1430	1.1607	1.1430	1.1800	1.1700	1.1490	1.1700
	a_0	(fm)	0.6900	0.6750	0.6900	0.6750	0.7240	0.7675	0.7510	0.9000
	W_0	(MeV)	1.6428	1.5150	1.9170	1.5230		1.4614	3.2260	3.2260
	r_0^w	(fm)	1.1633	1.1430	1.1633	1.1430		1.3250	1.3450	1.2000
	a_0^w	(fm)	0.6900	0.6750	0.6900	0.6750		0.6917	0.6030	1.7000
Surface	W_S	(MeV)	9.3566	9.5520	3.4390	5.5820	10.4210	11.6330	9.7860	9.7860
	r_S	(fm)	1.1633	1.3020	1.1633	1.3020	1.2700	1.3250	1.3940	1.3940
	a_S	(fm)	0.6900	0.5270	0.6900	0.5420	0.8210	0.6917	0.6870	0.6870
Spin-orbit	V_{so}	(MeV)	5.9000	5.3970	5.9000	5.3390	3.0000	3.1662	1.7790	1.7790
	r_{so}	(fm)	0.8638	0.9290	0.8638	0.9290	0.8760	1.0700	0.9720	0.9720
	a_{so}	(fm)	0.6300	0.5900	0.6300	0.5900	0.8760	0.6600	1.0110	1.0110
	W_{so}	(MeV)		-0.0750		-0.0930				
	r_{so}^w	(fm)		0.9290		0.9290				
	a_{so}^w	(fm)		0.5900		0.5900				

Table C.1: Optical potential parameters utilized in this work.

Appendix D

Resumo en galego

D.1 Motivación

En 1934 W. Elsasser amosou as primeiras evidencias da existencia dunha serie de números especiais de neutróns e protóns que confiren ao núcleo correspondente unha configuración particularmente estábel. Analogamente ao caso dos electróns atómicos, estes números asociáronse con capas pechadas dun modelo de partículas independentes ocupando niveis de enerxía xenerados por un pozo de potencial.

Ata fai moi pouco pensábase que estes números máxicos eran unha constante permanente na natureza, sen embargo, os recentes progresos tecnolóxicos e as novas instalacións de feixes de ións radioactivos permitiron estudar núcleos afastados do val da estabilidade (con ratios N/Z relativamente grandes), observando que os tradicionais números máxicos desaparecen e aparecen outros novos no seu lugar cando nos achegamos á drip line.

En particular, a desaparición do número máxico N=20 e a aparición dos novos números máxicos N=16 e N=14 foi observada en isotopos de osíxeno ricos en neutróns [27]. O principal obxectivo deste experimento é estudar a presenza destes novos números máxicos en isotopos de carbono ricos en neutróns localizando as enerxías de partícula independente dos orbitais $d_{5/2}$, $s_{1/2}$ e $d_{3/2}$ no ^{17}C a través da reacción de transferenza ^{16}C(d,p)^{17}C.

O estado fundamental do ^{17}C ten unha configuración $3/2^+$, mentres dous estados excitados foron observados a 217 keV e 335 keV, aos que se lles asignou espín e paridade $1/2^+$ e $5/2^+$ respectivamente [29]. Varios estados non ligados foron medidos, aínda que ningún puido ser identificado como $d_{3/2}$ pois non existen medidas directas de espín e paridade.

D.2 Dispositivo experimental

Neste experimento, os estados do ^{17}C foron poboados pola reacción de transferenza ^{16}C(d,p)^{17}C inducida bombardeando un branco de polietileno deuterano (CD_2) de 1.36 mg/cm^2 de espesor cun feixe de ^{16}C a 17.2 MeV/A e cunha intensidade de $5{\cdot}10^4$ pps, entregado polo espectrómetro LISE3 en GANIL. Antes de chegar ao branco, o feixe é monitorizado por dous detectores CATS co obxectivo de determinar o punto de impacto das partículas do feixe no branco e o seu ángulo de incidencia.

O array de detectores de silicio de alta eficiencia TIARA foi empregado para detectar partículas lixeiras a ángulos de laboratorio entre 36º e 169º, medindo a enerxía e o ángulo xa que ambos observabeis son necesarios para calcular a enerxía de excitación e obter distribucións angulares. As partículas lixeiras emitidas cara diante son detectadas en catro telescopios Si-CsI MUST2.

Catro detectores de xermanio hiperpuro EXOGAM son situados a 90º arredor do branco para medir os raios-γ emitidos polos estados ligados dos produtos da reacción. O telescopio Si-Si-CsI CHARISSA a 0º grados para identificar os fragmentos pesados medindo a enerxía, a perda de enerxía, o tempo de voo e o ángulo de dispersión.

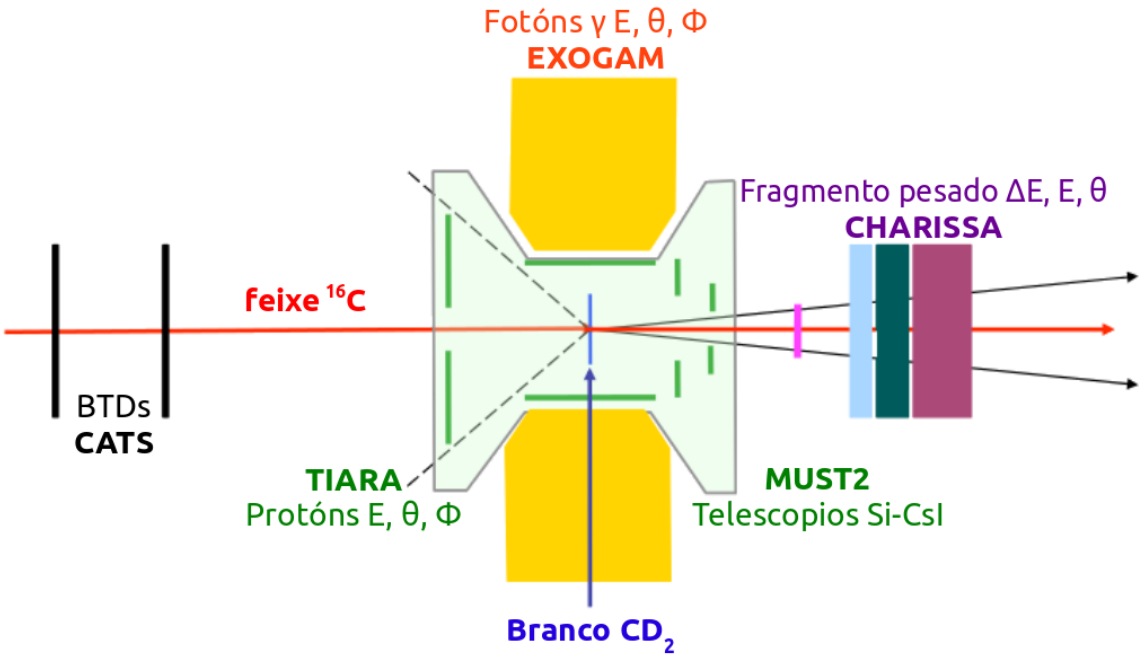

Figure D.1: Representación esquemática do dispositivo experimental.

Este dispositivo experimental permite realizar triple coincidencias evento por evento requirindo unha partícula lixeira, un fragmento pesado e un raios-γ.

D.3 Dispersión elástica

Distribucións angulares para a dispersión elástica do ^{16}C en protóns e deuteróns foron extraídas e comparadas con predicción teóricas. Os potenciais globais Chapel-Hill e Koning-Delaroche reproducen realmente ben a dispersión elástica en protóns (figura D.2a). Por outra banda, as parametrizacións globais de Bojowald, Daehnick e Haixia son incapaces de describir a dispersión elástica en deuteróns e un potencial adaptado, cunha difusividade na parte imaxinaria de 1.9 fm, foi necesario (figura D.2c).

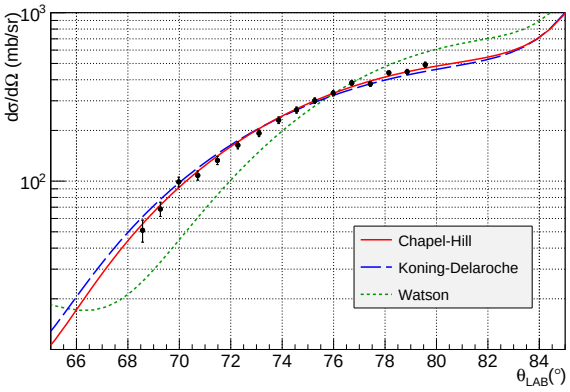

(a) Dispersión elástica do ^{16}C en protóns comparada cos potenciais globais de Chapel-Hill e Koning-Delaroche.

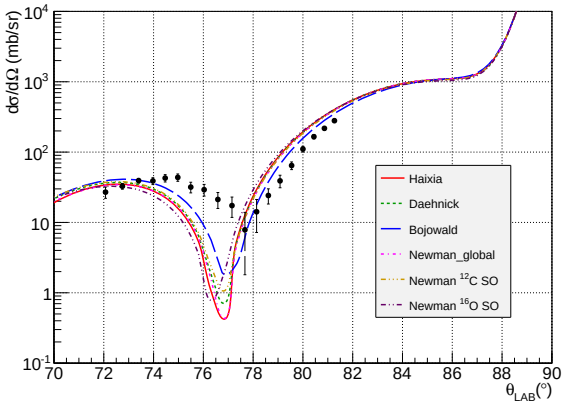

(b) Dispersión elástica do ^{16}C en deuteróns comparada cos diferentes potenciais globais, entre eles os de Daehnick, Bojowald e Haixia.

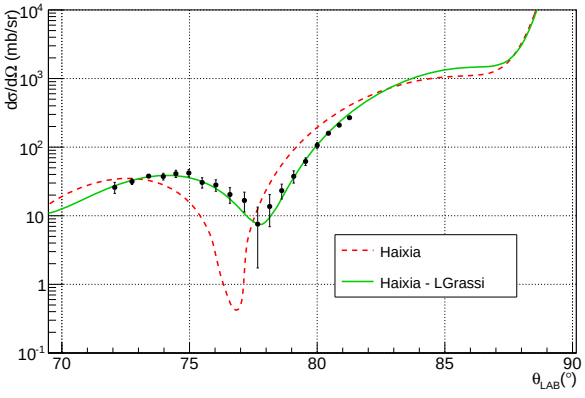

(c) Dispersión elástica do ^{16}C en deuteróns comparada cun potencial axustado aos datos experimentais, cunha difusividade na parte imaxinaria de a = 1.9 fm.

Figure D.2: Distribucións angulares da dispersión elástica do ^{16}C en protóns (a) e deuteróns (b,c), comparadas con potencias globais (a,b) e un potencial local (c).

D.4 Analise da reaccion ^{16}C(d,p)^{17}C

Dous estados excitados foron observados no ^{17}C a 217 e 335 keV e as correspondentes distribucións angulares foron extraídas, producindo unha asignación limpa e clara de espín e paridade $1/2^+$ para o primeiro estado excitado (figura D.3a) e unha medida directa do momento angular tranferido de $\ell = 2$ para o segundo estado excitado (figura D.3b), en bo acordo con medidas anteriores. Da distribución angular experimental do estado fundamental dedúcese un momento angular transferido de $\ell = 2$, en liña coa ben estabrecida asignación de espín e paridade $3/2^+$ (figura D.3c).

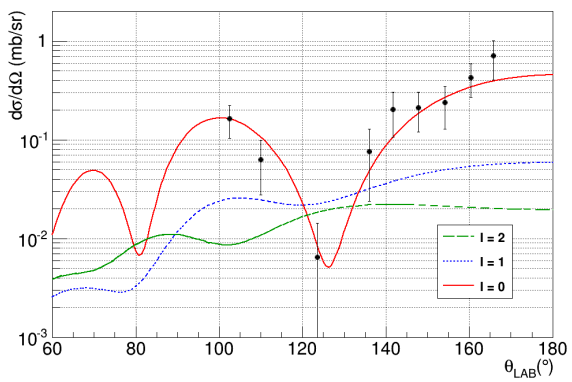

(a) Primeiro estado excitado a 217 keV

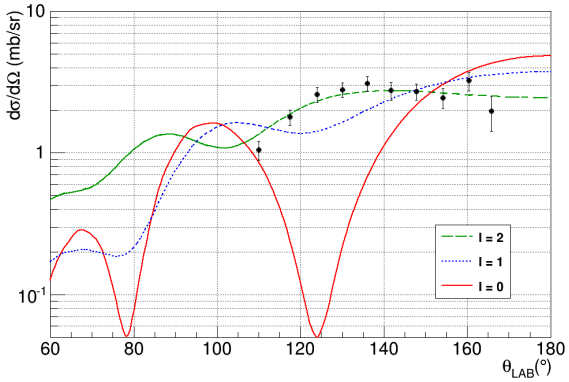

(b) Segundo estado excitado a 335 keV

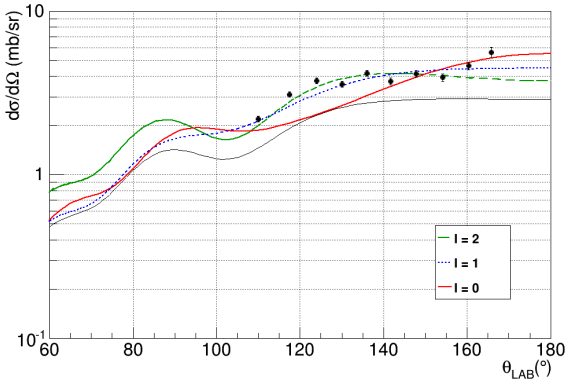

(c) Estado fundamental

Figure D.3: Distribucións angulares do primeiro (a) e segundo (b) estado excitado e do estado fundamental (c) do ^{17}C.

A orde dos estados ligados do ^{17}C é mellor reproducido pola interacción SFO-tls, mentres as interaccións WBP e WBT coinciden co espectro experimental dentro das desviación estandar dos cálculos do modelo de capas (figura D.4).

Por primeira vez, os factores espectroscópicos foron medidos para os estados ligados do ^{17}C. Os grandes factores espectroscópicos de 0.67 e 0.63 foron medidos para o primeiro e o segundo estado excitado empregando o potencial óptico Koning-Delaroche (pequenas variacións foron atopadas para o primeiro estado excitado cando se empregou

o potencial óptico Chapel-Hill), indicando a súa natureza de partícula independente. Un moi bo acordo foi observado coas predicións teóricas para ambos estados. Sen embargo, para o estado fundamental o factor espectroscópico preliminar (0.52) é unha orde de magnitude maior que o esperado polos cálculos do modelo de capas (0.03). Isto indica a existenza dunha forte contribución $d_{3/2}\otimes^{16}\mathrm{C}(0^+)$ no estado fundamental do ^{17}C que semella ser subestimada polos cálculos do modelo de capas.

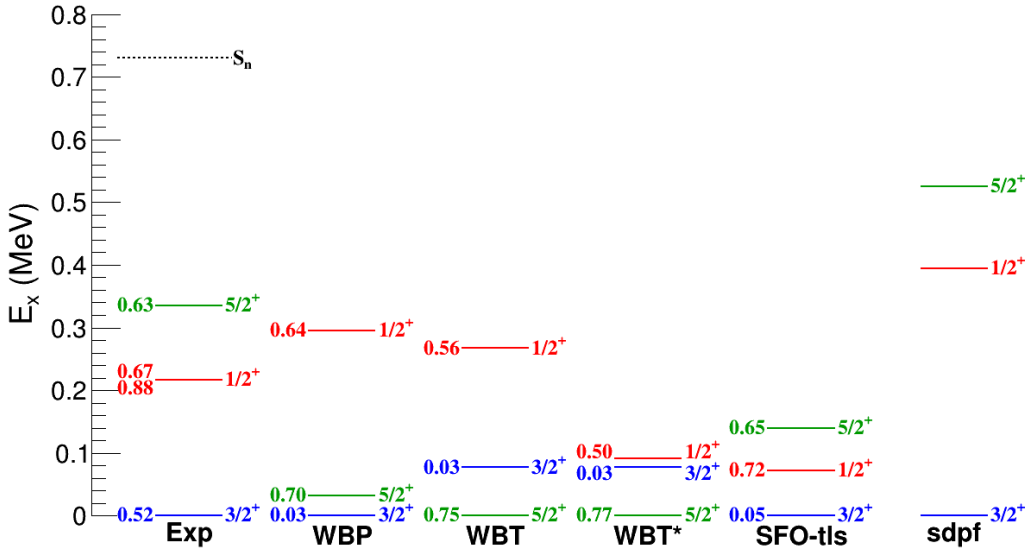

Figure D.4: Esquema de niveis experimental do ^{17}C, xunto con predicción teóricas empregando as interaccións WBP, WBT, WBT e sdpf.*

D.5 Halos nos estados ligados do ^{17}C

O primeiro estado excitado no ^{17}C foi suxerido como candidato a amosar halo debido a súa feble enerxía de separación e a súa configuración $\ell = 0$. Co propósito de estudar esta posibilidade, empregouse a lei de escala adimensional desenvolvida por K. Riisager para halos de 2 corpos [91].

Á vista dos resultados amosados na figura D.5, semella que o primeiro estado excitado do ^{17}C amosa un halo ben formado, comparable co ^{11}Be. Esta conclusión segue a tendencia observada nos isotopos de carbono ricos en neutróns e de masa impar: todos eles amosan un halo de un neutrón no orbital $s_{1/2}$ [39; 40].

Por outra banda, o estado fundamental e o segundo estado excitado do ^{17}C non presentan halo, a pesar da súa baixa enerxía de separación. Ter o neutrón de valencia poboando un orbital cun momento angular ℓ relativamente grande da lugar a un aumento da barreira centrífuga que confina moito máis a distribución de masa do núcleo e dificulta a formación de halos.

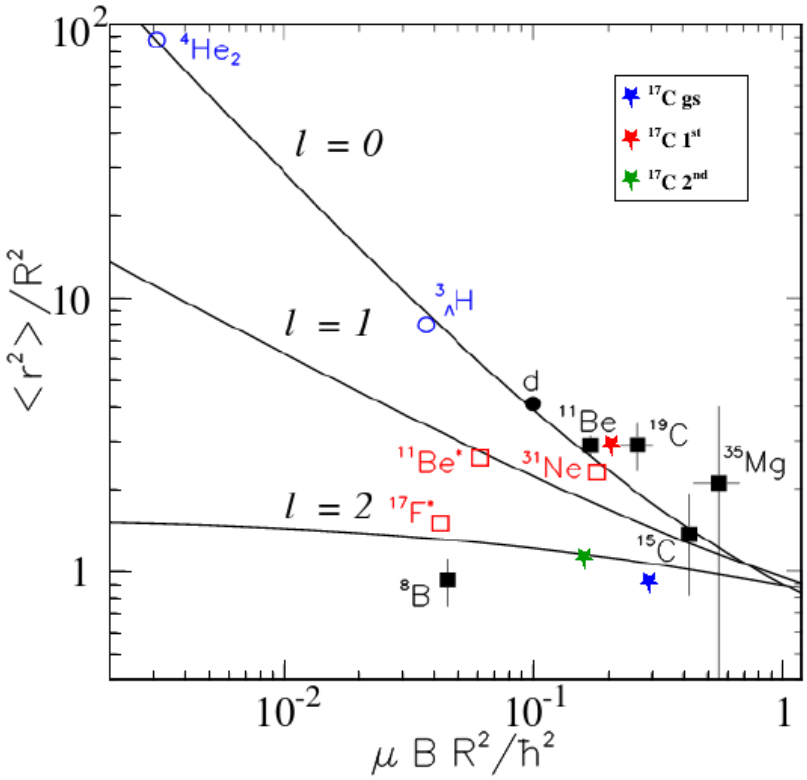

Figure D.5: Lei de escala adimensional definida por K. Riisager para halos de dous corpos. O puntos negro representa o deuteron, círculos azuis e cadrados vermellos baleiros indican modelizacións e cálculos teóricos, mentres cadrados negros baleiros son deducidos de datos experimentais. As estrelas azul, vermella e verde representan o estado fundamental e o primeiro e segundo estado excitado no ^{17}C (Adaptada de [91])

Appendix E

Résumé en français

E.1 Motivation

En 1934, W. Elsasser présenta les premières indications de l'existence d'une série de nombres spéciaux de neutrons et protons dits *nombres magiques* qui confèrent aux noyaux correspondants une configuration particulièrement stable. Par analogie avec le cas des électrons atomiques, ces nombres ont été associés à des couches fermées dans un modèle à particules indépendantes occupant les niveaux d'énergie produits par un puits de potentiel.

Jusqu'à récemment, on pensait que ces nombres magiques étaient une constante de la nature, cependant, l'avènement d'installations de faisceaux d'ions radioactifs a permis l'étude des noyaux éloignés de la vallée de stabilité (avec des rapports N/Z relativement élevés). Ces études indiquent que les nombres magiques traditionnels disparaissent et de nouvelles fermetures de couches apparaissent quand on s'approche de la limite d'existence des noyaux, appelée *drip line*.

En particulier, la disparition du nombre magique N=20 et l'apparition des nouveaux nombres magiques N=16 et N=14 ont été observées dans les isotopes d'oxygène riches en neutrons [27]. L'objectif principal de cette expérience est d'étudier la présence éventuelle de ces nouveaux nombres magiques dans les isotopes de carbone riches en neutrons en localisant les orbitales de neutron $0d_{5/2}$, $1s_{1/2}$ et $0d_{3/2}$ dans le ^{17}C à l'aide de la réaction de transfert ^{16}C(d,p)^{17}C.

L'état fondamental du ^{17}C a une configuration $3/2^+$, alors que deux états excités ont été observés à 217 keV et 335 keV, auxquels ont été attribués des spins et parités $1/2^+$ et $5/2^+$ respectivement [29]. Plusieurs états non liés ont été mis en évidence, bien qu'aucun n'ait pu être identifié comme correspondant à une configuration de neutron $0d_{3/2}$ car il n'existe aucune mesure directe de spin et parité.

E.2 Dispositif expérimental

Dans cette expérience, les états du ^{17}C ont été peuplés par la réaction de transfert ^{16}C(d,p)^{17}C induite en bombardant une cible de polyéthylène deuteré (CD_2) de 1.36 mg/cm^2 d'épaisseur avec un faisceau de ^{16}C d'énergie 17.2 MeV/A et d'intensité 5·10^4 pps, produit par le spectromètre LISE3 du GANIL. En amont de la cible, le faisceau était monitoré par deux détecteurs CATS avec l'objectif de déterminer le point d'interaction des particules du faisceau avec la cible et leur angle d'incidence.

Le détecteur silicium de haute efficacité TIARA a été utilisé pour détecter les particules légères à des angles entre 36° et 169° dans le laboratoire, et mesurer leur énergie et leur angle de diffusion, puisque les deux mesures sont nécessaires pour calculer l'énergie d'excitation et construire les distributions angulaires. Les particules légères émises à l'avant ont été détectés par quatre télescopes Si-CsI MUST2.

Quatre détecteurs germanium hyper pur EXOGAM étaient placés à 90° autour de la cible pour mesurer les photons γ émis par les états liés des produits de la réaction. Un télescope Si-Si-CsI CHARISSA a été placé à 0° degré pour identifier les fragments lourds et mesurer l'énergie, la perte d'énergie, le temps de vol et l'angle d'émission.

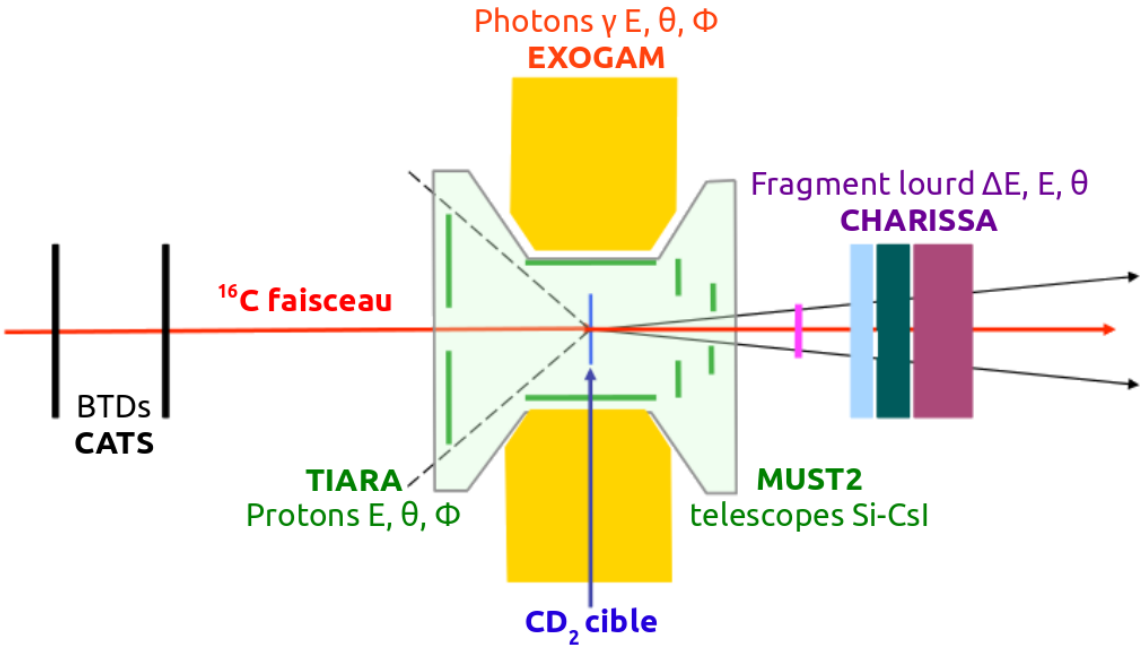

Figure E.1: Representation schématique du dispositif expérimental.

Ce dispositif expérimental permet de réaliser des coïncidences triples événement par événement en requérant une particule légère, un fragment lourd et un photon γ.

E.3 Diffusion élastique

Les distributions angulaires de la diffusion élastique du ^{16}C sur proton et sur deuton ont été extraites et comparées avec les prédictions théoriques obtenues par des calculs de type modèle optique. Les potentiels globaux Chapel-Hill et Koning-Delaroche reproduisent très bien la diffusion élastique sur proton (figure E.2a). En revanche, les paramétrisations globales de Bojowald, Daehnick, Haixia et Newman sont incapables de décrire la diffusion élastique sur deuton et un potentiel adapté, avec notamment une diffusivité de la partie imaginaire de 1,9 fm, est nécessaire (figures E.2b et E.2c).

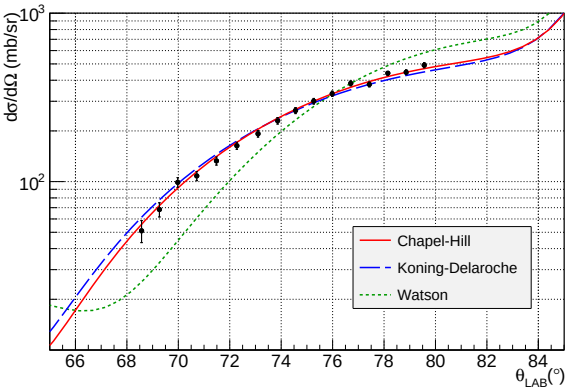

(a) Diffusion élastique du ^{16}C sur proton comparée avec les potentiels globaux de Chapel-Hill et Koning-Delaroche.

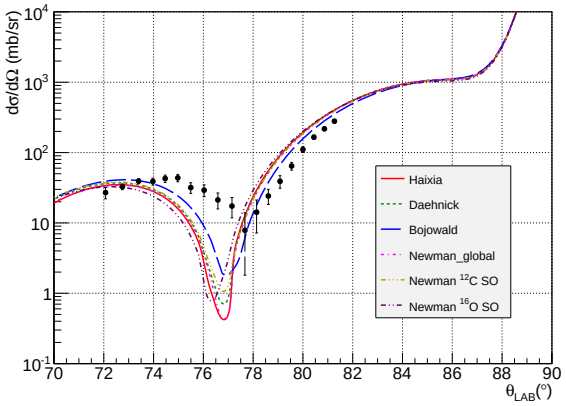

(b) Diffusion élastique du ^{16}C sur deutons comparée avec différents potentiels globaux, parmi lesquels ceux de Daehnick, Bojowald et Haixia.

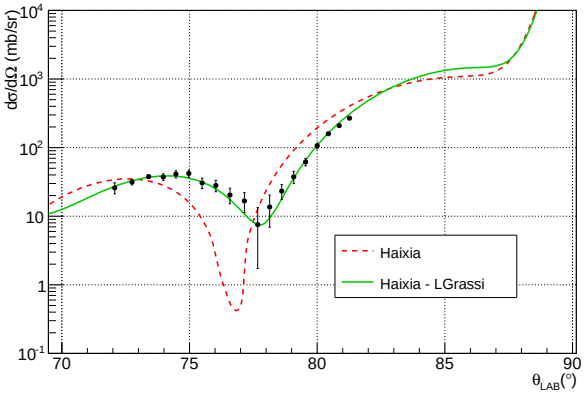

(c) Diffusion élastique du ^{16}C sur deutons comparée avec un potentiel adapté au ^{16}C, avec une diffusivité de la partie imaginaire de 1,9 fm [77].

Figure E.2: Distributions angulaires de diffusion élastique du ^{16}C sur proton (a) et sur deuton (b,c), comparées à des calculs utilisant des potentiels globaux (a,b) et un potentiel adapté (c).

E.4 Analyse de la réaction ^{16}C(d,p)^{17}C

Les distributions angulaires ont été comparées à des calculs théoriques réalisés dans l'approximation de l'onde distordue adiabatique (ADWA) afin de prendre en compte l'effet de la cassure du deuton sur le transfert.

Deux états excités ont été observés dans le ^{17}C à des énergies d'excitation de 217 et 335 keV, et les distributions angulaires correspondants ont été extraites, produisant une identification non ambiguë de spin parité $1/2^+$ pour le premier état excité (figure E.3a) et une mesure directe du moment angulaire transféré de $\ell = 2$ pour le deuxième état excité (figure E.3b), en accord avec études précédentes. De la distribution angulaire expérimentale de l'état fondamental est déduit un moment angulaire transféré de $\ell = 2$, en accord avec les valeurs de spin et parité $3/2^+$ bien établies (figure E.3c).

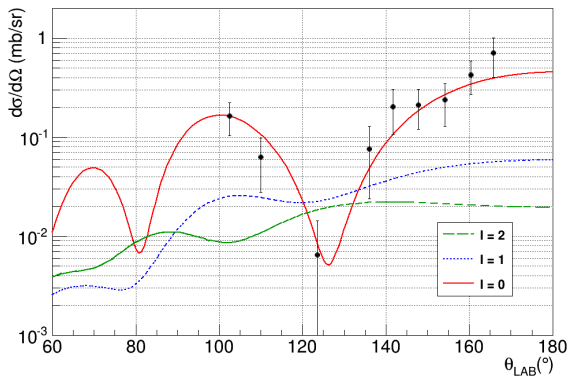

(a) Premier état excité à 217 keV

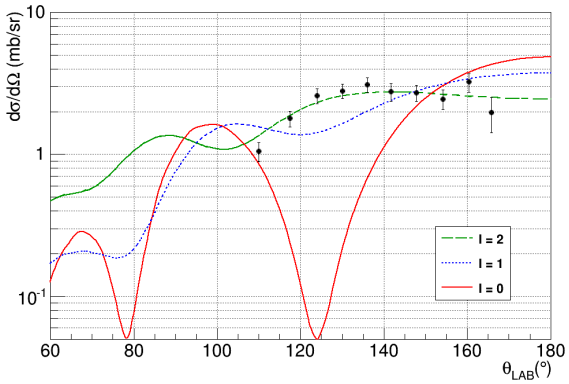

(b) Deuxième état excité à 335 keV

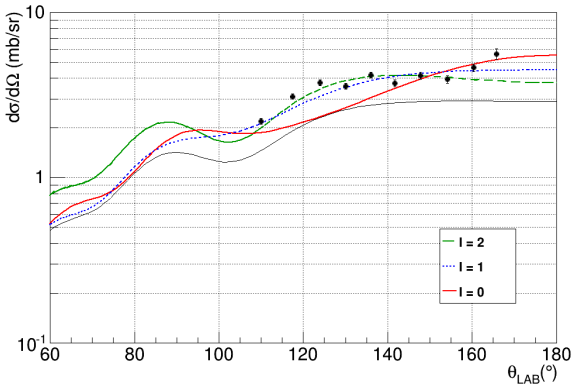

(c) État fondamental. Le courbe noire représente la somme des sections efficaces des états excités.

Figure E.3: Distributions angulaires des premier (a) et deuxième (b) états excités et de l'état fondamental (c) du ^{17}C.

Les énergies des états liés du ^{17}C ont été comparées à des résultats de calculs de type modèle en couches. L'ordre des états est mieux reproduit par l'interaction SFO-tls, alors que les interactions WBP et WBT produisent un spectre en accord avec le spectre expérimental dans la limite de la déviation standard des calculs du modèle en couches (figure E.4).

Pour première fois, les facteurs spectroscopiques ont été mesurés pour les états liés du ^{17}C. Des facteurs spectroscopiques relativement élevés ont été trouvés pour le premier (0.67) et le deuxième état excité (0.63) en utilisant la paramétrisation de Koning-Delaroche, indiquant un caractère de particule indépendante marqué. Le facteur spectroscopique du premier état excité apparaît comme plus sensible au choix de la paramétrisation du potentiel optique. Un très bon accord a été observé avec les prédictions théoriques pour les deux états excités. Par contre, pour l'état fondamental le facteur spectroscopique préliminaire (0.52) est un ordre de grandeur plus grand que celui prédit par les calculs du modèle en couches (0.03). Ce fait indique l'existence d'une forte composante $0d_{3/2}\otimes^{16}\mathrm{C}(0^+)$ dans l'état fondamental du ^{17}C qui paraît nettement sous-estimé par les calculs du modèle en couches.

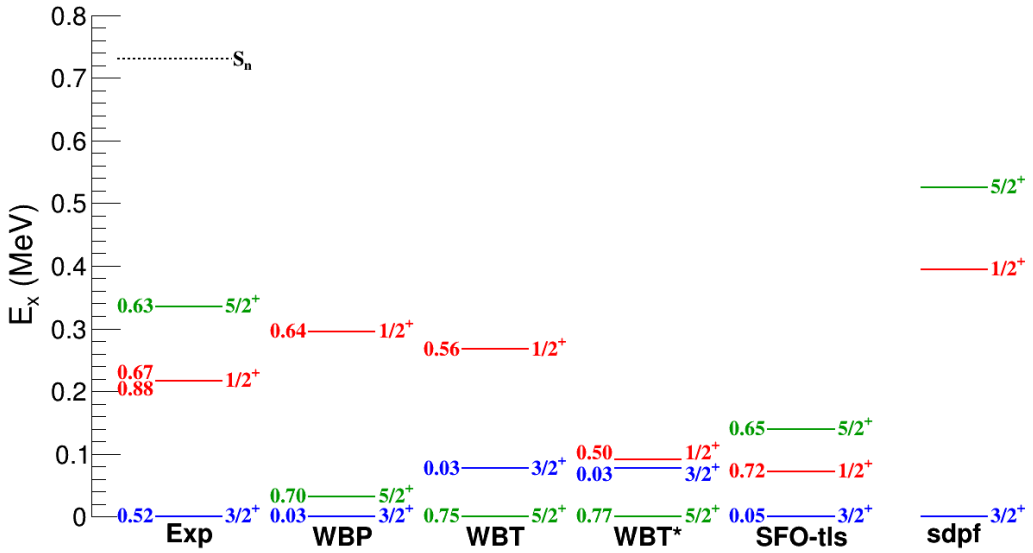

Figure E.4: Schéma de niveaux expérimental du ^{17}C, avec les prédictions théoriques utilisant les interactions WBP, WBT, WBT et sdpf. Les nombres à gauche des états indiquent les facteurs spectroscopiques*

E.5 Possibilité de halos dans les états du ^{17}C

Le premier état excité du ^{17}C a été suggéré comme candidat à l'apparition d'un halo à cause de sa faible énergie de séparation et sa configuration $\ell = 0$. Avec l'intention d'étudier cette possibilité, nous avons appliqué la loi d'échelle proposé par K. Riisager pour les halos d'un neutron ou d'un proton [91].

À la lumière des résultats présentes sur la figure E.5, il apparaît que le premier état excité du ^{17}C présente un halo bien développe, comparable à celui du ^{11}Be. Ainsi, les trois isotopes de carbone riches en neutrons de masse impaire liés ^{15,17,19}C présentent tous un halo d'un neutron dans l'état de configuration $1s_{1/2}$ [39; 40].

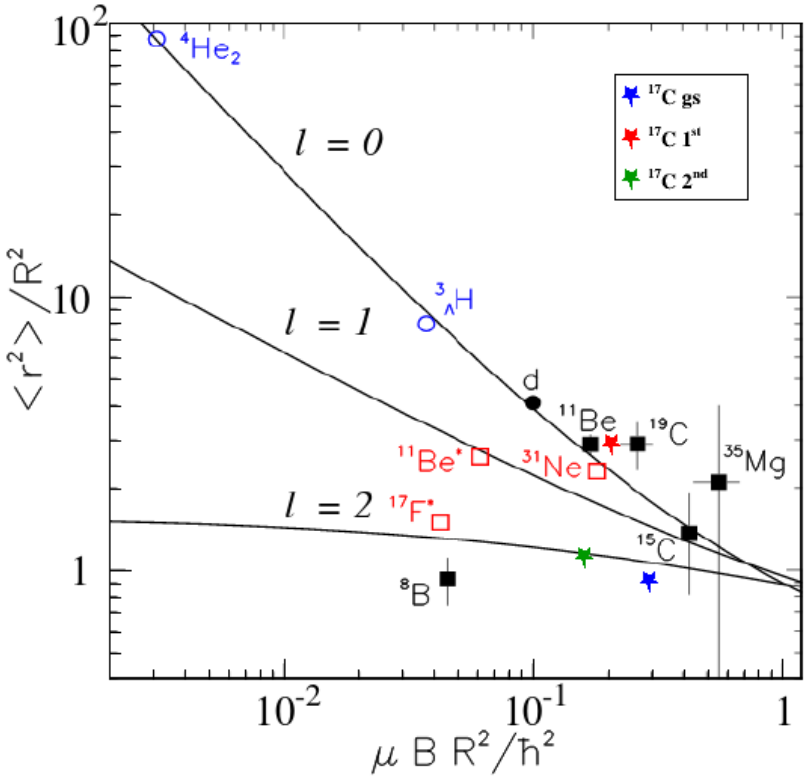

Figure E.5: Loi d'échelle proposée par K. Riisager pour halos d'un neutron ou d'un proton. Le point noir représente le deuton, les cercles bleus et les carrés rouges vides indiquent les modélisations et calculs théoriques, tandis que les carrés noirs vides sont déduits de données expérimentales. Les étoiles bleue, rouge et verte représentent respectivement l'état fondamental et les premier et deuxième états excités du ^{17}C (Adapté de [91])

D'un autre côté, l'état fondamental et le deuxième état excité du ^{17}C ne présentent pas de halo, malgré leur faible énergie de séparation. Le fait que le neutron de valence occupe une orbitale avec un moment angulaire ℓ relativement grand donne lieu à une augmentation de la barrière centrifuge qui confine beaucoup plus la fonction d'onde du neutron et empêche la formation d'un halo.

Bibliography

[1] G. Gamow, *Mass Defect Curve and Nuclear Constitution*, Proceedings of the Royal Society A **126**, 632-644 (1930).

[2] C.F.V. Weizsäcker, *Zur Theorie der Kernmassen*, Zeitschrift für Physik **96** 7-8, 431–458 (1935).

[3] N. Bohr, J.A. Wheeler, *The Mechanism of Nuclear Fission*, Phys. Rev. **56**, 426-450 (1939).

[4] K.S. Krane, *Introductory Nuclear Physics*, Wiley Sons, New York-Chichester, (1988).

[5] J. Lilley, *Nuclear Physics: Principles and Applications*, Wiley Sons, Manchester, (2001).

[6] B.L. Cohen, *Concepts of Nuclear Physics*, McGraw-Hill, New York, (1971).

[7] J.H. Bartlett, *Nuclear Structure*, Nature **130**, 165 (1932).

[8] W.M. Elsasser, *Sur le principe de Pauli dans les noyaux*, J. Phys. Radium **4**, 549-556 (1933).

[9] M. Goeppert Mayer, *On Closed Shells in Nuclei*, Phys. Rev. **74** 3, 235-239 (1948).

[10] M. Goeppert Mayer, *On Closed Shells in Nuclei II*, Phys. Rev. **75**, 1969 (1949).

[11] O. Haxel, J.H.D. Jensen, H.E. Suess, *On the "Magic Numbers" in Nuclear Structure*, Phys. Rev. **75**, 1766 2 (1949).

[12] R.D. Woods, D.S. Saxon, *Diffuse Surface Optical Model for Nucleon-Nuclei Scattering*, Physical Review **95** (2), 577–578 (1968).

[13] O. Sorlin, M.G. Porquet, *Nuclear magic numbers: New features far from stability*, Prog. Part. Nucl. Phys., **61**, 602 (2008).

[14] Y. Utsuno *et al.*, *Varying shell gap and deformation in N 20 unstable nuclei studied by the Monte Carlo shell model*, Phys. Rev. C **60**, 054315 (1999).

[15] T. Otsuka *et al.*, *Frontiers and challenges of nuclear shell model*, Eur. Phys. J A **15**, 151-155 (2002).

[16] T. Otsuka *et al.*, *Novel Features of Nuclear Forces and Shell Evolution in Exotic Nuclei*, Phys. Rev. Lett. **104**, 012501 (2010).

[17] T. Otsuka *et al.*, *Three-Body Forces and the Limit of Oxygen Isotopes*, Phys. Rev. Lett. **105**, 032501 (2010).

[18] A. Ozawa *et al.*, *New Magic Number, $N = 16$, near the Neutron Drip Line*, Phys. Rev. Lett., **84**, 5493 (2000).

[19] Z. Elekes *et al.*, *Spectroscopic Study of Neutron Shell Closures via Nucleon Transfer in the Near-Dripline Nucleus ^{23}O*, Phys. Rev. Lett., **98**, 102502 (2007).

[20] C. R. Hoffman *et al.*, *Determination of the N=16 Shell Closure at tje Oxygen Drip Line*, Phys. Rev. Lett., **100**, 152502 (2008).

[21] C. R. Hoffman *et al.*, *Evidence for a doubly magic ^{24}O*, Phys. Lett. B, **672**, 17-21 (2009).

[22] B. Fernández-Domínguez *et al.*, *Emergence of the N=16 shell gap in ^{21}O*, Phys. Rev. C **84**, 011301 (2011).

[23] J. R. Terry *et al.*, *Direct evidence for the onset of intruder configurations in neutron-rich Ne isotopes*, Phys. Lett. B, **640**, 86 (2006).

[24] W. N. Catford *et al.*, *Migration of Nuclear Shell Gaps Studied in the $d(^{24}Ne,p\gamma)^{25}Ne$ Reaction*, Phys. Rev. Lett. **104**, 192501 (2010).

[25] S. M. Brown *et al.*, *Low-lying neutron* f p*-shell intruder statse in ^{27}Ne*, Phys. Rev. C **85**, 011302 (2012).

[26] M. Stanoiu *et al.*, *N=14 and 16 shell gaps in neutron-rich oxygen isotopes*, Phys. Rev. C, **69**, 034312 (2004).

[27] M. Stanoiu *et al.*, *Disappearance of the N=14 shell gap in the carbon isotopic chain*, Phys. Rev. C, **78**, 034315 (2008).

[28] V. Maddalena *et al.*, *Single-neutron knockout reactions: Application to the spectroscopy of $^{16,17,19}C$*, Phys. Rev. C, **63**, 024613 (2001).

[29] Y. Kondo *et al.*, *One-neutron removal reaction of ^{18}C and ^{19}C on a proton target*, Phys. Rev. C, **79**, 014602 (2009).

[30] Z. Elekes *et al.*, *Low-lying excited states in $^{17,19}C$*, Nucl. Phys. A, **675**, 559-571 (2000).

[31] H.G. Bohlen *et al.*, *Spectroscopy of ^{17}C and $(sd)^3$ structures in heavy carbon isotopes*, Eur. Phys. J A **31**, 279-302 (2007).

[32] D. Suzuki *et al.*, *Lifetime measurements of excited states in ^{17}C: Possible interplay between collectivity and halo effects*, Phys. Lett. B, **666**, 222 (2008).

[33] D. Smalley *et al.*, *Lifetime measurements of ^{17}C excited states and three-body and continuum effects*, Phys. Rev. C, **92**, 064314 (2015).

[34] H. Ueno *et al.*, *β-delayed neutron and γ-ray spectroscopy of ^{17}C utilizing spin-polarized ^{17}B*, Phys. Rev. C, **87**, 034316 (2013).

[35] S. Kim *et al.*, *Invariant Mass Spectroscopy ^{17}C via One-neutron Knockout Reaction of ^{18}C*, JPS Conf. Proc., **6**, 030031 (2015).

[36] Y. Satou *et al.*, *Unbound excited states in $^{19,17}C$*, Phys. Lett. B, **660**, 320 (2008).

[37] M. Wang *et al.*, *The AME2012 atomic mass evaluation*, Chinese Physics C, **36**, 1603-2014 (2012).

[38] N.A. Orr, *Halo nuclei*, Few-Body Systems Suppl., **10**, 243-252 (1999).

[39] D.Q. Fang *et al.*, *One-neutron halo structure in ^{15}C*, Few-Body Systems Suppl., **10**, 243-252 (1999).

[40] D. Bazin *et al.*, *One-Neutron Halo of ^{19}C*, Phys. Rev. Lett. **74**, 18 (1995).

[41] W. Horiuchi, Y. Suzuki, *^{22}C: An s-wave two-neutron halo nucleus*, Phys. Rev. C, **75**, 034311 (2006).

[42] I. Tanihata *et al.*, *Measurement of interaction cross sections using isotope beams of Be and B and isospin dependence of the nuclear radii*, Phys. Lett. B, **206**, 592-596 (1988).

[43] R. Lewis, A. C. Hayes, *Deuteron stripping as a probe of the proton halo in ^{17}F*, Phys. Rev. C, **59**, 2 (1998).

[44] R. Morlock *et al.*, *Halo Properties of the First $1/2^+$ State in ^{17}F from the ^{16}O(p,γ)^{17}F Reaction*, Phys. Rev. Lett., **79**, 20 (1997).

[45] R.M. Eisberg, *Fundamentals Of Modern Physics*, John Wiley and Sons, New York, (1961).

[46] L.I. Schiff, *Quantum Mechanics*, McGraw-Hill, New York, (1968).

[47] J.G. Camacho, A.M. Moro, *A Pedestrian Approach to the Theory of Transfer Reactions: Application to Weakly-Bound and Unbound Exotic Nuclei*, Euroschool on Physics with Exotic Beams, Vol. **IV**, 39-66, Springer (2014).

[48] R.C. Johnson, P.J. Soper, *Contribution of Deuteron Breakup Channels to Deuteron Stripping and Elastic Scattering*, Phys. Rev. C, **1**, 976-990, (1970).

[49] R.C. Johnson, P.C. Tandy, *An approximate three-body theory of deuteron stripping*, Nucl. Phys. A, **235**, 56, (1974).

[50] G.F. Knoll, *Radiation Detection and Measurement*, John Wiley and Sons, New York, (2000).

[51] M. Huyse, *The Why and How of Radioactive-Beam Research*, Lect. Notes Phys., **651**, 1-32 (2004).

[52] P. Van Duppen, *Isotope Separation On Line and Post Acceleration*, Euroschool Lectures on Physics with Exotic Beams, Vol. **II**, 37-77, Springer (2005).

[53] David J. Morrissey, Brad M. Sherill, *In-Flight Separation of Projectile Fragments*, Euroschool Lectures on Physics with Exotic Beams, Vol. **I**, 113-135, Springer (2004).

[54] *LISE presentation*, (2004). Available at `http://pro.ganil-spiral2.eu/laboratory/experimental-areas/lise`.

[55] J.F. Ziegler, M.D. Ziegler, J.P. Biersack, *SRIM - The stopping and range of ions in matter (2010)*, Nucl. Instrum. Methods Phys. Res. B, **268**, 1818 (2010). Toolkit available at `http://srim.org/`.

[56] M.J. Berger, J.S. Coursey, M.A. Zucker, J. Chang, *ESTAR, PSTAR, and ASTAR: Computer Programs for Calculating Stopping-Power and Range Tables for Electrons, Protons, and Helium Ions*, version 1.2.3 (2005). Available at `http://physics.nist.gov/Star`.

[57] S. Ottini-Hustache *et al.*, *CATS, a low pressure multiwire proportionnal chamber for secondary beam tracking at GANIL*, Nucl. Instrum. Methods Phys. Res. A, **431**, 476 (1999).

[58] K.Lau, J. Pyrlik, *Optimization of centroid-finding algorithms for cathode strip chambers*, Nucl. Instrum. Methods Phys. Res. A, **366**, 298 (1995).

[59] F. Delaunay, *Structure des états du ^{11}Be excités par la réaction d(^{10}Be,p)^{11}Be*, PhD Thesis, Université Paris 6. (2003).

[60] T. Zerguerras, *Etude de l'emission proton et de deux protons dans les noyaux légers déficients en neutrons de la région A=20*, PhD Thesis, Université Pierre et Marie Curie - Paris VI. (2001).

[61] M. Labiche *et al.*, *TIARA: A large solid angle silicon array for direct reaction studies with radioactive beams*, Nucl. Instrum. Methods Phys. Res. A, **614**, 439 (2010).

[62] Micron Semiconductor, *Silicon Detectors Catalogue.*

[63] A. Matta, *Study of the very neutron-rich ^{10}He by one-proton transfer reaction $^{11}Li(d,^3He)$*, PhD Thesis, Université Paris-Sud XI. (2012).

[64] J. Simpson *et al.*, *The EXOGAM Array: A Radioactive Beam Gamma-Ray Spectrometer*, Acta Physica Hungarica A - Heavy Ion Physics, Vol. **11**, Nr. 1-2, 159-188, (2000).

[65] National Nuclear Data Center, *^{60}Co β^- decay radiation results*, (2013). Available at `http://www.nndc.bnl.gov/useroutput/AR_5EC10BA5F80BE602C2D10820743B12A7_2.html`

[66] National Nuclear Data Center, *^{133}Ba ϵ decay radiation results*, (2011). Available at `http://www.nndc.bnl.gov/useroutput/AR_5EC10BA5F80BE602C2D10820743B12A7_3.html`

[67] National Nuclear Data Center, *^{152}Eu β^- and ϵ decay radiation results*, (2013). Available at `http://www.nndc.bnl.gov/useroutput/AR_5EC10BA5F80BE602C2D10820743B12A7_5.html`

[68] Rene Brun, Fons Rademakers, *ROOT - An Object Oriented Data Analysis Framework*, Nucl. Instrum. Methods Phys. Res. A, **389**, 81-86 (1997). See also `http://root.cern.ch/`

[69] I. J. Thompson, *Fresco, Coupled Reaction Channels Calculations*, See also `http://www.fresco.org.uk/`

[70] R. L. Varner *et al.*, *A global nucleon optical model potential*, Phys. Rep., **201**, 57 (1991).

[71] A. Koning and J.P. Delaroche, *Local and global nucleon optical models from 1 keV to 200 MeV*, Nucl. Phys. A, **713**, 231-310 (2003).

[72] B. A. Watson, P. P. Singh and R. E. Segel, *Optical Model Analysis of Nucleon Scattering from 1p-Shell Nuclei between 10 and 50 MeV*, Nucl. Instrum. Methods Phys. Res. A, **614**, 439 (2010).

[73] W. W. Daehnick, J. D. Childs and Z. Vrcelj, *Global optical model potential for elastic deuteron scattering from 12 to 90 MeV*, Phys. Rev. C, **21**, 2253-2274, (1980).

[74] Haixia An and Chonghai Cai, *Global deuteron optical model potential for the energy range up to 183 MeV*, Phys. Rev. C, **73**, 054605, (2006).

[75] J. Bojowald *et al.*, *Elastic deuteron scattering and optical model parameters at energies up to 100 MeV*, Phys. Rev. C, **38**, 1153-1163, (1988).

[76] E. Newman *et al.*, *Deuteron elastic scattering at 34.4 MeV*, Nucl. Phys. A, **100**, 225-235 (1967).

[77] L. Grassi *et al.*, *Elastic scattering studies of* ^{16}C *at 50 MeV/A on proton and deuteron targets with the CHIMERA multidetector at INFN-LNS*, J. Phys.: Conf. Ser., **381**, 012088 (2012).

[78] S.N. Mukherjee *et al.*, *Deuteron breakup in the field of a heavy target*, Phys. Rev. C, **29**, 1095 (1984).

[79] Y. Sakuragi, *Energy and target dependence of projectile breakup effect in elastic scattering of* ^{6}Li, Phys. Rev. C, **35**, 2167 (1987).

[80] A. Bonaccorso and F. Carstoiu, *Optical potentials of halo and weakly bound nuclei*, Nucl. Phys. A, **706**, 322-334 (2002).

[81] J. A. Tostevin, *University of Surrey version of the code TWOFNR (M. Toyama, M. Igarashi and N. Kishida)*, See also `http://www.nucleartheory.net/NPG/code.htm`

[82] R.C. Johnson, P.C. Tandy, *An approximate three-body theory of deuteron stripping*, Nucl. Phys. A, **235**, 56-74 (1974).

[83] Jenny Lee, M.B. Tsang and W.G. Lynch, *Neutron Spectroscopic Factors from Transfer Reactions*, Phys. Rev. C, **75**, 064320 (2007).

[84] S. M. Brown, *Neutron Shell Breaking in Neutron-Rich Neon Isotopes*, PhD Thesis, University of Surrey. (2010).

[85] B. A. Brown, *Effective interactions for the* 0p1s0d *nuclear shell-model space*, Phys. Rev. C, **46**, 923-944 (1992).

[86] E. K. Warburton and B. A. Brown, *Effective interactions for the* 0p1s0d *nuclear shell-model space*, Phys. Rev. C, **46**, 923-944 (1992).

[87] T. Suzuki and T. Otsuka, *Exotic Magnetic Properties in* ^{17}C, Phys. Rev. C, **76**, 061301 (2008).

[88] J. Snyder *et al.*, *First observation of* ^{15}Be, Phys. Rev. C, **88**, 031303 (2013).

[89] J.L. Wiza and R. Middleton, *Study of* O^{19} *by the* $O^{17}(tp)O^{19}$ *and* $O^{18}(d,p)O^{19}$ *Reactions**, Phys. Rev. **143** 3, 676-682 (1966).

[90] J.L. Wiza and R. Middleton, *(d,p) Reaction on* ^{20}Ne, Phys. Rev. C, **3** 4, 1696-1698 (1971).

[91] K. Riisager, *Nuclear Halos and Experiments to Probe Them*, Lect. Notes Phys., **700**, 1-36 (2006).

[92] GEANT4 Collaboration (S. Agostinelli et al.), *GEANT4: A Simulation toolkit*, Nucl. Instrum. Methods Phys. Res. A, **506**, 250-303 (2003). See also `https://geant4.web.cern.ch/geant4/`